UNIVERSITY OF CATANIA

International Ph.D. in Chemical Sciences

XXXVI Cycle

Noemi Bognanni

NANOPARTICLES BASED ON CYCLODEXTRINS FOR BIOMEDICAL APPLICATIONS

Ph.D. Thesis

Coordinator: Prof. Salvatore Sortino

Tutor Prof.ssa: Graziella Vecchio

2020-2023

Table of Contents:

ABSTRACT

Nowadays scientists are looking to investigate new macro- or nanoscale systems to improve the efficacy of traditional therapy, mainly in patients with chronic diseases requiring long-term or even lifetime therapy. The most common side effects are linked to the toxicity of drugs and low bioavailability in the organism.

In this regard, new systems based on Cyclodextrin were designed and characterized. These were exploited and investigated as delivery systems for drugs or as nanotherapeutics to overcome the limitations of topical medicines.

Cyclodextrins, oligosaccharides with a truncate cone structure, were selected as the principal strategy exploit in this project. Their peculiarity is not only the encapsulation of lipophilic drugs but also their application as potential therapeutic nanocapsules. Moreover, cyclodextrin is a biocompatible system that shows low toxicity.

In light of this, the present work has the objective of investigating the role of the cyclodextrin cavity in different biological applications.

The first part of the thesis analyzed cyclodextrins as drug delivery systems, starting from dimers to linear or crosslinked polymers. All systems were designed and synthesized with β and γ cyclodextrin to investigate the role of the cavity, the backbone and specific target moieties chosen to increase the uptake.

The results have proven that some systems can increase the antiproliferative activity of drugs *in vitro*.

In the second part, the focus was the introduction of chelator units in cross-linked cyclodextrin polymers. In this way, the polymer can target and

overcome the problem of metal dyshomeostasis. The nanochelators can act in the bowel and may exceed systemic toxicity problems.

Finally, the last part was carried out in collaboration with the University of Boku in Wien. The project was based on the synthesis and study of metal nanoparticles coated with cyclodextrin polymers and a labeling unit. The internalization through the blood-brain barrier and the cholesterol-mopping action were studied *in vitro* proving a better action compared to free polymer alone.

INTRODUCTION

1. NANOPARTICLES

In the last century, nanoparticles (NPs) have fascinated scientists in particular for biomedical applications [1].

"Nano" is a prefix that describes materials with dimensions less than 100 nm in diameter. This term was introduced by physics Richard P. Feynman in 1959 when he famously stated, "There is plenty of room at the bottom" [2]. With Feynman began the revolutionary method based on the idea of manipulating matter at the atomic scale. This will lay the foundations in 1974 for introducing top-down theory [3] and only ten years later for the bottom-up approach when large systems are generated by atomic or molecular components. During the 20^{th} century, the concept of nanotechnology was born for the first time.

The advantage of particular NPs is the possibility to have good communication with the cell surfaces using the different biochemical and physiochemical properties of this last. One widely spread application of NPs is drug delivery (DD) or imaging [2]. In order to exploit the advantages of NPs is necessary to control the biostability, biocompatibility, and selectivity at a specific site in the body for systemic administration. Another important advantage to the use of NPs is the possibility to increase the concentration of the therapeutic substance in the specific pathological site of an organism, as well as the control of their size to evade the body's immune system, enabling them to circulate in the blood for a longer time [4]. These important characteristics of NPs enable using, active and passive targeting to interact with a cell or a tissue.

There are several types of NPs which can be classified according to their size, morphology, and physical and chemical properties (Figure 1). Typically,

the different nature of the NPs was linked to their function. Among the most used NPs, there are Carbon-based NPs, Inorganic NPs, Protein NPs, Polymeric NPs and Lipid NPs (Figure 1) [5].

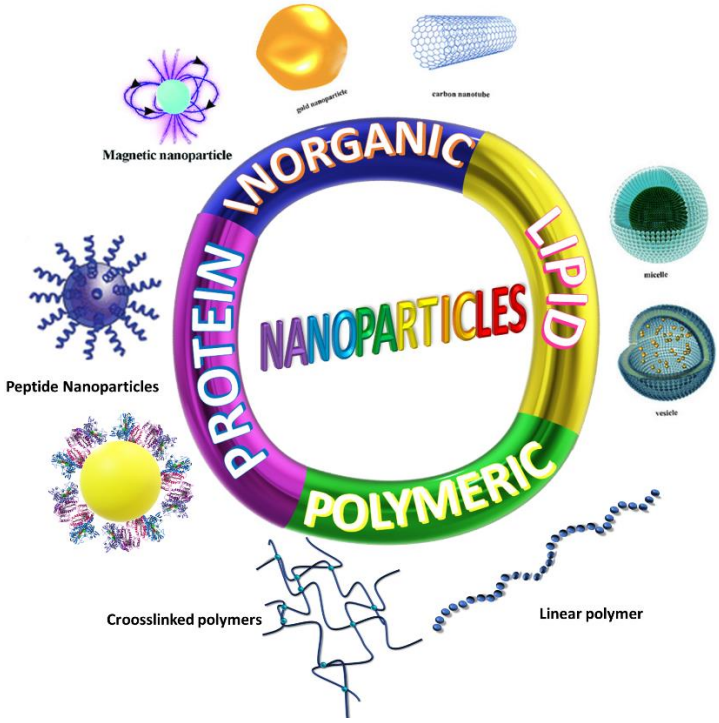

Figure 1. Types of Nanoparticles

1.1. POLYMERIC NANOPARTICLES

Polymeric NPs could be used as a drug delivery system (DDS) [6] in order to improve the selectivity, pharmacokinetic proprieties, drug solubility and safety administration.

In 1906, Ehrlich developed the theory of the "Magic bullet", based on the concept of the carrier. Subsequently, Helmut Ringsdorf designed the first model of "Polymer Therapeutics", which presents a polymer as a backbone. This polymer was used to introduce different units (Figure 2) in three main

areas: solubilizing residue, drug and targeting moiety. The first was the macromolecule soluble and nontoxic which fulfills the purpose of enhancing hydrophilicity [7], the second was the pharmakon and the third incorporated a transport system, which carried the whole polymer to the target cells [8].

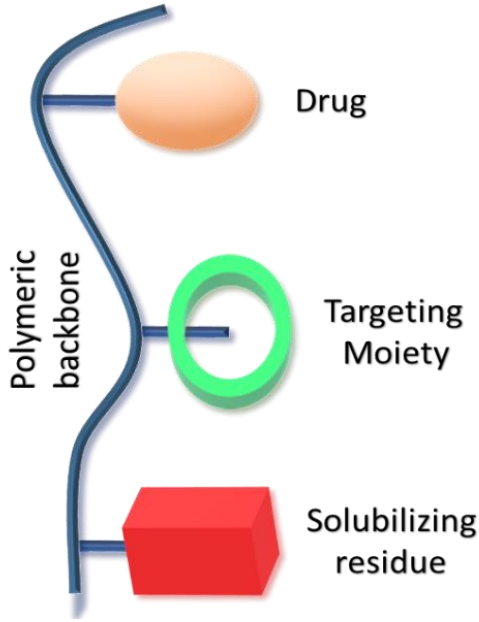

Figure 2. Therapeutic Polymers

The challenge of researchers is to reduce the side effects of drugs increasing the selectivity in a specific area of the organism. In fact, all types of drugs, with any type of dosage, can not carry out their action if they do not reach the specific site. Very often the drug is not active because it fails to reach the site of interest [9]. In this regard, the concept of "vectorization" has been developed, aiming to enhance the bioavailability of drugs or genes.

The polymeric NPs may exploit different strategies to increase the internalization in tumor cells. These include the synthesis of stimulus-sensitive nanocarriers [10], active targeting by the targeting moiety grafted on

the polymeric backbone and passive targeting achieved through the control of NP dimensions [11, 12].

There is a slight difference between the semi-permeability of the membrane of healthy and tumor cells, but this difference is useful to project NPs with a specific dimension capable of increasing the permeability. For this reason, NPs with a size of 50-200 nm are easy to be absorbed by tumor tissues via the Enhanced Permeability and Retention (EPR) effect [13].

For this purpose, it is important to modulate the size of the NPs to facilitate not only easier internalization but also better blood circulation. Larger sizes allow for circulation that is more prolonged but smaller particles make penetration into the tumor more effective [14]. Some studies show that the passive target is promoted using polymers with a mass of approximately 6×10^4 Da [15]. The higher molecular weight allows better absorption of the drug linked to NP than the drug alone [16]. This is possible especially in cancer cells because the condition of hypoxia produces an extravasation that leads to the formation of new vessels. Moreover, the NPs exploit the long retention in the body improving the pharmacokinetics and the selectivity of the drug. Conversely, small drugs alone can not use this unique feature because they are fast washout from the body [17]. Another advantage was proven by using polyamines and lipids for siRNA delivery [18]. Polymers were found to prolong gene transfer and increase penetration through the bladder barrier [19].

Recently, different strategies of synthesis were developed to prepare various NPs with disparate sizes and shapes. Different types of polymers may be designed: covalent crosslinked, linear, or branched polymers.

An example of a linear polymer is PGA, a homopolyamide of glutamic acid, which can exist in two different structures poly(α-L-glutamic acid) and poly(γ-L-glutamic acid). The difference among these is in the bonding pattern

between the amino and carboxyl groups. More precisely, the poly(α-L-glutamic acid) is characterized by amide linkages between α-amino and α-carboxyl groups [20], while in the poly(γ-L-glutamic acid), amide linkages form between α-amino and γ-carboxyl groups [21]. PGA is water-soluble, biodegradable and biocompatible, it degrades in water with hydrolytic enzymes secreted by fungi and bacteria [22, 23].

The presence of anionic carboxyl groups offers weak interactions with chemotherapeutic cationic drugs, such as Doxorubicin (Dox), without the need for covalent conjugation [24, 25]. The PGA-Dox complex can release Dox in a pH-dependent way (about 2.2) [26]. Another important advantage of this polymer is its capability to sustain drug release at the site of action, improve drug stability and enhance intracellular uptake [27]. Furthermore, it is possible to graft the PGA polymer with target units in order to increase active cellular uptake; an example is the system, in which folic acid (FA) was introduced as a target, along with deep eutectic solvents, to form micelle. This system, DES-g-PGA-FA micelles had demonstrated to increase *in vitro* the release of Paclitaxel [28]. Another example is the conjugation of PGA to epidermal growth factor receptor (EGFR) [29] antibody target to colon cancer cells, which presents a high over-expression of EGFR. Comparing the two systems; with and without EGFR; was observed that the targeted NPs enhanced the tumor-selective therapeutic efficacy for colon cancer.

1.1.2. TARGETED NPs FOR ACTIVE UPTAKE

The presence of specific receptors expressed by the cell allows an easier crossing of biological barriers by target molecules [30].

For this reason, is important to study the areas of the organism on which a specific gene or drug acts, in order to insert in the nanocarrier target molecules that are more expressed only by specific types of cells (Figure 3) [31]. This allows to increase the availability of the drug but also to reduce its toxicity.

In this connection is possible to select specific small molecules involved in the normal growth of the cells. The object is the recognition and binding among the targeting moiety and the surface receptors overexpressed on the cancer cells or in the tumor microenvironment [32].

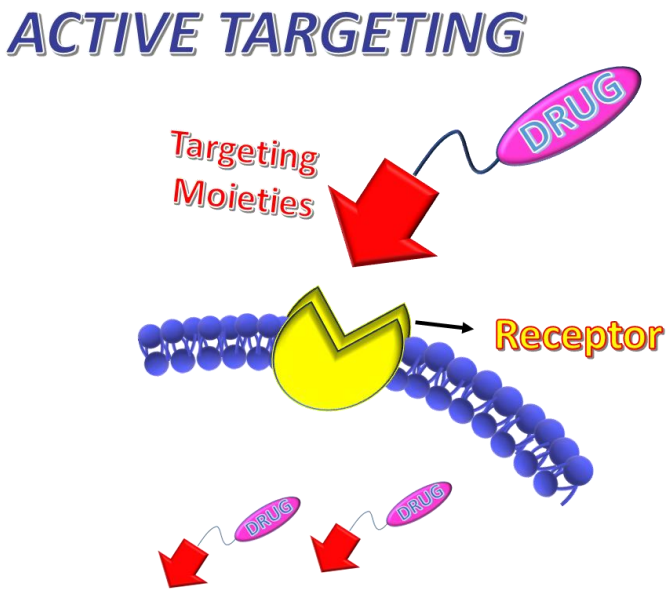

Figure 3. Target-Receptor recognition for active transport

Among the various receptors, the transferrin receptor is certainly of great importance. Transferrin (Tf) is an iron-binding blood glycoprotein that can facilitate the uptake of NPs to cancer cells via a receptor-mediated endocytosis pathway [33]. This protein is recognized by the transferrin receptors present in the blood-brain barrier (BBB). In the last years, Tf has

been used in the delivery of drugs/genes and therapeutic peptides or proteins into the brain [34, 35].

Another important molecule employed for active targeting is RGD. RGD is a tripeptide (arginine-glycine-aspartic acid) with a structural recognition motif for cell surface integrins, including $\alpha_v\beta_3$ (highly upregulated in vascular cells of tumors while minimal expression is found in resting or normal blood vessels) and $\alpha_5\beta_1$, that are associated with the process of anchoring cells to the extracellular matrix. These cell surface receptors are universally expressed by tumor cells and by normal cells. It is important to stress that integrins constitute an important class of cell adhesion receptors responsible for cell-matrix adhesion and for signaling bidirectional across the membrane. Integrins are involved in many biological processes, such as angiogenesis, thrombosis, inflammation, osteoporosis and cancer [36]. Studies have shown that to increase tumor-specific targeting delivery, it is possible to use, in addition to conventional RGD peptide, another bifunctional internalizing RGD peptide (iRGD) [37].

Other targeting systems that can be used are vitamins, such as Biotin (Bio) and folate. Bio is a vitamin of family H or B7, which is involved in different biological processes, including fatty acid synthesis, gluconeogenesis, amino acid metabolism and the growth of the cell [38]. It is well known that cancer cells are subject to a faster cell cycle than healthy cells; for this reason, Bio, being a cofactor for a wide range of carboxylases, is a necessary vitamin for cancer growth. It has been observed that the receptors for Bio SMVTs (Sodium-Dependent Multi-Vitamin Transporters) are among the most present on the surface of the cancer cells. Mammals, unlike bacteria, are not able to synthesize Bio. For this reason, it must be introduced exogenously via intestinal absorption. Following the above, high levels of expression have been found in intestinal and liver epithelial cells, including Caco-2 and HepG-

2 [39]. Another example of a vitamin used as a target unit is folic acid (FA). The passive transport of FA through cell membranes in physiological conditions is minimal. At physiological pH, FA has two groups of carboxylic deprotonated: the ionic molecule is poorly permeable to the membrane. In view of active transport, FA can recognize its specific receptor, folic receptors (FR) that in cancer cells are present on the cell surface in a variable percentage. Since folate is needed in the synthesis of nucleotide bases, and since rapidly dividing cells require nucleotide bases to replicate their DNA [40]. On the contrary, in healthy cells, there is a low expression of this receptor, which is observed only on macrophages, in the kidneys and at low levels in the thyroid.

In all tissues where the receptors of FR are expressed, it has been observed to internalize the attached vitamin/vitamin-conjugate via a process termed receptor-mediated endocytosis.

Another important feature that makes this vitamin an excellent targeting agent is that folate moiety maintains its affinity for the receptor even when the γ carboxylic group is involved in bonds with other molecules conjugated to it [41].

Molecules that allow better cell uptake also include positively charged systems. NPs positively charged can interact with negative charges of drugs or with oligonucleotides [42, 43]. The oligonucleotides are small fragments of RNA, about these, there is a short interfering RNA (siRNA) that is proving to be an excellent candidate for the fight against cancer; in fact, such fragments of oligonucleotides can down-regulate specific proteins by performing the silencing of the latter. The interaction between siRNA and positively charged systems can increase the internalization of the oligonucleotide but also prevent it from being degraded by the nucleases and promote its accumulation in the cells of interest [44].

Moreover, to exploit the active targeting effect, it is possible to utilize specific polymers that can recognize receptors, including for example hyaluronic acid (HA) [45]. HA is an endogenous polysaccharide composed of a repeating disaccharide of D-glucuronic acid and N-acetyl-D-glucosamine linked by β (1→3) and (1→4) linkages [46]. This polymer is the principal component of the extracellular matrix (ECM) and, is involved in different biological processes; such as cell proliferation, cell migration and the inflammatory state of the ECM. The biological activities change in function of the molecular weight of the polymer [47].

HA can have different molecular weights, the acronym LMW (lower than 200 kDa) [48] is used when it has a low molecular weight. On the other hand, if it has a higher molecular weight, it is indicated with HMW (more than 1000 kDa) [46]. In physiological conditions, the receptor of HA can interact with a polymer that has a weight of about 40-400 kDa, for this reason, the interaction with HALMW is associated with certain pathological conditions, including inflammation, cancer, and induction of angiogenesis [48]. HA can be recognized by different receptors (Figure 4) among these there are CD44, RHAMM for HA-mediated motility, and LYVE-1 a lymphatic vessel endothelial receptor-1, all of these are overexpressed on the surface of tumor cells. Furthermore, other receptors not specific to HA, can interact with it; an example is the TRL-4 (Toll-Like Receptor), a component of the innate immune system, distributed in the gastrointestinal tract [49]. Studies have shown that the interaction between HA-CD44 and HA-TRL-4 has increased cell proliferation, especially, since this last had an important role against cellular apoptosis in colon cancer [50].

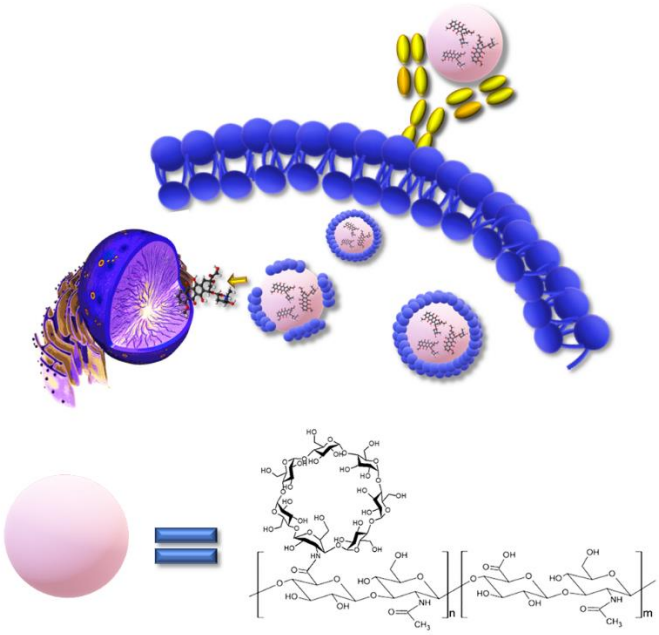

Figure 4. Active targeting between HA and CD44

The CD44 receptor is the most abundant and it belongs to a family of cell adhesion molecules (CAMs) [51]. It is a broadly distributed transmembrane glycoprotein that plays a critical role in malignant cell activities, including adhesion, migration, invasion, and survival. It is also strongly implicated in the cell signaling cascades associated with cancer initiation and progression. CD44 is a key component in the internalization and metabolism of HA and is endogenously expressed at low levels on various cell types in normal tissues. Tumor-derived cells, however, express CD44 in a high-affinity state that can promote the binding and internalization of HA [49]. In addition, significant CD44 cleavage increases were found in many cancers, 58% of gliomas, 67% of breast cancer, 45% of breast cancer not small cell pulmonary tumors, 90% of colon carcinomas and 25% of ovarian carcinomas [52].

HA has good biocompatibility, biodegradability, and nonimmunogenicity [49, 53]. Moreover, HA can be coated with positively charged nanocarriers and can achieve improved antitumor efficacy by releasing the drugs after specific stimuli, such as redox reactions or acidic pH of the tumor microenvironment that is in the range of 6.4-6.8 [54]. HA conjugation allows for an increase in drug solubility, stability in biological fluids, and enhanced blood circulation. HA-attached drugs/nanocarriers ensure increased drug accumulation specifically in CD44 overexpressing cancer cells. In addition to the targeting function, HA-modified delivery systems can enter cells more efficiently via the HA receptor-mediated endocytosis pathway [55]. One example is HA functionalized with Paclitaxel, which has proved as a good inhibitor of T47D human breast cancer cells compared to the drug alone [56]. Another important study has demonstrated that the conjugate of HA-oxalate-camptothecin, modified with nitroimidazole with the encapsulation of all-trans retinoic acid, can induce the differentiation of cancer stem-like cells. This, in turn, reduces stemness-related drug resistance, enhances the chemotherapeutic response, and suppresses cancer growth [57].

1.2. INORGANIC NANOPARTICLES

The inorganic NPs include different families of NPs such as quantum dots, metal, and magnetic NPs. The metal NPs include silver, platinum, and gold, which are employed in different biomedical applications. For instance, drugs are conjugated to gold NPs for controlled release using photothermal and photodynamic therapies [58]. Platinum NPs are commonly employed in electrocatalysis and induce the apoptosis of cancer cells, through DNA damage [59]. Recently, a system containing both gold and platinum has shown

efficacy against glioblastoma. This system seems to be an efficient drug nanocarrier, capable of enhancing anticancer activity by acting on targets EGFR and promoting the quality of life for the patients by minimizing conventional chemotherapy side effects [60]. On the other hand, silver NPs exhibit good antimicrobial properties and DD activity.

Another class is magnetic inorganic NPs broadly exploited in biomedical applications [61]. These NPs are characterized by an inorganic core of magnetic material. There are core-shell structures, where the metal core is coated with an organic layer, or multicore-shell structure, in which the outer coating is represented by an organic matrix. This inorganic core can exhibit ferromagnetic or superparamagnetic behavior. This characteristic enables interaction with a magnetic field, leading to their usage as contrast agents in magnetic resonance imaging (MRI), magnetically targeted DD, magnetically assisted gene transfection, magneto-mechanical actuators of cell surface receptors, magnetically triggered drug release and magnetic fluid hyperthermia (MFH) [62].

1.2.2. SPIONs

The broad field of application has heightened the interest of scientific society in the study of magnetic NPs, in particular for SPIONs. The acronyms indicate “Superparamagnetic iron oxide nanoparticles”. SPIONs are crystalline structures consisting of an iron oxide core that includes magnetite (Fe_3O_4), hematite (α-Fe_2O_3) and maghemite (γ-Fe_2O_3) [63]. The metal core surface normally is coated with organic materials, including polymers such as dextran, HA, poly (ethylene glycol) (PEG) or polypeptides. This shell modification provides stability in water or in physiological conditions and

prevents aggregation. The importance of core-shell lies in its hydrophobic nature, which facilitates the opsonization in the bloodstream by blood proteins, in order to facilitate aggregation. Consequently, this approach can improve the concentration in local tissues [64].

SPIONs can be used in different areas, from environmental to biomedical applications. However, to harness their full potential, it is essential to design them while paying attention to certain features. Therefore, it is important to control characteristics, including shape, size, hydrodynamic volume, surface charge and colloidal stability (Figure 5).

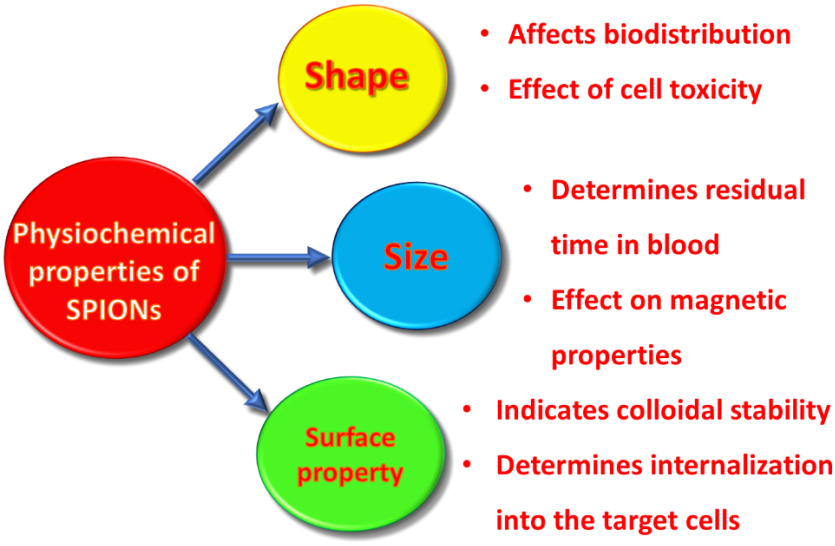

Figure 5. Physiochemical properties of SPIONs

The shape of the iron NPs was analyzed for the purpose of improving biodistribution. Studies have reported that rod-shaped and no spherical NPs show a longer blood circulation time compared to spherical particles [65–67]. Moreover, short-rods, which are more or less spherical, were found to accumulate in the liver and showed rapid clearance rates via urine, instead the long-rod-shaped NPs collected in the spleen and were hardly excreted.

Additionally, the shape was linked to cell toxicity. Nanosphere-shaped SPIONs indicated greater cellular toxicity compared with nanorods and colloidal nanocrystal clusters [68].

Regarding the time of circulation in the body, it depends on the size of the NPs. Particles with a smaller size of about 10 nm are removed by renal clearance, whilst particles with a dimension of 200 nm are more concentrated in the spleen or are phagocyted [64]. The optimum size is considered a range of 10-100 nm, this dimension ensures a long circulation and escape of the reticuloendothelial system in the body. The small size of SPIONs is also responsible for the enhanced permeability and retention effect, which leads to the concentration of the particles in the target tumor tissue. However, SPIONs with a particle size smaller than 2 nm are not suitable for medical use due to the increased potential of particles in this size range to diffuse through cell membranes, damaging intracellular organelles and thus exhibiting potentially toxic effects. Therefore, control of particle size during the preparation of SPIONs is of paramount importance.

Finally, the surface properties can increase the stability of the NPs. NPs with positive or negative charges have good dispersion stability. The surface charge is also important for increasing internalization in cells, a positive charge has proven to be more effective for internalization in human breast cancer cells than a negative charge SPION. For this reason, it is important to engineer the shell with polymers that are able to evade phagocytosis and increase the therapeutic efficacy [69].

These particles have been used for the diagnosis of progressive diseases using MRI and for therapy. Lately, SPIONs have been widely employed for drug or gene delivery to their site of action [70–72].

It is important to emphasize that the application of SPIONs in the biomedical field requires a sufficient internalization of NPs in the body for efficient treatment, therefore it is necessary to understand the risk associated with exposure to SPIONs [73]. In many cases is possible that the NPs can generate an adverse cellular response [74]. For this reason, numerous studies are focused on the analysis of maximum concentration that can ensure safety for a long time [75, 76]. It has been observed that uncoated SPIONs with different physiochemical properties do not present any toxicity at the concentration range < 100 μg ml^{-1} [77]. Other studies have shown that low doses of SPIONs (20.8 μg Fe_3O_4 Kg^{-1}), were completely cleared from the injection site in 3 weeks, indicating that these can be metabolized from the injection site. Nevertheless, SPIONs at high doses (520 μg Fe_3O_4 Kg^{-1}) have not been eliminated from the injection site, even up to 2 months [63]. Moreover, the iron NPs coated with tetramethylammonium 11-amino undecanoate (bipolar surfactant) are nontoxic to the glial cells at concentrations ranging from 0.1-10 μg mL^{-1} while cytotoxicity could be observed at 100 μg mL^{-1}. *In vivo* studies have shown that the NPs induced only mild side effects in a short duration. The SPIONs can be degraded by the liver, and after this, the iron will be used in the formation of red blood cells before being excreted via the kidneys. Researchers evaluated the toxicity in the organ tissue sections of iron NPs coated with silica [78]. Histological analysis showed that when the silica coated SPIONs were injected in experimental animals, no major organs showed lesions or necrosis until 7 weeks, and no signs of tissue toxicity were found. With the continuous development of SPION research, the challenge is to find a new system that increases biocompatibility [79].

1.2.2.1. MODIFICATIONS OF SPIONs

To prevent aggregation, precipitation and decrease the cytotoxicity of SPIONs, it is crucial to find a suitable coating. The best biocompatible coating should be able to be broken down into particles with diameters less than 5 nm, allowing excretion through the renal system with minimal cytotoxicity [80]. The coating can be based on a variety of materials including PEG, polyvinyl alcohol (PVA), HA, and dextran. Two examples are Sinerem and Endorem [81], the SPIONs coating with dextran that has demonstrated good biocompatibility. The two systems do not show any inflammation or toxicity at concentrations of 11.3 µg/ mL [80, 82]. In addition, dextran prevents the incorporation of SPIONs into hemoglobin and immediate degradation; in fact, degradation has been observed after about two months [83]. The presence of PEG polymer can increase the dimension of NPs [84] which translates to the extended circulation time in the blood. Additional evidence shows that PEG protects the NPs by cytotoxicity. Nevertheless, is important to control the size of PEG-coated SPIONs. Indeed, it was observed that when the size of the PEGylated SPIONs was increased as far as 129.3 nm and positively or negatively charged functionalization groups were introduced, an increase in inflammatory biomarkers, lipid peroxidation, and DNA damage was observed compared to the control mice [80]. Concerning PVA, it contains amino and carboxyl groups that can be used as an attachment point for proteins, peptides, antibodies and drugs. Additionally, this polymer can regulate the dimension of the NPs, obtaining a diameter of 45 nm. Toxicity studies have found that at low concentrations, about 6 or 24 µg of PVA-coated SPION, there are not immune responses *in vivo*. However, high concentrations induce an acute inflammatory response [85]. Another coating is represented by the conjugation of SPIONs with HA. This polymer is used to improve the uptake.

In the presence of HA, a decrease in T_2 transverse relaxation times has been observed, suggesting that HA-SPIONs could be used as a T_2 negative MRI contrast agent [86].

Finally, another strategy to enhance the active uptake is coating the SPIONs with target units, for example, FA. Two different studies have analyzed the efficiency of internalization in the presence of FA. Both have shown that in the MCF-7 cells, there is a higher level of NPs uptake. This could increase the efficiency of the DDS, for example, for Dox, but also significantly enhance signal intensities in the MRI technique [87, 88]. An example is the Fe_3O_4@PCA-PEG-FA system (Figure 6), which was obtained by precipitating Fe_3O_4 followed by coating with poly-citric acid (PCA) functionalized with PEG. Finally, the NPs were further surface functionalized with an FA as a targeting moiety.

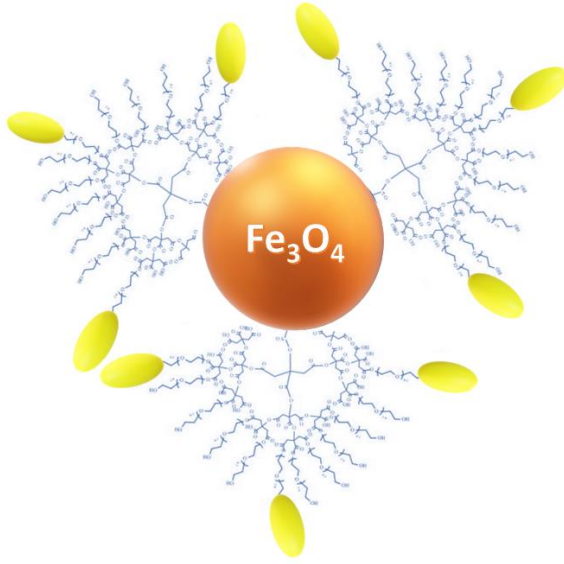

Figure 6. Schematic structure of Fe_3O_4@PCA-PEG-FA

The nanocarrier was analyzed for the delivery of Quercetin in two different cell lines: Hela and MDA-MB231. The data show that in the presence

of the nanocarrier, Quercetin exhibited greater toxicity compared to the drug alone, while the nanocarrier showed no apparent cytotoxicity against cancerous cell lines. Also, MRI studies prove that Fe_3O_4@PCA-PEG-FA NPs can be used as a negative contrast agent [89].

1.2.2.2. APPLICATIONS OF SPIONs

The SPIONs are considered NPs used for multimodal therapy, including magnetic targeting, hyperthermia, imaging, radiation and with a particular functionalization as chemotherapeutics, for photodynamic, cholesterol mopping activity and immunotherapy.

Radiotherapy and hyperthermia have complementary effects, in fact, the areas with poor perfusion are less sensitive to hyperthermia but resistant to ionizing radiation, which depends on the formation of toxic oxygen radicals. Therefore, these two techniques are usually combined. Regarding hyperthermia, heating is determined by the dimensions, structure, volume and concentration of NPs in the site of action. The ideal NP for hyperthermia has a high surface absorption rate, meaning that a small number of particles releases a large amount of heat in a short magnetization time window [90]. It is not yet established if size is the decisive factor in hyperthermia treatment. Studies show a change in results with an alteration of SPIONs' shape. It was observed that cubic SPIONs are more effective in hyperthermia than the spherical, but at high concentrations, they attempt to aggregate. Moreover, a substantial increase in temperature is not required to kill the cancer cells indeed, it could affect safety [91]. The mechanism of radiotherapy is based on the inhibition of DNA double strands and the binding of radionuclides to SPION-induced damage, promoting the apoptosis of target cells. Also,

SPIONs have shown their potential as X ray-enhancers for low-dose irradiation therapy. After radiation, the amount of toxic ROS in tumor cells with engulfed NPs substantially increases [92, 93].

The ideal SPIONs possess uniform physical and chemical properties to provide a homogenous signal via MRI [94, 95]. Currently, there are two different NPs based on SPIONs available in clinical, Feridex IV which thanks to the larger diameter, provides an increased negative contrast improving the result of imagining [95], and Ferumoxtran-10. This last has the advantage of being distributed to the reticuloendothelial system (RES) and lymph nodes [96]. SPIONs have a theranostic capability, in fact, they can give information about the progression of disease but at the same time, they can be used to administrate drugs because they can be phagocytized [97]. In addition to phagocytosis, SPIONs may also undergo a process that occurs more rapidly, called nanoparticle-induced endothelial leakiness where the SPION induces gaps of over 10 μm in size between endothelial cells by rearranging the cytoskeleton via the binding and phosphorylation of VE-Cadherin [98].

Moreover, the drug carried by SPIONs can be accumulated in a specific area using the external magnetic field. When the magnetic forces overcome the forces due to blood flow, the particle is absorbed in the tissue or in the organism of interest [99]. Nevertheless, this method is not entirely efficient because the release can not be fully controlled, so new techniques have been sought. A release that allows more control is achieved by changing the patient's physiological parameters such as temperature, pH, osmolality, etc [100]. The major limitation of DD is the external magnetic field strength; the necessary value exceeds the level suitable for the human body. However, this level can not generate a high enough magnetic gradient to control the targeted movement of NPs or to activate drug desorption because the magnetic gradient decreases with distance. Another problem that can occur in DD is a possible

agglomeration of magnetic NPs, especially as a result of the removal of the applied external magnetic field, due to their high surface energy. In addition, smaller NPs possess force weaker magnetic force. Thus, the ultrasmall size required for the NPs may result in greater difficulty in controlling the movement or position, especially in the presence of intense force due to the high blood flow [101]. Consequently, it is necessary to modify a metal core to avoid aggregation and protect the drug up to the area of interest but also to guide the NPs to a specific site.

1.3. NANOPARTICLES BASED ON CYCLODEXTRINS

Cyclodextrins (CyDs) have been widely used to build a variety of NPs. CyDs can overcome the limitations of NPs; increasing for example drug loading [102], while for magnetic NPs, CyDs could be used to stabilize them in an aqueous medium.

A multitude of NPs based on CyDs have been used as drug carriers for controlled and sustained drug release due to their controllable properties. CyDs have also been introduced into NPs because they have proven to be therapeutic agents, for example, they have shown good capabilities to deliver drugs or remove lipophilic molecules, such as cholesterol from cells [103–105].

In this context, it was observed that CyDs may directly interact with biological membranes, without readily penetrating them, in order to extract lipids such as cholesterol from cell membranes, thus modifying cell metabolism and functions [106].

Cholesterol is a component of the cell membrane that plays an essential role in physiological processes. Dyshomeostasis of this sterol can generate neurodegenerative diseases including Alzheimer's (AD), Parkinson's (PD), Huntington's disease (HD), and other atypical cognitive deficits that arise in old age [107]. Nowadays, CyDs and their derivates are widely employed in therapy. These molecules are able to improve solubility and disponibility. A lot of CyDs derivates such as KLEPTOSE®, CRYSMEB (βCyD 6 and 4 methyl groups, respectively) [106] and 2-hydroxypropyl-β-cyclodextrin (HPβCyD) are employed against different neurological disorders as well in the treatment of Niemann-Pick disease type C (NPC) [108]. NPC is a rare progressive genetic disorder characterized by an inability of the body to transport cholesterol and other fatty substances (lipids) inside cells. In NPC, the functional role of the protein regulating cholesterol trafficking in the cell is compromised, leading to an excessive accumulation of unesterified cholesterol in endolysosomes. This leads to the abnormal accumulation of these substances within various tissues of the body, including brain tissue. Symptoms of the disease change from person to person, and the disease can be fatal as early as the first months of life [109]. HPβCyD is a drug that is currently in phase I/II and phase II/III clinical trials for NPC treatment [110]. Other studies have been carried out using Nifedipine and Probucol on animal models, unfortunately, these drugs show a reduction of cholesterol in the liver but there is not improvement in brain pathology [111]. Probably the reason is linked to the possibility that the pharmacological agents used do not penetrate the BBB and, hence, do not affect the neurological progression of the disease [112].

1.3.1. CYCLODEXTRINS

CyDs, also called cycloamyloses, Schardinger dextrins, or Cycloglycopyranoses, are obtained through enzymatic degradation of amylose by the enzyme CyD glucosyl-transferase (CGTase) [113]. CyDs are cyclic oligosaccharides of D (1)-glucopyranosyl units linked by α-1, 4-glycosidic bonds, as in amylose.

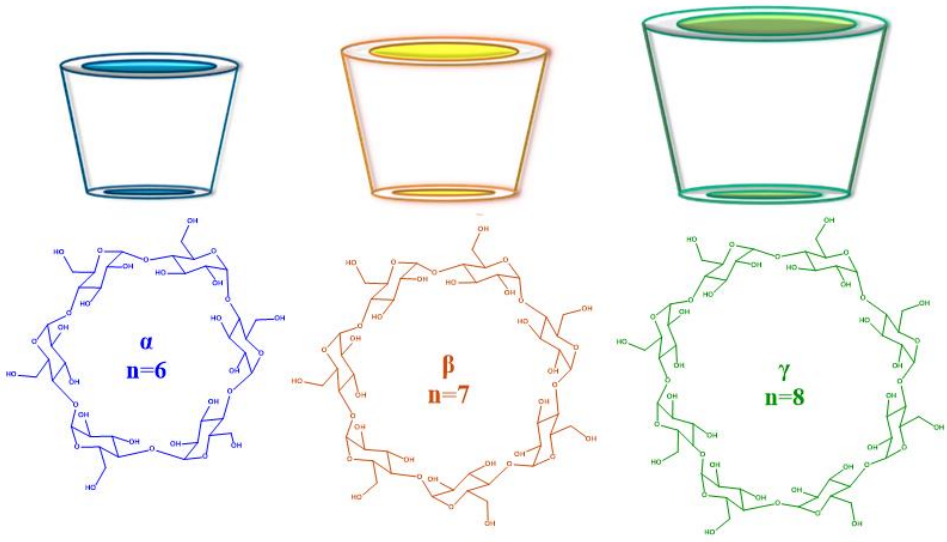

Figure 7. Three common structures of CyDs

The three most common structures are α, β and γ (Figure 7), which contain six, seven and eight glucose monomers in a ring [114]. All have a typical truncated cone structure, with a hydrophilic exterior and an inner hydrophobic cavity [115]. The larger opening of the molecule is surrounded by the secondary (C-2 and C-3, secondary rim) hydroxyl groups, while the primary (C-6, primary rim) hydroxyl groups constitute the smaller end of the cone. The presence of the primary and secondary hydroxyl groups on the outer

portion of the molecule makes the exterior face hydrophilic. The interior cavity, comprised of methylene linkages and glycosidic oxygen bridges, is relatively hydrophobic compared to polar solvents such as water. The OH groups are a point of structural modification and can be used to form cross-linked CyD polymers; each OH group has different reactivity [116].

α, β and γ CyDs have different and lower solubility than similar acyclic sugar molecules. This is understandable as the solid-state cyclic saccharides have high crystalline lattice energy.

Considering the three structures, the most rigid structure is βCyD, because it can form six H-bonds; this determines a reduced water solubility. On the other hand, this hydrogen bonding cycle is incomplete in αCyD because one glucopyranose unit is in a distorted position, forming only four hydrogen bonds; this structure increases the solubility. γCyDs have a more flexible non-planar structure and are the most water-soluble CyDs [117].

Furthermore, CyDs at millimolar concentration can form NPs in water with a size of about 200-300 nm [118]. The aggregation of these molecules has been studied with different techniques (DLS, TEM and NMR), identifying different shapes including spherical, rods and fibers [119, 120]. Despite this, the aggregates are metastable and affected by dilution, heating or solvent. For this reason, different methods are used to study their behavior in water and non-polar solvents. In this last class of solvents, the hydrodynamic diameter has been evaluated at about 80 nm with a very low polydispersity index. The electrostatic and dipolar forces stabilize the structures [121].

The most common structures are channels or cages. Cages can take shapes such as “herringbone” and “brick wall”, instead, the channel can be broken in two different orientations: head-to-head, or head-to-tail [120, 121].

Among the advantages of CyDs, one of the most important is definitely the capability to form inclusion complexes [122]. Molecular encapsulation may exist with different stoichiometry, stated in the order H/G, in which the CyD is the host (H) and the drug is the guest (G), the most common is 1:1, but are also known more other stoichiometries: 1:2, 2:1 and 2:2 [123].

In the aqueous environment, water molecules occupy the cavity of CyD, but other molecules can easily replace them. Furthermore, thanks to their chiral cavity can also act as chiral selectors, obtaining a complexation in a stereospecific way. The driving force for the formation of the H/G complex is determined by entropic and enthalpic contributions [124]. This produces a displacement of water molecules from the hydrophobic cavity of CyD, resulting in an increase in hydrogen bonds between solvent molecules. Simultaneously, it reduces the repulsive interactions between the hydrophobic guest molecule and the surrounding aqueous environment, and a rise of hydrophobic interactions when the guest molecule enters the apolar cavity of CyD. The formation of a complex between CyDs and poorly soluble molecules in an aqueous solution generates chemical-physical changes [125].

The forces that favor complexation are weak interactions; such as van der Waals interactions and hydrogen bonds [126].

Moreover, the capability of CyD to include lipophilic molecules can increase or inhibit their aggregation, modifying in some cases the binding strength [127]. The presence of CyDs can modify the drug aggregate, increasing the solubility in a particular solvent. An example is the addition of sulfobutiletereβCyDs in a solution of remdesivir, achieving the self-aggregation of the drug forming small clusters, stabilizing by 2-4 CyDs [128].

To enhance the complexation, it is also possible to use a single-cavity or multi-cavity system. The H/G interaction can be enhanced by modifying the OH groups of CyDs [129].

1.3.1.1. FUNCTIONALIZATION OF CYCLODEXTRINS

CyDs with different functionalization groups provide a very attractive approach, especially in the pharmaceutical field. Cavity modifications may increase the solubility in a specific solvent. CyD may be functionalized in one or more OH groups, at the primary or secondary rim [130]. The OH groups of CyD have different reactivity; 6-OH at the primary rim is more basic and more accessible to a reagent, in this position even the least reactive reagents can functionalize it. Conversely, the 2-OH is the most acid, and the 3-OH is the least accessible; they are usually functionalized only with very reactive agents [131].

The strategies to modify CyDs depend on the application. For example, whether the objective is to increase solubility for DD, such as HPβCyD, (Encapsin®) and sulphobutyl-ether- β CyD (Captisol®) used to improve the bioavailability of drugs [132].

A typical strategy to modify CyDs is the introduction of sulfonate groups. Is possible to obtain 6-sulfonate CyD or 2-sulfonate CyD [133]. 6-sulfonate can undergo a nucleophilic attack by iodide, azide, thiols, hydroxylamines, carboxylates, amines, and others [134].

2-sulfonate CyD can be obtained by tosylimidazole and can form with high-yield 3-functionalized CyD. The reaction is in three steps: the tosylation

at 2-OH, the formation of 3-manno-epoxide in a basic aqueous medium, and the opening of the epoxide by a nucleophile. During this third step, there is an inversion of the configuration of two chiral centers (C-2 and C-3) and the functionalized glucose rings of CyD become altrose units [134, 135].

Other examples are CyDs containing amphiphilic chains, including amphiphilic perfluoroβCyDs and perfluoroalkylthioβCyDs, investigated as oxygen carriers. These functionalized CyDs are obtained by protecting of the 6-OH groups, followed by esterification of 2- and 3-OH with decafluorooctanoyl chloride [136]. An application of this system is the formation of inclusion complexes with the prodrug, Molsidomine. The hydrophobic chains allow to retard the release of highly water-soluble drugs [137].

Furthermore, by modifying the cavity, it is possible to increase the interaction between the drugs and the CyD, a strategy is the synthesis of CyD dimers [138]. In the dimers, the presence of two CyDs can improve the stability of inclusion complexes. In this regard, some dimers linked through secondary faces (“tail to tail”) or primary faces (“head to head”) have been synthesized. In addition, linkers more or less rigid with different lengths have been studied. The length of the linker can also modify the flexibility of two CyDs changing the interaction between drug and cavity and the thermodynamic parameters of complexation [129, 139].

Finally, cyclodextrins have also been functionalized with specific chelators to reduce their toxicity or poor solubility. An example is the conjugation of CyD with Deferasirox, a clinical iron chelator used to treat hemosiderosis. In this system, CyD reduces the toxicity of the chelator and increases its solubility [140, 141]. Furthermore, they can be conjugated with ligands modulating properties of the metal center including charge, redox and magnetic activity, stability and so on [142].

1.3.1.2. CYCLODEXTRINS IN BIOMIMICRY

Enzyme mimetics are small molecules able to catalyze reactions in a similar way to natural enzymes operating under conditions hostile to a protein [143]. Artificial enzymes with modified specificities and activities have been developed in the last decades.

CyDs have been studied to catalyze reactions [144, 145]. The cavity can bind the substrate and catalyze specific reactions, mimicking the action of the natural enzyme [146, 147]. The functionalization of CyDs improves this capability.

An example is the lipase mimetic based on CyD that increases the hydrolyze of Glycerophospholipids (lyso-GPLs) under physiological conditions [148].

Another class of systems includes hemoglobin (Hb) mimetics. Typically, the Hb mimetics synthesized are iron complexes that can bind O_2 only in organic solvents and non-physiological conditions [149, 150]. In order to overcome these limits, Hb mimetics based on CyD have been investigated. CyDs can include Fe (II)-tetrasulfonate phenyl porphyrin (TSPP). Moreover, the presence of imidazole in the structure acts as an axial ligand, and the CyD facilitates the stabilization of Fe (II), similar to the native globins. This system has also been functionalized with PEG to increase blood circulation time and stability. It was observed that Hemo-CyD can complex CO with a higher affinity than Hb [149, 151].

Another similar system is Co (III)-PPIX@Py2CyD (Figure 8). This system is based on a per-O-methylated-cyclodextrin dimer (Py2CyD) combined with cobalt proto-porphyrin (Co^{III}-PPIX), forming the biomimetic

catalyzer defined as Co^{III}-PPIX@Py2CyD. This catalytic enzyme, inspired by vitamin B12 structure, has a high affinity to oxygenated substances that promote the reduction of hydrogen peroxide (H_2O_2) [152].

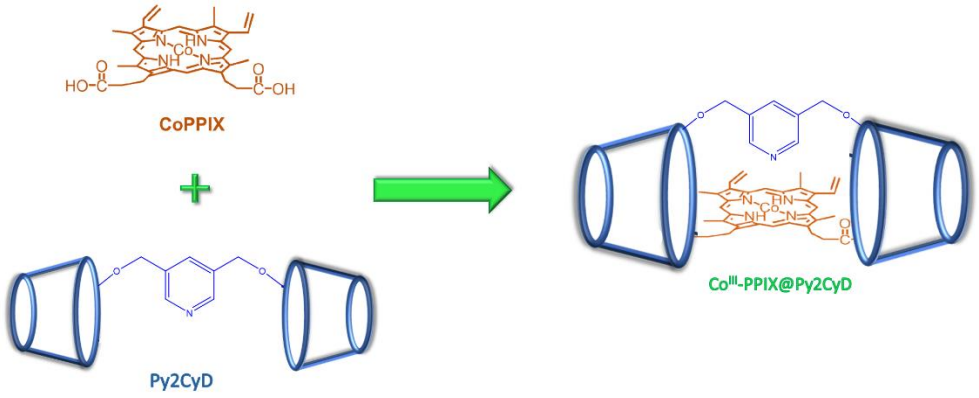

Figure 8. Scheme of Co (III)-PPIX@Py2CyD

Furthermore, superoxide dismutase and catalase mimetics have been developed.

SOD is a family of enzymes that catalyzes the reaction of superoxide ions into H_2O_2, O_2 and O_2^-.

SOD mimetics based on CyDs functionalized with redox metal complexes improved the SOD-like activity compared to the parent complex [153, 154]. In this case, the improved SOD activity is due to the microenvironment offered by the cavity. This last acts as a second sphere ligand that ensures a dielectric constant that modifies the redox potential of metal and confers rigidity [155]. Moreover, the hydroxylic groups of CyD can interact with the superoxide ion (O_2^-) and increase the activity of metalloenzyme mimetics [156].

Furthermore, CyD could also improve SOD activity through the steric effects of the cavity leading to structural distortion and mimicking the entatic state of the protein.

Even systems containing Mn^{3+} have been functionalized with CyD. The CyD was conjugated with Salen (Salicylaldehyde and ethylenediamine Schiff bases) ligands, EUK 108 and EUK 113. The presence of CyD has been proven to increase the solubility of EUK 108 and EUK 113 in water, and they have shown a SOD-like activity about 10 times higher than free EUK 108 [157, 158].

1.3.1.3. CYCLODEXTRINS AS MOLECULAR CHAPERONES

CyDs have also acted as a protein chaperone due to their ability to include aromatic side chains of amino acids [159]. The inclusion of an aromatic amino acid side chain in the cavity can avoid the aggregation of proteins.

The first study that showed that CyDs can counteract the aggregation of $A\beta_{40}$ in PC12 cells dates back to 1991 [160, 161]. This result paved the way for new studies that also demonstrated the effects of CyDs *in vivo* [162–164]. βCyD can reduce the aggregation of beta-amyloid peptides *in vitro* and *in vivo*. CyD exploits the cavity to include Phe19 and Phe20 side chains of Aβ [160, 165, 166].

Phe19 is considered a critical residue in amyloid peptide aggregation, for this reason, the substitution of this amino acid with proline would lead to a significant reduction in the process of aggregation [167]. Other studies have

suggested the higher antiaggregant activity of some functionalized CyDs with aromatic moieties. CyD dimers also acted as inhibitors of $A\beta_{40}$ aggregation [168].

An example is the per-6-alkylaminoβCyD, which has been shown to inhibit amyloid fibril formation modulating cholesterol efflux from cellular membranes. CyDs conjugated with curcumin were also studied against the aggregation of α-synuclein. In this case, the role of CyDs is to increase the antiaggregant activity. Moreover, this system has been proven to be able to break up the preformed aggregates [169]. Good results are also obtained using oligomers or polymers based on CyDs, which can inhibit aggregation at μM concentrations [170, 171].

Another example is the CyD-Crocetin (CRT) complex used against Aβ aggregation. CRT has a good neuroprotective effect [172], but its poor water solubility and bioavailability hinder pharmaceutical applications. These limits have been exceeded with the formation of the CRT-γCyD inclusion complex. Moreover, this inclusion complex did not show toxicity for normal neuronal cells [173].

1.3.2. LINEAR POLYMERS OF CYCLODEXTRINS

Despite the numerous advantages mentioned earlier, CyD monomers present specific problems such as poor pharmacokinetics, cytotoxicity, and hemolytic activity [174]. These problems can be overcome by incorporating CyDs into biocompatible polymers, allowing the benefits of the cavity to be synergistically combined with those of the polymers [175, 176].

CyDs can be integrated into the backbone or be a pendant of pre-existing polymers.

An example of a linear polymer containing CyDs is Cyclodextrin-polyethylene glycol (CyD-PEG). This co-polymer is the precursor of a successful system CRLX101 (Figure 9), used in the pharmaceutical field. Different lengths of this polymer have been characterized, controlling the number of PEG units in the polymer [177]. This polymer was investigated for the delivery of Camptothecin, a DNA topoisomerase-I inhibitor, covalently linked to the CyD-PEG polymer [178]. It has already exceeded the phase I and II clinical trials [179].

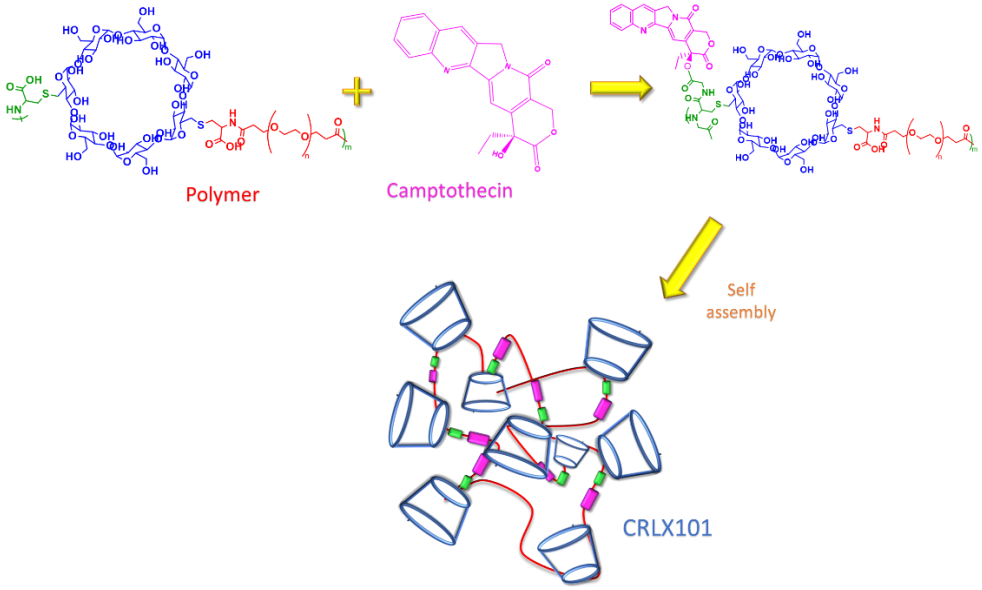

Figure 9. Structure of CRLX101

Generally, CyDs are grafted in the polymers encapsulation and transport of drugs with low solubility but high permeability (Biopharmaceutics Classification System, BCS II) or low solubility and permeability (BCS IV) [180].

An example of a system for the transport of drugs is based on PEG grafted with βCyD and linked to Ibuprofen (IbuprofeneCyDPEG) [181]. The *in vitro* release profile of Ibuprofen indicated that the activation of the polymeric conjugate occurred specifically in the rat colon. Moreover, the polymeric conjugate demonstrated a long and stable pharmacodynamic efficiency over a 24 h period in mice, including anti-inflammatory, analgesic, and antipyretic activities. Therefore, IbuprofenCyDPEG polymer holds promising as an orally administered, long-acting prodrug of Ibuprofen through colon-targeting delivery.

A recent example involves a polymer of Ɛ-lysine functionalized with glycineβCyD designed to deliver the Scutellarin drug [182]. Data evidenced that the inclusion complex increases the thermal stability and the solubility properties of the drug in comparison with the CyD monomer. Furthermore, the positive surface enhances the internalization through endocytosis. The system was tested as a delivery system *in vitro* and the polymer was found to better inhibit tumor growth compared to the free drug of Scutellarin conjugated to CyD [182].

Good results were also obtained by loading poly (lactic-co-glycolic acid) (PLGA) and sulfobutyl ether βCyD (SBEβCyD) NPs with an antitumor drug, Erlotinib. The complex enabled a 3-fold increase in antitumor activity against non-small-cell lung carcinoma via apoptosis and autophagy. These promising results suggest extending the study to preclinical animal models [183].

Another successful example of a linear polymeric NP based on CyDs is CALAA-01 (Figure 10), designed as a gene delivery system. It is characterized by four regions: a polycationic CyD polymer, PEG adamantine, transferrin as the target system and siRNA [184]. CALAA-01 is a DDS in Phase II [44, 176]. In this system, the CyD was chosen to include a transferrin

derivative to target transferrin receptors up-regulated in human tumor cells, including melanoma [185].

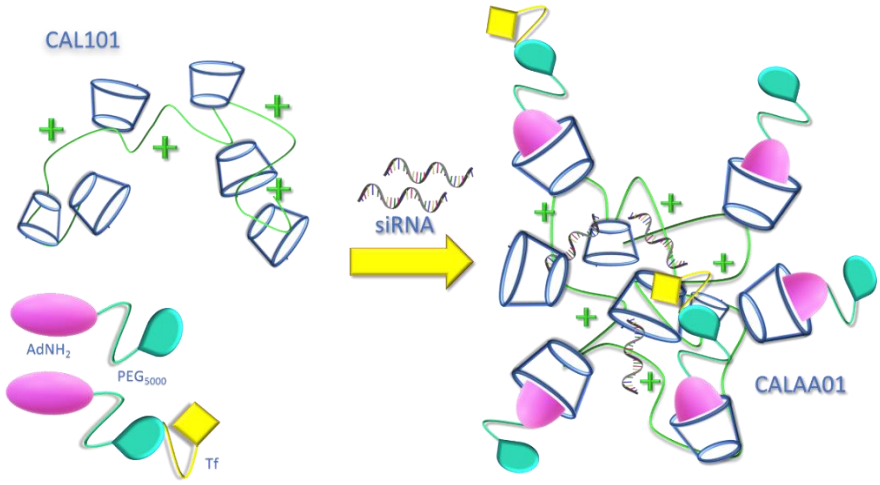

Figure 10. Schematic structure of CALAA01 polymer

Recently HA was used as a backbone in which was introduced one or more CyDs [186–188]. The advantage of these conjugations is to exploit the advantages of both molecules: HA and the recognition by CD44 receptors and CyDs' capability to encapsulate lipophilic drugs. Many studies have used Dox as a drug model in both *in vitro* and *in vivo* experiments, revealing the ability of the new NPs to improve antiproliferative activity and inhibit the Dox side effects, particularly, cardiovascular effects [186, 187].

1.3.3. CROSS-LINKED POLYMERS OF CYCLODEXTRINS

The cross-linked CyD polymer was first synthesized around 1997 when E. Renard demonstrated that it was possible to obtain a cross-linked polymer

using βCyD and epichlorohydrin (EPI), through a polycondensation process [189]. These polymers can weigh approximately 100 kDa, and the average molecular weight can be modulated by the experimental conditions. Polymerization occurs by reaction of the cross-linked EPI groups with deprotonated hydroxyl groups of CyD, in water. This is a cascade process (Figure 11), in fact, CyD products can react with another CyD molecule, forming a dimer, or with OH^-, forming CyD functionalized with a glycerol moiety. These species can further react with EPI and increase the polymer length [190].

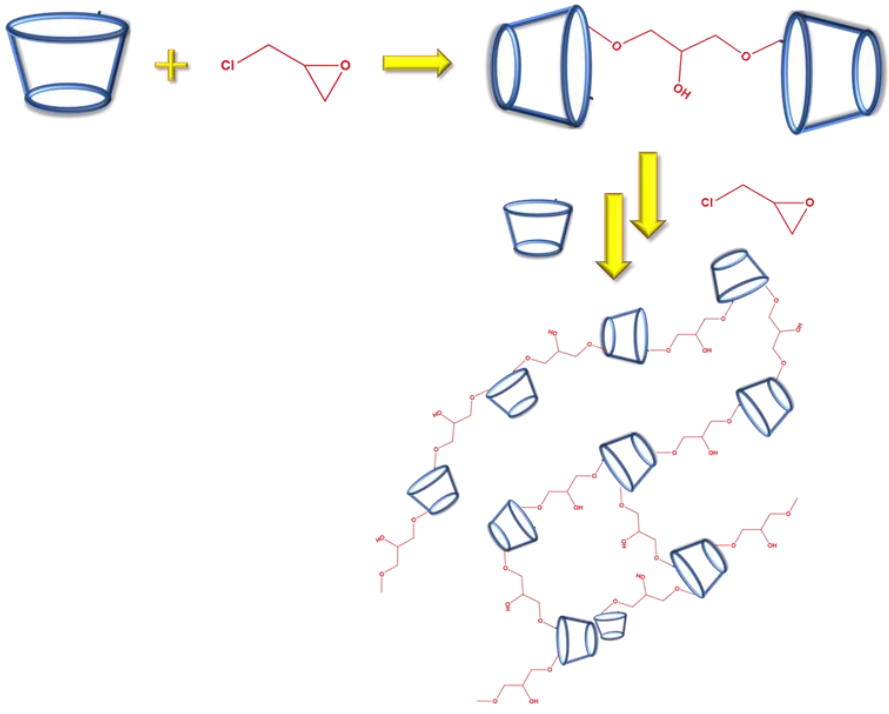

Figure 11. Synthesis of Crosslinked CyD polymer with EPI

As mentioned above, the reaction environment has an important role; in fact, the concentration of NaOH can influence the EPI-CyD ratio and molecular weight. The disadvantage of this reaction mechanism is its

polydispersity. Other synthesis strategies include, for example, using amino groups in the EPI-pCyD network, starting from amino tert-butoxy carbonyl (BOC) protected CyDs [191]. This synthesis method permits obtaining oligomers of cross-linked CyD polymers of about 11kDa. Recently, a cross-linked CyD polymer (3D matrix system, MAX) was obtained by conducting the reaction in the presence of the drug. In this case, the reaction was started by the Sulfobutyl βCyclodextrin SBEβCyD and pre-absorbed Moxiflacina with 1,6-hexamethylene diisocyanate (HMD) as a linking agent in molar excess [192].

The advantage of MAX is that it increases the dissolution of the hydrophobic drug compared to native CyD.

Among other examples of polymer-based CyD for the transport of drugs, there is the citric acid cross-linked γCyD with a different number of cavities. The binding constants show that the presence of the polymer improves the inclusion of Dox. Including Dox in the citric acid cross-linked γCyD polymer stabilizes the monomer Dox, a pharmacologically active species, against the formation of dimers, thereby improving their effectiveness. The interaction with Dox was favored by the presence of negatively charged carboxy groups that stabilize the positive charge of the drug and by the 3D frame of the γCyD polymer [193].

Finally, a new amino βCyD cross-linked polymer with a pyromellitic anhydride was synthesized, via the oxoanion (or epoxide) intermediate. This strategy makes it possible to obtain a negative cross-linked polymer or a polymer with many cationic and anionic groups. These polymers could be used in different fields, for example, to improve the water solubility of molecules, synthesize new DDS or remove heavy metals [190, 194, 195].

1.3.4. SPIONs MODIFIED WITH CYCLODEXTRINS

All the above properties of βCyD make it an excellent surface modifier for SPIONs. It allows magnetite NPs to become water-dispersible magnetically targetable nano vehicles suitable for hydrophobic anti-cancer DDS, magnetic hyperthermia, and theragnostic applications [196]. Some studies report that guest molecular docking also induces the self-assembly of SPIONs [197]. An example is Poly-paclitaxel/cyclodextrin-SPION nano-assembly, which exhibited anticancer effects *in vivo* and *in vitro* owing to magnetically induced targeting effects. Moreover, the presence of the cavity has facilitated the formation of nano-assembly with cluster structures of SPIONs [198].

Another example is the α-CyD-OEI-SPION complex, a system that contains a metal core (SPIONs) coated with a cationic star polymer based on αCyD grafted on multiple oligoethylenimine (OEI) chains. This system allows the delivery of a gene thanks to positive charges on the polymer and increases the water solubility of the hydrophobic SPIONs [199]. Another study was carried out to modify SPIONs with βCyDs to deliver Dox. This system improves the colloidal stability of particles and the loading capacity by supramolecular host-guest and electrostatic interactions between the two systems [200].

Another field in which the SPIONs coated with βCyDs have shown their potential is their ability to cross the BBB, proving to be a promising system against neurodegenerative diseases [201]. This is possible because they can reach a hydrodynamic diameter of only 30 nm.

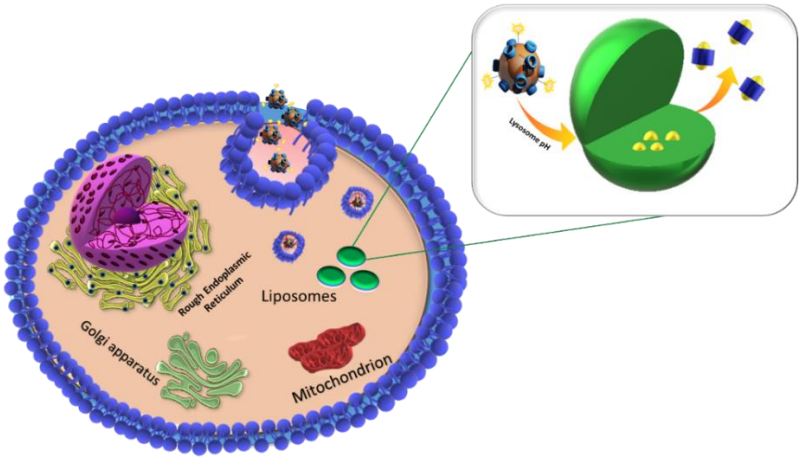

Figure 12. Mechanism of internalization and action of SPIONs

Moreover, SPIONs respond specifically to alternating magnetic fields due to their unique magnetic properties. This interaction of magnetic nanocarriers and magnetic fields may increase drug transition across the BBB, thus contributing to therapeutic efficacy in treating various neuronal diseases [202]. Additionally, enhancing the transport ability of SPIONs across the BBB can be achieved by coating them with biocompatible/biodegradable polymers [203]. Based on the results obtained by CyDs cholesterol mopping activity and the properties of SPIONs, a colloidally stable nanoparticle system (CySPION) has been synthesized [204]. This system is based on a SPION core and a functional PMOXA shell. Its nano-architecture was engineered to release its CyD payload at slightly acidic pH levels, which are suitable for lysosomal delivery and therapy (Figure 12). The packaging of CyDs into a nano-architecture such as CySPION and its smart pH-triggered release have demonstrated significant advantages over the current administration of CyDs in its monomeric form [204].

1.4. AIM OF THE THESIS

Over the years, a major challenge for scientists has been to overcome side effects and achieve targeted administration of conventional drugs. The undesirable effects of a drug can lead to severe consequences for the entire organism, mainly if the drugs are used to treat chronic diseases and are administered over very long periods.

In light of this, the main aim of this thesis is to design nanoparticles based on CyDs chemistry that may overcome these problems. In particular, three application areas were focused on (Figure 13):

- Drug delivery of anticancer drugs
- Chelation therapy to modulate metal dyshomeostasis
- Therapeutical nanocarrier systems for removing biological molecules.

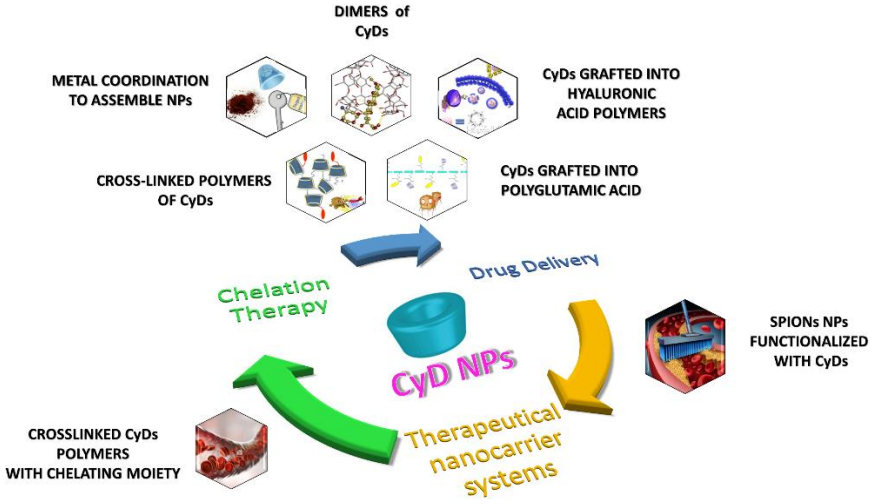

Figure 13. CyD NPs and their applications

The aim of the first part is to design and study CyD systems from dimers to polymers (Figure 14). They were functionalized with different targeting

moieties. Also, the polymeric NPs of β or γ CyDs have linear or crosslinked structures, positive or negative charges. The objective was to investigate systems with different dimensions and structures as potential drug delivery systems and compare their selectivity for specific cancer cells. The encapsulation of the most common drugs used for cancer therapy was assayed *in vitro*.

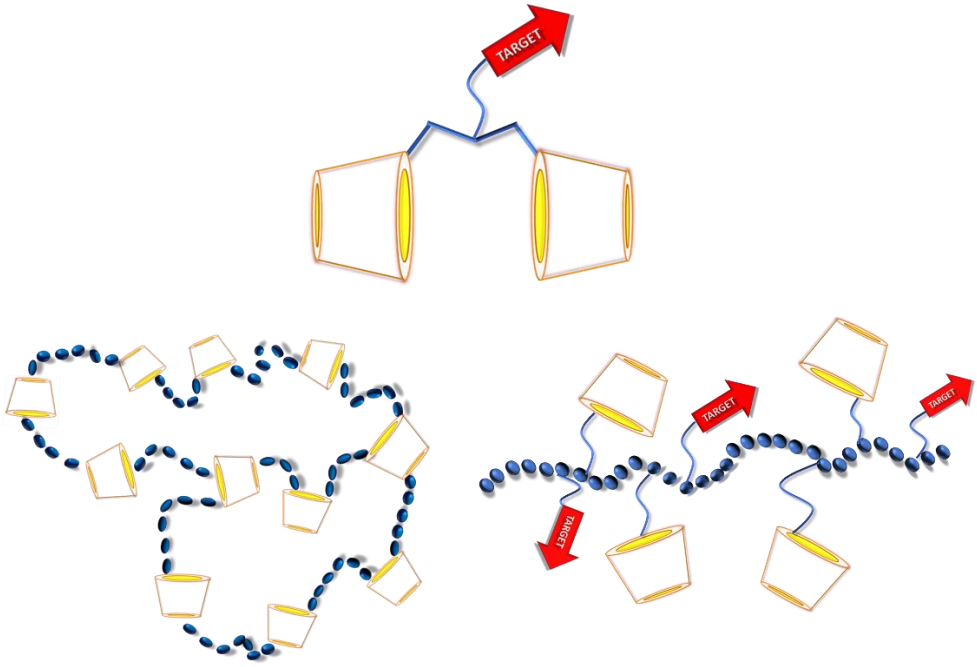

Figure 14. Schematic structures of products used as Drug Delivery systems

The aim of the second part is the synthesis of new nanochelator NPs (Figure 15) that can chelate metal ions, such as copper. One of the goals is to exploit the capability of polymers to act in the bowel, overcoming the problems of common chelators used in diseases, such as Wilson's disease. These polymers contain histidine and carcinine, bioligands in the body with an essential physiological role. Moreover, they are known for their antioxidant

activity. The SOD-like systems can protect the cells from oxidative damage due to a dyshomeostasis of copper.

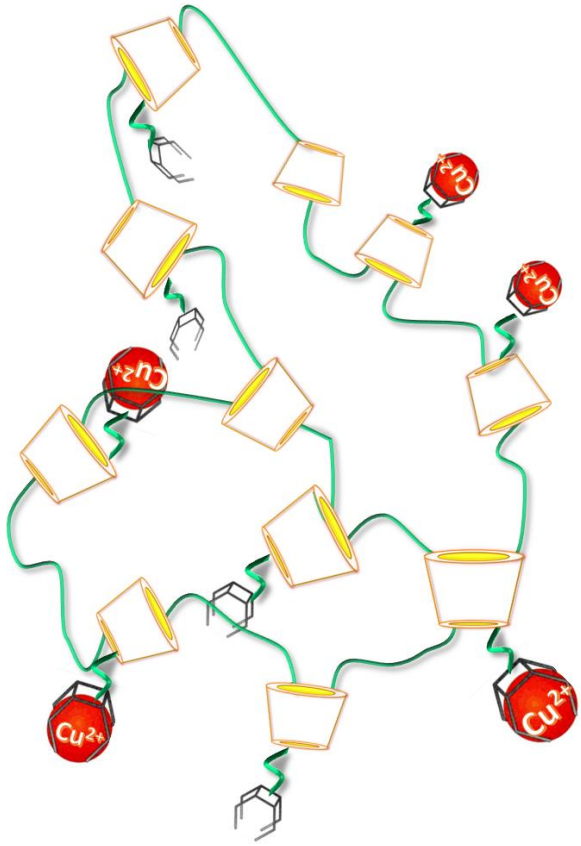

Figure 15. Schematic structure of new nanochelators

In the last part, in collaboration with the University of Wien (Natural Resources and Life Sciences), metal NPs coated with two different polymers were designed (Figure 16). This study aimed to exploit the capability of SPIONs coated with CyDs to overcome the BBB and remove cholesterol from the cells, as already well-known in literature for free CyDs. Therefore, a ferric oxide core was coated with CyDs polymer and a fluorescent polymer ended with fluorescein. This approach allowed us to study the internalization of NPs by confocal microscopy and quantify the concentration of CySPIONs that

overcome the BBB. The successful crossing of the BBB indicates a decisive advantage of the responsive nanoparticle delivery system.

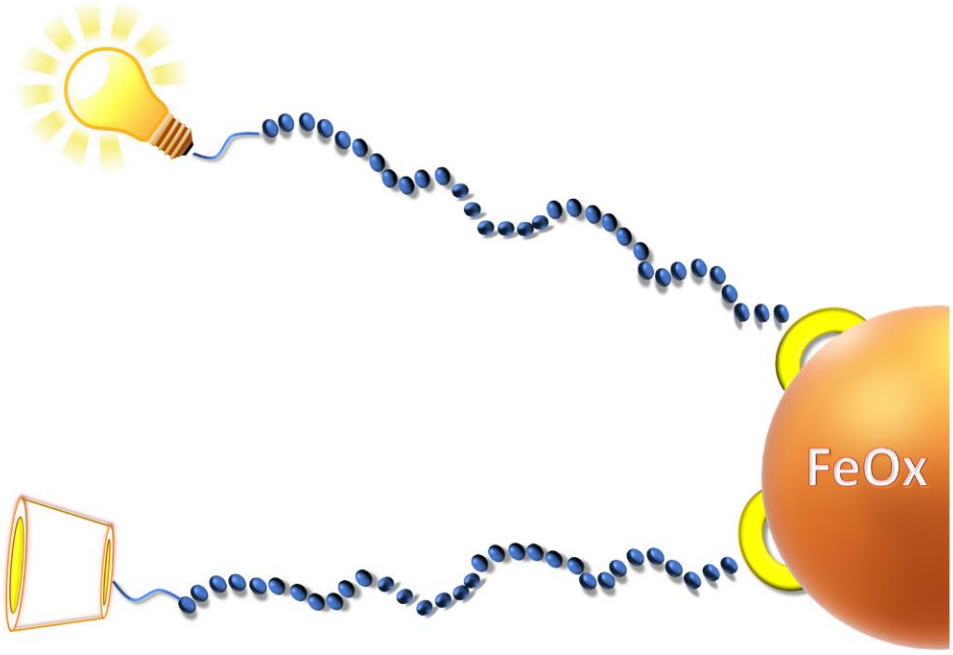

Figure 16. Schematic structure of metal NPs used as a therapeutical nanocarrier

2. RESULTS AND DISCUSSION

2.1. DRUG DELIVERY SYSTEMS

Multicavity systems based on CyDs with different molecular weights, functionalizations and charges were synthesized and characterized to study how the differences between these systems can enhance the DD (Figure 17).

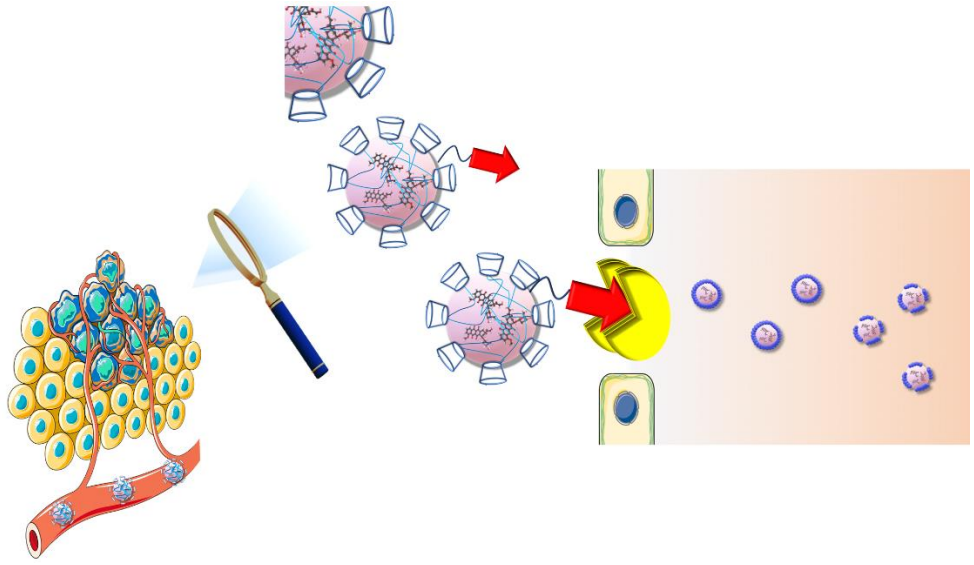

Figure 17. NPs based on CyD functionalized to increase active targeting.

This section is divided as sketched in Figure 18: CyD Dimers, linear CyD, crosslinked CyD polymers and NPs based on iron (III) coordination to build targeted and labeled systems.

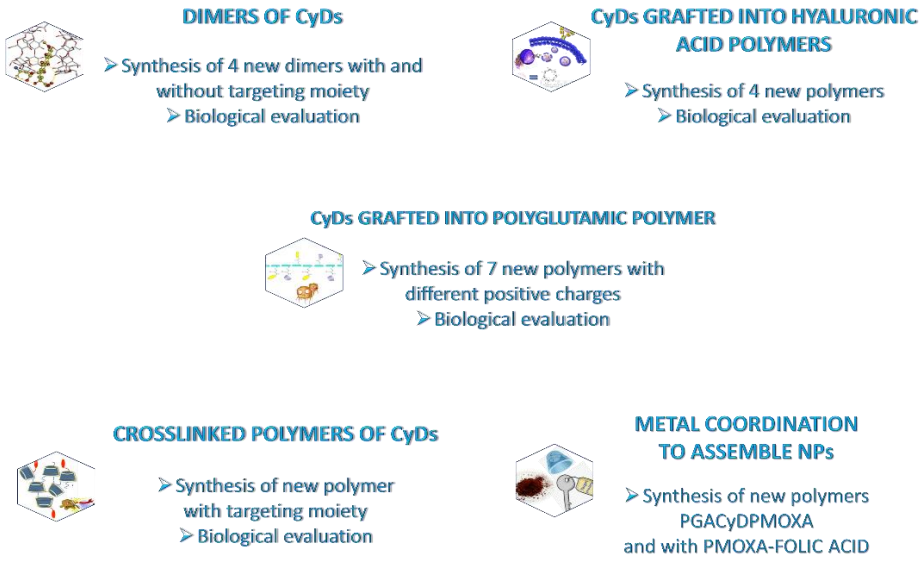

Figure 18. Scheme of systems studied for DD.

2.1.1. DIMERS OF CyDs

The dimers have been investigated as potential nanocapsules. The two CyDs can improve the encapsulation, solubility and stability of guest molecules rather than the single cavity. Furthermore, recent studies have shown that β and γCyD dimers participate in complexing guests such as Dox with a 2:1 host/guest stochiometry [129]. CyD2Glu dimers (Figure 19) were functionalized with biotin (Bio) as the targeting moiety.

Bio is among the most used targeting moiety due to its involvement in the growth of cancer cells. Hence, this vitamin can be recognized by the receptors SMVT, ((the biotin receptor is codified by SLC5A6 gene (human chromosome 2p23.3)) overexpressed in different cancer cells including mammary epithelium, placenta, intestine, brain, liver, lung, kidney, cornea, retina and heart [205].

The drug selected to test the dimers *in vitro* and for the solubility assay is Dox, an anthracycline drug with low water solubility at physiological pH and side effects such as cardiotoxicity [206]. Furthermore, Dox is an antitumor model drug used in the study of DD, and its complexation with CyDs is well-known characterized [187, 207].

CyD2GluAc systems were also synthesized for comparison with the targeted systems CyD2GluBio (Figure 19). The amido group cannot be protonated, allowing a more significant comparison with the biotinylated systems.

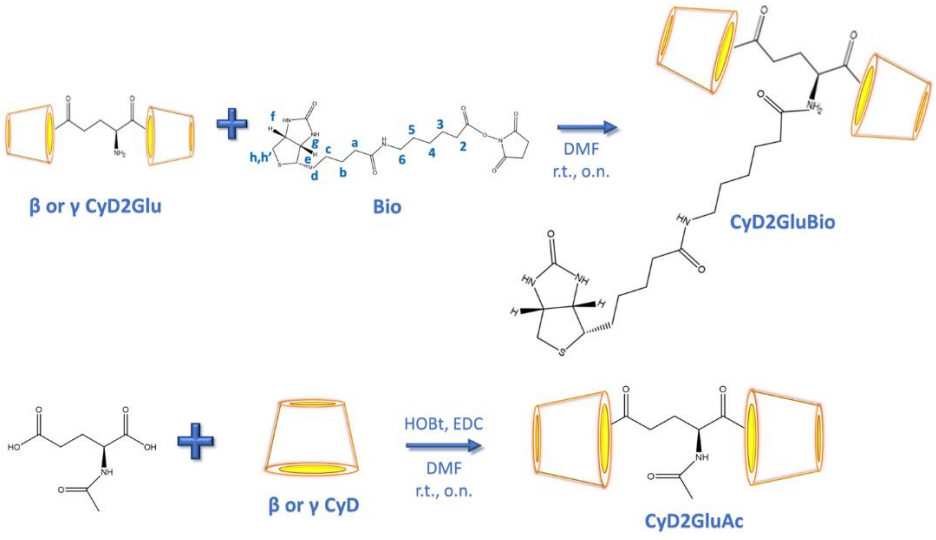

Figure 19. Synthetic scheme of β or γ CyD dimers

2.1.1.1. SYNTHETIC ASPECT

The CyD2GluAc dimers were synthesized as reported for CyD2Glu [129], starting from γCyDNH$_2$ or βCyDNH$_2$ and Glutamic acid acetylate (Ac-Glu-OH) using HOBt and EDC as activating agents (see Figure 19).

CyD2GluBio derivatives were synthesized from CyD2Glu [129] and Bio, with amino-hexanoic acid as a linker activated by the N-Succinimidyl group (see Figure 19). Amino-CyDs contain an altrose unit due to the preparation methods of 3-functionalized CyDs.

All of the products were characterized by NMR spectroscopy, and the spectra confirmed the identity of the products (Figures 20 and 21, Figures S79-S89).

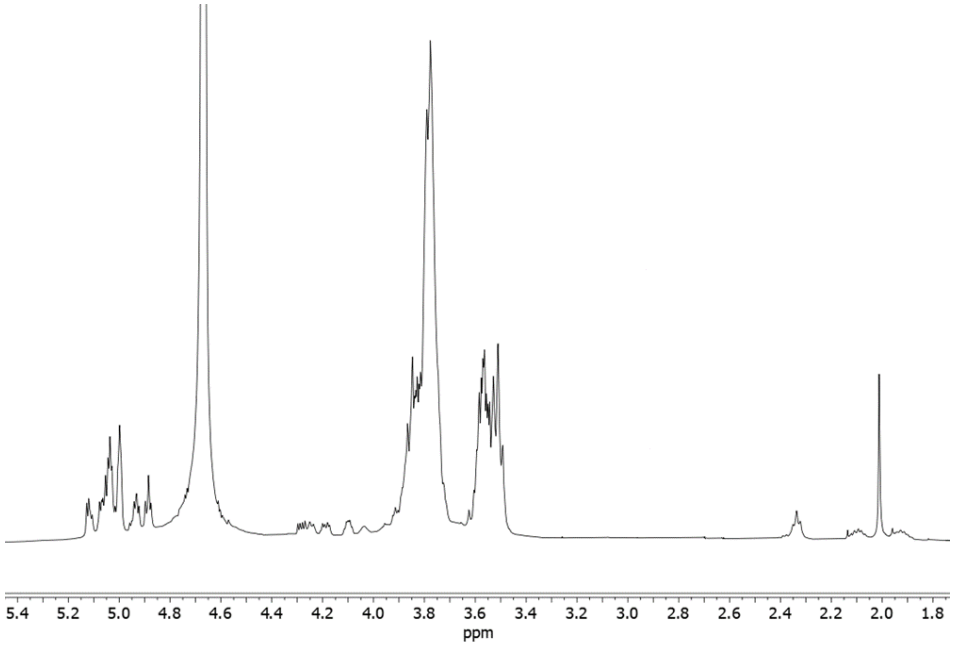

Figure 20. ^{1}H NMR spectrum of γCyD2GluAc (D_2O, 500 MHz)

The spectrum of γCyD2GluAc (Figure 20) shows the signals of CyD and Glu. In the region at 5.17-4.95 ppm, the signals of H-1 of glucose and altrose are observed. The other signals of CyD are identified in the range of 3.4 to 4.1 ppm, while the signals of glutamate linker are clearly identified at 4.3,1.9 and 2.3 ppm. Similar patterns are observed for βCyD2GluAc (Figure S83).

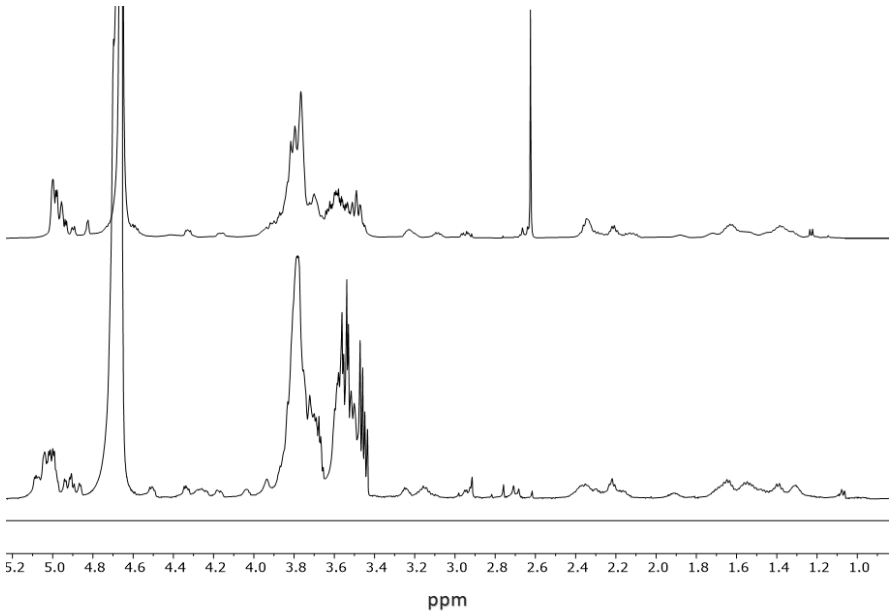

Figure 21. ^{1}H NMR spectra in D_2O (500 MHz): βCyD2GluBio (top) and γCyD2GluBio (bottom)

In the spectra of CyD2GluBio, the signals due to the Bio moiety and the hexane linker can be assigned using 2D spectra (COSY, HSQC, HMBC, TOCSY, ROESY) (Figures S84-S89).

Also in this case, it is possible to distinguish the signals of CyDs at 5.1-4.8 ppm for the H-1 and from 4.0 to 3.4 ppm for the other protons of CyDs. The signal of Bio and its chain is observed in the range of 4.5-4.3 and 1.7-1.2 ppm.

Additionally, the spectra of β and γ CyD2GluBio showed slightly different chemical shifts of the Bio moiety protons. Differences are also evident in the H-1 CyD region. ROESY spectra of the dimers suggest the interaction of the Bio and hexanoic chain with the cavities. Particularly in βCyD2GluBio spectra (Figure S89), the hexane chain, h and e Bio protons showed more intense ROE correlation with the H-5, -3 region.

2.1.1.2. SOLUBILITY EXPERIMENTS

The interaction of CyD2GluAc with Dox was investigated at physiological pH (pH=7.4). The affinity for Dox was determined using the phase solubility method as described elsewhere by Higuchi and Connors [208]. The Dox concentration increased linearly with increasing CyD concentration, obtaining an A_L-type phase diagram. These diagrams were fitted with the following equation, considering the concentration of dimers CyD:

$$SDox = SoDox + [K11So/ (1 + K11So)] \times [CyD]$$

The diagram was obtained by plotting the concentration of the drug versus the concentration of dimers, as can be observed in Figure 22. The angular coefficient of the straight line was <1 for both systems, indicating an A_L-type graph.

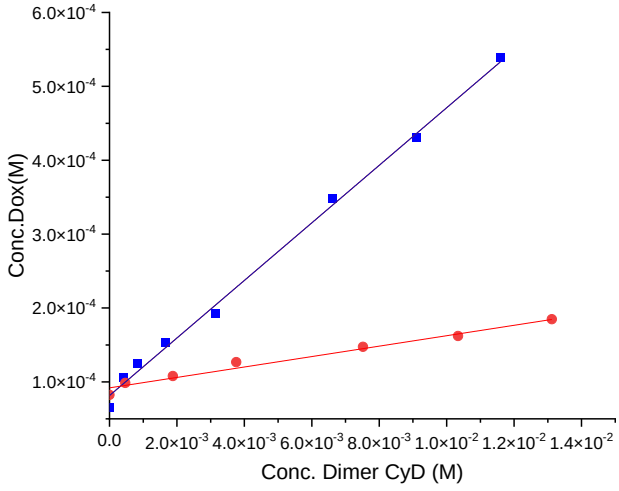

Figure 22. Dox solubility (phosphate buffer, pH= 7.4) versus the concentration of βCyD2GluAc (●) or γCyD2GluAc (■).

The complexation efficiency (CE) was evaluated, considering the slope of the line. The γCyD2GluAc at 0.01 M concentration increased the solubility

of Dox about 10 times. The CE for γCyD2GluAc is significantly higher (six times) than that of βCyD2GluAc. This trend is in keeping with the higher affinity of the γCyD cavity for Dox, as reported elsewhere [209]. Furthermore, data are in keeping with the different structures obtained from molecular docking studies for βCyD2Glu and γCyD2Glu dimers [129].

2.1.1.3. ANTIPROLIFERATIVE ACTIVITY

In order to select the best cell model for vitro studies, the expression level of SLC5A6 was evaluated by Human Transcriptome Array analysis (HTA 2.0) in five human cell lines and here, the transcript levels are reported as RMA values (Figure 23): CACO-2 (RMA 6.74), HCT-116 (RMA 7.77), HT-29 (RMA 7.19), MCF-7 (RMA 8.81) and PC-3 (RMA 7.78). SLC5A6 resulted in a higher expression in the MCF-7 cell line, thus it was used for subsequent experiments to evaluate the cell viability.

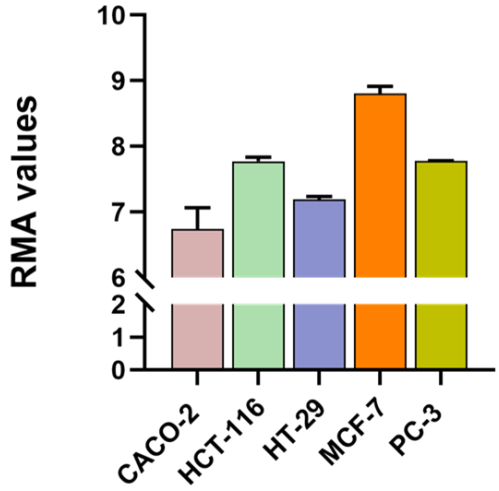

Figure 23. The expression level of the biotin carrier SMVT in tumor cell lines

Inclusion complexes of Dox with CyD dimers acetylate and biotinylate were studied in MCF-7 cells to obtain the dose-response curve (Figure S90)

and determine the half-maximal inhibitory concentration (IC_{50}) of the Dox. The graphic was obtained by plotting the logarithms of molar concentration on the x-axis and the responses on the y-axis.

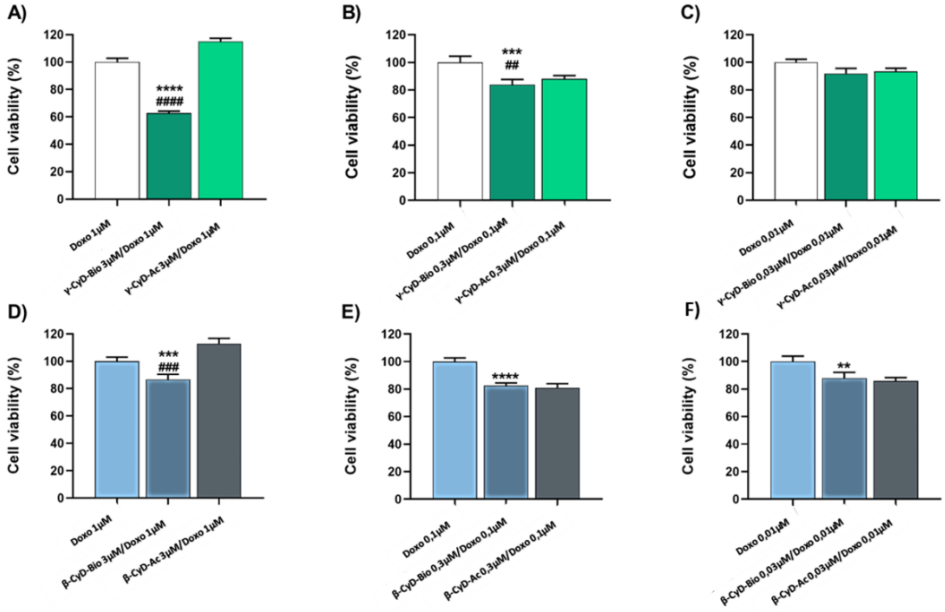

Figure 24. Effect of Dox, γCyD2GluBio/Dox, γCyD2GluAc/Dox on the viability of MCF-7 (A, B, C), Effect of Dox, βCyD2GluBio/Dox, βCyD2GluAc/Dox on the viability of MCF-7 (D, E, F)

γCyD2GluBio/Dox vs only Dox **** p-value <0,0001; γCyD2GluBio/Dox vs γCyD2GluAc/Dox #### p-value <0,0001 (A). γCyD2GluBio/Dox vs only Dox *** p-value <0,001; γCyD2GluBio/Dox vs γCyD2GluAc/Dox ## p-value <0,01 (B). βCyD2GluBio/Dox vs only Dox *** p-value <0,001; βCyD2GluBio/Dox vs βCyD2GluAc/Dox ### p-value <0,001 (D). βCyD2GluBio/Dox vs only Dox **** p-value <0,0001 (E). βCyD2GluBio/Dox vs only Dox ** p-value <0,01 (F).

In all cases, data showed higher toxicity compared to free Dox, although in some cases low. The most interesting data for γCyDGluBio/Dox at 1μM concentration (Figure 24 **A)**) for which the cell viability is approximately 60% of free Dox. At the same concentration (1μM), a similar result can be observed comparing γCyDGluBio and γCyDGluAc. This result suggests that the increase in concentration of CyD2GluBio promotes a higher cytotoxicity of Dox, reasonably due to the better internalization of the drug. In this view, it would seem that Bio has a role in the DD by being recognized by the SMVT

receptor. Moreover, data suggest that the system with γCyD may promote better Dox internalization compared to the system with βCyD. This can be explained by the higher affinity of Dox for the CyD cavity.

2.1.2. CyDs GRAFTED INTO HYALURONIC ACID POLYMERS

Two different HA polymers with molecular weights (HAL 8-15 kDa and HAH 40-50 kDa) were functionalized with $\beta CyDNH_2$ (Figure 25), in order to investigate the difference between the two weights and the capability of CyDs for DD. HAHβCyD and HALβCyD, were tested with a Dox *in vitro* at two drug/polymer molar ratios (8/1 and 16/1) in cancer neuroblastoma cell lines: SK-N-SH and SK-N-SH-PMA. SK-N-SH-PMA overexpress CD44 receptors.

Moreover, the neuroblastoma cell lines were selected because studies have proven that Dox is one of the chemotherapeutics administrated in high-risk neuroblastoma carcinoma [210].

$\gamma CyDNH_2$ was grafted to HA polymers and tested with Sorafenib (Sor). The commercial name of Sor is Nexavar, it is an inhibitor of kinase protein approved for the treatment of kidney, liver and thyroid carcinoma [211]. In spite of it being widely used, Sor exhibits many side effects such as hypertension, bilirubin elevation and very low water solubility. Notwithstanding this, Sor remains the first-line drug against hepatocellular carcinoma [212]. This drug was associated with γCyD because the dimension of the cavity can increase the host/guest complexation. A study has analyzed both types of the cavity in the presence of Sor, showing that Sor in γCyD achieved superior therapeutic efficacy and also exhibited promising outcomes in the treatment by intratumoral injections compared to the same system with

βCyD [213]. For this reason, CyD was investigated to increase the solubility and decrease the administrated dose. The HAγCyD polymers were tested in three different cell lines: A2780 (ovarian cancer), SK-HeP-1 (adenocarcinoma) and MDA-MB-453 (breast cancer) with a ratio of CyD cavities/drug 2:1.

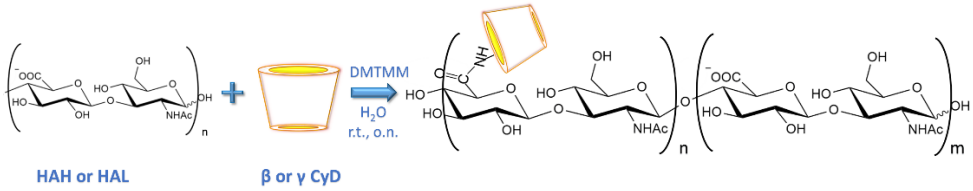

Figure 25. Synthetic scheme of synthesis of HACyD conjugates

2.1.2.1. SYNTHETIC ASPECT

The synthesis of HA conjugates with CyD3NH_2 was carried out under green conditions using water as the solvent and DMTMM as the activating agent. In all cases, the conjugates were obtained with a good yield (about 50%).

^{1}H NMR spectra of HAHCyD and HALCyD showed common patterns: the Hs-1 of CyD resonates at about 5 ppm, and the broad signals between 3 and 4 ppm are due to the protons of HA and CyD sugar rings. The peaks observed at 4.3-4.4 ppm are due to the Hs-1 of the glucuronic acid and glucosamine units of HA. The singlet peak at 1.9 ppm corresponds to CH_3 of the N-Acetyl group of HA.

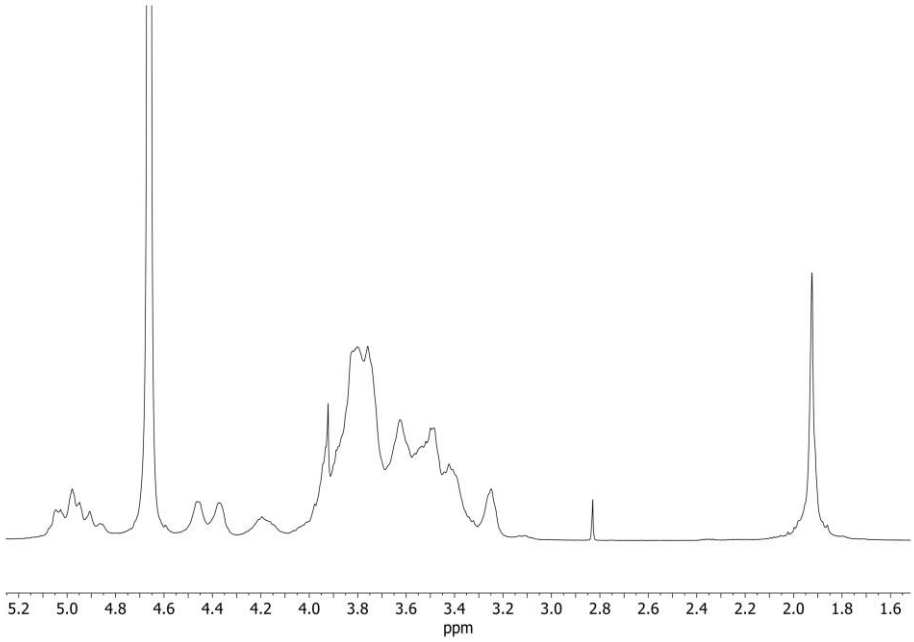

Figure 26. ^{1}H NMR spectrum of HALβCyD (D_2O, 500 MHz)

For all polymers, the degree of substitution (DS) was evaluated by the ratio between the integral of the CH_3 signal at 1.9 ppm and CyD Hs-1 at 4.9 ppm. In the case of HAβCyD polymers, the integration shows that about 15% of carboxylic groups of HAHβCyD were functionalized with CyD (about 16 units), while 30% of carboxylic groups of HALβCyD (Figure 26) were functionalized with CyD units (about 8 units) (Figures S91 and S92).

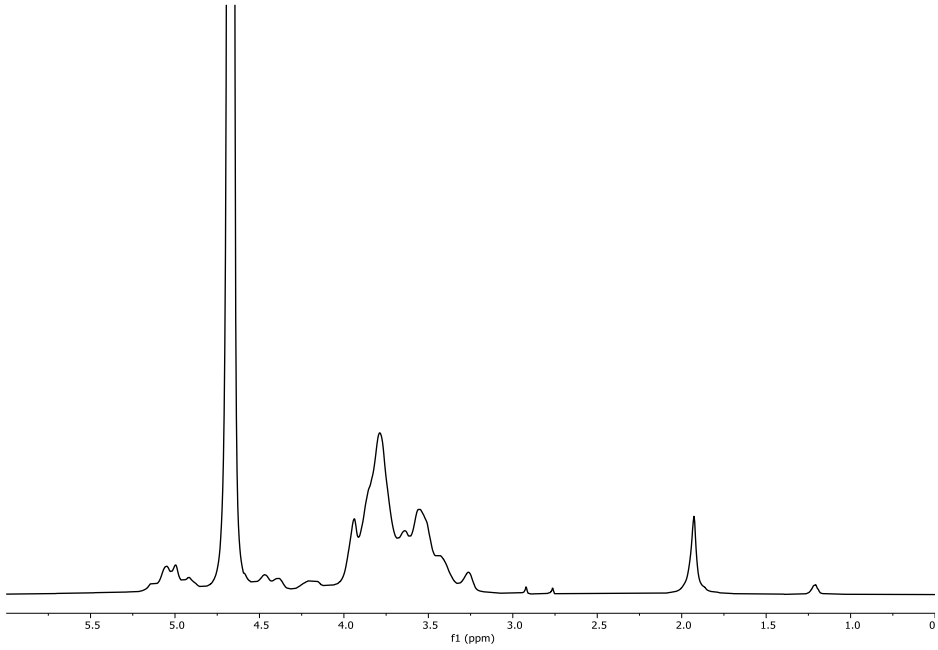

Figure 27. ^{1}H NMR spectrum of HALγCyD (D_2O, 500 MHz)

In the case of the HAγCyD polymers, the integration of signals showed that about 45% of the carboxylic groups of HAH were functionalized with CyD (about 50 cavities), while about 50% of carboxylic groups of HAL (Figures 27 and S93) were functionalized with CyD units (about 14 cavities).

2.1.2.2. SIZE OF NPs

The hydrodynamic diameter was measured by Dynamic Light Scattering (DLS) (Table 1). HA can form self-assembled NPs with a hydrodynamic diameter of about 40 nm (Figure S94). The conjugates with β or γCyD show a common pattern (Figures S95 and S96), the NPs based on HAH show a higher dimension than those based on HAL. The samples were investigated at a concentration of 1mg/ml in phosphate buffer (pH= 7.4, 100 mM).

Table 1. Z-Average (d, nm) of HA polymers grafted to CyDs

HACyD POLYMERS	Z-Average (d. nm)
HAH	53±8
HAL	30±3
HAHγCyD	531±60
HALγCyD	90±5
HAHβCyD	424±40
HALβCyD	176±15

In the spectra (Figures S95 and S96), is possible to observe the distribution of intensity of NPs. The HALCyD polymers present more peaks compared to the same systems with HAH.

2.1.2.3. SOLUBILITY EXPERIMENTS

The polymers of HAβCyD were assayed as solubilizing agents of Dox. The CE and the apparent stability constants were reported in Table 2 for drug/CyD complexes [214, 215]. Solubility experiments were carried out at physiological pH= 7.4 (Figure S97).

Table 2. CE and apparent stability constant (K) values for Dox with HAHβCyD and HALβCyD (25 °C, Phosphate buffer, pH 7.4)

Host	CE	K_{11} (M^{-1})	Slope	S_{int}
HALβCyD	0.018	480(±50)	0.018	3.50×10^{-5}
HAHβCyD	0.034	971(±80)	0.033	3.78×10^{-5}

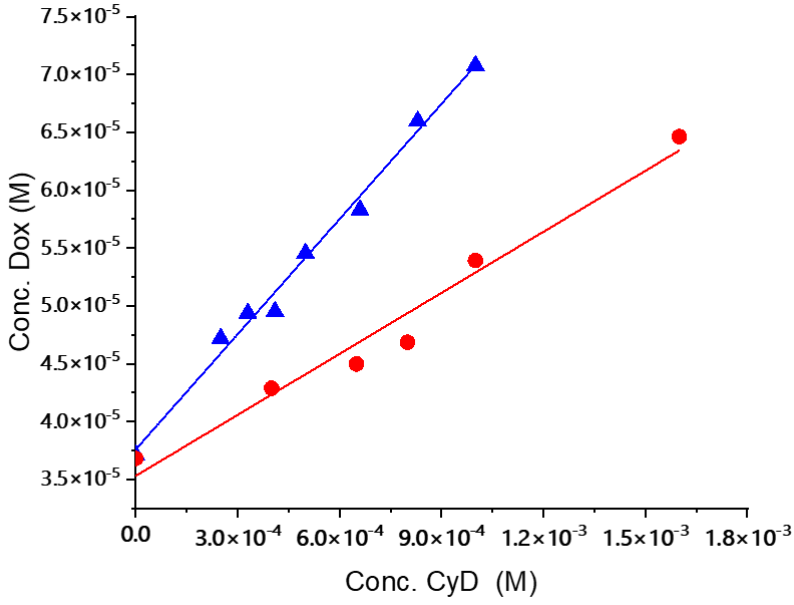

Figure 28. Dox solubility (phosphate buffer, pH=7.4) versus the amount of HAHβCyD (▲) or HALβCyD (●) (reported as CyD cavity concentration)

In particular, the graph (Figure 28) reported the concentration of Dox solubilized versus the concentration of CyD cavities in polymers.

CyD polymers have many binding sites, which were assumed to be identical and independent. The apparent stability constant (K) can be calculated as $K= nK_{11}$ (n is the number of CyDs in the polymer) [215]. The constants were calculated, and K is 3840 (M^{-1}) for HALβCyD and 15,536 (M^{-1}) for HAHβCyD. Carboxylate groups can also contribute to the affinity for Dox, which is protonated at physiological pH.

The CE and K_{11} values are in the same range as those obtained for other βCyD systems [105, 193].

Data in Table 2 show that CyD in HAHβCyD (DS = 16) is more effective than CyD in HALβCyD (DS = 8). This behavior is in keeping with

the general trend reported for CyD grafted to dextrans [216]. It has been noted that in CyD-based polymers, CE is inversely proportional to DS [216]. In fact, for higher DS, the cavity becomes less accessible due to steric hindrance at the binding site [216].

2.1.2.4. ANTIPROLIFERATIVE ACTIVITY OF Dox with HAβCyD CONJUGATES AND INTRACELLULAR ACCUMULATION

The antiproliferative activity for HAβCyD polymers was performed using Dox alone and in the presence of HALβCyD and HAHβCyD. The drug and the complexes were tested in both cell lines, neuroblastoma with and without the overexpression of CD44 receptors (SK-N-SH and SK-N-SH-PMA). Table 3 shows the IC_{50} values of the drug and complexes drug/polymer.

Table 3. Antiproliferative activity (IC_{50}, nM) of Dox with CyD polymers in SK-N-SH and PMA stimulated SK-N-SH-PMA cells

Cell line	Dox	Dox/ HALβCyD 8/1	Dox/ HAHβCyD 8/1	Dox/ HALβCyD 16/1	Dox/ HAHβCyD 16/1
SK-N-SH	79.3± 23.5	83.5±21.4	92.3±13.4	22.1±9.8[a]	24.6±8.5[a]
SK-N-SH-PMA	82.7± 11.9	58.8±13.4[b]	40.7±13.8[a,c]	25.3 ± 8.7	26.2±3.9[a]

[a] $p < 0.001$ vs. Dox, [b] $p < 0.021$ vs. Dox,[c] $p < 0.001$ vs. cells SK-N-SH treated with Dox/HAHβCyD 8/1.

Data show that the antiproliferative activity in SK-N-SH-PMA cells is significantly higher than free Dox, for all complexes and in both ratios. Contrariwise, in the SK-N-SH cell line, was observed a double trend. In the case of ratio 8/1, both complexes showed an antiproliferative activity comparable to Dox, instead at a higher ratio (16/1), the IC_{50} observed for Dox/HAHβCyD and Dox/HALβCyD was considerably lower than Dox.

The experiment suggested that antiproliferative activity depends on the Dox/polymer molar ratio and the CD44 receptor expression.

SK-N-SH-PMA, which overexpresses CD44 receptors, seems to be more sensitive to treatment with the Dox/HAHβCyD and Dox/HALβCyD complexes 8/1 ratio. The hypothesis was that the CD44 receptor-mediated endocytosis of the complexes determined a lower IC_{50} in cells overexpressing the CD44 receptor. The lower IC_{50} value for Dox/HAHβCyD may be due to the higher affinity of HAHβCyD for Dox.

At the highest Dox/polymer ratio, there is a considerable reduction in IC_{50} values (on average, reduced by about 70% of free Dox) and no selectivity for cells overexpressing the CD44 receptor. The highest molar ratio may increase the concentration of the Dox inclusion complex and enhance its uptake in cancer cells.

The differences in antiproliferative activity between the two cancer cell lines suggest that the HAβCyD polymers may play a role in the uptake of cancer cells. Thereby, Dox internalization was evaluated in both SK-N-SH and SK-N-SK-PMA cell lines, administrating 2 μM drug alone and in the presence of the polymers.

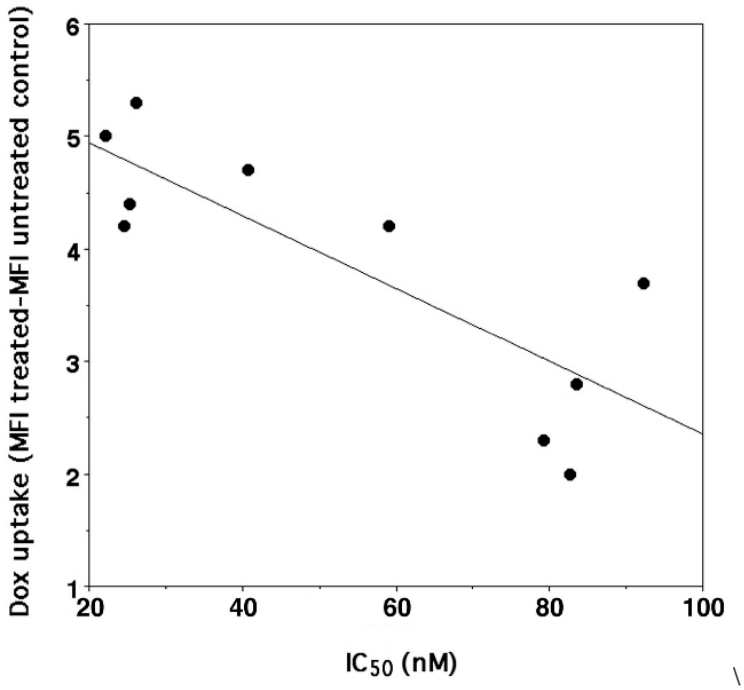

Figure 29. Correlation between IC_{50} of Dox (y = −0.0323X + 5.5905, r^2 0.670, n = 10, p < 0.004) either administered as parent drug or as CyD polymer complexes and its uptake into SK-N-SH and SK-N-SH-PMA cells.

The results in Figure 29 confirm that, in general, higher antiproliferative activity correlates (n = 10, r^2 = 0.670, p < 0.004) with a higher Dox accumulation in the cells (Figure S98). In addition, data revealed that higher Dox uptake is also linked to CD44 overexpression in SK-N-SH-PMA cells, but only after treatment with Dox/HAHβCyD and Dox/HALβCyD complexes 8/1 (Table 4). This trend may suggest that Dox complexes at the highest molar ratio studied (16/1) are probably per se sufficient to reach the maximum possible antiproliferative activity being able to saturate Dox molecular targets even in the SK-N-SH cells, which do not overexpress CD44 (only 53% of CD44 receptors).

Table 4. Correlation between IC_{50} of complexes Dox/HALβCyD 8/1 and Dox/HAHβCyD 8/1 and their Dox uptake

Cell line	MTT Dox/ HALβCyD 8/1(IC_{50}nm)	MFI Dox/ HALβCyD 8/1[a]	MTT Dox/ HAHβCyD 8/1(IC_{50}nm)	MFI Dox/ HAHβCyD 8/1[a]
SK-N-SH	83.5 ± 21.4	2.8 ± 1.6	92.3 ± 13.4	3.7 ± 0.7
SK-N-SH-PMA	58.8 ± 13.4 [b]	4.2± 1.0	40.7 ± 13.8 [c]	4.8 ± 2.0

[a] Values were normalized as absolute MFI calculated as MFI of treated cells-MFI of control cells. [b]p = 0.0536 vs. SK-N-SH cells, as evaluated by the Student's t-test for independent means.[c] p = 0.0008 vs. SK-N-SH cells, as evaluated by the Student's t-test for independent means.

2.1.2.5. ANTIPROLIFERATIVE ACTIVITY OF SORAFENIB AND HAγCyD CONJUGATES

The cell proliferation assays were performed for HAγCyD polymers with Sor on A2780 (ovarian cancer), SK-HeP-1 (adenocarcinoma) and MDA-MB-453 (breast cancer) cells, with a ratio of 25/1 for HAHγCyD/Sor and 17/1 for HALγCyD/Sor (Table 5).

Table 5. Antiproliferative activity of HACyDs polymers with Sor in: A2780, SK-HeP-1 and MDA453

Cell line	Sor	Sor/HALγCyD	Sor/HAHγCyD
A2780	6.58±1.03	4.60±1.01 p<0.02	5.81±3.21
SK-HeP-1	11.7±1.1	7.04±2.79 p<0.02	8.15±2.57 p<0.05
MDA453	14.9±1.6	3.67±0.69 p<0.001	15.5±4.8

Data showed a significant improvement in the antiproliferative activity of the inclusion complexes of Sor compared to the free drug, especially in the case of the polymer with lower molecular weight, which showed an activity increase of about 75% in MDA453 cell lines. Conversely, a smaller increment was observed in the A2780 cell line for both systems, improving about 30% for the HALγCyD and 22% for the HAHγCyD.

2.1.3. CyDs GRAFTED INTO POLYGLUTAMIC POLYMER

PGA polymer was functionalized with $CyDNH_2$ (both β and γ), Arginine methyl ester (Arg) or γ-Guanidinobutyric Acid (GBA). The chosen PGA was characterized by 20 repeat units, with a molecular weight of 3 kDa. C terminal amino acid is amidated with butyl-amine.

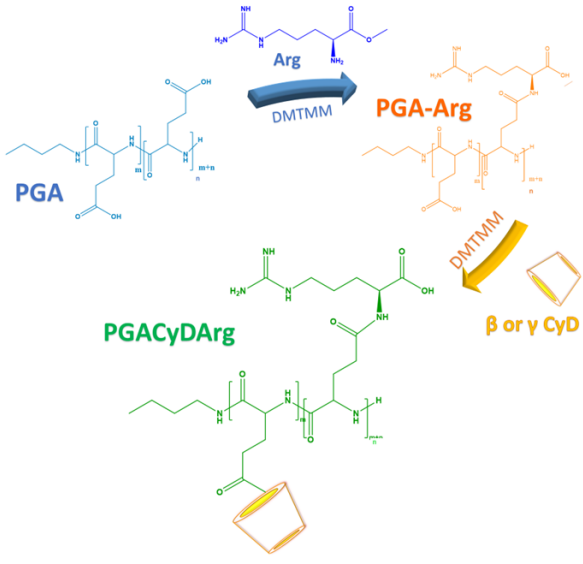

Figure 30. Synthetic scheme for PGACyDArg polymers

A potential role of positive charges is to improve the inclusion of anionic drugs or oligonucleotides, such as siRNA. The carboxyl groups of PGA can offer attachment points for the conjugation with other molecules [217].

Furthermore, PGA can modulate the drug release according to pH, allowing the drug transport to the cancer cell where the pH value is slightly acidic [218]. In addition, depending on the starting polypeptide the molecular weight of the products may be selected [219].

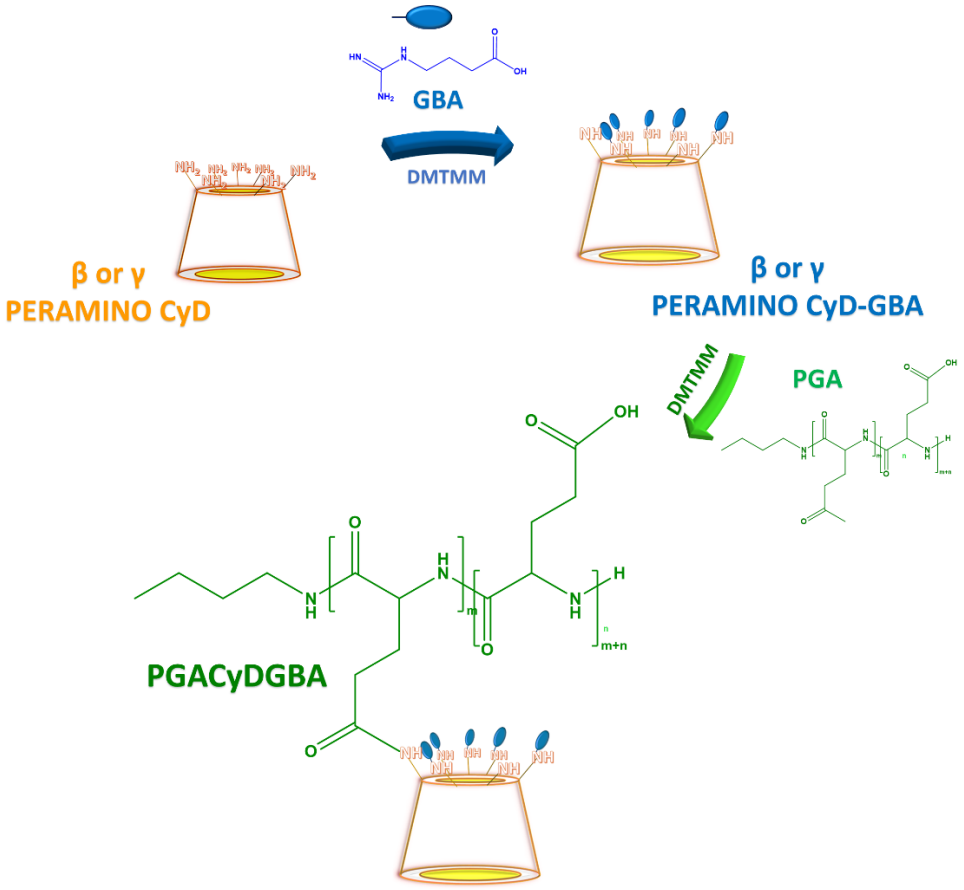

Figure 31. Synthetic scheme for PGACyDGBA polymers

2.1.3.1. SYNTHETIC ASPECT

PGACyDArg polymers were synthesized through condensation reactions between the carboxyl groups of PGA and the NH_2 groups of CyDs and Arg methyl ester (Figure 30).

PGACyDGBA polymers were synthesized via condensation reactions from PGA and 6-per-amine CyD previously modified with GBA (Figure 31). The condensation reactions in the experimental conditions give high yields and enable the modulation of the number of CyDs and the positive moieties in the final product (Table 6).

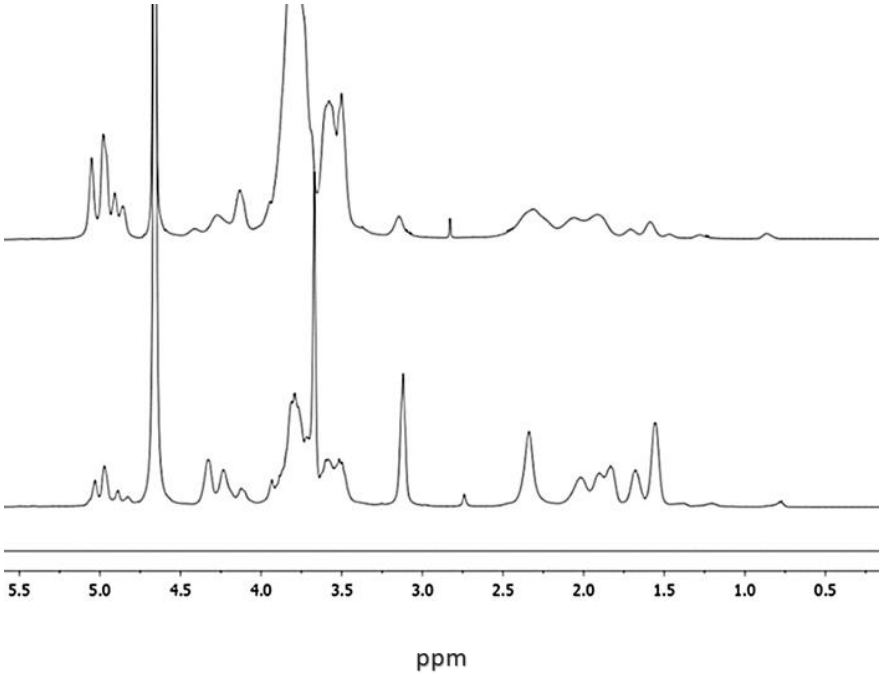

Figure 32. ^{1}H NMR spectra of PGAβCyDArg 1 (top), PGAβCyDArg4 (bottom) (D_2O, 500 MHz).

All the polymers were characterized by NMR spectroscopy (Figure 30, Figures S99- S106, Figures S108-S110).

The ^{1}H NMR spectra of PGACyDArg derivatives show common patterns; CyD protons resonate at 5 ppm (H-1), and 4.0-3.4 ppm (H-3, -6,-5,-4,-2). Protons of Arg and the side chain of PGA resonate at 3.3 ppm and 2.5-1.8 ppm. Butyl protons of PGA are also evident between 1.5 ppm and 1.0 ppm. The number of CyD units linked to the PGA backbone was calculated for each polymer derivative by determining the integral ratios of the CyD Hs-1 signal, the PGA signal of the ethylene chain protons or the N-butyl chain protons. Furthermore, the integral ratio of the signal due to the γ-CH_2 of Arg moieties at 3.3 ppm and the signals of PGA ethylenic protons or the N-butyl protons was used to value the number of Arg moieties grafted onto the polymer. The results obtained by NMR for each bioconjugate are reported in Table 6.

Table 6. Features of newly PGACyDArg/GBA bioconjugates

Name	Average number of CyDs	Average number of Arg and GBA	Average Molar Mass (kDa)
PGAβCyDArg1	19±1	4±1	25
PGAβCyDArg2	15±1	7±1	22
PGAγCyDArg3	12±1	10±1	21
PGAβCyDArg4	6±1	15±1	16
PGAγCyDArg5	5±1	15±1	13
PGAβCyDGBA6	7±1	32±1 (about 6 for cavity)	17
PGAγCyDGBA7	5±1	31±1 (about 6 for cavity)	15

The ^{13}C NMR spectra of the PGACyDArg derivatives reveal signals due to guanidium carbons at about 160 ppm and signal around 174 ppm attributed

to the carboxyl group of PGA and arginine methyl ester, in addition to the signals of CyD units in the aliphatic region.

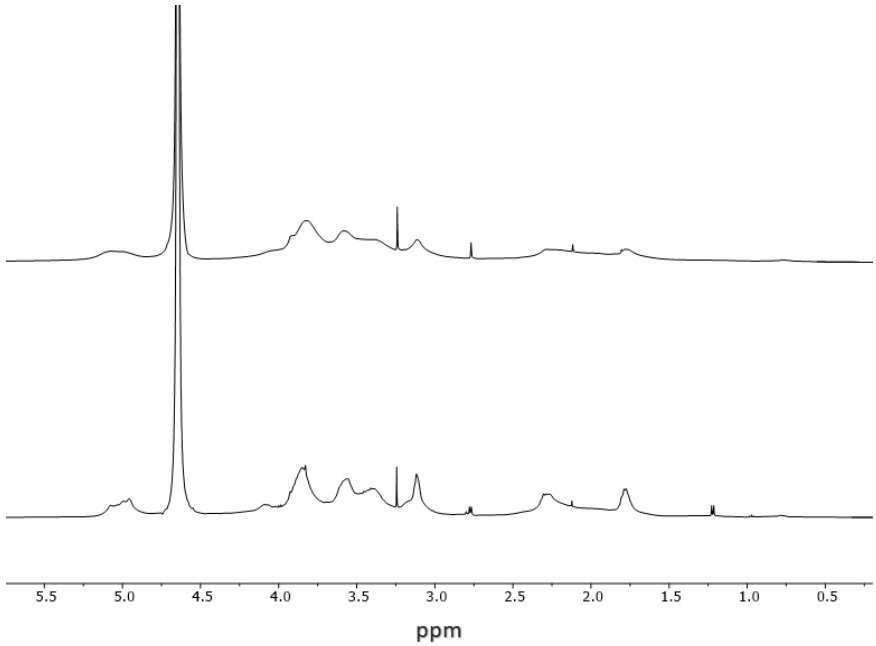

Figure 33. ^{1}H NMR spectra of PGAβCyDGBA (up) and PGAγCyDGBA (down), (D_2O, 500 MHz).

As for PGACyDGBA polymers, ^{1}H NMR spectra (Figure 33, Figure S108- S110) show the signals of CyD protons that resonate at 5 ppm (H-1), and about 3 ppm (H-3,-6,-5,-4,-2). Protons of γ-GBA and PGA chains resonate at 3 ppm and 2-1.6 ppm. PGA butyl proton signals are also evident between 1 ppm and 0.7 ppm. For both the derivatives, the integral ratios of CyD Hs-1signal and the signal of the n butyl protons allowed to determine the number of CyD units, about 8, functionalizing the PGA backbone. Moreover, the integral ratio of signal due to the CH_2 at 3.2 ppm and the signals of n butyl protons suggested the number of GBA moieties, approximately 35 (Table 6).

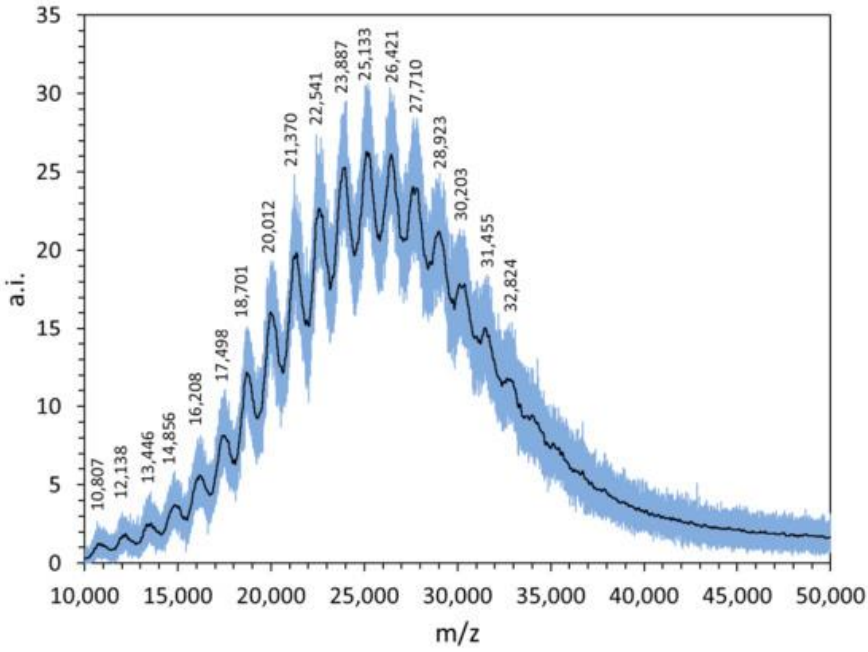

Figure 34. MALDI-TOF MS spectrum of PGAβCyDArg1. The raw spectrum (blue line) was properly smoothed (black line) in order to obtain the m/z values of all the relative peaks.

Mass spectrometric measurements were also conducted to further characterize the structural features of the new polymers. The MALDI spectra recorded in linear mode (Figure S107) mainly contain a wideband; the *m*/*z* values of the highest peaks match those obtained by the NMR studies (Table 6), within the experimental errors, confirming the calculated molecular weight (Mw) of the new CyD polymers.

As for PGAβCyDArg1, the MALDI spectrum is resolved into several components (Figure 34). The average difference between two successive relative peaks is 1280 ± 20. This value suggests that the repeat unit contains both the CyD (MW 1135) and glutamic acid (MW 147) moieties, as expected.

2.1.3.2. SIZE AND ZETA POTENTIAL

The hydrodynamic diameters of the synthesized PGACyDArg polymers were determined using DLS. Size data are reported in Table 7. Data indicate that the polymers form NPs.

Table 7. Z-Average (d. nm) of PGACyDArg polymers

Name	Z-Average size (d. nm)
PGAβCyDArg1	49±5
PGAβCyDArg2	35±2
PGAγCyDArg3	29±3
PGAβCyDArg4	79±8
PGAγCyDArg5	59±6

In the case of PGACyDArg polymers, the Z-Average (Figure S111) value increased when the number of CyD cavities decreased. This increase of Z-Average value suggests that CyD cavities disfavor self-aggregation. Systems containing fewer CyDs showed populations with larger sizes, which are close to that found for PGA alone. The number size distributions suggested that the main population for almost all systems had hydrodynamic diameters in the range of 5-9 nm.

For PGACyDGBA polymers, the hydrodynamic diameters (Figure S112) were determined in water at different ionic strengths (NaCl 0.5M). Size data are reported in Table 8.

Table 8. Z-Average (d.nm) of PGACyDGBA polymers

Name	Z-Average size (d. nm)
PGAβCyDGBA	23±2
PGAβCyDGBA*	7±2
PGAγCyDGBA	18±1
PGAγCyDGBA*	13±1

***NaCl 0.5 M**

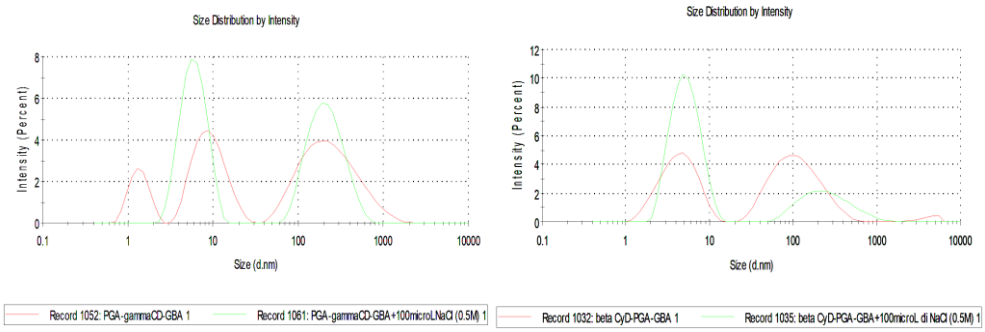

Figure 35. Intensity Size Distribution (DLS) of PGA β and γCyDGBA

Data reported in Table 8 showed notable differences in the size distribution between the NaCl and water solutions. In water, the NP size is about 20 nm. The size variation might be due to the high number of positive charges, generating an electrostatic repulsion and forming elongated structures. In the presence of Cl^-, the positive charges are shielded, forming smaller NPs. DLS data show (Figure 35) an increase in the intensity of the population with a smaller size compared to the water solution as reported for similar systems [220, 221].

Finally, the Z-Potential of the systems at physiological pH (100 mM) was evaluated, and the data are in agreement with the expected.

Table 9. Z-Potential surface (mV) of PGACyDs polymers

Name	Z-Potential (mV)
PGAβCyDArg1	8±1
PGAβCyDArg2	7.7±0.5
PGAγCyDArg3	2.3±0.5
PGAβCyDArg4	45±5
PGAγCyDArg5	37±3
PGAβCyDGBA	41±5
PGAγCyDGBA	27±2

PGA alone shows a negative potential value of -58 mV (Figure S113).

Both PGACyDGBA and PGACyDArg, having a permanent positive charge that can significantly increase the potential, showed Z values from +7 to +45 mV (Table 9), depending on the number of GBA or Arg moieties grafted onto the polymer (Figures S114-S116).

2.1.3.3. SOLUBILITY EXPERIMENTS

The interaction of PGACyDArg polymers with Dox at pH 7.4 was investigated with solubility experiments by adding Dox hydrochloride (0.017 M, water solution) to solutions containing different polymer concentrations (25 mg/ml, 12 mg/ml, 6 mg/ml) in phosphate buffer (50 mM, pH 7.4).

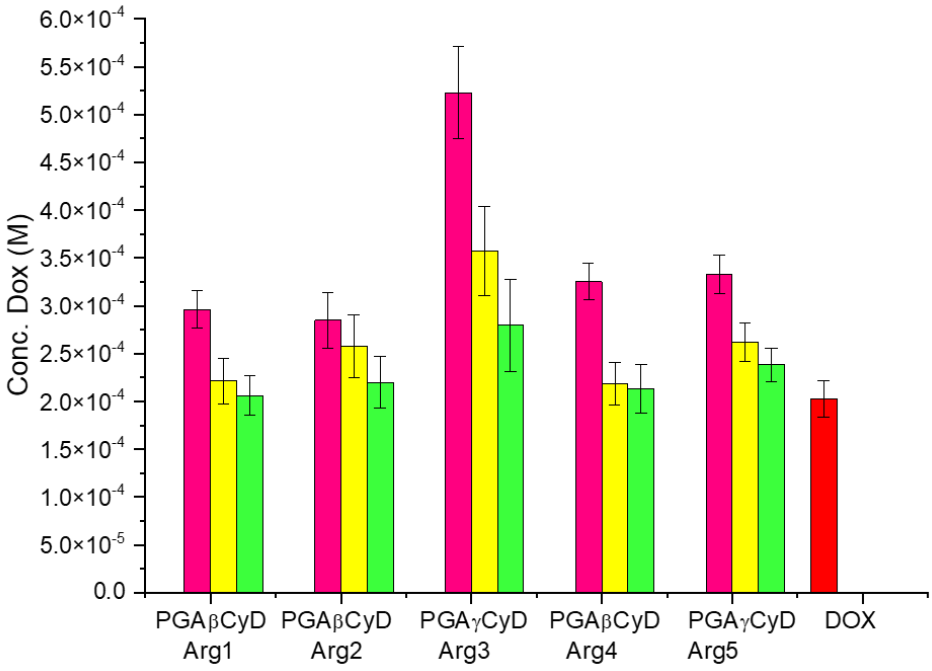

Figure 36. Solubility diagram of PGACyDArg polymers at three different concentrations: pink 25 mg/ml, yellow 12 mg/ml and green 6 mg/ml

The diagram (Figure 36) shows that all polymers, at all concentrations, enhance the solubility of Dox. This trend is more marked for the PGAγCyDArg3, which shows a significant increase in solubility even at 6 mg/ml. This enhancement could be attributed to both a higher number of cavities compared to PGAγCyDArg5 and the larger dimension of the γCyD cavity. The role of the cavity was further confirmed through a comparison between PGAβCyDArg4 and PGAγCyDArg5, which contain the same average number of cavities and charges, differing only in the cavity type. Besides, in this case, the polymer grafted with γCyDs shows an increase of solubility more evident, especially at concentrations of 6 mg/ml and 12 mg/ml.

2.1.3.4. ANTIPROLIFERATIVE ACTIVITY

PGACyDArg systems were studied as DDS for the Dox. Cell proliferation assay was performed on A2780, A549 lung adenocarcinoma and MDA-MB-231 epithelial human breast cancer cell lines. Complexes of polymer/Dox (1:10 molar ratio) were prepared and assayed.

Data obtained are reported in Table 10. Polymers alone did not show toxicity for cells (data not shown).

Table 10. Half maximal inhibitory concentration (IC_{50}) values (nM) of doxorubicin (Dox) in the presence of CyD polymers in human tumor cells.

Cell Line	PGAβCy DArg1	PGAβCy DArg2	PGAγCy DArg3	PGAβCy DArg4	PGAγCy DArg5	Dox
A2780[a]	4.7 ± 1.7 [b]	5.9 ± 1.6	12.7 ± 2.4 [c]	10.0 ± 1.7 [d]	11.7 ± 0.4 [e]	7.7 ± 3.9
A549	55.2 ± 10.0	52.2 ± 10.1	70.0 ± 16.6	52.6 ± 4.4	56.2 ± 2.9	54.6± 19.2
MDA-MB-231	37.7 ± 11.8	40.9 ± 6.5	50.6 ± 22.5	60.2 ± 15.2	65.3±16.7	40.9± 13.8

[a]p= 0.0003, as detected by ANOVA;[b]p= 0.0657 vs. Dox;[c]p= 0.0001 vs. PGAβCyDArg1;[d]p= 0.0016 vs. PGAβCyDArg1;[e]p= 0.0007 vs. PGAβCyDArg1, all calculated by Bonferroni/Dunn posthoc analysis of data.

Overall, the data show that the polymers did not significantly change the antiproliferative activity of Dox. In fact, in the A549 and MDA-MB-231 cell lines, IC_{50} values do not significantly change depending on the type of functionalization. Conversely, in A2780 cells, the complexes with PGAγCyDArg3 (p= 0.0028), and PGAβCyDArg5 (p= 0.0738) showed higher IC_{50} values than free Dox.

In the case of the polymers based on γCyD, the higher affinity for Dox suggested by solubility data may explain the effect on cytotoxicity, as reported for similar systems studied previously [219]. The reduction in the antiproliferative effect was observed for many systems, and only *in vivo* studies may provide information on the potential of the drug carriers [222].

Only PGAβCyDArg1/Dox showed a slightly higher antiproliferative activity (p= 0.0657) than free Dox and a significant difference compared to PGAγCyDArg3, PGAγCyDArg4, and PGAβCyDArg5 (Table 10).

2.1.4. METAL COORDINATION TO ASSEMBLE NPs

Iron (III) coordination was exploited to modify and upgrade CyD linear polymers. This family of NPs is sketched in Figure 37.

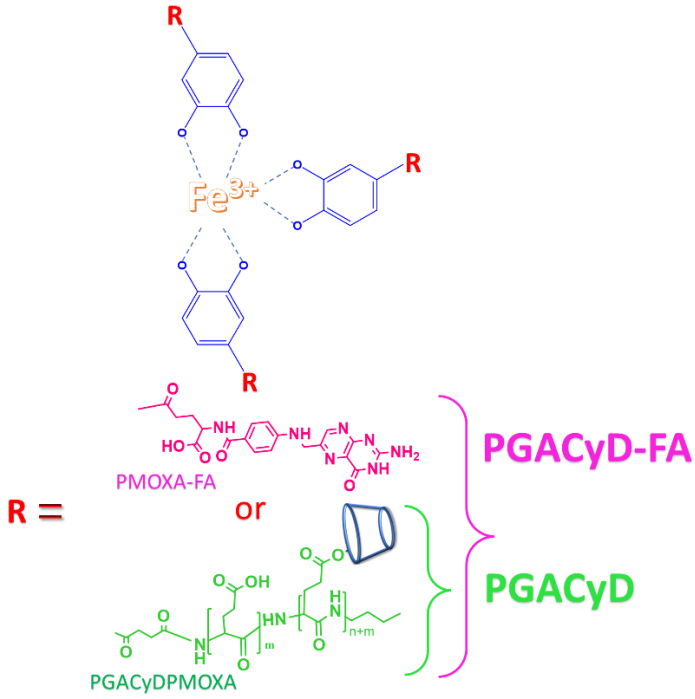

Figure 37. The metal complex with PGACyD-FA or PGACyD

All polymers synthesized have a termination of poly (2-methyl-2-oxazoline, PMOXA). PMOXA was used because it has similar biomedical properties to the broadly used PEG, including long-term chemical stability and excellent antifouling properties [223, 224].

For all systems, PMOXA was synthesized with a double termination. One termination was ended to an amino group, while the other one was used to introduce a nitro-dopamine anchor (NDA) [225, 226]. Catecholate NDA can form iron (III) complexes with high stability [227]. In this way, a single metal ion can coordinate different polymers, obtaining different NPs (Figure 37):

- PGACyD, with PGACyDPMOXA polymer only
- PGACyD-FA, with PGACyDPMOXA polymers and PMOXA-FA (about 10%)

PGACyDPMOXA is a linear backbone functionalized with a high number of CyDs that increase the delivery and solubility of the drug in the cell. The high molecular weight of PGA was selected to increase the size of the final complex and promote the EPR effect in passive uptake.

The PGACyDPMOXA was synthesized with a multi-step reaction (Figure 39).

The PMOXA-FA is ended by a folic acid that may drive and promote active uptake of the complex (Figure 40). FA is an essential vitamin. There are three different types of folate receptors: FRα, FRβ and FRγ. FRα is widely expressed in various types of carcinoma cells [228]. The recognition between FA and FR is promoted by the carboxyl group of vitamins, particularly the γCOOH [229, 230]. The long PMOXA spacer could make the FA unit available for interaction with a specific receptor. Furthermore, FA has the advantage of being recognizable by confocal microscopy, with a fluorescence

emission between 400 and 500 nm [231, 232]. In this way, it is possible to distinguish the fluorescence of the FA based ligand from that of Dox (λ_{em}=595 nm) [233] and exploit FA as a label.

The Fe^{3+} ion has been added in polymer/metal 3:1 molar ratio to promote the formation of octahedron complexes with the catechol units.

All ligands were characterized by NMR, DLS and fluorescence spectroscopy.

2.1.4.1. SYNTHETIC ASPECT

In the first step, the backbone of PMOXA was synthesized (Figure 38) via Cationic Ring-Opening Polymerization (CROP) [234].

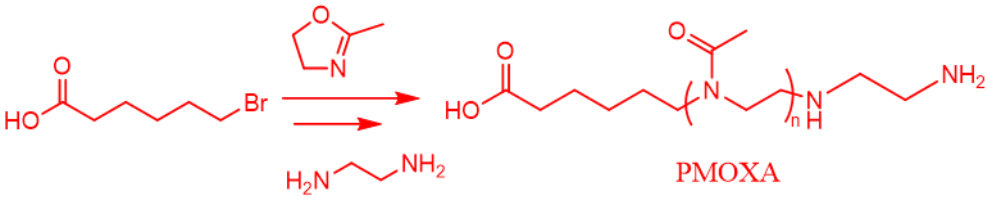

Figure 38. Scheme of synthesis of PMOXA

After the synthesis of PMOXA (Figure 38), the two functional groups were modified to introduce NDA. Subsequently, NDAPMOXA was reacted with succinic anhydride to introduce a COOH group that can react with the NH_2 of PGA, functionalized with $\beta CyD6NH_2$ (Figure 39).

PGA was about 15 kDa with about 100 carboxyl groups. The final condensation steps, first between PGA and CyD and then between PGACyD and NDAPMOXASUC (Figure 39), were carried out in water using DMTMM as activating agent.

All intermediate products were purified by dialysis (cut-off 3.5 kDa) or by precipitation. The purity of the compounds was evaluated by NMR spectroscopy and GPC (Figures S117- S123).

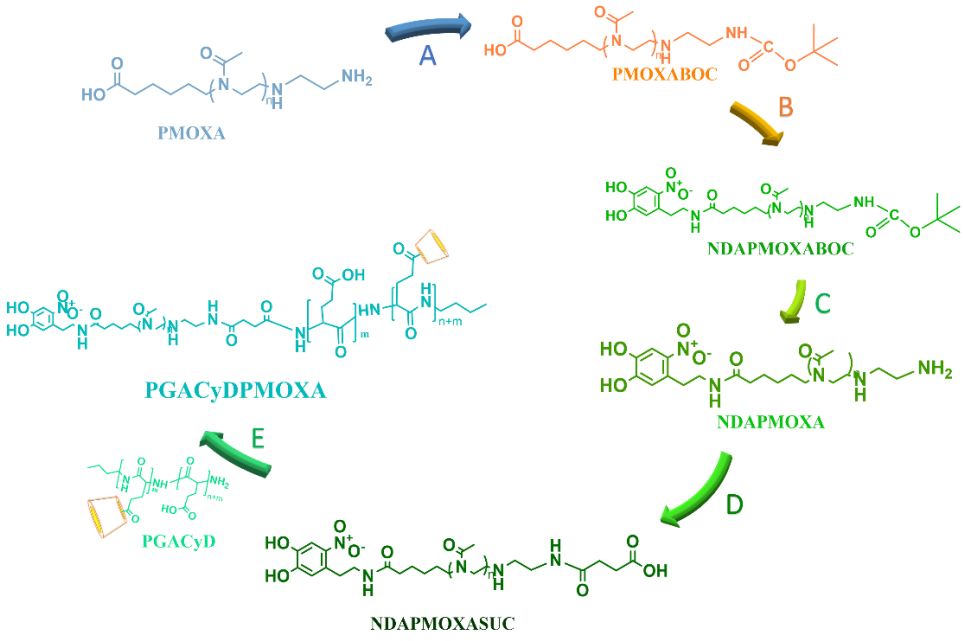

Figure 39. Synthetic scheme of PGACyDPMOXA. A) BOC in DMF with TEA o.n., B) NDA in DMA with TBTU and DIPEA o.n., C) in DCM with TFA 4h, D) succinic anhydride with hydroxide of sodium o.n., E) DMTMM and TEA in water o.n.

The PMOXA-FA polymer was synthesized through a condensation reaction from PMOXA and FA in DMA using DCC and NHS as activating agents (Figure 40). γCOOH group of FA is the most reactive and the most accessible.

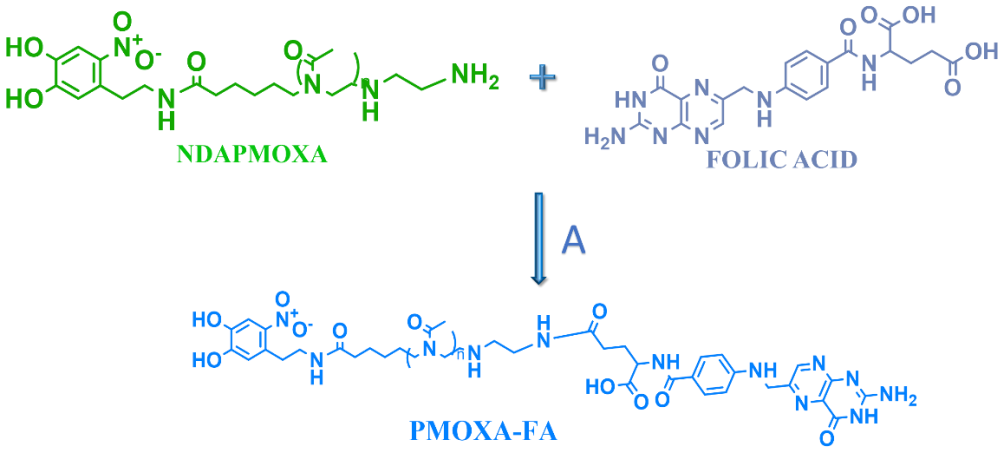

Figure 40. Scheme of synthesis of PMOXA-FA, A) in DMA with DCC and NHS

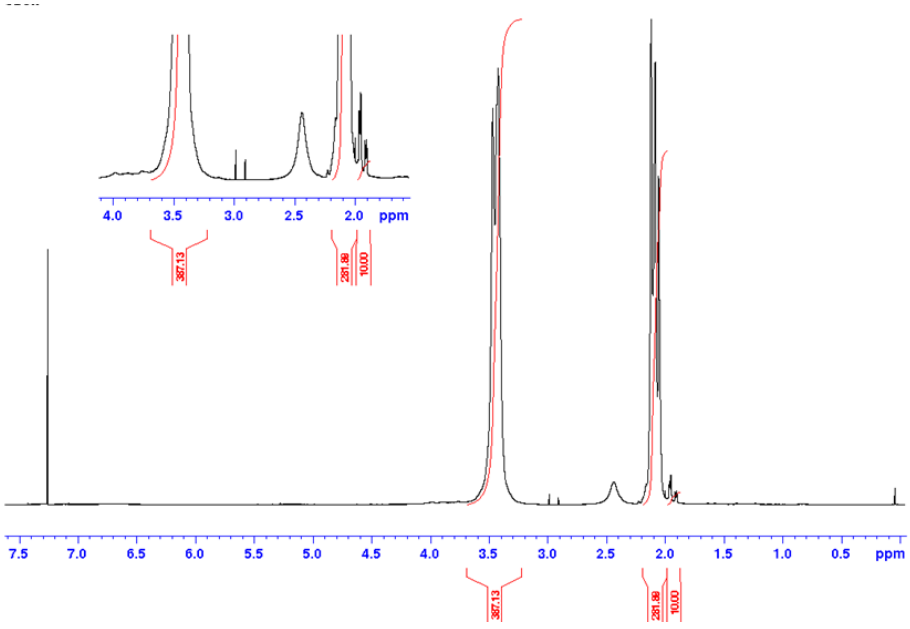

Figure 41. ^{1}H NMR of PMOXA ($CDCl_3$, 300 MHz)

^{1}H NMR spectrum of PMOXA (Figure 41) shows the protons of monomer units at 3.4 and 2.1 ppm, while the protons of the chain of hexanoic acid at about 1.8-2 ppm.

Integrating NMR signals between the protons of bromohexanoic acid and the methyl group of the repeated unit allowed the calculation of about 95 repeating units for the polymer, corresponding to a molecular weight of around 8.000 Da (Figure S124).

This molecular weight agrees with the data obtained from GPC analysis (Figure S124).

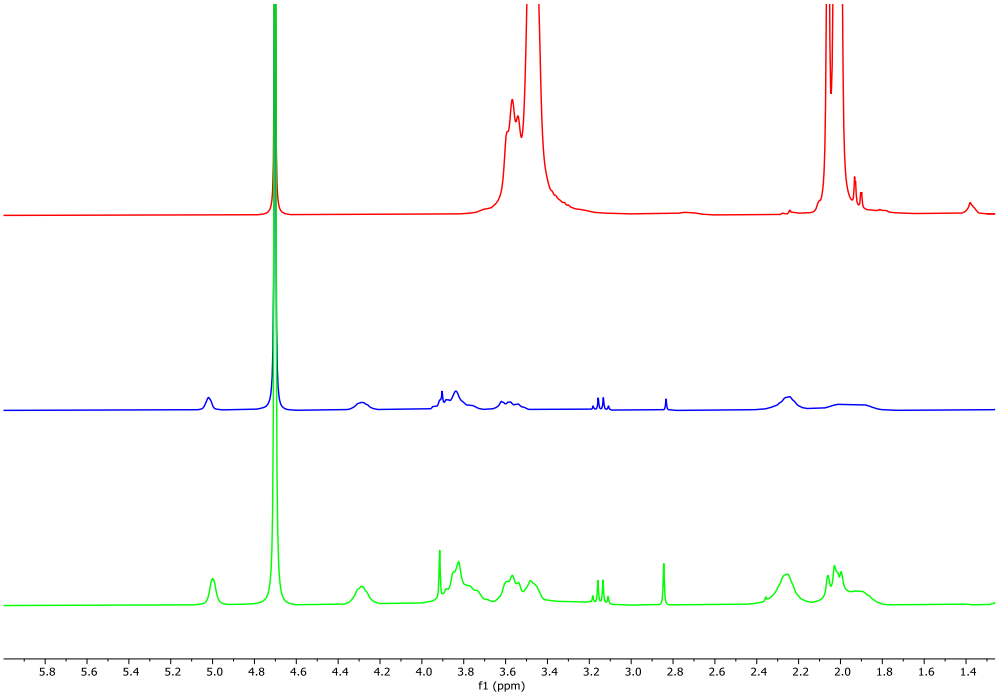

Figure 42. ^{1}H NMR spectra of PMOXABOC (red), PGACyDs (blue) and PGACyDsPMOXA (green) ($CDCl_3$, 300MHz)

The ^{1}H NMR spectrum of PMOXABOC (red) shows a pattern characteristic of PMOXA described above (Figure 41). Additionally, at 1.4 ppm, the 9 protons of BOC are observed (the low-intensity signal is due to the fewer number of protons in the BOC compared to the protons of polymers).

^{1}H NMR spectrum of PGACyDs (blue) shows the protons of CyD resonating at 5 ppm (H-1), and 4.0-3.4 ppm (H-3, -6, -5, -4, -2). Protons of the

glutamic acid side chain of PGA resonate in the 2.5-1.8 ppm region. Butyl protons of PGA are also visible between 1.5 ppm and 1.0 ppm.

The number of CyD units linked to PGA was determined through integral ratios of the signal of Hs-1 of CyD and the ethylene chain protons of PGA or the N-butyl chain protons.

In the ^{1}H NMR spectrum of PGACyDPMOXA (green), both the signal of the PMOXA spacer and the PGACyD polymers are observed. Integration of peaks of PGA at 4.3 ppm and of PMOXA at 2 ppm proves that there is approximately one PGA chain functionalized for each PMOXA chain (Figure 42).

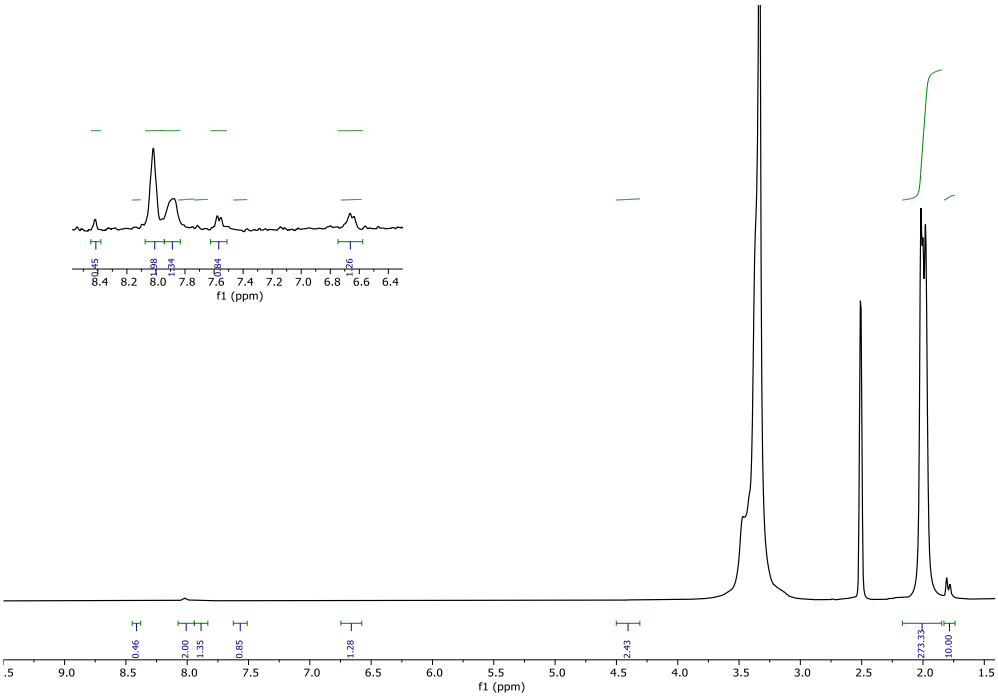

Figure 43. ^{1}H NMR of PMOXA -FA ($CDCl_3$, 300 MHz)

^{1}H NMR spectrum (Figure 43) shows the peaks of PMOXA as described earlier, with the characteristic peak of FA resonating between 8.4 and 7.6 ppm.

The NMR spectrum shows that the polymer was functionalized with about 65% FA.

2.1.4.2. SIZE OF NPs

PGACyDPMOXA formed NPs with a diameter of 288 nm. When was added Fe^{3+}, the dimension of NPs increased, but it is interesting to observe (Figure 44) that two different populations are distinguishable, one at approximately 150 nm and the second at about 577 nm (Z-Average increase to 330 nm). All systems were investigated at a concentration of 6 mg/0.6 ml.

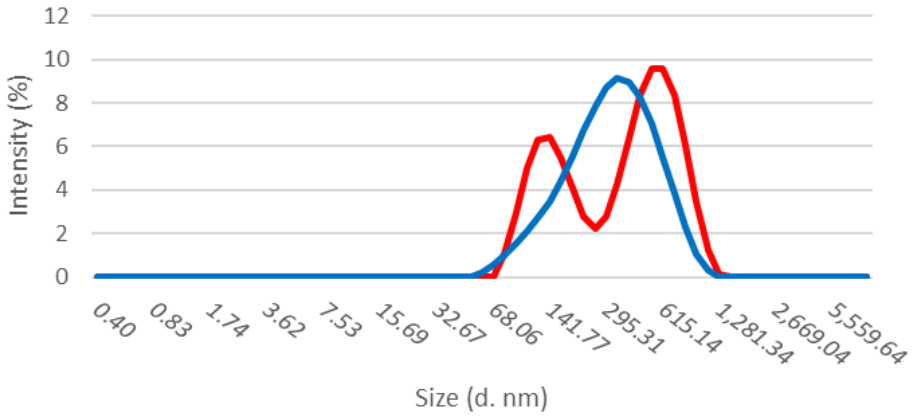

Figure 44. Z-Average (d.nm) of PGACyDPMOXA polymer (blue) and PGACyD complex (red) (6 mg/ 0.6ml)

The trend of the hydrodynamic diameter of NPs containing FA, both in the presence and absence of iron ions (Figure 45), is similar to that described above for PGACyDPMOXA. In this case, as well, the polymers show a main population. However, in the presence of Fe^{3+}, there are two peaks. The Z-Average of hydrodynamic diameter increases from 199 nm to 221 nm.

The increase in Z-Average suggests that the complexation has occurred.

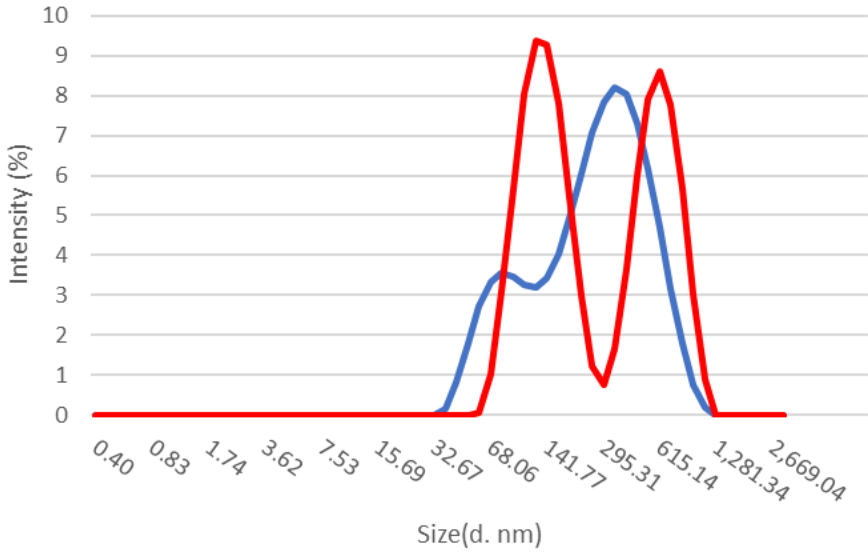

Figure 45. Z-Average (d.nm) of PGACyDPMOXA and PMOXA-FA polymers (blue) and PGACyD-FA complex (red)

2.1.4.3. ABSORPTION AND FLUORESCENCE SPECTRA

The UV-vis spectrum of the iron (III) complex PGACyD-FA (concentration 2 mg/0.6 ml) showed the typical peaks of FA at 279 and 355 nm (Figure 46 **A)**). Moreover, the fluorescence spectrum (Figure 46 **B)**) obtained using an excitation wavelength of 270 nm (concentration 0.2/0.6 ml) revealed a typical trend of FA with two peaks at 354 nm and 443 nm. The data obtained from the fluorescence spectrum prove that the distance between the iron ion and the vitamin is enough to avoid the quenching of fluorescence (more than the Förster radius) and that the FA molecule is a labeling unit in the complex, allowing the study of the internalization mechanism *in vitro*.

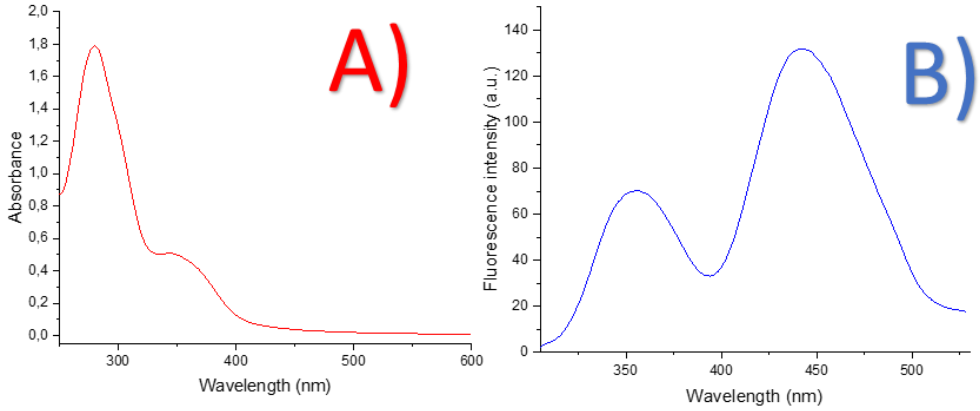

Figure 46. Spectra of PGACyD-FA complex of Absorbance A) and Fluorescence B)

2.1.5. CROSS-LINKED POLYMERS OF CyDs

Three different cross-linked polymers of CyDs, pγCyD (54 cavities), the anionic polymer of γCyD (pγCyDA, 28 cavities) and the anionic polymer of βCyD (pβCyDA, 54 cavities) were studied as carriers for; Dox or Oxaliplatin (Oxa, 1,2-diamino cyclohexane platinum) [235–237]. Oxa was patented in 1976 [238]. It has shown efficacy against many cancers, including colorectal, lung, gastric, ovarian and prostate cancer. One of the most widespread side effects is neuropathy, which includes muscular contractions and tetanic spasms [239]. Other side effects are thrombocytopenia, nausea, gastrointestinal dysfunction, and liver function abnormalities [235, 237, 240, 241]. Oxa can be included in both β and γCyD cavities with similar stability constants [236].

2.1.5.1. SIZE AND Z POTENTIAL

The dimensions and the charges of anionic polymers were evaluated at physiological pH (phosphate buffer 100 mM, pH= 7.4). Data suggest that the polymers form NPs with a small hydrodynamic diameter. Despite the negative charges, the crosslinked structure of the polymers could favor the formation of small NPs. Finally, Z-Potential was measured. The data are reported in Table 11 and Figure S125 and Figure S126.

Table 11. Z-Average (d. nm) and Z-Potential (mV) of polymers in phosphate buffer pH=7.4

Polymers	Z-Average (d. nm)	Z-Potential (mV)
pβCyDA	25±2	-14±0.06
pγCyDA	53±5	-18±1

2.1.5.2. SOLUBILITY EXPERIMENTS

All three polymers were investigated *in vitro* with both drugs but only the solubility of Dox with polymers was studied given that the solubility in water of Oxa is 4 mg/ml, about 10^{-2} M while for Dox is 7.40×10^{-5} M pH 7.4.

The solubility of Dox was investigated in the presence of pγCyDA, pβCyDA and pγCyD at pH 7.4. The purpose was to evaluate if the anionic polymers with COO^- functional groups can better interact with Dox, a cationic drug and improve its solubility at physiological pH [242] (Figure 47, Figure S127).

In particular, the Dox solubility was reported versus the CyD units concentration for a better comparison among the different polymers. CE values of CyDs cavity are 0.083 for pγCyDA, 0.082 for pβCyDA and 0.011 pγCyD. Data suggest that the presence of carboxylate groups improves the affinity for the guest. Indeed, the pγCyD slightly improves the solubility of

Dox, unlike the other polymers, negative charges increase the solubility of Dox very significantly, suggesting a higher interaction with the positive drug. Data do not show a better affinity of pγCyDA compared to pβCyDA (Figure 47, Figure S127). The polymers are EPI cross-linked polymers and an influential role of the network in the Dox interaction can also be proposed.

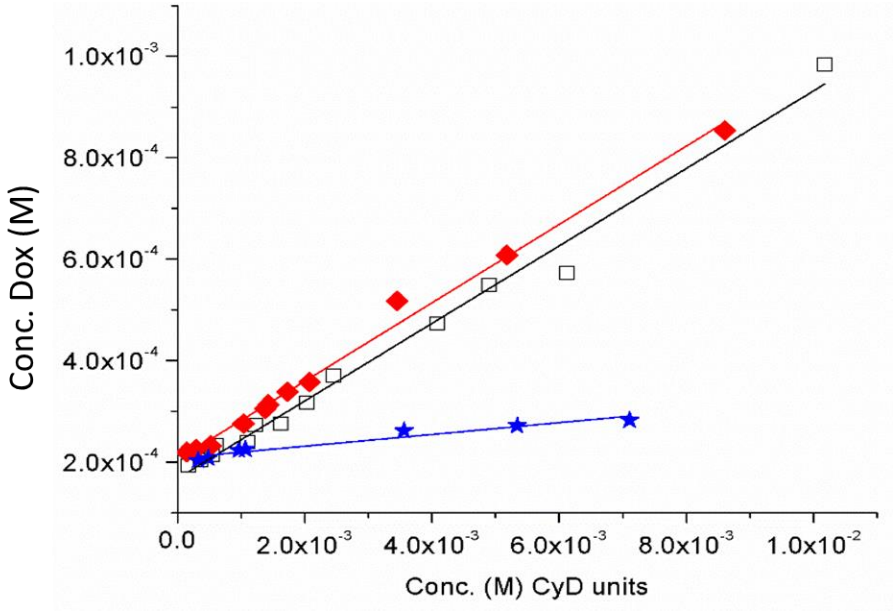

Figure 47. Dox solubility (pH=7.4) versus the amount of pγCyDA (■), pβCyDA (□) and pγCyD (★) (reported as CyD cavity concentration)

2.1.5.3. ANTIPROLIFERATIVE ACTIVITY AND DRUG ACCUMULATION IN CELLS

Cell proliferation assay was performed with Dox and Oxa in the presence of pγCyDA, pβCyDA, and pγCyD and compared to free drugs (Figure 48).

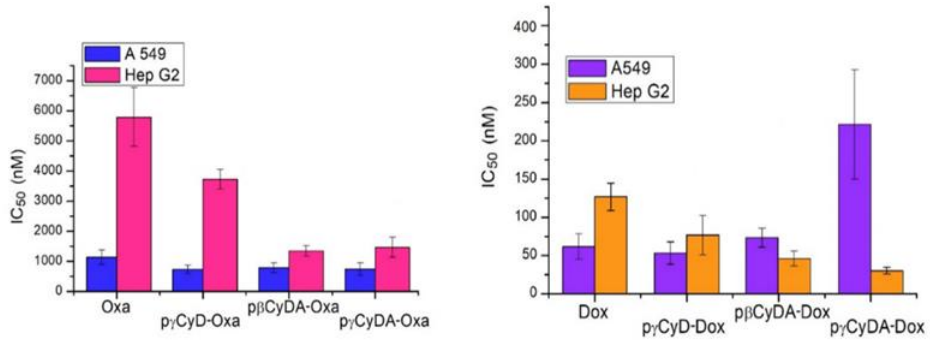

Figure 48. IC_{50} (nM) of CyD polymer-Dox/Oxa in human A549 and HepG2 tumor cells.

All polymers alone did not show any toxicity at μM concentration.

Both drugs with polymers were studied in A549 and HepG2 cell lines, showing different trends.

Oxa, when administered in the presence of pγCyDA, pβCyDA and pγCyD improved antiproliferative activity compared to the treatment with Oxa alone (Figure 48).

Conversely, in A549 cells, the presence of polymers during treatment with Dox showed a similar or even significantly lower antiproliferative activity (pγCyDA-Dox) than free Dox.

On the contrary, in HepG2 cells, pγCyDA-Dox, pβCyDA-Dox and pγCyD-Dox always showed a significant decrease of IC_{50} value compared to Dox alone.

To explain the antiproliferative activity data, Dox uptake was evaluated in A549 and HepG2 cells. Equal concentrations of Dox/pCyD complexes and Dox alone were added to the cell. In this way, it was possible to prove that the antiproliferative activity of Dox/pCyD compared to free Dox was determined by a differential Dox accumulation into target cells.

Cytofluorimetrically evaluations clarified that Dox accumulation was strictly linked to the type of CyD-polymer utilized for DD (Figure 49).

These results are inversely correlated with the analysis of the antiproliferative activity of such complexes, which always had IC_{50} values lower than that of the parent compound alone (Figure 48).

In HepG2 cells, the Dox uptake in the presence of the CyD polymers was always significantly greater than the accumulation of free Dox.

On the contrary, in A549 cells, where Dox-pCyD complexes always had lower antiproliferative activity than Dox alone, the accumulation of this drug was mainly lower for Dox/CyD polymers than for the parent compound (Figure 49, Figures S128 and S129).

Altogether, these data demonstrate that the enhanced antiproliferative activity of the complexes is associated with the higher ability of CyD complexes to target and accumulate Dox in the cells (Figure 49).

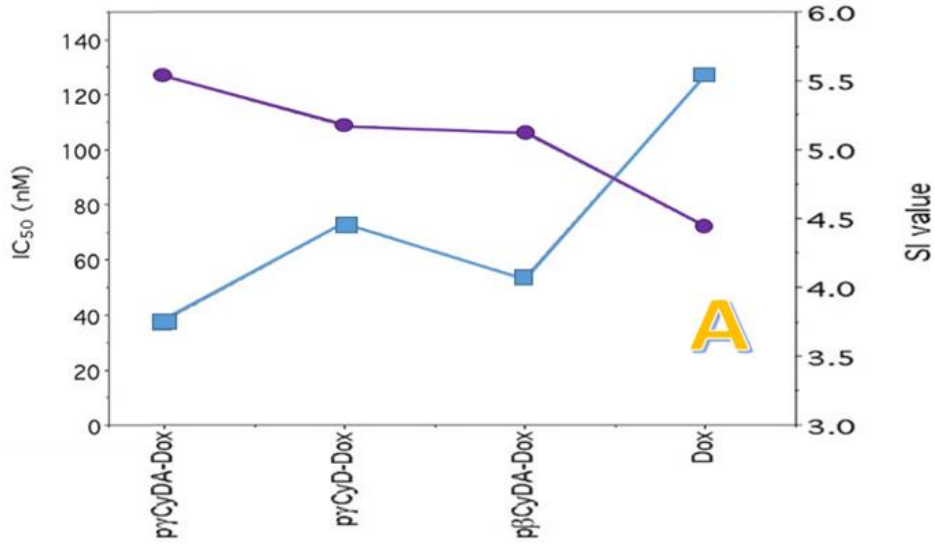

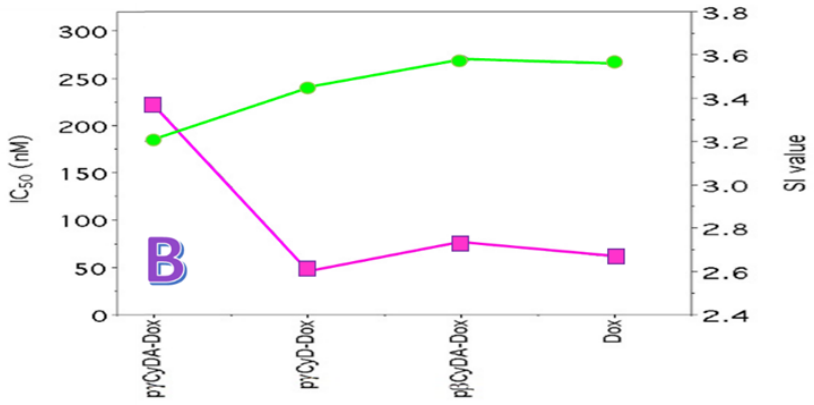

Figure 49. Correlation between IC_{50s} (■) and staining index (●) values calculated as described in Materials and Methods. A, HepG2 cells; B, A549 cells.

2.1.6. BIOCONJUGATE OF CYCLODEXTRIN POLYMER WITH BIOTIN

2.1.6.1. SYNTHETIC ASPECT

From the results obtained for pCyD systems, pβCyDA was functionalized with a targeting moiety, such as Bio (pβCyDBio), via a PEG3-Amine linker (Figure 50). The linker could promote the exposure of the target to cancer cells.

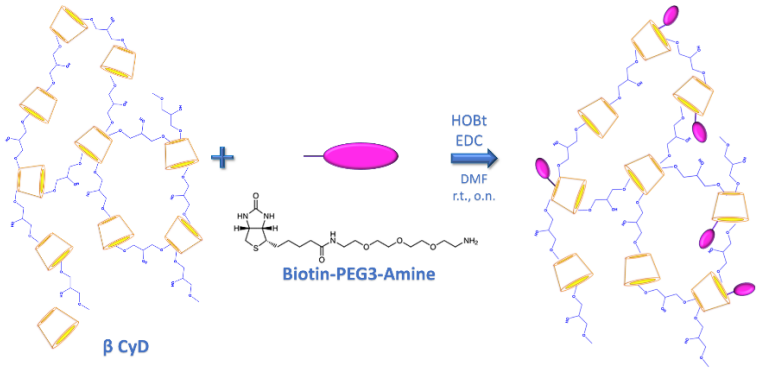

Figure 50. Synthetic scheme of polymer pβCyDBio

The pβCyDA was selected due to its high MW and the potential for achieving a highly functionalized polymer. This polymer contains many carboxyl groups (three for cavity) in which is possible to insert targeting units such as Bio.

The synthesis was carried out in DMF solution using HOBt and EDC as activating agents (Figure 50).

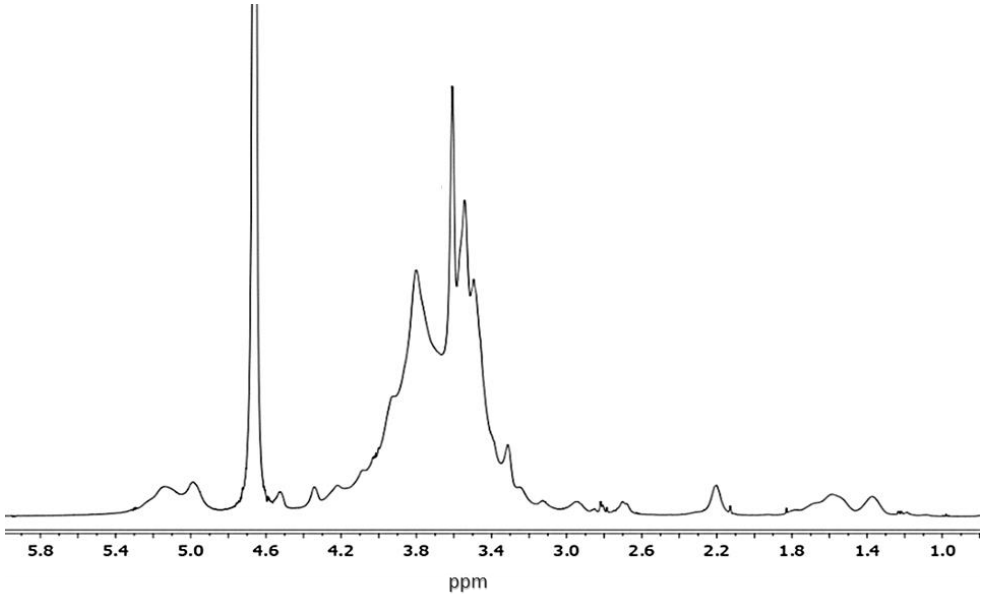

Figure 51. ^{1}H NMR spectrum of Polymer of pβCyDBio

^{1}H NMR spectrum of pβCyDBio (Figure 51) shows signals of CyD protons resonating around 5 ppm (H-1) and between 4.4 and 3.2 ppm (H-3,-6,-5,-4,-2). Signals at about 2.2 and 1.4 ppm are the proton of CH_2 of Bio (H-3,-2,-4,-1). PEG proton signals were overlapped with those of CyD. The number of Bio units was determined from the integral ratio of the signals of Bio (1.6-1.4 ppm) to the CyD H-1 signal at 5.2 ppm.

This value suggested that about 93% of CyD units were functionalized with Bio, corresponding to about 50 units of Bio in the polymer.

2.1.6.2. ANTIPROLIFERATIVE ASSAY

Cell proliferation assays were performed using Dox in the presence of the polymer functionalized with Bio (in ratio 2:1 CyD/Dox) on A2780, A549 and MDA-MB-453. Data obtained are reported in Table 12. It is important to note that the polymer alone did not exhibit any toxicity toward the cells (data not shown).

Table 12. Antiproliferative of pβCyDBio with Dox in relation to the drug alone in three different cell lines: A2780, A549 and MDA-MB-453

Cell lines	pβCyDBio	Dox
A2780	6.88±0.12	7.7±3.6
A549	47.0±3.9	58±14
MDA-MB-453	204.9±4.5	178±26

The results of the antiproliferative activity demonstrate that the polymers did not significantly modify the activity of Dox. The small size of the linker might not allow for adequate exposure of the target unit to the external environment, potentially reducing the efficacy of the active target.

2.2. NANOCHELATOR BASED ON CYCLODEXTRINS

The excess of metals can lead to problems for the entire organism, as metal ions participate in physiological and pathophysiological reactions [243]. Dyshomeostasis of metal is correlated to many diseases and damage to the nervous system, including Wilson and Menkes diseases, AD, and PD.

Chelation therapy is a medical treatment that removes metals from the body using specific chelators that bind to the metals and reduce their absorption in the system. An important limitation of chelating agents used to treat metal overload is their potential for toxicity. One example is the D-penicillamine, used to treat Wilson's disease, which has been replaced with triethylenetetramine (TETA) due to its reduced side effects [244]. For this reason, it is important to develop new biocompatible systems that form stable complexes (binder-metal) and remove metals from the body [245].

For this purpose, polymer systems were synthesized based on crosslinked CyDs polymers grafted with biocompatible chelating moieties. The advantage of CyDs is that they may be administrated orally without significant degradation in the stomach and intestine [246].

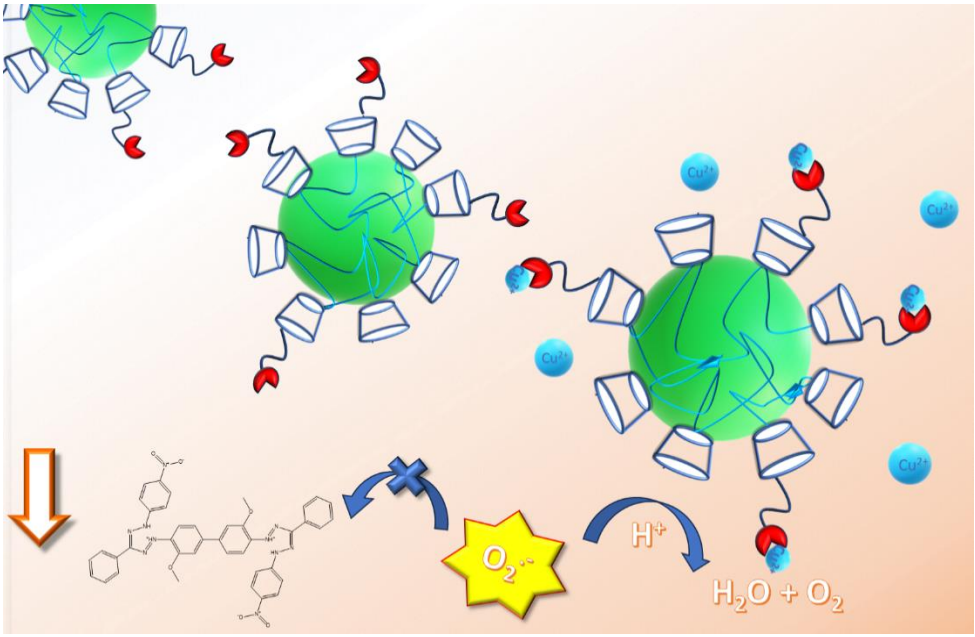

Figure 52. Scheme nanochelators based on CyD as SOD-like systems.

2.2.1. CROSS-LINKED CYCLODEXTRIN POLYMERS WITH CHELATING MOIETY

The cross-linked CyD polymers are biocompatible and soluble in water and can be excreted from the body without degradation [247, 248]. For this reason, they were functionalized with chelators to exploit their chelating ability in the bowel.

Chelator polymers were synthesized using cross-linked anionic polymers of β and γCyD and carcinine or L-histidine as chelator units (Figure 53). These units were chosen for their biological roles and their antioxidant activity. L-histidine (His) is a metal-coordinating amino acid [249, 250]. Carcinine (Carc, β-alanyl-histamine) is metabolically related to L-carnosine (concentration of carnosine 10-20 mM in skeletal muscle) [251]. Based on the results of several studies [252–254], Carc has a therapeutic role, acting as a natural antioxidant. Moreover, it plays an important role in stress regulation and functions as a pharmacological chaperone in biological systems [255].

The superoxide dismutase (SOD) activity of copper (II) complexes was also investigated, comparing the activity of the polymers functionalized to the single His and Carc in the presence of copper (II) (Figure 52). This activity was selected because oxidative stress is frequently associated with metal dyshomeostasis. The copper complex formed in situ can mimic the activity of SOD to protect cells from oxidative damage.

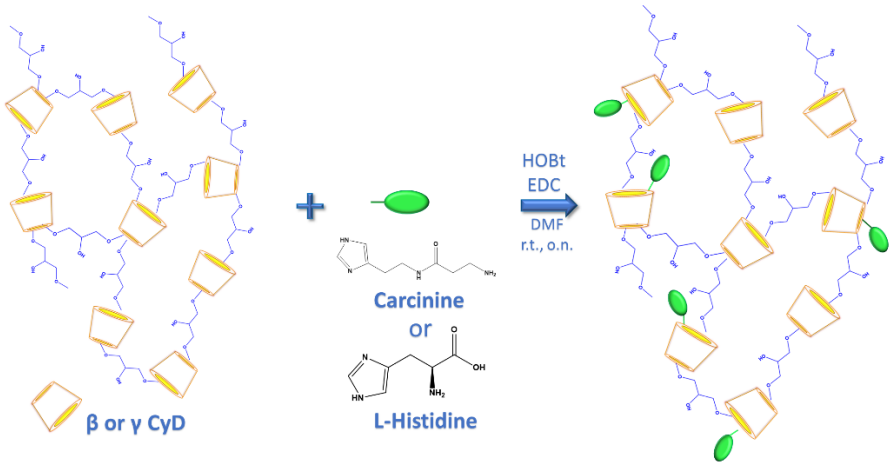

Figure 53. Synthetic scheme for His and Carc of pCyDs

2.2.1.1. SYNTHETIC ASPECT

Functionalization of pCyD with chelators was carried out through a condensation reaction using HOBt and EDC as activating agents in DMF. In both of the cases, a high degree of functionalization was obtained. However, an excess of Carc was needed for the Carc derivatives to obtain a functionalization degree comparable to that of the His derivates (60%).

All novel compounds were characterized by ^{1}H NMR, UV-vis spectroscopy and DLS.

^{1}H NMR spectra of all derivates show common patterns (Figures 54 and 55, Figures S130- S137),

The spectra show the proton of CyD and the moiety signals. The peaks are broad due to the high molecular mass of the polymers. As for pCyDCarc, the CH_2 signal of beta-alanine residue resonates at about 2.4 ppm and the CH_2 in alpha to imidazole ring resonates at 2.8 ppm. Imidazole protons are evident

in the aromatic region. For His derivatives, the signals of the ABX spin system can be seen in the spectra.

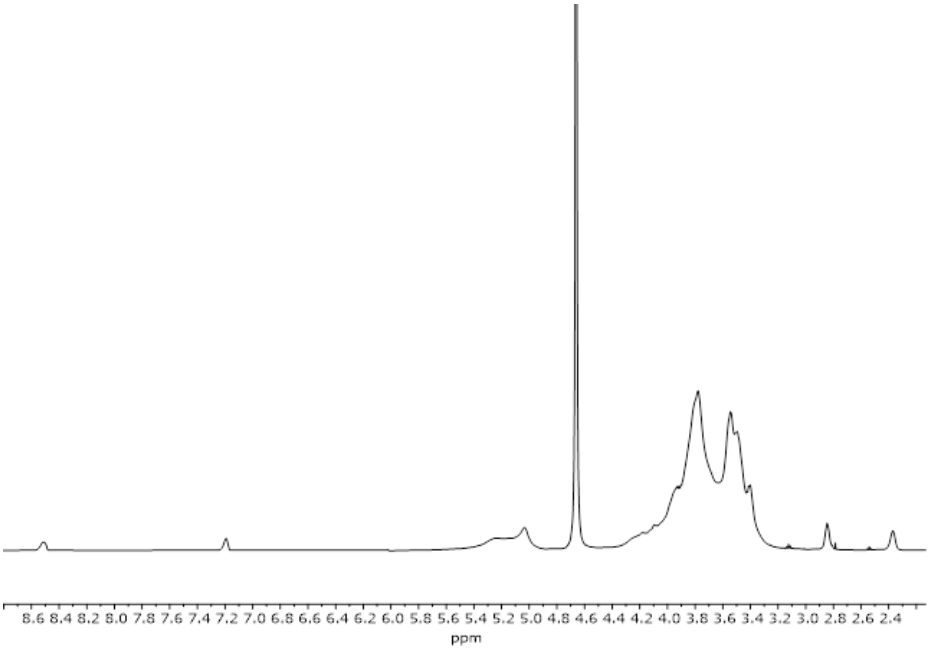

Figure 54. ^{1}H NMR spectrum of pγCyDCarc60 (D_2O, 500MHz)

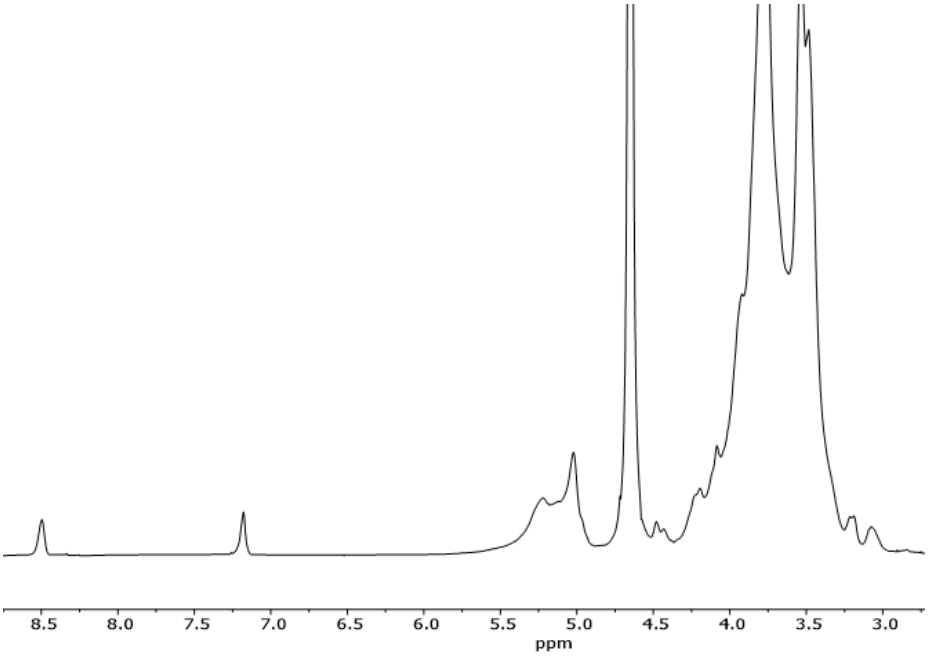

Figure 55. ^{1}H NMR spectrum of pγCyDHis (D_2O, 500MHz)

The number of carcinine units can be calculated from the ratio between the integral of imidazole signals at 7.2 ppm and those of CyD H-1, at 5.2 ppm. Particularly, the two products isolated have 30% (pβCyDCarc30 and pγCyDCarc30) and 60% (pβCyDCarc60 and pγCyDCarc60) of the pCyDA cavities functionalized with Carc units (Figure 54).

The functionalization degree of pCyDHis was also determined from signal integration values. Both pβCyDHis and pγCyDHis were modified with His in approximately 60 % of the cavities (Figure 55).

2.2.1.2. SIZE OF NPs

DLS measurements showed that all the polymers form NPs (Figures S138- S139). As for the commercial pCyDA, the polymers functionalized present a higher hydrodynamic diameter for pβCyD than pγCyD with the same functionalization. This is due to the different molecular weights of the parent cross-linked polymers. The functionalization slightly modified the dimensions of the systems.

2.2.1.3. AMYLASE CLEAVAGE

In order to evaluate the capability of polymers to survive in the bowel, their stability towards amylase enzymes was determined at different pH; 7.4, 4.0 and 3.0, and the results were compared to free β and γCyD. Results demonstrated that the polymers did not hydrolyze into smaller units in the experimental conditions used. Only the free γCyD showed a slight degradation, in keeping with the literature data [246, 256]. In particular, γCyD

can be slightly hydrolyzed by amylase due to its size and flexibility. In the case of the pγCyD polymer, the network structure stabilizes the CyD structure against enzymatic hydrolysis.

2.2.1.4. METAL COMPLEXES

UV-vis spectra of Cu^{2+}complexes of pCyDCarc60 or pCyDHis were studied at physiological pH in HEPES buffer solution. HEPES buffer was selected because it is commonly labeled as a non-coordinating buffer. The complexes were investigated in molar ratio 1:2 M/L, L being Carc or His moiety. The UV-vis spectra showed weak absorption bands in the Vis region (Figure S140) due to the d-d transitions. The λ value for the Cu^{2+}-pCyDCarc60 system (650 nm) is slightly higher than those reported in the case of the free Cu^{2+}-Carc complex (628 nm), and it is also very similar to the value reported for the copper (II) complex of the simple βCyDCarc (652 nm) [257]. A similar trend was found for the Cu^{2+}-pCyDHis systems: the d-d band is at 666 nm, higher than that for the Cu^{2+}-His complex (642 nm) [258, 259]. This difference could reasonably be due to the metal coordination environments in the pCyD polymers. In particular, the amino group of the free ligands (Carc or His) became an amide group in pCyDHis and pCyDCarc.

2.2.1.5. SOD ACTIVITY OF COPPER (II) COMPLEXES

The SOD-like activity of Cu^{2+} complexes of pCyDCarc60 and pCyDHis was determined by an indirect assay of kinetics competition using NBT as a target [260]. Many CyD functionalized metal complexes have been investigated as SOD mimetics and have shown higher SOD activity than free moiety complexes [261]. Similar behavior has also been found for monomer

CyDs conjugated with Carc [257]. The IC_{50} value (the concentration that causes the 50% inhibition of NBT reduction) was determined in the presence of the polymer complex and with Carc and His complexes for comparison. The IC_{50} is the complex concentration for $V_0 = 2V_c$ (Table 13). The data representations are reported in Figures 56 and S141.

Table 13. IC_{50} values (μM) for SOD activity of Cu^{2+}-pCyD polymers (Cu/L 1 : 2, L is the chelating moiety Carc or His, pH 7.4 HEPES buffer). His and Carc complexes are reported for comparison.

Complexes	IC_{50} (μM)×10^7
Cu^{2+}-pβCyDHis	1.7±0.2
Cu^{2+}-pγCyDHis	3.1±0.3
Cu^{2+}-His	0.4±0.4
Cu^{2+}-pβCyDCarc60	3.4±0.4
Cu^{2+}-pγCyDCarc60	3.7±0.5
Cu^{2+}-Carc	6.0±0.7
Cu^{2+}	1.2±0.2

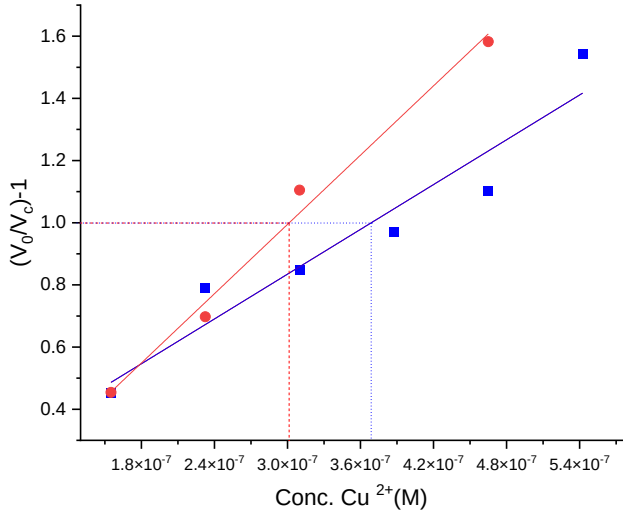

Figure 56. Superoxide dismutase activity assay: V_0 is the NBT reduction rate and Vc is the NBT reduction rate in the presence of Cu^{2+}-pγCyDHis(•)or pγCyDCarc60 (▪). The IC_{50} value is the complex concentration for which $(V_0/V_c)-1=1$

The ligands did not show any activity, as expected. All the systems (pH=7.4, molar ratio 1: 2 M/L, L is Carc or His moiety) showed a high SOD activity. Cu^{2+}-pγCyDCarc60 and pβCyDCarc60 systems showed SOD activity with an IC_{50} value lower than that of the free Carc complex. The pCyDHis complexes exhibited an antioxidant activity better than pCyDCarc systems. The IC_{50} values were slightly higher compared to the free Cu^{2+}-His system.

Due to the formation of the amide from the amino group, the different coordination environments of copper in the polymers could partly explain the differences between Carc and His complexes. However, other effects may occur, such as the polymer network, unfunctionalized COOH groups and different stability constant values that can modify the speciation of the systems.

2.3. THERAPEUTICAL NANOCARRIER SYSTEMS

The central point of this section is the design, synthesis, characterization, and application of new magnetic NPs. These NPs CySPION-FLUO, are based on the metal core (SPIONs) coated with two types of polymers, one ended with CyDs and one with fluorescein (FLUO) (Figure 57).

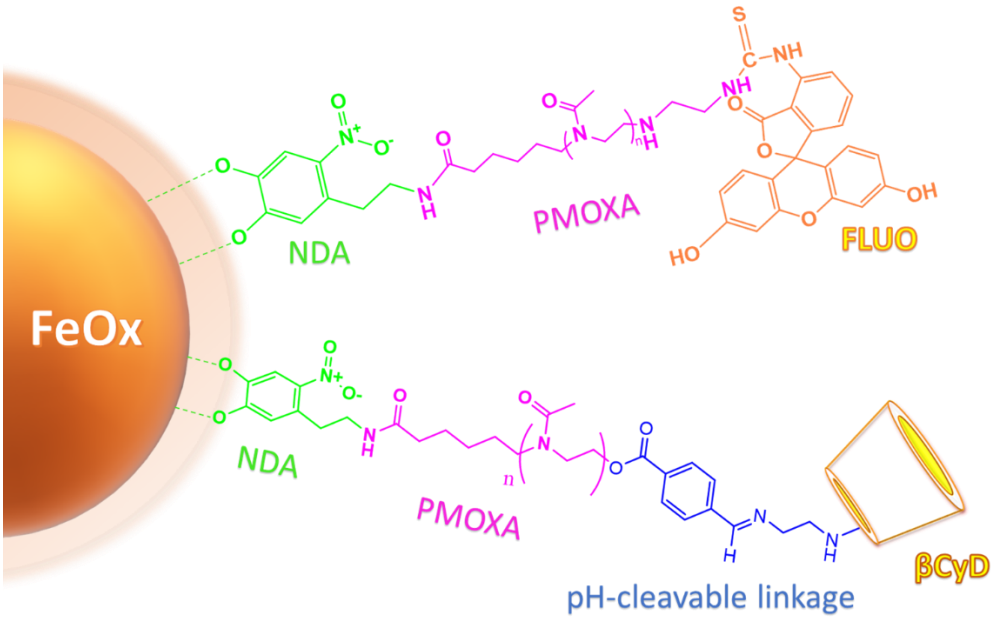

Figure 57. Schematic structure of CySPION-FLUO

The CyD was anchored to PMOXA polymer with a pH-cleavable linkage. This allows the CySPIONs (the same NPs without FLUO) to release the macrocycle of the NP surface into the lysosome, where the cholesterol tends to accumulate, and the pH is slightly acidic (Figure 58). Thus, through their ability to form an inclusion complex [262], CyDs can facilitate cholesterol mobilization from the lysosome into the cytosol.

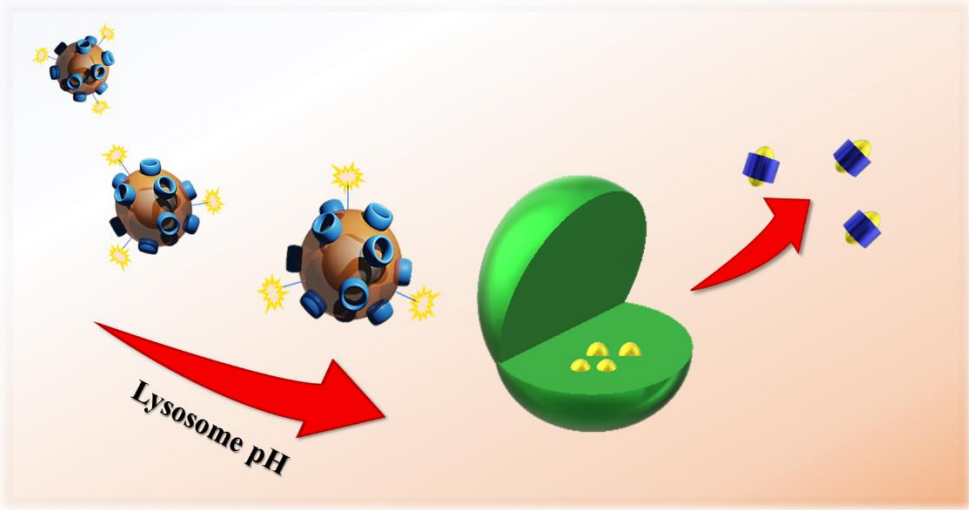

Figure 58. Scheme of the system studied for Cholesterol Mopping

The biological activity of CySPIONs *in vitro*, assessing their potential as a therapeutic platform for lysosomal cholesterol removal, in comparison to monomeric CyDs. Moreover, CySPION-FLUO ability to cross BBB was studied on membrane models. This investigation exploits the presence of a labeling unit that allows the quantification of NPs concentration that can overcome the BBB.

Experiments *in vitro*, in the presence of Dox, were carried out using CySPION-FLUO, in order to study the capability of the system also as a DD nanocarrier.

2.3.1. SYNTHETIC ASPECTS

The CySPION nano-architecture consists of a superparamagnetic iron oxide NP core coated with bi-functional polymers.

These NPs were coated by a backbone PMOXA (Figure 59), in which isocyanate fluorescein was introduced as a label for cellular uptake [263], and PMOXA-CyD was obtained according to a previously published protocol [204].

The synthesis of the NDAPMOXA-FLUO involved two steps (Figure 59). The first step involves the condensation of amino-terminated PMOXA (synthesized as described in Figure 38) and isothiocyanate FLUO, while the second step involves the reaction between the carboxyl group of PMOXA and the amino group of NDA.

The novel compound was characterized by ^{1}H NMR, GPC, TEM and TGA.

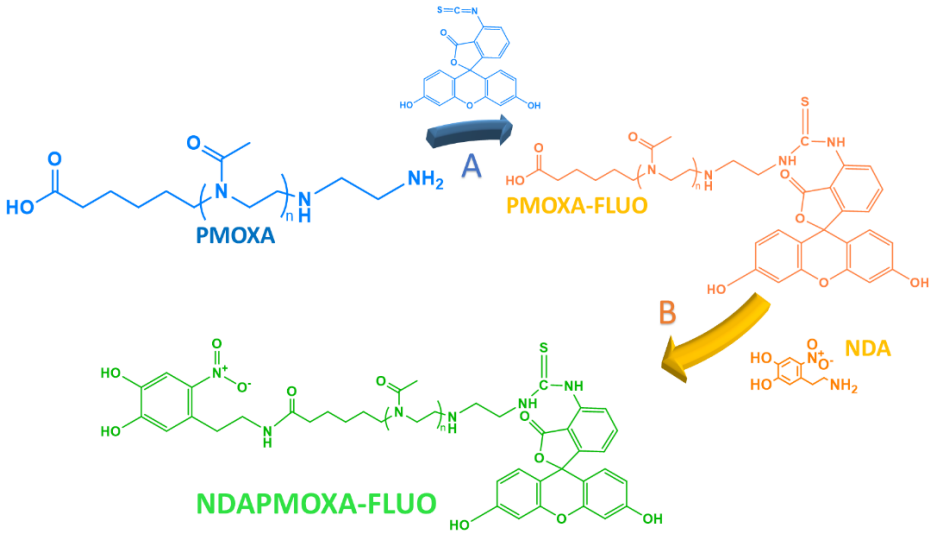

Figure 59. Synthetic scheme for NDAPMOXA-FLUO, A) in DMA with TEA, B) in DMA with TBTU and DIPEA

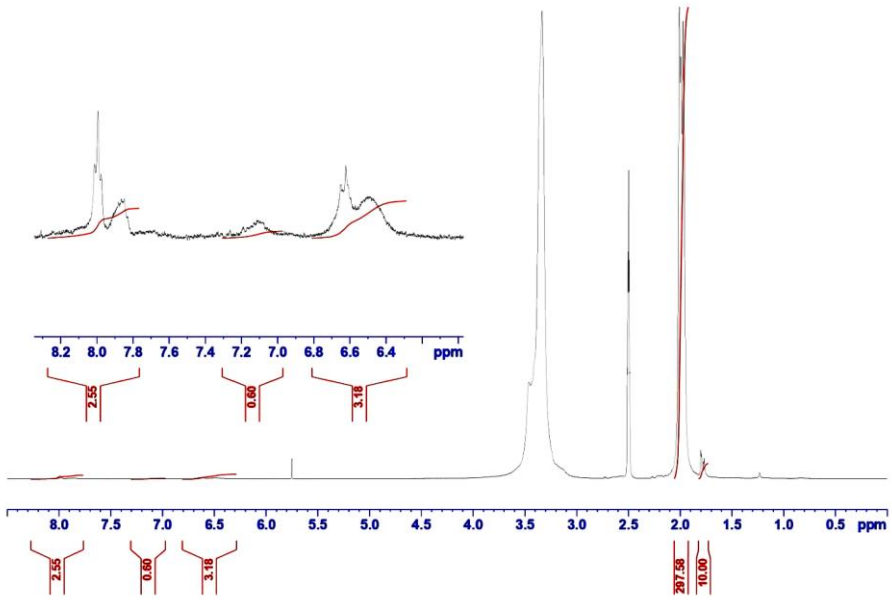

Figure 60. ^{1}H NMR of NDAPMOXA-FLUO ($CDCl_3$, 300 MHz)

^{1}H NMR spectrum of PMOXA-FLUO (Figure 60) shows the presence of fluorescein and NDA in the polymer backbone. The fluorescein has a specific signal in the aromatic region at 7.8-8 ppm and at 6.3-6.7 ppm. Conversely, the NDA has a signal at about 7-7.3 ppm.

From integral ratios between the signals of FLUO and CH_3 of PMOXA repeated unit at 2.00 ppm, it was determined that about 70% of the polymer was functionalized with FLUO. Similarly, from the integral ratios between the signals of the amide of NDA at 5.7 ppm and CH_3 of PMOXA at 2.00 ppm, a 70% functionalization of the polymer with NDA was determined.

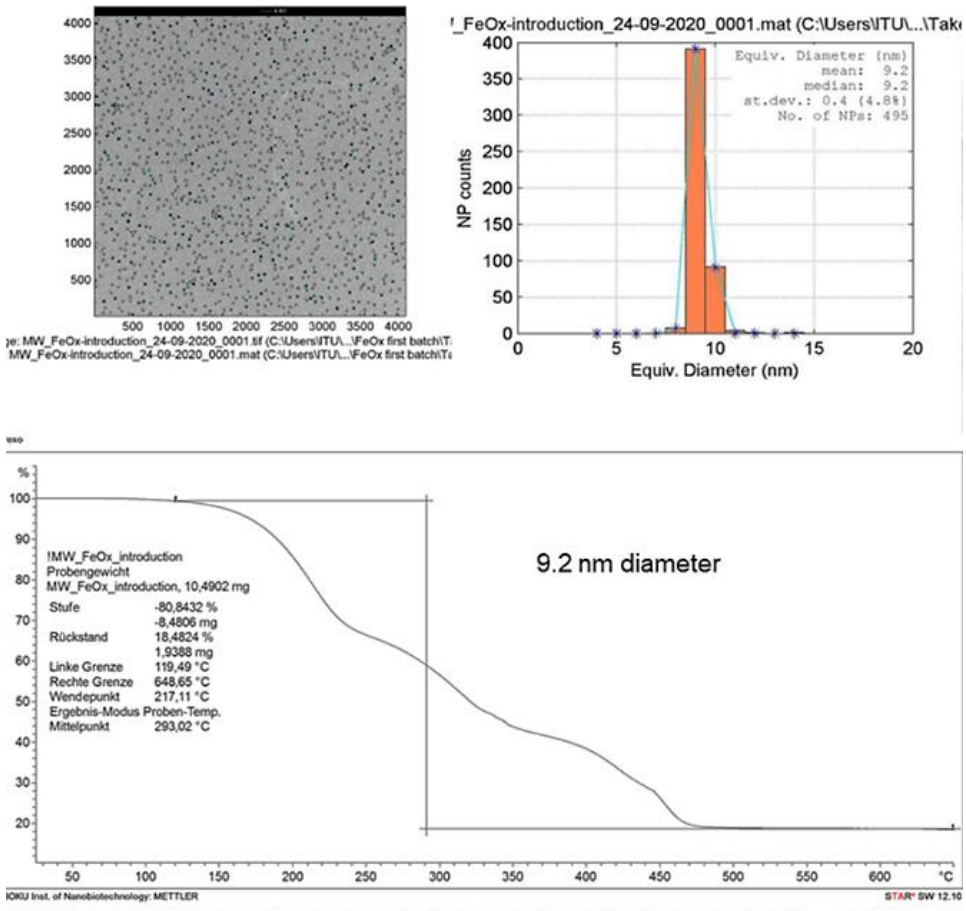

Figure 61. TEM and DSC of oleic acid-coated SPIONs

The iron oxide NPs oleic acid (OA)-coated were synthesized as reported [204], the size is controlled by the Fe $(CO)_5$ OA ratio. The monodisperse SPION average size was 9.2 nm via transmission electron microscopy (TEM). Furthermore, the inorganic fraction of the OA-coated SPIONs was determined to be 30.7% of the total weight of the sample by thermogravimetric analysis (TGA) (Figure 61).

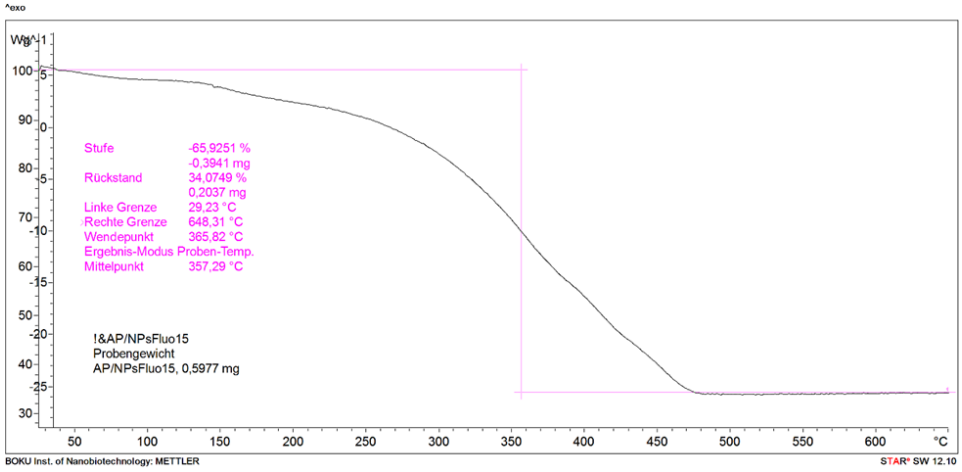

Figure 62. TGA CySPIONs dopped with 15% NDAPMOXA-Fluo

After the ligand exchange, the grafting density was calculated with TGA. The grafting density was calculated to be ~2.5 NDA-PMOXA/nm (Figure 62).

2.3.2. FLUORESCENCE SPECTROSCOPY

The two NPs, CySPION-FLUO and CySPION, were investigated at the same concentration (0.3 mg/ml) (Figure 63).

Fluorescence spectra showed a significant fluorescence emission of the CySPION-FLUO compared to CySPION. The data confirm that the fluorophore fluorescence is not quenched by the metal core, which indicates that the fluorophore is separated by more than the Förster radius from the core [264].

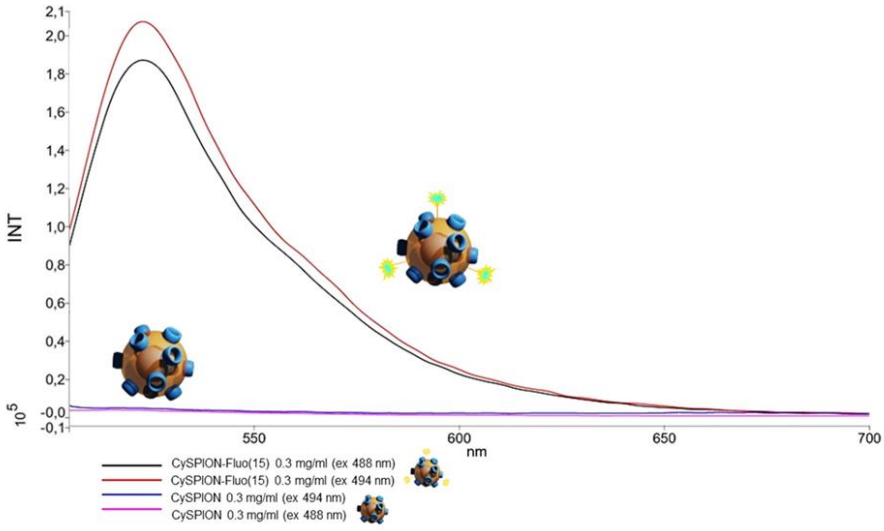

Figure 63. Fluorescence spectra of CySPION and CySPION-FLUO at 488 nm and 494 nm

2.3.3. ANTIPROLIFERATIVE ACTIVITY

The cytotoxicity profile, *in vitro* activity and cellular uptake on Npc1-deficient Chinese Hamster Ovary (CHO) of CySPIONs were investigated. In this experiment, this particular cell line was chosen with mutations in the NPC1 gene [265], leading to defects in intracellular cholesterol metabolism and subsequent accumulation [266].

CySPIONs did not show any significant cytotoxicity in the Resazurin viability assay on CHO cells within the explored concentration range (0.1 mg/ml, 0.2 mg/ml, 0.5 mg/ml, and 1 mg/ml) (Figure 64).

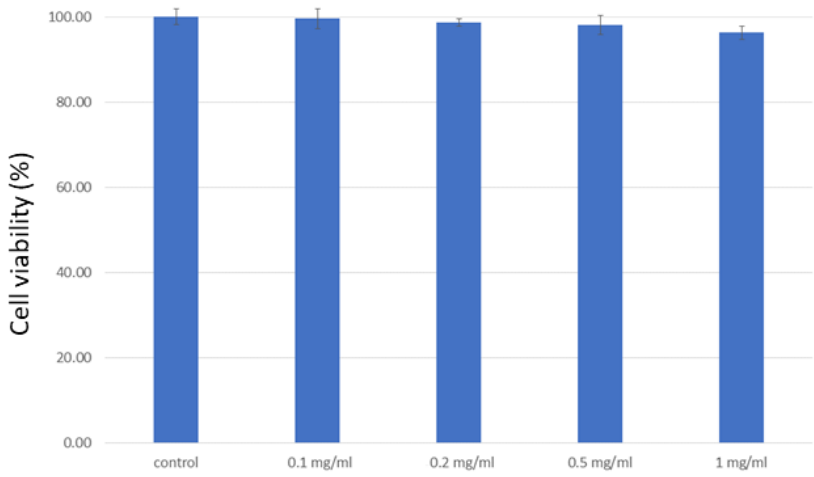

Figure 64. Resazurin viability assay on Npc1-deficient CHO cells after 24 h incubation with different high concentrations of CySPION and 48 h regeneration compared to a control, showing no significant cytotoxicity.

2.3.4. CHOLESTEROL MOPPING ACTIVITY

The cholesterol solubilizing activity of the CySPION in CHO "null" cells was assessed via a Cholesterol Assay Kit (Sigma-Aldrich MAK043) [267]. The solubilizing activity was compared to the 6-ethylendiamine βCyD (CyDen) capacity, at the same concentration estimated in CySPION (Figure 65). The average number of CyDs was estimated per CySPION via TGA. 1 mg/ml of CySPION was previously found to be equivalent to 120 µM in CyD [204]. Free CyDen removed significant cholesterol from the CHO cells at 0.5 mg/ml. Instead, CySPIONs at twice the concentration of free CyDen are able to solubilize the same amount of cholesterol. Although the quantification of CyD grafted to the CySPION may be not precise, these results suggest that the accessibility of cholesterol to CyD on the CySPION or their uptake and release is slightly less efficient than those of free CyDen. This could tentatively be remedied by optimizing the assay to account for both uptake and cleavage of CyD from CySPION, as only cholesterol mobilized by cleaved-off CyD

leaving the cell will be quantified by the assay. In contrast, monomeric βCyD could also remove cholesterol from the membrane and make it directly detectable in the supernatant.

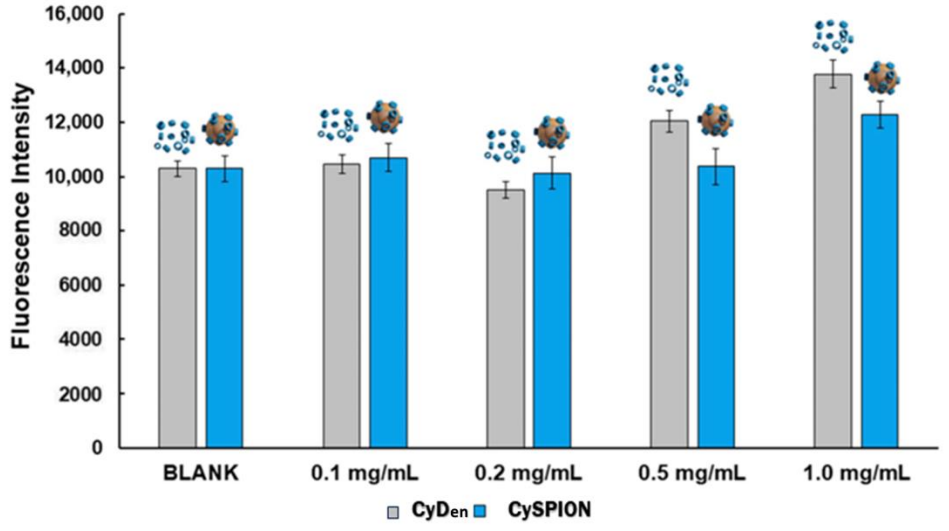

Figure 65. Cholesterol quantification assay using an enzymatic kit in Npc1-deficient CHO cells for CySPION and CyDen.

2.3.5. LYSOTRACKER STAINING VIA FLOW CYTOMETRY

The first major potential advantage of using NPs to administer CyD is the expected higher endosomal internalization of NPs compared to free CyDen. From the endosome, an NP releasing CyD could sequester cholesterol directly from the lysosome, where it is enriched in cells in cholesterol-related pathologies. Hence, it was interesting first to demonstrate that CySPIONs are predominantly taken up via the endosome/lysosome and second to determine their effect on the CHOs and their enlarged lysosome.

With this in mind, the total size of the lysosome was measured in control cells without and in the presence of CyDen or CySPION using the LysoTrackerTM assay and flow cytometry [268] HPβCyD was also tested as

a reference. LysoTracker TM probes are weakly basic amines that selectively build up in the lysosomal acidic compartments and fluorescence emission is proportional to the total volume of these compartments within the cell. It is generally assumed that the higher fluorescence of mutant CHO cells compared to wild-type (WT) CHO cells is due to larger individual lysosomal vesicles, swollen by the high amounts of accumulated cholesterol. The lysosome tracker signal was expected to go down on average if cholesterol is extracted from the lysosome by CyDen or CySPION, making the lysosome compartments smaller.

LysoTrackerTM assay results showed a significant decrease in lysosomal volume when CHOs are treated with CySPION (Figure 66). In line with the cholesterol mopping activity measurements, the lysosome decrease was less than that seen in the control with an equivalent concentration of free CyDs, with HPβCyD performing much better than CyDen (Figure 66). Striking is also that the lysosome size is, at best, weakly dependent on the CySPION concentration at the tested conditions. At low (0.12 mg/ml) concentrations, the reduction in lysosome size is equal between CySPION and the equivalent amount of free CyDen. While the lysosomal size reduction is enhanced by increasing the concentration of CyDen, the lysosome size remains near-constant as the CySPION concentration is increased to 1 mg/ml.

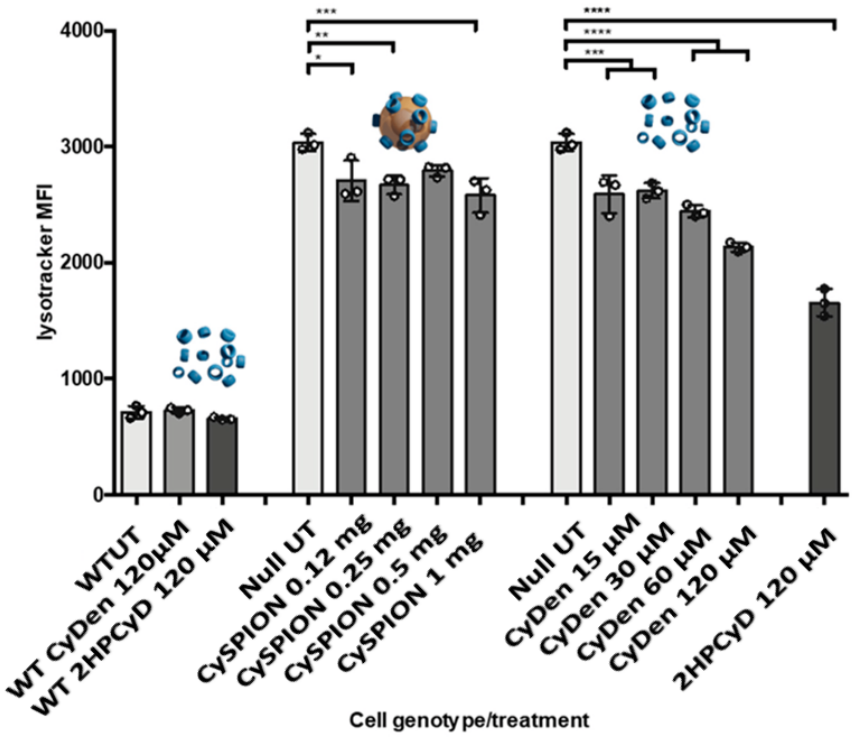

Figure 66. Lysotracker™ staining of CyDen treated CHO cells. LysoTracker™ staining of WT and Npc1-deficient CHO cells treated with the indicated doses of CySPION, CyDen and 2HPCyD for 72 h. 1 mg CySPION dose is equivalent to 120 µM CyDen. Data are mean ± SD, *N*= 3 replicates per sample. Statistical analysis, one-way ANOVA, *****p*< 0.0001, ****p*< 0.001, ***p*< 0.01, **p*< 0.05. Data are representative of two independent experiments.

The hypothesis was that the larger volume occupied by the CySPION in the lysosome, in comparison to the free CyDen, combined with the kinetics associated with lysosome uptake and subsequent CyD cleavage from the CySPION shell, leads to saturation of activity. However, this could potentially in turn, lead to a more extended effect of keeping the cholesterol concentration down over a longer time.

Supporting this view is that the sideways scattering in the flow cytometry measurements (Figure 67) showed an increase in the presence of

the NPs. An increase in sideways scattering could be explained by both uptakes of clusters of NPs into the lysosome and the association of NPs clusters to the cell surface, which is a prerequisite to cell uptake.

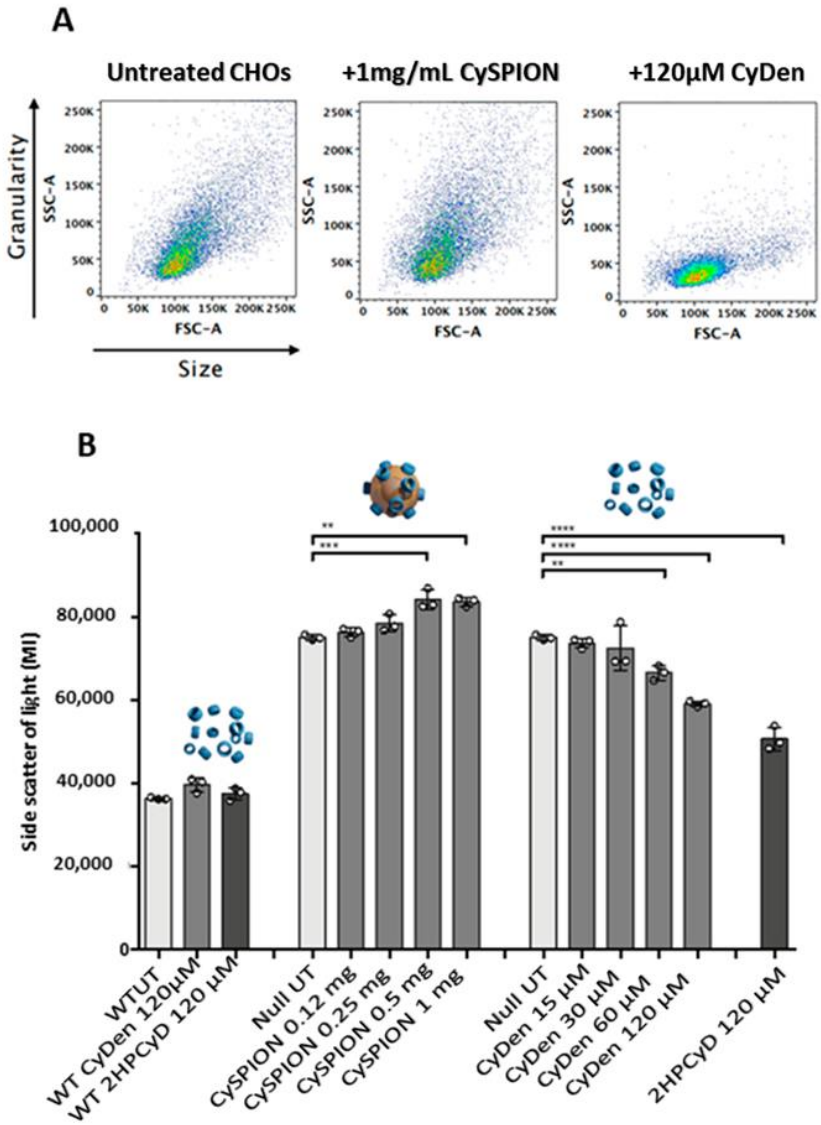

Figure 67. (A) Npc1-deficient CHO Cell profile on flow cytometer. Side scatter (SSC-A) vs. forward scatter (FSC-A). (B) Side scatter of WT and Npc1-deficient CHO cells treated with the indicated doses of CySPION, CyDen, or 2HPCyD for 72 h. A 1 mg CySPION dose is equivalent to 120 µM CyDen. Data are mean ± SD, *N*= 3 replicates per sample. Statistical analysis, one-way ANOVA, ****p< 0.0001, ***p< 0.001, **p< 0.01. Data are representative of two independent experiments.

2.3.6. CONFOCAL RESULTS

CHO “null” cells were exposed to the fluorescently labeled CySPION-FLUO to follow their uptake and distribution within the cells. Figure 68 shows confocal fluorescence images of the cell nuclei (blue), the green-emitting CySPION and the LysoTrackerTM stain for the lysosome (red), and an overlay of these channels. These images show the location of the lysosomes close to the nuclei and a very strong co-localization between CySPION-FLUO and lysosomes. There is little indication of free CySPION-FLUO in the cytosol and NPs outside the cells. It is possible to conclude that they are predominantly endocytosed cells, as expected for NPs of this size [269].

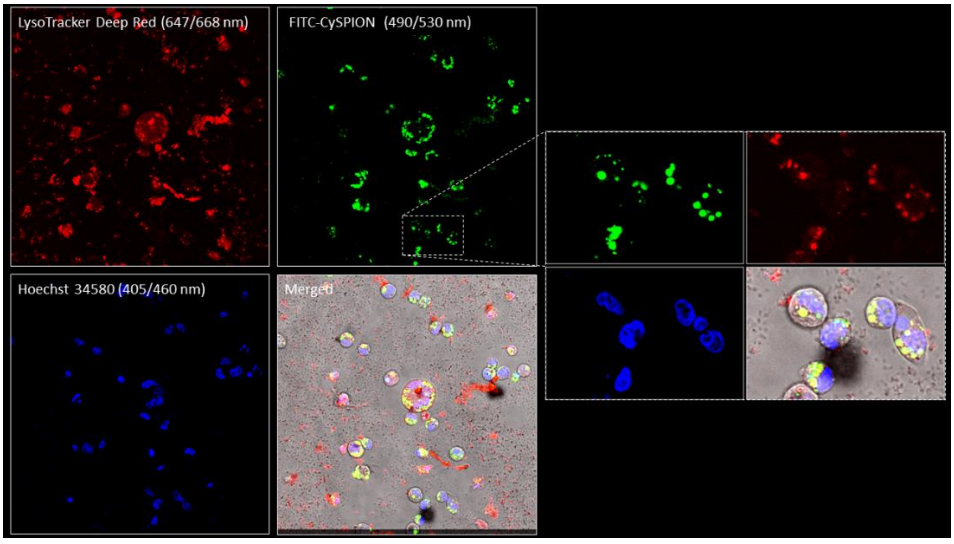

Figure 68. Confocal micrographs of CHO “null” cells after incubation with 0.1 mg/ml CySPION-FLUO for 72 hours show colocalization of CySPION-FLUO (green) in the lysosomal compartment (red). Cells were labeled with DNA staining Hoechst 34580 and LysoTracker Deep Red

2.3.7. TRANSMISSION ELECTRON MICROSCOPY MEASUREMENT

TEM thin-section images of fixed CHO films exposed to CySPION further supported the hypothesis that CySPIONs get internalized into the cell by showing NPs clusters both in the endosome/lysosome and associated with the cell surfaces (Figure 69). The clustering of the CySPION for uptake creates a very high local concentration of CyD but would slow down both uptake and release.

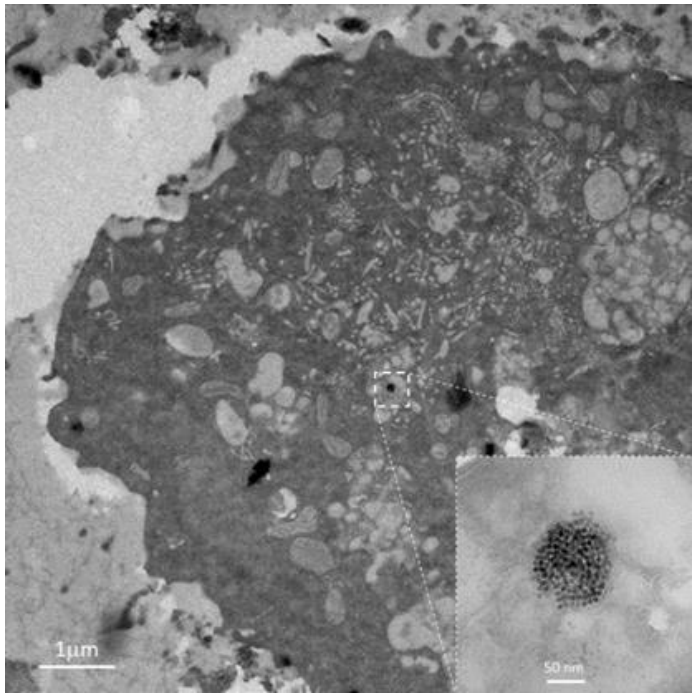

Figure 69. TEM thin section micrographs of fixed and embedded Npc1-deficient CHO exposed to CySPION supporting nanoparticles' cellular internalization.

2.3.8. BBB PERMEABILITY STUDY

The ability of CySPION-FLUO to cross the BBB was investigated, as this is one of the main obstacles for CyDs in the treatment of neurodegenerative diseases. The permeability of SPIONs through an *in vitro* BBB model has already been explored with promising results [270]. This *in vitro* BBB model was created by cultivating a human brain microvascular endothelial cell line (HBEC-5i) and a mouse astrocyte cell line (C8-D1A). A Lucifer Yellow (LY) permeability test was conducted to establish the integrity of the BBB model, by measuring that the permeability was in the accepted range ($<2\times10^{-6}$ cm/s after 30 min).

In order to assess the effectiveness of the NPs in promoting BBB crossing, CySPION-FLUO was compared with an equivalent amount in mass and composition of the blend of free polymers (85% CyD-PMOXA + 15% PMOXA-FLUO) used to make such NPs. The permeabilities of free polymer and CySPION-FLUO, respectively, were then measured in the BBB model via determining their concentrations transported across the layer from the fluorescence signal of FLUO-labeled PMOXA and CySPION-FLUO. Free polymer or CySPION-FLUO was seeded on the apical side of the BBB model, while a Ringer's HEPES solution was added to the basolateral side. The fluorescence (in RFU values) of the test samples transported through the barrier was then measured after 30 min and the permeability values were calculated using calibration curves for the samples (Tables S14-S16).

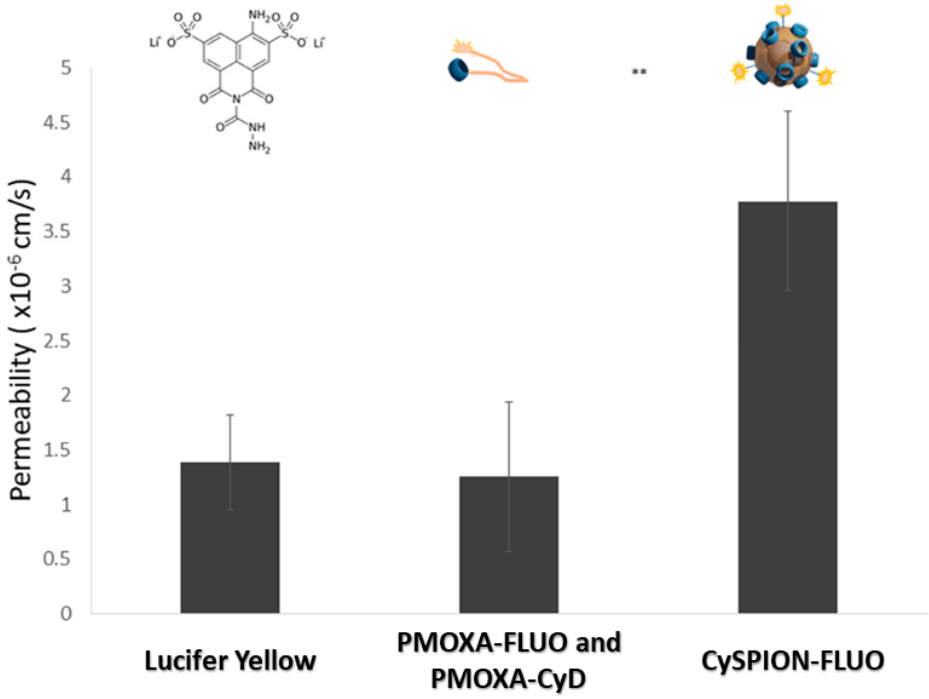

Figure 70. Permeabilities obtained by passing LY, PMOXA-FLUO, or CySPION-FLUO for 30 min on the fifth day of the Transwell® BBB model obtained by co-cultivating HBEC-5i and C8-D1A cells. It shows a significantly higher permeability of CySPION-FLUO. The data were statistically analyzed by unpaired, two-tailed *t*-test method using the GraphPad Prism 8 program ($p < 0.005$).**

It was found that the permeabilities of free polymers (PMOXA-FLUO and PMOXA-CyD) and CySPION-FLUO were $1.25\times10^{-6} \pm 6.89\times10^{-7}$ cm/s, and $3.78\times10^{-6} \pm 8.27\times10^{-7}$ cm/s, respectively (Figure 70). These data suggest that the NP systems cross the BBB approximately three times higher than the free polymer, as reported for similar systems [271].

The higher BBB crossing capacity for the nanosystem indicates great potential as a therapeutic system in cholesterol-impaired diseases.

2.3.9. CELLULAR UPTAKE OF CySPION-FLUO AS DRUG DELIVERY SYSTEM

CHO "null" cells were exposed to the fluorescently labeled CySPIONs-FLUO and Dox to follow its release in the cells. Figure 71 shows confocal fluorescence images of the cell nuclei (blue), the green-emitting CySPION-FLUO, Dox emission violet and the LysoTrackerTM stain for the lysosome (red), as well as an overlay of these channels. These images show that the drug was located in the lysosomes and is in the same space where CySPION-FLUO. This suggests that the NPs can also be used as a DD nanocarrier since they promote cellular internalization.

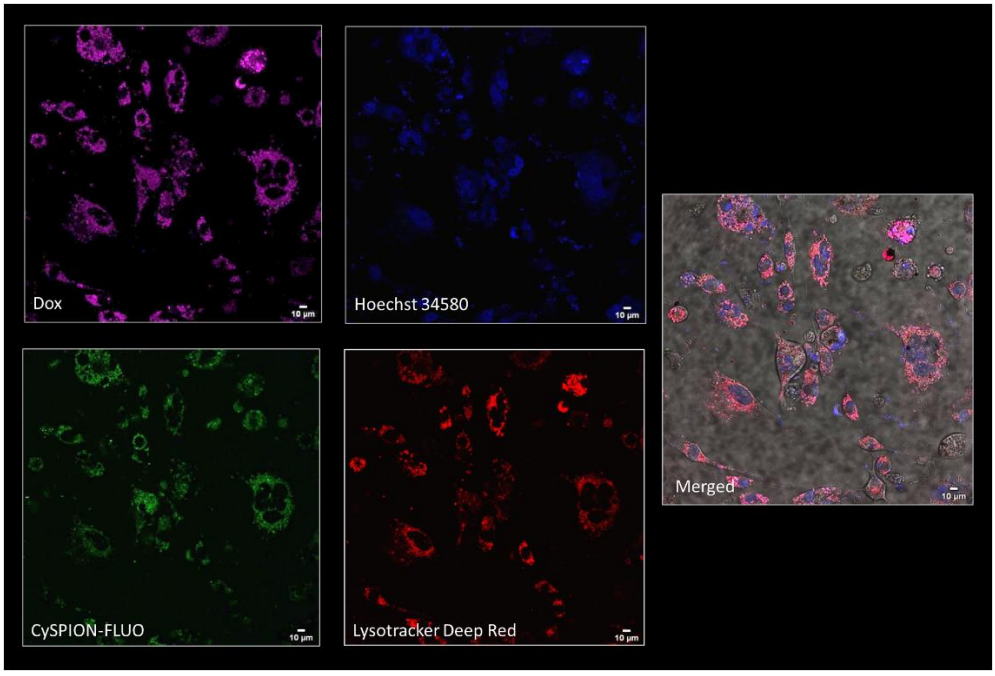

Figure 71. Confocal micrographs of CHO "null" cells after incubation with 0.1 mg/ml CySPIONs and 0.1 µM Dox for 72 hours showing colocalization of CySPIONs (green) and Dox (violet) in the lysosomal compartment (red). Cells were labeled with DNA staining Hoechst 34580 and LysoTracker Deep Red

3. EXPERIMENTAL SECTION

3.1. MATERIALS AND METHODS

Commercially available reagents were used directly without purification. The activating agents such as 1-(3-Dimethylaminopropyl)-3-ethyl-carbodiimide hydrochloride (EDC), arginine methyl ester dihydrochloride $ArgOCH_3$ DMTMM, EDC, and HOBt. 3A - amino-3 A -deoxy-2 A (S),3A (R)-β and γCyclodextrin ($CyD3NH_2$) Biotin-PEG3-Amine, Dox, Oxa and Sor, Ac-Glu-OH, N-Succinimidyl 6-Biotinamidohexanoate were acquired by TCI Tokyo Chemical Industries. Hyaluronic acid sodium salt polymers (HMW 40-50 kDa and LMW 8-15 kDa) were obtained from Biosynth Carbosynth. Soluble cross-linked γCyD polymer (pγCyD, 101 kDa, 54 CyD cavities), anionic γCyD polymer (pγCyDA, 54 kDa, 28 CyD cavities, average number of carboxymethyl group for cavity is 3) were purchased from Cyclolab. Octakis-(6-amino-6deoxy)-γ-Cyclodextrin 8HCl and heptakis (6-deoxy-6-amino)-β-cyclodextrin 7HCl were purchased from Cyclodextrin-Shop.

L-histidine methyl ester dihydrochloride ($HisOCH_3$), and α-amylase of hog pancreas were purchased from Merck, Carc was purchased from Baker. N-butyl-polyglutamic acid sodium salt (15 kDa, 3 kDa) was purchased from IRIS biotech.

2-methyl-2-oxazoline, bromohexanoic acid, anhydrous dimethylacetamide, folic acid, 4-γ-Guandinobutyric acid and fluorescein isothiocyanate were purchased from Sigma-Aldrich (Hamburg, Germany). 2-methyl-2-oxazoline was dried over CaH_2 and distilled before use.

Free base $ArgOCH_3$ and $HisOCH_3$ were obtained using a DEAE (OH^- form) anionic column.

Sephadex G-15 and Sephadex C-25 were used for column chromatography.

Membrane Dialysis with a molecular weight cut-off of 3.5 kDa was used after the evaluation of compatibility with 10% of solvents such as DMA and DMF.

Thin Layer Chromatography (TLC) was carried out on silica gel plates (Merck 60-F254). Carbohydrate derivatives were detected on TLC by UV and the anisaldehyde, iodine and ninhydrin tests.

3.2. NMR SPECTROSCOPY

^{1}H and ^{13}C NMR spectra were recorded at 25 °C with a Varian UNITY PLUS-500 spectrometer at 499.9 and 125.7 MHz respectively, using standard pulse programs from the Varian library. 2D experiments (COSY, TOCSY, gHSQCAD, gHMBC, ROESY) were acquired using 1k data points, 256 increments and a relaxation delay of 1.2 s. ^{1}H NMR spectra were referred to as the solvent signal.

3.3. DYNAMIC LIGHT SCATTERING (DLS)

Dynamic light scattering (DLS) measurements were performed at 25 °C with Zetasizer Nano ZS (Malvern Instruments, UK) operating equipped for backscattering at 173° with at 633 nm (He–Ne laser). The mean hydrodynamic diameter (d) of the NPs was calculated from intensity measurement after averaging the five measurements. The samples were diluted in phosphate buffer (pH = 7.4) or in water solution and prepared in ultrapure filtered water (0.2 µm filter).

3.4. UV-vis SPECTROSCOPY

UV-vis spectra were recorded with the Agilent Cary 8500 spectrophotometer equipped with a Peltier cell holder. The samples were diluted in HEPES or phosphate buffer (50 or 100 mM, pH 7.4).

3.5. AMYLASE CLEAVAGE ASSAY

α-Amylase hydrolysis tests were carried out at 37 °C in buffer at pH 7.4 (phosphate buffer 50 mM) or pH 4.0 (acetate buffer 50 mM). The polymers at 10 mM at two concentrations (2.5 mg/ml and 5.0 mg/ml) were incubated under stirring alone and in the presence of α-amylase of hog pancreas. TLC monitored hydrolysis at different times, at regular intervals up to 24 h. β and γCyD were used for comparison. TLC was eluted with PrOH/AcOEt/H_2O/NH_3 5 : 1 : 3 : 3.

3.6. SOD ACTIVITY

The reaction mixture was composed of 4-Nitro blue tetrazolium chloride (NBT, 200 μM), Phenazine methosulfate (PMS, 6.2 μM), Nicotinamide adenine dinucleotide NADH (312 μM) in HEPES buffer (50 mM, pH=7.4). During the experiment, the solutions of reagents were kept cool in an ice bath. The complexes were prepared in HEPES buffer at M/L (L is Carc or His moiety) 1:2 molar ratio. The reaction started when the PMS solution was added to the mixture in the cuvette, under stirring. The absorbance of the NBT was monitored at 560 nm every 30 sec. for 5 min at 25 °C. All tests were

carried out in triplicate. A graphical representation of experimental data was obtained by plotting the V_0/V_c-1 against the complex concentration, yielding a straight line. V_0 is the uninhibited reduction rate of NBT and V_c is the reduction rate of NBT in the presence of the complex. The IC_{50} value is the complex concentration for which $V_0=2V_c$, (V_0/V_c) -1=1.

3.7. SOLUBILITY EXPERIMENTS

Dox hydrochloride (50 µL, 0.017 M, water solution) was added to 0.200 mL of eight solutions of the CyD polymers in phosphate buffer (100 mM, pH 7.4) at different concentrations as reported elsewhere [272]. The suspensions, formed due to the Dox precipitation at 7.4 pH, were sonicated for 10 min and incubated at 25 °C in the dark. After 18 h, suspensions were centrifuged at 10,800 rpm for 10 min at 25 °C. The Dox concentration of the samples was determined in the supernatant with UV/vis spectroscopy at the wavelength of maximum absorbance (λ_{max}) 482 nm. A linear calibration plot for free Dox in phosphate buffer at pH 7.4 was previously obtained to obtain the Dox molar absorptivity ε 10,858 (mol^{-1} L cm^{-1}). The CE (complexation efficient) was calculated from the straight-line slope obtained. CE = Slope/(1 − Slope). The apparent stability constant K_{11} = CE/S_0 was calculated.

3.8. CHOLESTEROL QUANTIFICATION

The cholesterol concentration was determined via a coupled enzymatic reaction using a Cholesterol Quantification Assay Kit (Sigma-Aldrich) that contains Assay Buffer (CS0005A), Cholesterol Standard (CS0005B), Probe (CS0005C), Enzyme Mix (CS0005D) and Cholesterol Esterase (CS0005E).

After sample preparation, the fluorescence intensity was measured at λ_{ex}= 535 nm and λ_{em}= 595 nm.

3.9. TEM ANALYSIS

TEM studies were performed on an FEI Tecnai G2 20 transmission electron microscope operating at 120 or 200 kV for high-resolution imaging. Samples were prepared by dropping toluene dispersions of oleic acid-coated iron oxide core nanoparticles onto a 300-mesh carbon-coated copper grid and subsequently evaporating the solvent in the air.

TEM thin section was used to visualize the uptake of CySPIONs with CHO cells. Embedding of cells was done in LR-White acrylic resin according to a modified protocol of Glauert and Lewis [273]. Briefly, cells after uptake, were washed twice in 0.1 M sodium cacodylate pH 7.4 and fixed in fixative containing 2.5% glutardialdehyde, 2.5% paraformaldehyde, 2.5 mM $CaCl_2$, and 1% tannic acid in 0.1 M sodium cacodylate pH 7.4 for 4 h. Fixation was repeated with fixative without tannic acid for 20 h at 4 °C. After washing with sodium cacodylate, followed by distilled water, cells were postfixed with 1% OsO_4, 1.5% $K_3[Fe(CN)]_6$ potassium hexacyanoferrate(III) in water for 1 h, followed by 2% OsO_4 in water for an additional 2 h at room temperature. After brief washing in water, cells were dehydrated using a graded ethanol series in water (70% - 80% - 90% - 2 × 100%) for 10 min each. Cells were infiltrated with LR-White for 30 minutes, followed by an additional incubation with fresh resin overnight at 4 °C. Samples were transferred into gelatin capsules size 00 and filled with plain resin. Blocks were cured at 60 °C for a minimum of 24 h and stored at room temperature. Ultrathin sections were cut using Leica Ultracut UC-7. 70 nm slices of fixed and embedded cells were transferred onto

150 mesh hexagonal copper grids coated with Pioloform. After air drying, samples were investigated without further staining.

3.10. THERMOGRAVIMETRIC ANALYSIS AND DIFFERENTIAL SCANNING CALORIMETRY (DSC) MEASUREMENTS

Thermograms were recorded on a Mettler-Toledo TGA/DSC 1 STAR system in the temperature range 25–650°C with a ramp of 10 K/min in a synthetic air stream of 80 ml/s to ensure complete combustion of ligands as NDA was found to polymerize by pyrolization under N_2. 70 µL aluminium oxide crucibles were filled with 0.5–1.5 mg of sample, and the total organic content (TOC) was evaluated as the mass loss fraction at 500°C by horizontal setting. The density of grafted polymer was calculated from the inorganic/organic fraction of purified CySPIONs as reported in our previous work, which in turn allowed us to estimate that the equivalent concentration in appended CyD, that is 1 mg/ml CySPION, was equivalent to ~120 µM in monomeric CyD.

3.11. LYSOTRACKER FLOW CYTOMETRY

CHO lines were grown in DMEM/F12 TC media (Gibco: 31330-038) supplemented with 10% FBS, glutamine and pen-strep. 20,000 CHO NPC-/- (null) cells or WT CHO were plated in 12 well TC plates and allowed to adhere. Media was then replaced with CySPION, CyDen and 2HPβCyD at different concentrations and the plates were incubated at 37°C, 5% CO_2 for 72 hours.

3.12. LYSOTRACKER FLOW STAINING

LysoTrackerTM staining was performed as described previously [268]. In brief, cells were washed twice in situ with PBS and harvested using Trypsin/EDTA. Cells were rewashed with PBS and stained with 200 nM LysoTrackerTM-green DND-26 (ThermoFisher) for 10 min in the dark. Cells were washed a final time with PBS and re-suspended in a buffer containing 5 µg/ml Propidium iodide (Sigma) to allow for the exclusion of dead cells and immediately analyzed on a BD FACS-Canto II (Beckton Dickinson). At least 10,000 events were collected for each sample and relative fluorescence values were calculated using FlowJo software (Version 10, FlowJo, LLC).

3.13. CO-CULTURED BBB MODEL

An *in vitro* BBB model was created by cultivating a human brain microvascular endothelial cell line (HBEC-5i, CRL-3245TM, ATCC®, USA) and a mouse brain astrocyte cell line (C8-D1A, CRL-2541, ATCC®, USA). The cell cultures were incubated in a 37 °C, 5% CO_2 and 95-98% humidified incubator (SteriCycle 160i, Thermo Scientific, Germany). Dulbecco's modified eagle's medium F12 (DMEM-F12, D6421, Sigma-Aldrich, USA), containing 40 µg/mL of endothelial cell growth supplement (ECGs, E2759, Sigma-Aldrich, USA), 10% fetal bovine serum (FBS, 16000044, Gibco, USA) and DMEM (D6046, Sigma-Aldrich, USA) media supplemented with 10% FBS were used for the cultivation of endothelial and astrocyte cells, respectively. The culture media were changed every other day, and the cells were passaged at a 1:3 split ratio until obtaining desired cell numbers. Cell culture inserts (353095, Falcon® Corning, USA) were conditioned in an

endothelial growth medium for 2 h. Inserts were turned upside down, and astrocytes were seeded onto the underside of the insert membrane at 5×10^5 cell/cm^2 concentration. After the astrocyte cells were incubated for 4h, the inserts were turned, and endothelial cells were seeded on the apical surface of the membrane at 1×10^6 cell/cm^2 concentration. Obtained BBB models were incubated for 5 days, and Lucifer Yellow (LY) permeability was determined for the characterization of the model.

3.14. PERMEABILITY STUDY

The above-described cocultured BBB model was used to test the permeability of CySPION and free polymer samples. First, BBB integrity was assessed via LY permeability analysis. Ringer's HEPES solution (150 mM NaCl, 3.4 mM $CaCl_2$, 1.2 mM $MgCl_2$, 5.2 mM KCl, 0.5 mM $NaHCO_3$, 2.8 mM glucose, and 10 mM HEPES) was prepared in type-I ultra-pure water. Lucifer Yellow CH dipotassium salt (LY, L0144, Sigma-Aldrich, Germany) was dissolved in Ringer's HEPES solution (1 mM). After rinsing the BBB model with Ca^{2+} and Mg^{2+} free PBS, LY solution was added to the apical part, and Ringer's HEPES solution was added to the basolateral part of the model. LY solution was transported through the models for 30 min, and RFU values of the solution in the basolateral part were measured using a fluorospectrometer (NanoDrop 3300, Thermo Scientific, USA) at 530 nm. Concentration values corresponding to the RFU values obtained were determined using the calibration graph ($R^2 = 0.9997$) of the LY solution (Figure S143). Permeability values were calculated according to the formulae below (where P is the permeability, V is the volume of the media in the basolateral part, A is the surface area of the insert membrane, and [C] is the concentration of the LY).

$$P(\frac{cm}{s}) = \frac{V(cm^3)}{A(cm^2) \times [C]_{apical}(\frac{g}{mL})} \times \frac{\Delta[C]_{basolateral}(\frac{g}{mL})}{\Delta t(s)}$$

A permeability value <2×10^{-6} cm/s for LY is an indication of the establishment of a good cell barrier layer [274]. The model used in this permeability study had a lower LY permeability value than models in the literature [275]. The optimal permeability value of LY was obtained at 30 min ($1.39\times10^{-6} \pm 4.41\times10^{-7}$ cm/s) in this study, which was chosen as a suitable assay time. The test samples were prepared in Ringer's HEPES solution at 1 mg/ml concentration. Calibration graphs were obtained for both free polymer (R^2 = 0.9997) and CySPION (R^2 = 0.9902) for the relationship between concentration and RFU values at 520 nm using fluorospectrofotometery, with the fluorescence provided by the FLUO tag attached to both PMOXA-FLUO and CySPION-FLUO (Figure S144 for calibration curve of PMOXA-FLUO and Figure S145 for calibration curve of CySPION-FLUO). The permeabilities for free polymer and CySPION, respectively, were calculated using the same formula as for the LY assay, using these calibrations.

3.15. MASS SPECTROMETRY

MALDI-TOF MS experiments were performed using an AB SCIEX MALDI-TOF/TOF 5800 Analyzer (AB SCIEX, Foster City, CA, USA) equipped with a nitrogen UV laser (λ = 337 nm) pulsed at a 20 Hz frequency by using a set up previously described [219]. The mass spectrometer operated in the linear mode, and the laser intensity was set above the ionization threshold (4500 in arbitrary units). Mass spectra were processed using Data Explorer 4.11 software (Applied Biosystems, Warrington, UK). 2,5-di-hydroxybenzoic acid (DHB) was used as the matrix, dissolved in water/acetonitrile 1:1 containing 0.03% of CF_3COOH. Molar-mass averages (Mn and Mw) values were also

calculated using Data Explorer software (Applied Biosystems, Warrington, UK).

ESI mass spectra were acquired with an API 2000-ABSciex spectrometer.

3.16. SYNTHESIS OF ACETILATE DIMER CyDs

EDC (1-ethyl-3-(3-dimethylaminopropyl) carbodiimide) (17 mg, 0.088 mmol) and HOBt (1-hydroxybenzotriazole) (12 mg, 0.088 mmol) were added to Ac-Glu-OH (8.3 mg, 0.044 mmol) in dry DMF. After 10 min, $\beta CyDNH_2$ (100 mg, 0.088 mmol) and triethylamine (0.012 mL, 0.088 mmol) were added to the solution. The reaction mixture was stirred at 25°C for 24 h under stirring. The solvent was evaporated, and the reaction mixture was purified by Sephadex CM C-25 column (NH_4^+ form) using water as the eluent.

TLC: RF: 0.72 (PrOH/AcOEt/NH_3/H_2O 4:1:2:1),

Yield: 38%

^{1}H NMR (500 MHz, D_2O) δ (ppm): 5.07-4.87 (m, 12H, H-1 CyD), 4.84 (m, 2H, H-1A CyD), 4.33 (m, 1H, CHα Glu), 4.28 (m, 1H, H-3A CyD), 4.16 (m, 3H, H-3A and H-5A of CyD), 3.96-3.45 (m, 84 H, H-2A, H-4A, H-3, H-5, H-6, H-2, H-4 CyD), 2.31 (m, 2H, H-γ of Glu), 2.12 (s, 3H, CH_3), 2.01 (m, 1H, H-β of Glu), 1.96 (m, 1H, Hβ- of Glu).

Synthesis of γCyD2GluAc

γCyD2GluAc was synthesized and purified as reported for βCyD2GluAc, starting from $\gamma CyDNH_2$ (100 mg, $7.71x10^{-5}$mol) and Ac-Glu-OH (7.2 mg, $3.85x10^{-5}$ mol).

TLC: RF: 0.82 (PrOH/AcOEt/NH_3/H_2O 4:1:3:1)

Yield: 40%

^{1}H NMR (500 MHz, D_2O) δ (ppm): 5.17-4.84 (m, 14H, H-1 CyD), 4.88 (m, 2H, H-1A CyD), 4.28 (m, 1H, CHα Glu), 4.24 (m, 1H, H-3A CyD) 4.18 (m, 1H, H-3A CyD), 4.10 (m, 1H, H-5A), 4.04 (m, 1H, H-5A), 3.96–3.45 (m, 84 H, H-2A, H-4A, H-3, H-5, H-6, H-2, H-4 CyD), 2.33 (m, 2H, H-γ of Glu), 2.01 (m, 1H, H-β of Glu), 2.00 (s, 3H, CH_3), 1.93 (m, 1H, Hβ- of Glu).

^{13}C NMR (125 MHz, D_2O) δ (ppm): 175.9 (γ-CO of Glu), 168.6 (CO of Glu), 100.47 (C-1A of CyD), 99.1 (C-1 of CyD), 78.0 (C-4 of CyD), 79.9 (C-4 of CyD), 69.6-70.9 (C-5, C-2, C-3 of CyD), 57.9 (C-6 of CyD), 50.8 (C-α of Glu), 48.9 (C-3A of CyD), 29.9 (C-γ of Glu), 25.3 (CH Glu), 19.8 (C-β of Glu).

3.17. SYNTHESIS OF BIOTINILATE DIMER CyDS

N-Succinimidyl 6-Biotinamidohexanoate (3.8 mg, 8.4 µmol) and triethylamine (5.8 µl, 4.3 µmol) were added to βCyD2Glu (20 mg, 8.4 µmol) in dry DMF. The reaction mixture was stirred at room temperature for 24 h under stirring. The solvent was evaporated, and the reaction mixture was purified by the Sephadex CM C-25 column (NH_4^+ form) and the DEAE Sephadex column (form OH^-) with water as the eluent.

TLC: RF: 0.74 (PrOH/AcOEt/NH_3/H_2O 4:1:3:1)

Yield: 33 %

^{1}H NMR (500 MHz, D_2O) δ (ppm): 5.12-4.91 (m, 12H, H-1 CyD), 4.90 (m, 1H, H-1A), 4.82 (m, 1H, H-1A CyD), 4.59 (m, g biotin), 4.39 (m, 1H, CH Glu), 4.32 (m, f bio), 4.28 (m, 1H, H-3A CyD), 4.25 (m, 1H, CH Glu), 4.16 (m, 1H, H-3A), 4.03–3.40 (m, 82 H, H-2A, H-4A, H-3, H-5, H-6, H-2, H-4 CyD), 3.27-3.15 (m, 2H, e bio, H-6 Hex), 3.08 (m, 1H, H-6’ Hex), 2.94 (m, 1H, h bio), 2.69 (m, 1H, h bio), 2.42-2.04 (m, 4H, H-γ of Glu, H-2 Hex), 2.21

(m, 2H, a bio), 2.11 (m, 1H, H-β of Glu), 1.88 (m, 1H, H-β' of Glu), 1.76-1.26 (m, 12H, H-3, -4, -5 hexane b, c, d bio and hexane chain).

^{13}C NMR (125 MHz, D_2O) δ (ppm): 180.8 (CONH hex), 176.7 (CONH Bio), 176.1 (γ-CO of Glu), 172.8 (CO of Glu), 164.3 (NHCONH Bio), 103.3 (C-1A of CyD), 101.6 (C-1 of CyD), 81.5 (C-4 of CyD), 79.3 (C-4 of CyD), 74.5-71.0 (C-5, C-2, C-3 of CyD), 62.4 (C-f Bio), 60.3 (C-6 of CyD), 56.7 (C-g Bio), 53.4 (C-α of Glu), 50.4 (C-3A of CyD), 55.9 (e), 40.4 (C-h), 39.2 (CH_2NH Hexanoic chain), 35.8 (C-a Bio), 35.2 (CH_2CONH hex), 32.2 (C-γ of Glu), 30.4 (CH Glu), 27.0 (C-β of Glu), 29.1-24.5 (CH_2 hexane, C-b, -c, -d).

Synthesis of γCyD2GluBio

γCyD2GluBio was synthesized and purified as reported for βCyD2GluBio starting from γCyD2Glu (10 mg, $3.7x10^{-6}$mol) and N-Succinimidyl 6-Biotinamidohexanoate (1.7 mg, $3.7x10^{-6}$mol).

TLC: RF: 0.75 (PrOH/AcOEt/NH_3/H_2O 4:1:3:1)

Yield: 30 %

^{1}H NMR (500 MHz, D_2O) δ (ppm): 5.12 - 4.88 (m, 15H, H-1 CyD), 4.86 (m, 1H, H-1A CyD), 4.51 (m, g biotin), 4.33 (m, f bio), 4.28 (m, 1H, H-3AX CyD), 4.25 (m, 1H, CH Glu), 4.16 (m, 1H, H-3AY), 4.03 (m, 1H H-5A of CyD), 3.9 (m, 1H H-5A of CyD), 3.90–3.40 (m, 92 H, H-2A, H-4A, H-3, H-5, H-6, H-2, H-4 CyD), 3.24 (m, 1H, e bio), 3.19 (m, 2H, 6 CH_2 Hex), 2.94 (m, 1H, h bio), 2.69 (m, 1H, h' bio), 2.42-2.13 (m, 7H, H-γ of Glu, a bio, 2-CH_2 Hex H-β of Glu), 1.91 (m, 1 H, β'- of Glu), 1.76-1.26 (m, 12H, b, c, d bio and 3, 4, 5 CH_2 hex).

^{13}C NMR (125 MHz, D_2O) δ (ppm): 174.8 (γ-CO of Glu), 174.2 ($COCH_3$), 172.4 (CO of Glu),102.3 (C-1A of CyD), 101.6 (C-1 of CyD), 80.3 (C-4 of

CyD), 73.1 (C-5 CyD), 72.3 (C-2) 71.9 (C-3 of CyD), 62.4 (C-f Bio), 60.2 (C-6 of CyD), 60.2 (C-g Bio), 53.4 (C-α of Glu), 50.4 (C-3A of CyD), 41.6 (C-e), 39.4 (C-6 hex), 36.3 (C-a Bio), 35.4 (C-3A), 32.2 (C-γ of Glu), 30.4 (CH Glu), 27.1 (C-β of Glu), 26.1-25.0 (C-3, -4, -5 hexane, C-b, -c, -d).

3.18. SYNTHESIS OF HACyD CONJUGATES

Synthesis of HAHβCyD

DMTMM (37 mg, 0.1 mmol) and βCyD3NH_2 (126 mg, 0.1 mmol) were added to HAH (100 mg, 2 μmol) in 10 mL water in three aliquots (every 30 min). The reaction mixture was stirred at 25 °C for 24 h.

The final product was dialyzed against water (cut-off 3.5 kDa).

Yield: 45%

^{1}H NMR: (500 MHz, D_2O) δ(ppm):1.90 (s, CH_3 of N-Acetyl), 3.03–4.00 (m, H-3, -6, -5, -2, -4 of CyDs and HA), 4.17 (m, H-3-A of CyD), 4.36–4.45 (d, H-1 of glucuronic acid and glucosamine), 4.83–5.02 (m, H-1 of CyD).

Size (DLS, Z-Average), d: 424 ± 40 nm.

Synthesis of HAHγCyD

HAHγCyD was synthesized as HAHβCyD, DMTMM (46 mg, 0.17 mmol), γCyD3NH_2 (173 mg, 0.13 mmol) and HAH (50 mg, 1 μmol).

Yield: 35%

^{1}H NMR: (500 MHz, D_2O) δ(ppm): 1.90 (s, CH_3 of N-Acetyl), 3.1–4.03 (m, H-3, -6, -5, -2, -4 of CyDs and HA), 4.17 (m, H-3-A of CyD), 4.37–4.47 (d, H-1 of glucuronic acid and glucosamine), 4.96–5.16 (m, H-1 of CyD).

Dimension (DLS, Z-Average), d: 531 ± 60 nm.

Synthesis of HALβCyD

The synthesis was carried out as reported for HAHβCyD starting from HAL (100 mg, 9.1 μmol), DMTMM (126 mg, 0.46 mmol) and βCyD3NH_2 (310 mg, 0.28 mmol).

Yield: 48%

^{1}H NMR: (500 MHz, D_2O) δ(ppm): 1.90 (s, CH_3 of N-Acetyl), 3.20–3.90 (m, H-3, -6, -5, -2, -4 of CyDs and HA), 4.17 (m, H-3-A of CyD), 4.30–4.50 (d, H-1 of glucuronic acid and glucosamine), 4.83–5.02 (m, H-1 of CyD).

^{13}C NMR: (125 MHz, D_2O) δ (ppm): 30.4 (CH_3), 101.2 (H-1 CyD), 60.4 (C-6 CyD and HA), 70.0–74.0 (C-2, 3, 5, CyD and HA), 80.9 (C-4 CyD); 178.0 (COOH), 175.8 ($COCH_3$); 172.0 (NHCO).

Size (DLS, Z-Average), d: 176 ± 15 nm.

Synthesis of HALγCyD

The synthesis was carried out as reported for HAHβCyD starting from HAL (50 mg, 5 μmol) DMTMM (63 mg, 0.23 mmol) and γCyD3NH_2 (177 mg, 0.14 mmol).

Yield: 53%

^{1}H NMR: (500 MHz, D_2O) δ(ppm): 1.92 (s, CH_3 of N-Acetyl), 3.21–4.03 (m, H-3, -6, -5, -2, -4 of CyDs and HA), 4.19 (m, H-3-A of CyD), 4.35–4.52 (d, H-1 of glucuronic acid and glucosamine), 4.83–5.16 (m, H-1 of CyD).

Dimension (DLS, Z-Average), d: 90 ± 5 nm.

3.19. SYNTHESIS OF PGACyDArg

Synthesis of PGAβCyDArg1

βCyD3NH_2 (50 mg in 1 mL of H_2O), and DMTMM (18.26 mg in 350 μL) were added to PGA (6.61 mg in 350 μL) every 30 min in three aliquots. The pH of the reaction mixture was adjusted to 8. After 24 h, ArgOCH_3(2 mg) and DMTMM (18 mg) were added to the solution (for 30 min). The reaction mixture was stirred at r.t. for 24 h.

The polymer was isolated with Sephadex G-15 column chromatography. The various fractions collected were examined using TLC, (eluent PrOH/AcOEt/H_2O/NH_3 5:2:3:1). The main product was characterized by NMR spectroscopy.

^{1}H NMR (500 MHz, D_2O) δ (ppm): 5.20-4.80 (H-1 of CyD); 4.28 (s, CH Glu); 4.2 (m, CH Arg); 4.2-3.2 (m, H-3, -6, -5, -2,-4 of CyD, OCH_3); 3.2 (m, γ CH_2 Arg); 2.60–1.50 (m, β- and γ-CH_2 PGA); 1.35 (m, CH_2butyl chain of PGA); 1.26 (m, CH_2 butyl chain of PGA), 0.88 (m, CH_3 butyl chain of PGA).

^{13}C NMR (125 MHz, D_2O) δ (ppm): 24.5 (β-CH_2 of Arg), 26.8 (α-CH_2 of Arg), 31.8 (β-CH_2 of PGA), 40.5 (δ CH_2 butyl chain of PGA), 52.3 (CH Arg), 52.9 (C-2 of CyD and OCH3 of Arg), 53.0 (CH of Glu), 60.0 (C-6 of CyD), 71.6 (C-3 of CyD), 73.0 (C-5 of CyD), 80.4 (C-4 of CyD), 101-105 (C-1 of CyD), 160 (C=N of Arg), 173–174 (CNH PGA-CyD, PGA-Arg), 174.72 (CO methyl ester of Arg).

Dimension (DLS, Z-Average): d: 49 ± 5 nm

Zeta potential: 8 ± 1 mV (pH = 7.4).

The other polymers were synthesized in the same manner as PGAβCyDArg1 with different amounts of the reagents.

Synthesis of PGAβCyDArg2

The synthesis was carried out as described above with PGA (7 mg), DMTMM (18 mg), $ArgOCH_3$ (6 mg), DMTMM (10 mg) and $\beta CyD3NH_2$ (50 mg).

^{1}H NMR (500 MHz, D_2O) δ (ppm): 5.16-4.75 (H-1 of CyD); 4.28 (s, CH Glu); 4.20 (m, CH Arg); 4.10-3.20 (m, H-3, -6, -5, -2, -4 of CyD, OCH_3); 3.13 (m, γ-CH_2 Arg); 2.58-1.60 (m, γ-CH_2 PGA,); 1.35 (m, CH_2 butyl chain of PGA), 1.6 (m, CH_2 butyl chain of PGA); 1.28 (m, CH_2 butyl chain of PGA), 0.89 (m, CH_3 butyl chain of PGA).

Dimension (DLS, Z-Average): d: 35 ± 2 nm

Zeta potential: 7.7 ± 0.5 mV (pH = 7.4).

Synthesis of PGAγCyDArg3

The synthesis was carried out for PGAβCyDArg2 with PGA (10 mg), DMTMM (19 mg), $ArgOCH_3$ (8 mg), DMTMM (20 mg) and $\gamma CyD3NH_2$ (67 mg).

^{1}H NMR (500 MHz, D_2O) δ (ppm): 5.20–4.77 (m, H-1 of CyD); 4.32 (m, CH Arg); 4.23 (s, CH Glu); 4.12 (m, H-3A of CyD); 3.93–3.49 (m, H-3, -6, -5, -2, -4 of CyD and OCH_3 of Arg); 3.12 (γ-CH_2 Arg); 2.57–1.45 (β- and δ- CH_2 PGA, CH_2 Arg); 1.38 (m, CH_2 butyl chain of PGA), 1.21 (m, CH_2 butyl chain of PGA); 0.77 (m, CH_3 butyl chain of PGA).

Dimension (DLS, Z-Average): d: 29 ± 3 nm

Zeta potential: 2.3 ± 0.5 mV (pH = 7.4).

Synthesis of PGAβCyDArg4 and PGAγCDArg5

The synthesis was carried out as described above with PGA (25 mg), DMTMM (48 mg), $ArgOCH_3$ (33 mg), DMTMM (21 mg) and $\beta CyD3NH_2$ (59 mg) or $\gamma CyD3NH_2$ (72 mg).

PGAβCyDArg4

^{1}H NMR (500 MHz, D_2O) δ (ppm): 5.22–4.80 (m, H-1 of CyD); 4.32 (m, CH Arg); 4.23 (s, CH Glu); 4.12 (m, H-3A of CyD); 3.93-3.50 (m, H-3, -6, -5, -2, -4 of CyD and OCH_3 of Arg); 3.12 (γ-CH_2 Arg); 2.60-1.49 (β- and δ- CH_2 PGA, CH_2 Arg); 1.39 (m, CH_2 butyl chain of PGA), 1.20 (m, CH_2 butyl chain of PGA); 0.78 (m, CH_3 butyl chain of PGA).

^{13}C NMR (125 MHz, D_2O) δ (ppm): 24.4 (β-CH_2 of Arg), 27.6 (α-CH_2 of Arg), 31.3 (β-CH_2 of PGA), 40.5 (δ CH_2 butyl chain of PGA), 52.34 (CH Arg), 52.8 (C-2 of CyD and OCH_3 of Arg), 52.9 (CH of Glu), 60.0 (C-6 of CyD), 71.4 (C-3 of CyD), 72.5 (C-5 of CyD), 80.3 (C-4 of CyD), 101. 7 (C-1 of CyD), 160 (C=N of Arg), 173–174 (C-NH PGA-CyD, PGA-Arg), 174.7 (CO methyl ester of Arg).

Dimension (DLS, Z-Average): d: 79 ± 8 nm

Zeta potential: 45 ± 5 mV (pH = 7.4).

PGAγCyDArg5

^{1}H NMR (500 MHz, D_2O) δ (ppm): 5.22–4.70 (m, H-1 of CyD); 4.32 (m, CH Arg); 4.23 (s, CH Glu); 4.12 (m, H-3-A of CyD); 4.05–3.32 (m, H-3, -6, -5, -2, -4 of CyD and OCH_3 of Arg); 3.12 (γ-CH_2 Arg); 2.59-1.46 (β- and δ- CH_2 PGA, CH_2 Arg); 1.37 (m, CH_2 butyl chain of PGA), 1.21 (m, CH_2 butyl chain of PGA); 0.78 (m, CH_3 butyl chain of PGA).

^{13}C NMR (125 MHz, D_2O) δ (ppm): 24.4 (β-CH_2 of Arg), 27.7 (α-CH_2 of Arg), 31.3 (β-CH_2 of PGA), 40.4 (δ CH_2 butyl chain of PGA), 52.4 (CH Arg), 52.8 (C-2 of CyD and OCH_3 of Arg), 52.9 (CH of Glu), 60.0 (C-6 of CyD), 71.5 (C-3 of CyD), 72.0 (C-5 of CyD), 80.4 (C-4 of CyD), 101. 7 (C-1 of CyD), 160 (C=N of Arg), 173–174 (CNH PGA-CyD, PGA-Arg), 174.72 (CO methyl ester of Arg).

Dimension (DLS, Z-Average): d: 59 ± 6 nm

Zeta potential: 37 ± 3 mV (pH = 7.4).

3.20. SYNTHESIS OF PGACyDGBA

Synthesis of PGAβCyDGBA

DMTMM (143 mg, 0.5 mmol) and γ-Guanidinobutyric Acid (GBA) (30 mg, 0.2 mmol) were added in three aliquots to βCyD (143 mg, 0.1 mmol). The pH of the reaction mixture was adjusted to 8. After 24 h, PGA (20 mg, 7 μmol) and DMTMM (38 mg, 0.1 mmol) were added to the solution (for 1 h). The reaction mixture was stirred at room temperature for 24 h.

The solution of the reaction was purified by Sephadex G-15 column chromatography.

Yield: 25%

^{1}H NMR: (500 MHz, D_2O) δ(ppm): 0.78 (m, CH_3 butyl chain of PGA); 0.97(m, CH_2 butyl chain of PGA); 1.78 (m, α-CH_2 of Arg), 1.2 (m, β-CH_2 of Arg); 2.3-2.24 (m, β-CH_2 of PGA and m, α-CH_2 of PGA); 3.12 (m, δ CH_2 butyl chain of PGA and m, γ-CH_2 GBA); 3.8-3.4 (m, H 3, -6, -5, -2, -4 of CyD); 5.0 (m, H-1 of CyD); 4.08 (s, CH Glu).

Dimension (DLS, Z-Average) d: 23 ±2 nm

Zeta potential: 41 ± 5 mV (pH = 7.4).

Synthesis of PGAγCyDGBA

The synthesis was carried out as reported for PGAβCyDGBA: DMTMM (143 mg, 0.5 mmol) and GBA (30 mg, 0.2 mmol), γCyD (164 mg, 0.1 mmol). After 24 h, PGA (20 mg, 7 μmol) and DMTMM (38 mg, 0.1 mmol).

Yield: 21%

^{1}HNMR: (500 MHz, D_2O) δ(ppm): 0.77 (m, CH_3 butyl chain of PGA); 1.35-1.18(m, CH_2 butyl chain of PGA); 1.77 (m, α-CH_2 of Arg); 2.3- 2.2 (m β- CH_2 of PGA, m α-CH_2 of PGA, m α-CH_2 of GBA, m, β-CH_2 of GBA); 3.11 (m, δ CH_2 butyl chain of PGA and γ-CH_2 GBA); 3.6-3.4 (m, H 3, -6, -5, -2, -4 of CyD); 5.04 (m, H-1 of CyD); 3.8 (s, CH Glu).

Dimension (DLS, Z-Average): d: 18 ±1 nm

Zeta potential: 27 ± 2 mV (pH = 7.4).

3.21. SYNTHESIS OF PGACyDPMOXA

6-bromohexanoic acid (6BHA) 100 mg (0.513 mmol) was used as the initiator and reacted at 110 °C with 8 ml of 2-methyl-oxazoline (MO) (94.5 mmol; x184) in 15 ml of anhydrous dimethylacetamide (DMA) for 22 h under a dry nitrogen atmosphere. The reaction mixture was then brought to 80 °C and reacted with 1 ml of ethylenediamine (x30 excess) for 22 h to terminate the reaction [276]. After this time, the solution was cooled to room temperature, and the polymer precipitated twice in diethyl ether (200 ml). Finally, the polymer was dialyzed (cut off: 3.5 kDa) overnight and lyophilized to yield about 5 g of PMOXA.

^{1}H NMR: (300 MHz, $CDCl_3$) δ (ppm): 1.00–2.00 (10H, 6BHA), 2.10 (282H, -CH_3CO-), 3.45 (387H, -OC-N-CH_2-CH_2-N- and ethylenic chain of en).

GPC: Mn 8,890, Mw 14,467, Mw/Mn 1.6

After the synthesis of PMOXA, the second step is protecting the amino group with BOC. 0.5 g of PMOXA (59 µmol) was solubilized in 2 ml of DMF and added 3 equivalents of BOC 41 µl (0.18 mmol) in the presence of 1.5

equivalents of triethylamine 10 µl (88 µmol). The reaction was stirred at r.t. overnight. After the reaction, the product was precipitated in EtO_2 (100ml) to eliminate the BOC and DMF. Finally, the product was lyophilized.

0.48 g of PMOXA-BOC (54 µmol) was dissolved in 6 ml of anhydrous DMA in an inert atmosphere. Thereafter, 28 mg of TBTU (73 µmol) and 10 µl of DIPEA (56 µmol) were added and stirred for 15 min to activate the carboxyl group. After, 17 mg of NDA (73 µmol) was added as a solution in anhydrous DMA. The reaction was stirred in the dark for 24 hours. The product was purified with dialysis, using a cut-off of 3.5 kDa in order to eliminate the solvent and activating agents.

^{1}H NMR: (300 MHz, $CDCl_3$) δ (ppm): 1.37 (s, CH_3 BOC), 1.88-1.95 (10H, 6BHA), 2 (282H, -CH_3CO-), 3.51 (387H, -N-CH_2-CH_2-N-), 6.56-7.54 (s, 2H, aromatics of the NDA group)

NDA-PMOXA-BOC 0.4g (46 µmol) was dissolved in 5 ml DCM and treated with concentrated 8.5 µl of TFA (X1.15 µmol), for 4 h to eliminate the protection group. Vacuum evaporation of the solvent is sufficient to isolate the product.

After the deprotection, PMOXA-NDA 0.4 g (46 µmol) was dissolved in water 4 ml with 909 mg of succinic anhydride (X2, 91 µmol) and with 3.6 mg of hydroxide of sodium (X2, 91 µmol) at room temperature, overnight. Also, this product was purified by dialysis (cut-off 3.5 kDa) and after it was lyophilized.

^{1}H NMR: (300 MHz, DMSO) δ (ppm): 1.72-1.83 (10H, 6BHA), 1.98 (282H, -CH_3CO-), 2.73 (t, CH_2 Succinic acid) 3.38 (387H, -N-CH_2-CH_2-N-), 7.08-7.54 (s, 2H, aromatics of the NDA group)

PGA functionalization CyDs: 0.42 g of PGA (29 µmol) was solubilized in 3 ml of water with 158 mg of DMTMM (0.57 mmol). After 5 minutes 6 amino-CyDs were added 333 mg (0.28 mmol) previously activated with 80µl of TEA

(0.57 mmol). The reaction was carried out at r.t. overnight. The product was purified by dialysis (cut-off 3.5 kDa).

^{1}H NMR: (300 MHz, D_2O) δ (ppm): 0.82 (m, CH_3 butyl chain of PGA), 1.22 (t, CH_3 of triethylamine), 1.39 (m, CH_2 butyl chain of PGA), 1.76-2.42 (m, β- and γ-CH_2 PGA), 3.13 (q, CH_2 of triethylamine), 3.46-3.99 (m, H-3, -6, -5, -2, -4 of CyD), 4.28 (s, CH Glu), 4.94-5.01 (H-1 of CyD).

Finally, 0.4 g (43 μmol) NDA-PMOXA-SUC was activated with 0.029 g of DMTMM (0.1 mmol). After 5 minutes was added 0.74 g of PGA-CyD (28 μmol). The reaction was conducted in water at room temperature overnight. The product was purified with precipitation in chloroform.

^{1}H NMR: (500 MHz, D_2O) δ (ppm): 0.81 (m, CH_3 butyl chain of PGA), 1.84-1.91 (m, $CH_2$10H, 6BHA PMOXA), 1.96-2.04 (282H, -CH_3CO- PMOXA, $CH_2$10H, 6BHA PMOXA and β- CH_2 PGA, CH_2 of succinic acid) 2.15-2.33 (γ-CH_2 PGA), 3.38-3.45 (m, H-2, and H-4 of CyD), 3.47-3.9 (m, 387H, OC-N-CH_2-CH_2-N- PMOXA and ethylenic chain of en H-3, -5, -6, of CyD and CH_2 of NDA), 4.26 (s, CH Glu), 4.97-5 (H-1 of CyD).

^{13}C NMR: (125 MHz, D_2O): 19.74 (-CH_3CO- PMOXA), 26.20-28.04 (CH_2, 6BHA, $CH_2$10H PMOXA, β- CH_2PGA and CH_2 of succinic acid), 32.59 (γ-CH_2 PGA), 42.45-47.53 (ethylenic chain of en, OC-N-CH_2-CH_2-N- PMOXA and CH_2 of NDA), 53.47 (CH Glu), 60.0 (C-6 of CyD), 70.02 (C-3 of CyD), 71.99 (C-2 of CyD), 73.04 (C-5 of CyD), 81.24 (C-4 of CyD), 101.22 (C-1 of CyD)

Dimension (DLS, Z-Average): 288 ±10 nm

3.22. SYNTHESIS OF POLYMER WITH FOLIC ACID

20 mg of FA (40 μmol) was dissolved in DMA and was added 20 mg of DCC (81 μmol) and 10 mg of NHS (81 μmol) to activate γ-COOH. After 5 minutes, 230 mg of polymer PMOXA-NDA were added to the solution. The reaction was carried out overnight at r.t. The product was purified with dialysis (cut-off 3.5 kDa) to eliminate solvent and NHS and DCC were eliminated by filtration.

^{1}H NMR: (300 MHz, DMSO) δ (ppm): 1.74-1.83 (10H, 6BHA), 1.99 (282H, -CH_3CO- and CH_2 of glutamic acid of Folic Acid), 3.53 (387H, -N-CH_2-CH_2-N-), 4.4 (m, CH_2 of FA), 6.67-7.56 (d, H aromatic of FA), 8.41 (s, H of pteridine ring of FA).

Dimension (DLS, Z-Average): d: 199 ± 9 nm

3.23. SYNTHESIS OF pβCyDBio

HOBt (4.6 mg, 34 μmol) and EDC (6.5 mg, 34 μmol) were added to pβCyDA (50 mg, 0.57 μmol) in DMF under stirring. After the activation, PEG3- Amine Biotin was added (13 mg, 30 μmol). The reaction was stirred at room temperature for 24 h. The product was isolated with a Sephadex G-15 column.

Yield: 57%

^{1}H NMR (500MHz, D_2O) δ(ppm):1.4-1.6 (bs, CH_2, H-3,-2,-4 of Bio.), 2.2 (bs, CH_2, H-1 of Bio.), 2.6-3.1 (bs, H- 8,-8', -5 of Bio), 3.2-4.4 (m H-3,-6,-5,-4,-2 βCyD), 4.3(bs, CH H-6 of Bio),4.5 (bs, CH H-7 of Bio), 5 (m, H-1 βCyD).

3.24. SYNTHESIS OF POLYMERS WITH CHELATORS

Synthesis of pγCyDHis

$HisOCH_3$ Dihydrochloride was converted to the base form using a DEAE-Sephadex column (form OH^-). HOBt (14.0 mg, 0.103 mmol) and EDC (16.0 mg, 0.103 mmol) were added to pγCyDA (200 mg, 3.7 μmol) in DMF. After 10 min, $HisOCH_3$ (18 mg, 103 mmol) was added. The reaction mixture was stirred at room temperature for 24 h. The product was isolated by a Sephadex G-15 column. The methyl ester of His was hydrolyzed by a solution of NaOH 1 % (1 mL) for 2 h. The final product was purified using CM Sephadex C-25 (NH_4^+ form) and water as the eluent.

Yield: 20 %

^{1}H NMR: (500M Hz, D_2O) δ(ppm): 3.1 (m, CHA His); 3.2 (m, CHB His); 3.2–4.4 (m, H-3, -4, -5, -6 of CyD), 4.5 (m, CHX His); 4.9–5.5 (m, H-1 of CyD), 7.2 (s, H-2, Im), 8.5 ppm (s, H-5, Im).

^{13}C NMR (125 MHz, D_2O) δ(ppm): 27.3 (CH_2 His), 60.4 (C-2 CyD), 62.4 (C-3 CyD), 67.0–76.0 (C-6, C-5, C EPI), 80 (C-4 CyD), 100.0 (C-1 CyD); 116.8 (C-3 Im), 129.7 (C-2 Im); 132.9 (C-4 Im); 133.2 (C-5 Im); 175.8 (CONH); 178.0 (COOH).

Size (DLS, Z-Average): d:14±2 nm.

Synthesis of pβCyDHis

The synthesis was carried out as reported for pγCyDHis, starting from pβCyDA (200 mg, 2.3μmol), HOBt (17.4 mg, 129 mmol), EDC (20 mg, 129 mmol) and $HisOCH_3$ (22 mg, 129 mmol).

Yield: 25 %

^{1}H NMR: (500 MHz, D_2O) δ(ppm): 3.1 (m, CHA His); 3.2 (m, CHB His); 3.2–4.4 (m, H-3, -4, -5, -6 of CyD, H EPI), 4.5 (m, CHX His); 4.9-5.5 (m, H-1 of CyD), 7.2 (s, H-2, Im), 8.5 ppm (s, H-5, Im).

^{13}C NMR (125 MHz, D_2O) δ(ppm): 27.4 (CH_2 His), 60.3 (C-2 CyD), 53.3 (CH His); 62.4 (C-3 CyD), 67.0–76.0 (C-6, C-5,C EPI), 80.0 (C-4 CyD), 100.4 (C-1 CyD); 116.8 (C-3 Im), 129.7 (C-2 Im); 132.9 (C-4 Im); 133.4 (C-5 Im); 175.9 (CONH); 178.2 (COOH).

Size (DLS, Z-Average): d: 19±2 nm.

Synthesis of pγCyDCarc

HOBt (14.0 mg, 0.100 mmol) and EDC (16.0 mg, 0.100 mmol) were added to pγCyDA (200 mg, 3.7 μmol) in DMF. After 5 min, Carc (20.0 mg, 0.100 mmol) was added. The reaction mixture was stirred at room temperature for 24 h. The product was isolated with a Sephadex G-15 column using water as the eluent and was dialyzed against water. pγCyDCarc30.

Yield 43 %

^{1}H NMR: (500 MHz, D_2O) δ(ppm): 1.9 (bs, H-2 Ala); 2.3 (bs, H-2 Histamine (Hm)); 3.5-4.2 (m, H -3, -6, -5, -2, -4 γCyD, H-1 Ala and Hm and H EPI); 5.0–5.6 (m, H-1 γCyD); 7.2 (s, H-2, Im); 8.5 (s, H-5, Im).

^{13}C NMR (125 MHz, D_2O) δ(ppm): 24.0 (C-2 hm), 35.0 (C-2 Ala), 35.5 (C-1 Ala); 38.1 (C-1 Hm); 60.4 (C-2 CyD), 63.0 (C-3 CyD), 67.0-76.0 (C-6, C-5, C EPI), 80 (C-4 CyD), 100.0 (C-1 CyD); 117.0 (C-3 Im), 130.0 (C-2 Im); 132.0 (C-4 Im); 133.0 (C-5 Im); 173.8 (CONH); 177.0 (COOH).

The synthesis was carried out with a higher Carc/pCyD molar ratio in order to obtain a higher degree of substitution. After the activation step, Carc (40 mg, 0.200 mmol) was added to the reagents. pγCyDCarc60.

Yield 54 %

^{1}H NMR: (500 MHz, D_2O) δ(ppm): 2.0 (bs, H-2 Ala); 2.2 (bs, H-2 Histamine); 3.6–4.2 (m, H-3, -6, -5, -2, -4 γCyD, H-1 Ala and Hm); 5.1–5.6 (m, H-1 γCyD); 7.2 (s, H-2, Im); 8.6 (s, H-5, Im).

^{13}C NMR (125 MHz, D_2O) δ(ppm): 24.4 (C-2 Hm), 35.0 (C-2 Ala), 35.8 (C-1 Ala); 38.2 (C-1 Hm); 60.4 (C-2 CyD), 63.0 (C-3 CyD), 67.0-76.0 (C-6, C-5,C EPI), 80 (C-4 CyD), 100.0 (C-1 CyD); 117.0 (C-3 Im), 130.0 (C-2 Im); 132.5 (C-4 Im); 133.7 (C-5 Im); 173.9 (CONH); 177.2 (COOH). Size (DLS, Z-Average): d: 44±4 nm.

Synthesis of pβCyDCarc

The synthesis was carried out as reported for pγCyDCarc starting from pβCyDA (200 mg, 2.3 μmol), HOBt (17.4 mg, 129 mmol), EDC (20 mg, 129 mmol) and Carc (24 mg, 129 μmol). pβCyDCarc30.

Yield 56 %.

^{1}H NMR: (500 MHz, D_2O) δ(ppm): 2.3 (bs, H-2 Ala); 2.6 (bs, H-2 Hm); 3.25-4.5 (m, H-3, -6, -5, -2, -4 CyD, H-1 Ala and Hm); 5.0-5.6 (m, H-1 CyD); 7.2 (s, H-2, Im); 8.55 (s, H-5, Im).

The synthesis was carried out with a higher Carc/pCyD molar ratio in order to obtain a higher degree of substitution. After the activation step, Carc (50 mg, 0.258 mmol) was added to the reagents. pβCyDCarc60.

Yield 50 %

^{1}H NMR: (500 MHz, D_2O) δ(ppm): 2.3 (bs, H-2 Ala); 2.6 (bs, H-2 Hm); 3.5–4.5 (m, H-3, -6, -5, -2, -4 CyD, H-1 Ala and Hm); 5.0-5.6 (m, H-1 CyD); 7.2 (s, H-2, Im); 8.6 (s, H-5, Im).

^{13}C NMR (125 MHz, D_2O) δ(ppm): 24.5 (C-2 hm), 35.3 (C-2 Ala), 36.0 (C-1 Ala); 38.9 (C-1 Hm); 60.4 (C-2 CyD), 63.5 (C-3 CyD), 67.5-76.2 (C-6, C-5,

C EPI), 80.5 (C-4 CyD), 100.0 (C-1 CyD); 117.0 (C-3 Im), 130.2 (C-2 Im); 132.5 (C-4 Im); 133.0 (C-5 Im); 174.0 (CONH); 177.5 (COOH).

Size (DLS, Z-Average): d: 49 ± 5 nm

3.25. SYNTHESIS LABELING NANOPARTICLES OF CySPION-FLUO

2 g of PMOXA (0.25 mmol) was added with 100 mg of fluorescein isocyanate (0.25 mmol) in the presence of 36 µl of TEA in 10 ml of DMA 100 °C overnight. The polymer was then dialyzed (cut off: 3.5 kDa) to remove DMA and the excess of fluorescein to obtain 1.52 g of PMOXA-FLUO.

^{1}H NMR (300 MHz, DMSO): δ (ppm): 1.00-1.64 (CH_2 of hexanoic acid moiety), 1.80-1.84 (CH_2 in alpha COOH of hexanoic acid), 2.00 (-CH_3CO-), 3.21-3.55 (-N-CH_2-CH_2-N-, and ethylenic chain of en), 6.40-8.10 (fluorescein H, NHCS), 10.09 (broadband, OH).

Finally, 1 g of the carboxy-terminated PMOXA-FLUO (0.125 mmol) dissolved in 12 mL anhydrous DMA in an inert atmosphere. Thereafter, 55 mg (0.145 mmol) TBTU and 22 µL DIPEA (0.126 mmol) were added and stirred for 15 min. NDA (35 mg, 0.125 mmol) was added as a solution in anhydrous DMA. The reaction solution was stirred in the dark for 24 h. The polymer was dialyzed (cut off: 3.5 kDa) against water to remove DMF, the excess of NDA, and the coupling agents to yield about 840 mg of PMOXA-FLUO.

^{1}H NMR (300 MHz, DMSO): δ (ppm): 1.00-1.64 (CH_2 of hexanoic acid moiety), 1.80-1.84 (CH_2 in alpha COOH of hexanoic acid), 2.00 (-CH_3CO-), 3.21-3.55 (-N-CH_2-CH_2-N- and ethylenic chain of en), 5.80 (CONH), 6.40-8.10 (fluorescein, NHCS and NDA), 10.09 (broadband, OH).

Core-shell fluorescent nanoparticles - CySPION-FLUO - were prepared via ligand exchange using a blend of CyD-terminated PMOXA (85% in weight) and PMOXA-FLUO (15% in weight) yielding monodisperse, colloidally stable nanoparticles.

100 mg of wet oleic acid-coated SPIONs (from EtOH washing) were dispersed in 10 mL of DMF together with 500 mg of PMOXA-CyD, representing about 17-fold excess with respect to the grafting density of 1 NDA-terminated with polymer/nm^2 and 92 mg of PMOXA-FLUO. The dispersion was sonicated for 5 mins at room temperature, and the mixture was shaken at 4 °C for 6 days. After this time, the DMF suspension was precipitated with 25 mL of Et_2O and centrifuged at 4000 RPM for 5 mins. The supernatant was discarded, and the residue was washed twice with Et_2O to remove residual DMF and free oleic acid, leaving a sticky precipitate containing the functionalized nanoparticles and the excess of free polymer.

The core-shell nanoparticles were then purified by dispersing the obtained solid residue in DI water and removing the excess of free polymer using centrifugal filters (Amicon® Ultra-15 Centrifugal Filters, RC 30 kDa MWCO) at 3000 RPM for 15 mins. The operation was repeated several times until the separated solution appeared clear of polymer.

Size (DLS, Z-Average): d: 240 ±19 nm (Figure S142)

3.26. ANTIPROLIFERATIVE ACTIVITY

3.26.1. LINEAR AND CROSS-LINKED POLYMERS OF CyD

A2780, A549, HepG2 and MDA-MB-231 cells (all obtained from ICLC, Genova, Italy) were grown as monolayers in Roswell Park Memorial Institute (RPMI 1640) or Dulbecco's Modified Eagle's Medium (DMEM) media (EuroClone, Pero, Italy) supplemented with 10% fetal bovine serum (FBS) (Euroclone), antibiotics (EuroClone), and non-essential amino-acids (only DMEM, EuroClone). For the assay, cells plated into flat-bottomed 96-well microtiter plates were treated after 6-8 h with the Dox or Oxa alone or loaded in CyD polymers. Seventy-two hours later, cells were analyzed by the 3-(4,5-dimethylthiazol-2-yl)-2,5-diphenyltetrazolium Bromide (MTT) assay as described elsewhere [277].

Concentrations inhibiting 50% cell growth (IC_{50}) values were calculated from the analysis of single concentration-response curves. The final values are the mean of 4-12 experiments.

3.26.2. HAβCyD POLYMERS

The human cell line SK-N-SH (neuroblastoma), stimulated for seven days with 10 nM phorbol myristate acetate (PMA) in order to allow cells to overexpress CD44 receptor [278], SK-N-SH-PMA were plated in 180 µL into flat-bottomed 96-well microliter plates at 2.22×10^4 cells/mL in complete DMEM added with 10% fetal calf serum (FCS). After 6–8 h, cells were administered with 20 µL containing five concentrations of Dox alone or in the

presence of CyD polymers at 8/1 and 16/1 Dox/polymer molar ratio diluted in PBS. Plates were then processed as described elsewhere [279].

The compound IC_{50} was calculated based on the analysis of the concentration-response curves. Each experiment was repeated 5–7 times.

3.26.3. SPIONs NPs

NPC1-deficient CHO cells were a gift of Frances Platt, Department of Pharmacology, University of Oxford. CHO cells seeded in DMEM containing GlutaMax and HEPES, supplemented with 10% fetal calf serum and 100 units/ml of penicillin/streptomycin, were grown as monolayers at 37°C with 5% CO_2.

3.27. CELL VIABILITY OF DIMERS

Human cancer cells ($2.5–3.0 \times 10^3$ cells/0.33 cm^2) were plated in 96 well plates from Nunc™ MicroWell™ (Thermo Fisher Scientific, Cat No. 24365) and were incubated at 37 °C. After 24 h, cells were treated with the following single compounds (Dox, βCyD2GlyAc, γCyD2GlyAc, βCyD2GlyBio, γCyD2GlyBio) or Dox complexes with the above β and γ dimers (concentration 0.03, 0.3 and 3 μM). Untreated cells were used as controls. Microplates were incubated at 37 °C in a humidified atmosphere of 5% CO_2/95% air for 72 hours. Then the cellular vitality and/or the cellular cytotoxicity was evaluated by a colorimetric assay based on the use of a tetrazolium salt MTT [3-(4,5-dimethylthiazol-2-yl)-2,5-diphenyl tetrazolium bromide] as previously reported [280–282]. After 72 hours of treatments, MTT solution was added and maintained for 3 hours. The purple formazan dye, obtained from the metabolism of vital cells, was solubilized by 150 μl/well of dimethyl sulfoxide (DMSO). The optical density values were read

on a multiwell scanning spectrophotometer (Plate Reader AF 2200 Eppendorf BioSpectrometer® Eppendorf BioPhotometer® D30), using a wavelength of 600 nm. Each value was the average of 10 wells).

3.28. HUMAN CELL CULTURES

Five human cell lines were used for transcriptomic analysis. CACO-2 (ATCC No. HTB-37, colorectal adenocarcinoma), HCT-116 (ATCC No. CCL-247, Colorectal Carcinoma), HT-29 (ATCC No. HTB-38, colorectal adenocarcinoma), MCF-7 (ATCC No. HTB-22, breast adenocarcinoma) and PC-3 (ATCC No. CRL-1435, Prostate adenocarcinoma) cell lines were obtained from the American Type Culture Collection (Rockville, MD, USA).

CACO-2, HT-29 and MCF-7 were cultured in Dulbecco's Medium 4.5g/dL Glucose w/Glutamax (1X Gibco® Cat No. 12430054), HCT-116 was maintained in McCoy's 5a Medium Modified (1X Gibco®, Cat No. 12330031), while PC-3 was cultured in DMEM/F12 medium nutrient mixture (1X; GIBCO, Cat. No. 21331). Each medium was supplemented with 10-20%% fetal bovine serum (FBS, Cat. No. 10270-106; Life Technologies, Monza, Italy) and 1% of 1/1 penicillin–streptomycin (Cat. No 15140- 122; Life Technologies).

The cell cultures were grown in flasks (25 cm^2) and incubated at 37 °C in humidified atmosphere with 5% of CO_2 and 95% of air. The culture medium was changed twice a week.

3.29. TRANSCRIPTOME ANALYSIS

Transcriptome analysis was performed from 100 ng of total RNA extracted by cell lines by amplification and target hybridization to the Gene-Chip Human Transcriptome Array (HTA) 2.0 [283].

Array scanning and data analysis were performed with the Affymetrix® Expression ConsoleTM software version 1.4 (Affymetrix, Inc., Santa Clara, CA, USA) and the Affymetrix® Transcriptome Analysis Console (TAC) software (Affymetrix, Inc., Santa Clara, CA, USA). Transcript level analysis was performed using the normalization method based on the processing algorithm called robust multi-array average (RMA). Data submitted to a public repository "Gene Expression Omnibus-GEO" (www.ncbi.nlm.nih.gov/geo) [283].

3.30. IMMUNOFLUORESCENCE STUDY OF CD44 EXPRESSION

SK-N-SH and SK-N-SH-PMA cells were harvested and washed twice with phosphate-buffered saline (PBS) plus 2% FCS. Then pelleted 2.0×10^5 cells were incubated at 22 °C for 30 min with 50 µL (1:1000) of an anti-CD44 monoclonal antibody (ab254530, Abcam, Cambridge, UK). Cells were then washed twice with PBS plus 2% FCS and incubated again with 50 µL FLUO (Fluorescein) AffiniPure F(ab')2 fragment goat anti-mouse IgG+IgM (H+L) 1:200 dilution (Jackson ImmunoResearch, Ely, UK). After being rewashed twice, cells were evaluated by flow cytometry (Cytoflex-S, Beckman Coulter, Milan, Italy) and analyzed by FlowJo software v10.8 (BD).

3.31. CYTOFLUORIMETRIC STUDY OF INTRACELLULAR ACCUMULATION OF Dox

SK-N-SH and SK-N-SH-PMA cells were plated in 96-well plates in 180 µL medium 4 × 10^4 cells/well. After incubation at 37 °C for 24 h, once reached 75 -85% confluence, cells were treated with 2 µM Dox alone or in the presence of CyD polymers at 8/1 and 16/1 Dox/polymer molar ratio. After 1 h, cells were washed twice with 200 µL of PBS and fixed with 100 µL of 3.7% paraformaldehyde in PBS (containing 2% sucrose) for 15 min [284]. Cells were rewashed with PBS and resuspended in 100 µL PBS containing 2% FCS. Untreated cells were assayed as well.

The intracellular mean fluorescence intensity (MFI) of cells was determined directly in plates by a Glomax Discover microplate reader (Promega Italia, Milan, Italy), using 475 nm excitation and 580-640 nm emission wavelengths. Values were normalized as absolute MFI calculated as MFI of treated cells-MFI of control cells.

3.32. STATISTICAL ANALYSIS

Student's *t*-test for independent means was used for the analysis of data.

3.33. EVALUATION OF INTRACELLULAR ACCUMULATION OF Dox

A549 and HepG2 cells were plated in 6-well plates at 2.0 and 2.5 × 10^4 cells/well in 3 mL, respectively. After 16 h, cells were treated with 1.2 µM

Dox or Dox/CyD complexes. After 2 h cells were detached by exposure to trypsin-EDTA at 37 °C for 5 min, washed quickly once with cold PBS, and fixed with 0.3 mL of 3.7% paraformaldehyde in PBS containing 2% sucrose.

Untreated cells were assayed as well. The intracellular median fluorescence intensity of Dox was determined by flow cytometry (MACSQuant Analyzer 8, Miltenyi Biotec, Bologna, Italy) using 488 nm excitation and 655–730 nm emission filters. Data were analyzed with FowJo 10.7.2 software (Becton Dickinson, Milano, Italy)

Values were normalized using the Staining Index (SI):

$$\frac{[Mean/Median\ treated] - [Mean/Median\ control]}{2 \times SD\ control}$$

3.34. CONFOCAL MICROSCOPY

CySPION-FLUO uptake in CHO "null" cells and the colocation in the lysosomes was determined by means of confocal laser scanning microscopy (CLSM) using an SP8 by Leica. The DNA label Hoechst 34580 was excited with the 405 nm diode laser while the fluorescein in the nanoparticle and the Lysotracker Deep Red were excited with the 495 nm and 653 nm lines of the microscope's white laser. To minimize the crosstalk between the signal from the DNA label and the nanoparticle, mainly caused by the 405 nm laser exciting the fluorescein, we also applied line-based sequential scanning where the DNA (380nm-385nm) and 3.19. The Lysotracker (658nm-776nm) was first localized and the CySPIONs (500nm-617nm) subsequently. The transmitted was also collected at 495 nm light during the second exposure to produce a transmission micrograph.

4. CONCLUSION

In this thesis, new systems have been designed with innovative strategies of synthesis to obtain promising conjugates.

The first section focuses on synthesizing new nanoparticles as drug delivery systems. From cyclodextrin dimers to various cyclodextrin polymeric systems were explored, introducing positive charges, and vitamins (folic acid and biotin). Synthesis methods were tuned to improve conjugation degrees and yields. Many condensation reactions were carried out in green conditions employing water as the reaction solvent. This functionalization strategy allowed the study of the effect of the molecular weight, functionalization moiety and charges of the conjugates on different drug delivery systems. Furthermore, the antiproliferative activity of commonly administrated drugs (Doxorubicin, Sorafenib and Oxaliplatin) in current cancer therapies was assessed *in vitro*.

In all of the cases, the new nanosystem had proven to increase the antiproliferative activity and solubility of the drugs.

A successful strategy was the introduction of Cyclodextrin into the linear backbone of hyaluronic acid with two different molecular weights. This approach enabled combining the CyD properties as a solubilizer of the drugs with the capability of hyaluronic acid to recognize CD44 receptors. The HAβCyD conjugates had shown an increase of the Doxorubicin solubility at physiological conditions. Moreover, the HAβCyD polymers were investigated *in vitro* in a neuroblastoma cell line, overexpressed CD44 receptors. A significant reduction of IC_{50} was achieved (70%) compared to Doxorubicin alone (Figure 72). The HAγCyD conjugates were assessed in the presence of Sorafenib and also in this case, the polymers improved significantly the

antiproliferative activity (up to 70% in the MDA-MB-453 cell line) compared to the free drug, particularly with the low molecular weight polymer.

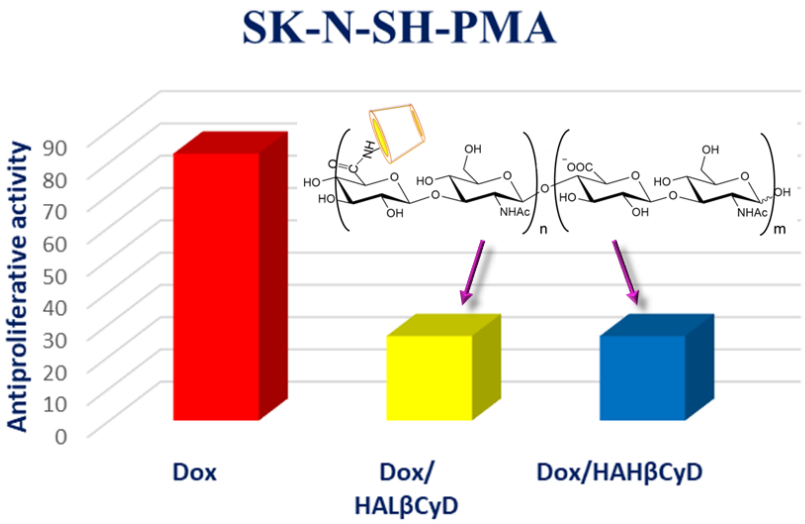

Figure 72. Antiproliferative of Dox in SK-N-SH-PMA cell line with HAβCyD polymers

As for targeting strategy, the best results were obtained for the cyclodextrin dimers. These dimers exhibited a significant capability to increase Doxorubicin solubility and decrease cell viability *in vitro*. In particular, the biotinylate dimers, at higher concentration (μM) had proven an enhanced activity of Doxorubicin (about 40%). This enhancement was not only when compared to the drug alone but also over the untargeted analogous. The functionalization seems to promote active targeting in MCF-7 cell lines (Figure 73). Cross-linked polymer functionalized with biotin did not show any improvement in Doxorubicin cytotoxicity. Probably, the linker was entrapped in the polymer and could not adequately recognize the SMVT receptor.

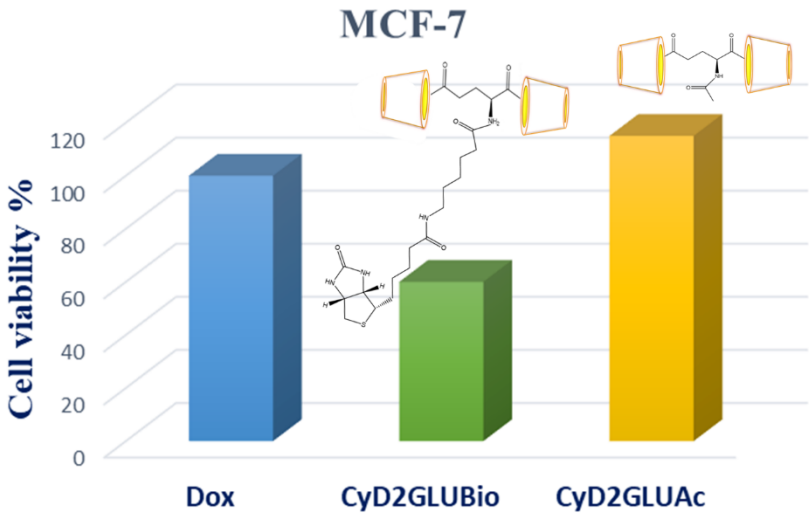

Figure 73. Cell viability at µM concentration of CyD2GLUAc and CyD2GLUBio with Dox

Other effective systems were the cross-linked polymers of CyDs, investigated as drug delivery systems of Oxaliplatin and Doxorubicin. Polymers tested *in vitro* using two cell lines, A-549 and Hep-G2, showed significant antiproliferative activity against the Hep-G2 cell line with Doxorubicin, whereas the complexation with Oxaliplatin notably improved its antitumor activity in both cell lines (Figure 74). Furthermore, the accumulation of Doxorubicin was studied in the cell and the results proved that the polymers determined the differential uptake of the drug.

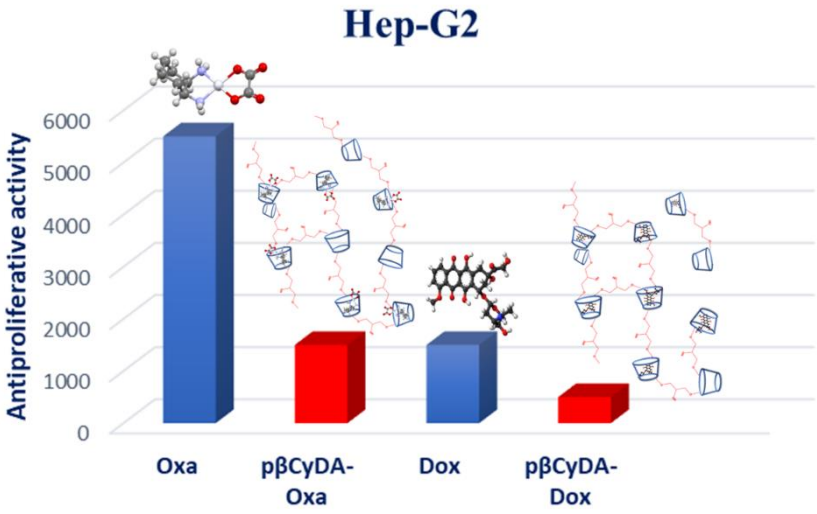

Figure 74. IC_{50} of Oxa and Dox in Hep-G2 cell line in the presence of cross-linked polymer

The second section of the thesis focused on the synthesis of new copper (II) nanochelator, functionalized with carcinine or histidine. Carcinine and histidine are well-known bio-ligands. The polymers can form copper(II) complexes like free carcinine or histidine. In addition, the nanochelators showed to preserve the SOD activity of carcinine and histidine (Figure 75). Furthermore, a study in the presence of α-amylase at different pH, was showed that the enzyme did not degrade the polymers.

These results suggest the potential of these systems in sequestering copper from dietary sources before its intestinal absorption. Consequently, the nanochelators may reduce oxidative stress via copper (II) chelation and SOD activity conferred by the resultant complex.

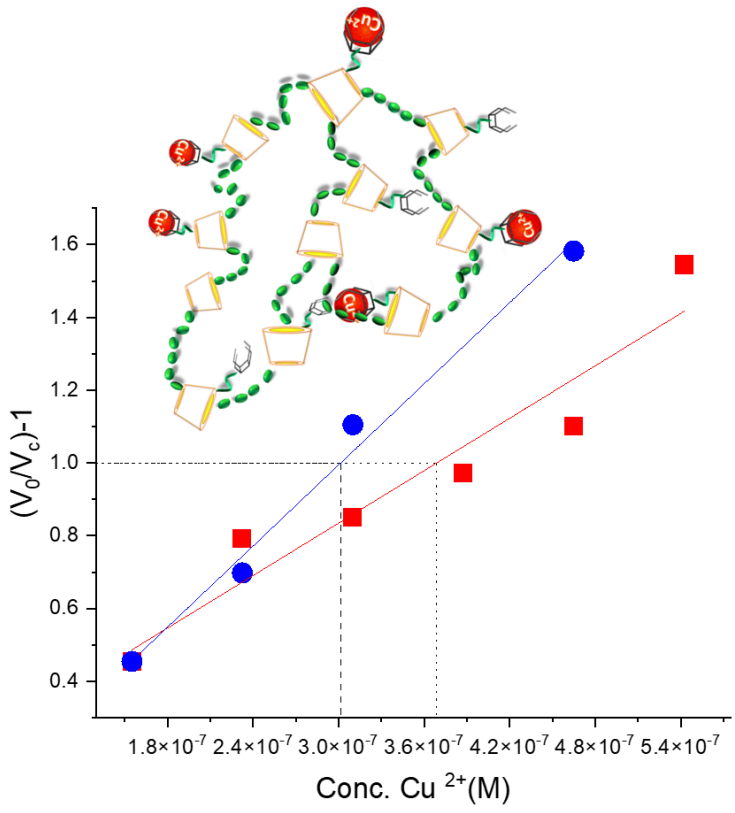

Figure 75. Superoxide dismutase activity assay in the presence of Cu^{2+}-pγCyDHis (•) and pγCyDCarc (▪).

The latest line of research in this thesis was the synthesis of CySPION-FLUO nanoparticles. In this case, the ability of Cyclodextrin to remove the cholesterol from the cell was combined with the potential of SPIONs to cross the blood-brain barrier. The multifunctional nanoparticles showed negligible cytotoxicity in CHO cell lines. Moreover, both TEM and confocal microscopy demonstrated that the nanoparticles were strongly endocytosed and localized in the lysosome of the cells (Figure 76). This aspect is particularly important as lysosomes represent sites of cholesterol accumulation and possess a lower pH environment, allowing the cleavage of ester bond and the release of CyD into the action site.

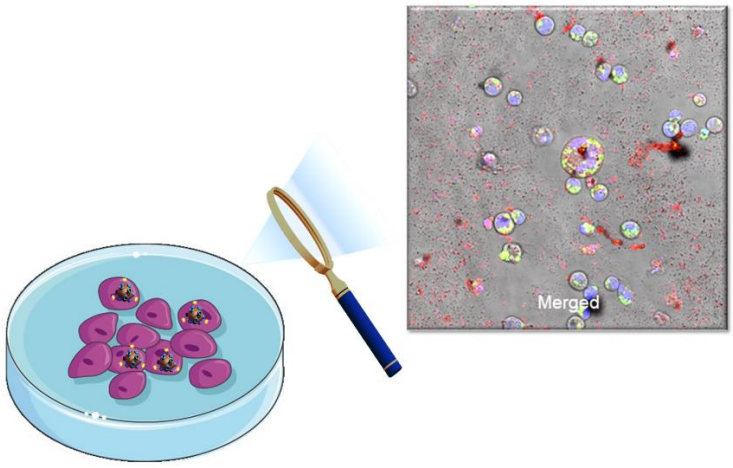

Figure 76. Confocal image of CySPION-FLUO internalized in CHO cell line.

The cholesterol-mopping activity of CySPION was also investigated, showing that the activity of CySPION is likewise to monomeric CyD. However, another advantage of CySPION is its longer retention time, slower uptake and release than monomeric CyD. Finally, the significantly higher transport rate of CySPION across a model blood-brain barrier compared to the free polymer may indicate an advantage of the responsive, nanoparticle-based delivery system (Figure 77). This last measure underscores the excellent potential of the system, not only for cholesterol removal but also for drug delivery for neuronal diseases. This idea is strengthened by preliminary confocal microscopy studies, indicating that CySPION-FLUO was able to deliver Doxorubicin inside the cell.

Figure 77. Permeability of Blood-Brain Barrier in the presence of CySPION-FLUO

In conclusion, these findings highlight the promising potential of these nanotherapeutics in various contexts, including cancer treatment, diseases related to copper dyshomeostasis and oxidative stress, and neurodegenerative conditions affected by cholesterol imbalance (Figure 78). Based on these results, the cyclodextrin conjugates described here merit further investigation through both *in vitro* and *in vivo* studies to explore their potential fully.

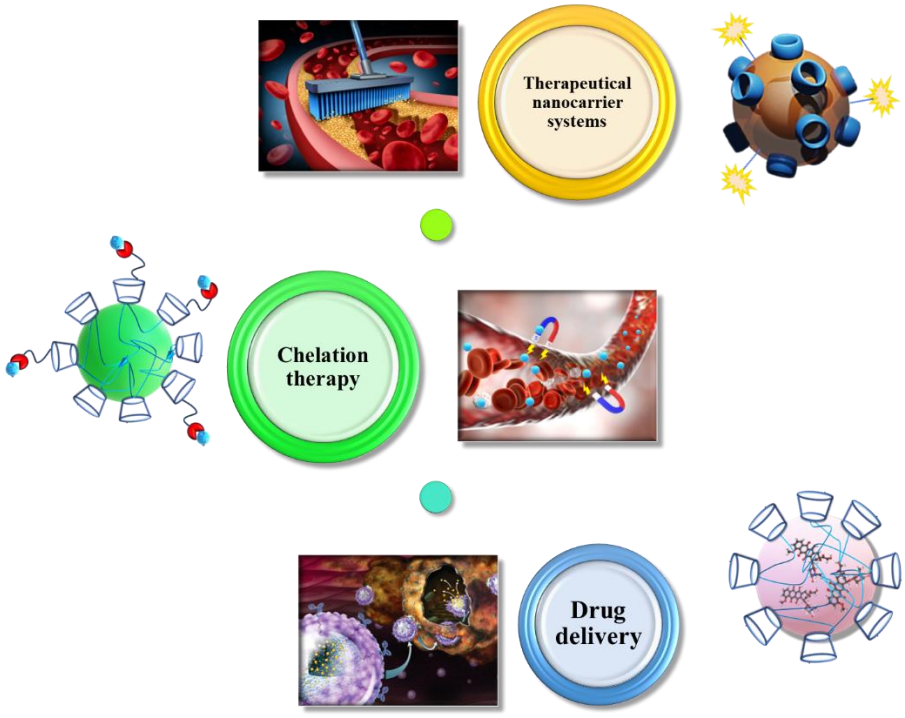

Figure 78. Biological application of CyD conjugates

ACKNOWLEDGEMENTS

A thank you goes to everyone who has contributed in various ways to the realization of this thesis.

A heartfelt thanks goes to my tutor, Graziella Vecchio, who has allowed me to grow both scientifically and personally. Thank you for every encouragement, for every "reprimand," but above all for always believing in me and giving me confidence at every moment. Furthermore, I express my gratitude to her for passing on her ethics, part of her professional experience to me, and for guiding me on my research path with valuable advice. Thanks also for being able to rely on her in the moments of joy or discouragement during my Ph.D., sharing with me the moments of difficulty and always trying to comfort and cheer me up. Finally, I would like to thank her because, without her support and wise guidance, this thesis would not exist.

I would also like to thank Professor and Ph.D. coordinator Salvatore Sortino for always supporting me in a jovial manner. I will always carry his teachings and his example of professionalism and ethics with me.

Thanks also to Erik Reimhult for hosting me in Vienna during my six-month internship. I would also like to thank my boss in Vienna, Dr. Nino Puglisi, for supporting me throughout the six months abroad. Thank you for all the laughter. I also said a sincere thanks to Tiziana and Pascal for contributing to always feeling at home.

A warm thanks goes to all those who have collaborated on this work: Dr. Maurizio Viale from the hospital in Genoa, Professor Vincenza Barresi from Biometec, Dr. Fabrizia Brisdelli, and Professor Mariagrazia Perilli from the University of L'Aquila, Dr. Francesco Bellia from CNR Catania, Researcher Peter van Oostrum from Vienna, the entire research group from the University of Oxford and Bornova.

I would also like to thank the secretaries Sabrina Tosto and Giuseppina Marino for their cooperation and advice.

I also want to express my gratitude to the entire bioinorganic laboratory group, my colleagues and friends Luana, Chiara, Livia, Sara, Valentina and Roberta for their support and for making this journey even more enjoyable. A special thanks to Giusi for sharing this journey with me from day one, celebrating every achievement together and supporting each other in the less happy moments.

Last but not least, thanks to my parents for always being there and to my boyfriend, Francesco Amato, for believing in me from the beginning and encouraging me at every moment.

APPENDIX 1: ABBREVIATIONS

6BHA 6-bromohexanoic acid

A2780 Ovarian cancer cell line

A549 lung cancer cell lines

Ac Absorbance of control

Ac-Glu-OH Glutamic acid acetylate

AD Alzheimer's disease

APP Amyloid Precursor Protein

ArgOCH$_3$ Arginine methyl ester

As Absorbance of the sample

Aβ Amyloid beta

BBB Blood–Brain Barrier

BCS Biopharmaceutics Classification System

Bio Biotin

BOC Ter-Butilossicarbonile

C8-D1A Mouse brain astrocyte cell line

CALAA-01 Polycationic CyD polymer, PEG adamantine, transferrin and siRNA

CAMs Cell Adhesion Molecules

Carc Carcinine

CDCl3 Deuterated Chloroform

CE Complexation efficiency

CHO Chinese Hamster Ovary

CLSM Confocal Laser Scanning Microscopy

CRLX101 Cyclodextrin-polyethylene glycol-Camptothecin

CROP Cationic ring-opening polymerization

CRT Crocetin

CRYSMEB β Cyclodextrin with 5 methyl groups

CTRL Control

CyD Cyclodextrin

CyD2GluAc CyD Dimers acetylate

CyD2GluBio CyD Dimers Biotinylated

CyDen 6-ethylendiamine βCyD

CyDNH2 Amino-cyclodextrin

CyD-PEG Cyclodextrin-polyethylene glycol

D2O Deuterated Oxide

Da Dalton

DCC N,N′-Dicyclohexylcarbodiimide

DCM Dichloromethane

DD Drug Delivery

DDS Drug Delivery System

DHB 2,5-di-hydroxybenzoic acid

DIPEA N,N-Diisopropylethylamine

DLS Dynamic light scattering

DMA Dimethylacetamide

DMEM Dulbecco's Modified Eagle's Medium

DMF Dimethylformamide

DMSO Dimethyl Sulfoxide

DMTMM 4-(4,6-Dimethoxy-1,3,5-triazin 2-yl)-4-methylmorpholinium chloride

Dox Doxorubicin

DS Degree substitution

DTS Dispersion Technology Software

ECM Extracellular Matrix

EDC (1-Ethyl-3-(3-dimethylaminopropyl)carbodiimide)

EGFR Epidermal growth factor receptor

enCyD Ethyl Diamino-B-Cyclodextrin

EPI Epichlorohydrin

EPR Enhanced Permeation and Retention

EtO2 Diethyl ether

FA Folic acid

FBS Fetal Bovinum Serum

FCS Fetal calf serum

Fe3O4@PCA-PEG-FA Fe3O4 coated with poly-citric acid, polyethylene glycol and folic acid

FLUO Fluorescein-5-isothiocyanate

FR Folate Receptor

G Guest

GBA γ-Guanidinobutyric Acid

GPC Gel Permeation Chromatography

H Host

HA Hyaluronic acid

HAHMW Hyaluronic acid at Higher Molecular weight

HALMW Hyaluronic acid at Lower Molecular weight

Hb Hemoglobin

HBEC-5i Endothelial cell line

HEPES 2-[4-(2-hydroxyethyl)piperazin-1-yl]ethanesulfonic acid buffer

HepG2 Liver carcinoma

His Histidine

HMD Hexamethylene diisocyanate

HMW Higher Molecular Weight

HOBt Hydroxybenzotriazole

HPβCyD 2-hydroxypropyl-β-cyclodextrin

HTA 2.0 Human Transcriptomic Array

IC50 Half maximal inhibitory concentration

iRGD Internalizing RG peptide

J_{1en} PMOXA-NH2

K Apparent stability constant

KLEPTOSE β Cyclodextrin with 6 methyl groups

LMW Low Molecular Weight

LY Lucifer Yellow

MAX 3D Matrix system

MCF-7 Breast cancer cell

MDA-MB-453 Breast cancer cell

MFH Magnetic Fluid Hyperthermia

MFI Mean fluorescence intensity

MO 2-methyl-oxazoline

MRI Magnetic Resonance Imagine

MTT 3-(4,5-dimethylthiazol-2-yl)-2,5-diphenyltetrazolium Bromide

MW Molecular weight

NADH Nicotinamide adenine dinucleotide

NBT 4-Nitro blue tetrazolium chloride

NDA Nitrodopamide Anchor

NHS N-Hydroxysuccinimide

NMR Nuclear Magnetic Resonance

NPC Niemann-Pick disease type C

NPs Nanoparticles

OA Oleic acid

OEI Oligoethylenimine

Oxa Oxaliplatin

PBS Phosphate buffer saline

PCA Poly citric acid

pCyD Polymer of Cyclodextrin

pCyDA Anionic polymer of Cyclodextrin

pCyDBio Anionic polymer of Cyclodextrin Polyethylene glycol Biotin

pCyDCarc Anionic polymer of Cyclodextrin Carcinine

pCyDHis Anionic polymer of Cyclodextrin Histidine

PD Parkinson diseases

PEG Poly (ethylene glycol)

PGA Polyglutamic Acid

PGACyD Complex of Fe3+ and only PGACyDPMOXA polymer

PGACyDArg N-butyl-polyglutamate Cyclodextrin Arginine

PGACyD-FA Complex of Fe3+ with PGACyDPMOXA and PMOXA-FA polymers

PGACyDGBA N-butyl-polyglutamate Cyclodextrin γ-Guanidinobutyric Acid

PLGA Poly (lactic-co-glycolic acid)

PMOXA Poly (2-methyl-2-oxazoline)

PMS Phenazine methosulfate

PVA Polyvinyl alcohol

RES Reticuloendothelial system

RGD Arginine-glycine-aspartic acid

Salen Salicylaldehyde and ethylenediamine Schiff bases

SBEβCyD Sulfobutyl ether βCyD

SI Staining Index

siRNA Short interfering RNA

SK-HeP-1 Adenocarcinoma cell line

SK-N-SH Neuroblastoma cell line

SK-N-SH-PMA Neuroblastoma cell line with overexpression of CD44 receptors

SMVT Sodium-Dependent Multi-Vitamin Transporters

SOD Superoxide dismutase

Sor Sorafenib

SPIONs Superparamagnetic Iron Oxide Nanoparticles

TBA Tertiary butyl alcohol

TBTU 2-(1H-Benzotriazole-1-yl)-1,1,3,3-tetramethylaminium tetrafluoroborate

TEA Triethylamine

TEM Transmission Electron Microscopy

Tf Trasferrin

TFA Trifluoroacetic acid

TEA Triethylamine

TGA Thermogravimetric Analysis

TLC Thin Layer Chromatography

TOC Total Organic Content

TRL-4 Toll-Like Receptor

TSPP Fe(II)-tetrasulfonate phenyl porphyrin

WT Wild type

APPENDIX 2: PUBBLICATIONS

1. *Bognanni, N.*; Bellia, F.; Viale, M.; Bertola, N.; Vecchio, G. Exploring Charged Polymeric Cyclodextrins for Biomedical Applications. Mol. 2021, Vol. 26, Page 1724 2021, 26, 1724,

2. *Bognanni, N.;* Viale, M.; Distefano, A.; Tosto, R.; Bertola, N.; Loiacono, F.; Ponassi, M.; Spinelli, D.; Pappalardo, G.; Vecchio, G. Cyclodextrin Polymers as Delivery Systems for Targeted Anti-Cancer Chemotherapy. Mol. 2021, Vol. 26, Page 6046 2021, 26, 6046.

3. *Bognanni, N.;* Viale, M.; La Piana, L.; Strano, S.; Gangemi, R.; Lombardo, C.; Cambria, M.T.; Vecchio, G. Hyaluronan-Cyclodextrin Conjugates as Doxorubicin Delivery Systems. Pharmaceutics 2023, 15, 374.

4. *Bognanni, N.*, Brisdelli, F., Piccirilli, A., Basile, L., La Piana, L., Di Bella, S., ... & Perilli, M. (2023). New polyimidazole ligands against subclass B1 metallo-β-lactamases: Kinetic, microbiological, docking analysis. Journal of Inorganic Biochemistry, 112163.

5. Puglisi A, *Bognanni N*, Vecchio G, Bayir E, van Oostrum P, Shepherd D, Platt F, Reimhult E. Grafting of Cyclodextrin to Theranostic Nanoparticles Improves Blood-Brain Barrier Model Crossing. Biomolecules. 2023; 13(3):573.

6. *Bognanni, N.*, Bellia, F., Vecchio G. (2023). Cyclodextrin polymers functionalized with histidine and carcinine as chelating therapeutics for copper dyshomeostasis.

7. Basile, L., Piccirilli, A., Brisdelli, F., Perilli, M., *Bognanni, N.*, La Piana, L., ... & Vecchio, G. (2023). The in vitro inhibitory activity of polypyridine ligands towards subclass B1 metallo-β-lactamases. Results in Chemistry, 100986.

8. *Bognanni N.*, Scuderi C., Spiteri F., La Piana L., Barresi V., Vecchio G. Cyclodextrin dimers functionalized with biotin for doxorubicin delivery. Submitted.

9. *Bognanni N.*, Viale M. and Vecchio G. Linear polymers of Hyaluronan-Cyclodextrin as carriers for Sorafenib. Submitted.

10. *Bognanni N.*, Brisdelli F. and Vecchio G. Biological studies of copper complexes based on polyimidazole ligands. Submitted.

APPENDIX 3: PROCEEDINGS

1. Noemi Bognanni, Alessandra Piccirilli, Mariagrazia Perilli, Luigi Principe, Stefano Di Bella, Graziella Vecchio, *Polyimidazole ligands as metallo-β-lactamase inhibitors*, *Biomet Congress*, (April 2021).

2. Noemi Bognanni, *Positive cyclodextrin polymers for biomedical applications*, European School of Medicinal Chemistry, (June 2021).

3. Noemi Bognanni, Francesco Bellia, Graziella Vecchio, *Cross-linked cyclodextrin polymers for chelation therapy*, International Cyclodextrin Symposium, (June 2022).

4. Noemi Bognanni, Antonino Puglisi, Peter van Oostrum, Graziella Vecchio, Erik Reimhult, *Fluorescent nanoparticles based on cyclodextrin with cholesterol mopping activity*, International Summer School of Cyclodextrin (ISSCD 2022), (September 2022).

5. Noemi Bognanni, Chiara Scuderi, Vincenza Barresi, Graziella Vecchio, *Dimers of cyclodextrin as doxorubicin delivery system*, Suprachemdays2023 (May 2023).

6. Noemi Bognanni, Chiara Scuderi, Vincenza Barresi and Graziella Vecchio, *New drug delivery system based on cyclodextrin dimers functionalized with biotin*, 7th European Cyclodextrin Conference, (Sept.2023).

7. Noemi Bognanni, Maurizio Viale and Graziella Vecchio, *New conjugates of γ-Cyclodextrins-grafted Hyaluronic acid for release of drugs in cancer cells*, 7th European Cyclodextrin Conference, (Sept.2023).

8. Noemi Bognanni, Fabrizia Brisdelli, Alessandra Piccirilli, Mariagrazia Perilli and Graziella Vecchio, *Polyimidazole ligands: biological activity of their copper complexes*, 49° Congresso Nazionale di Chimica Inorganica, (Sept. 2023).

9. Noemi Bognanni, Fabrizia Brisdelli, Alessandra Piccirilli, Mariagrazia Perilli and Graziella Vecchio, *Biological studies of copper complexes based on polyimidazole ligands*, Convegno Nazionale della Divisione di Chimica dei Sistemi Biologici (Sept. 2023).

10. Noemi Bognanni, Maurizio Viale and Graziella Vecchio, *Linear polymers of Hyaluronan-Cyclodextrin as carriers for Sorafenib*, AMYC-BIOMED 2023, (Oct.2023)

SUPPLEMENTARY MATERIAL

The following supporting information shows:

Figures S79-S89 NMR spectra 1 and 2D of CyD2GluAc and CyD2GluBio, Figure S90 the dose-response curve of Dox in MCF-7 cell line.

Figures S91-S93 ^{1}H NMR of HACyD conjugates, Figures S94-S96 HA and HACyD DLS, Figure S97 UV-vis spectra of saturated solution of Dox in the presence of an increasing concentration of the polymer; Figure S98 Dose-response curves of SK-N-SH (top) and SK-N-SH-PMA (bottom) cells treated with Dox, Dox/HALβCyD, or Dox/HAHβCyD.

Figures S99-S106 NMR spectra 1 and 2D of PGACyDArg polymers, Figure S107 MALDI-TOF MS spectra of the PGAβCyDArg polymers. Figures S108-S110 NMR spectra 1 and 2D of PGACyDGBA polymers, Figures S111 and S112 DLS of PGACyDGBA and PGACyDArg polymers, Figures S113- S116 Zeta Potential of PGA, PGACyDGBA and PGACyDArg.

Figures S117- S123 NMR spectra 1 and 2D of PGACyDPMOXA, Figure S124 GPC of PMOXA.

Figure S125 DLS of pCyDA polymers, Figure S126 Zeta Potential of pCyDA polymers, Figure S127 UV-vis spectra of Dox-pCyDA, Figures S128 and S129 Representative experiment of Dox accumulation in HepG2 and A549 cells.

Figures S130- S137 NMR spectra 1 and 2D of pCyDCarc and pCyDHis, Figures S138 and S139 DLS of pCyD conjugates, Figure S140 UV-vis spectrum of Cu^{2+}-pβCyDCar60 and Cu^{2+}-pγCyDHis, Figure S141 Superoxide dismutase activity assay in the presence of Cu^{2+}-pβCyDHis and pβCyDCarc60.

Figure S142 DLS of CySPION-FLUO, Figures S143 and S144 Calibration curve of LY and PMOXA-FLUO, Table S14 Calibration curve of LY, Table S15 Calibration curve PMOXA-FLUO, Figure S145 Calibration curve of CySPION-FLUO, Table S16 Calibration of CySPION-FLUO, Table S17 Permeability values for LY, PMOXA-FLUO and CySPION-FLUO.

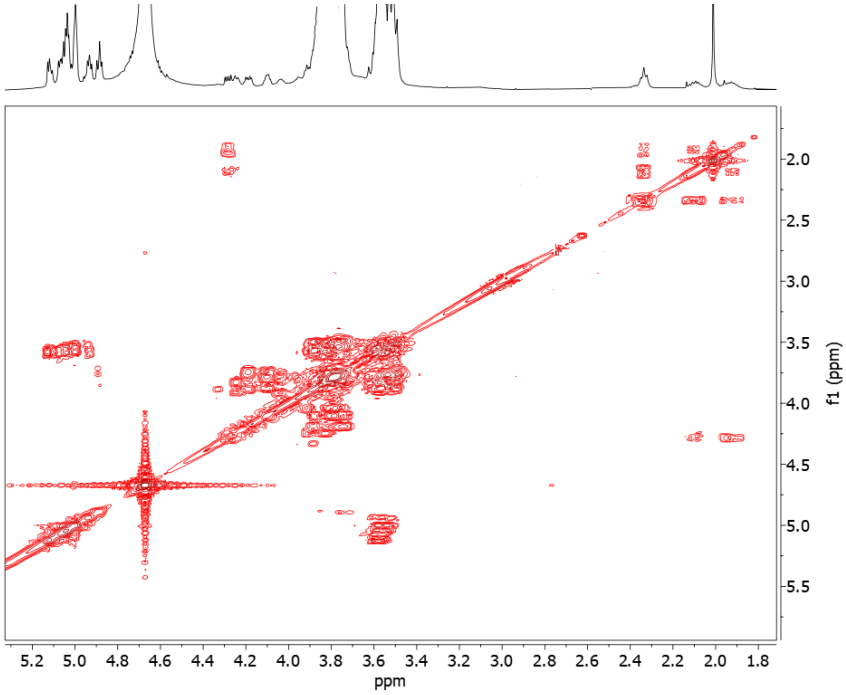

Figure S79. COSY spectrum of γCyD2GluAc (D_2O, 500 MHz)

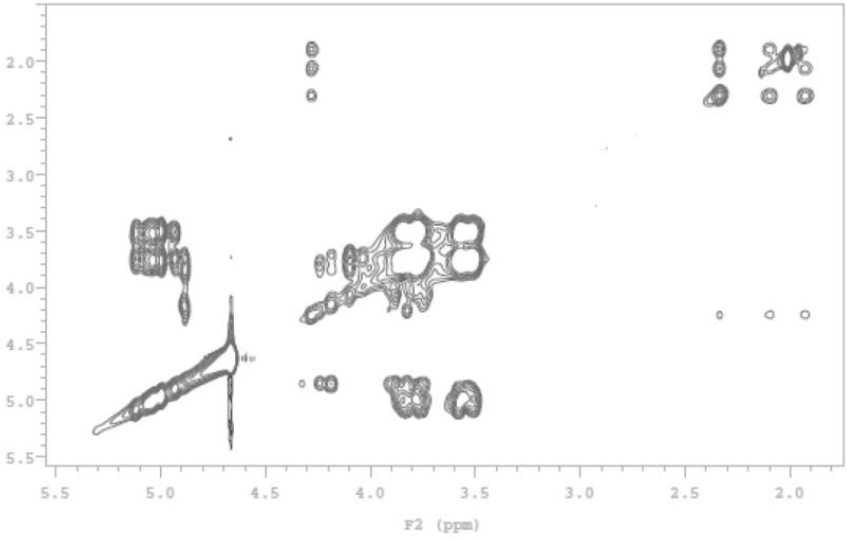

Figure S80. TOCSY spectrum of γCyD2GluAc (D_2O, 500 MHz)

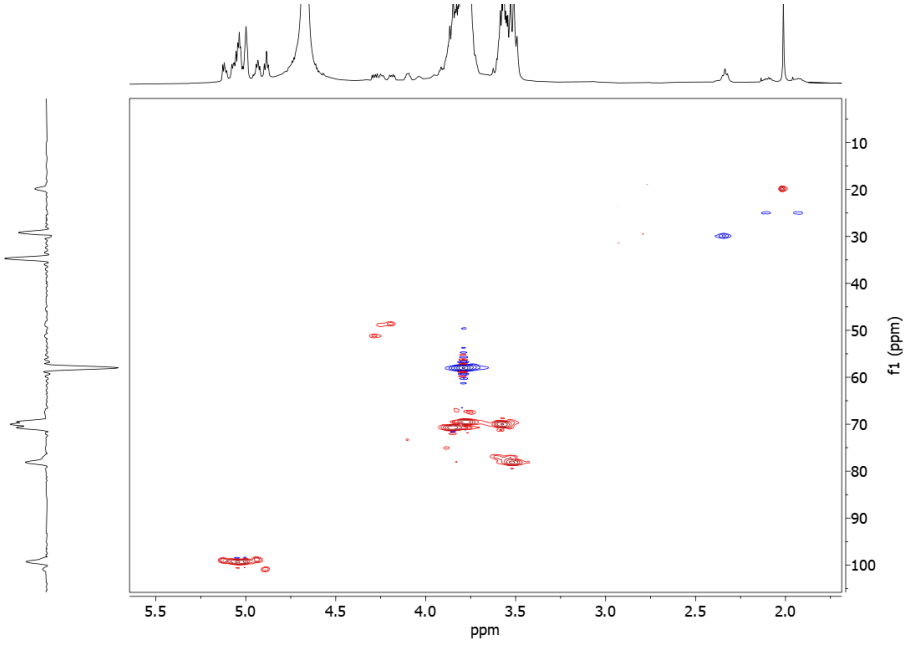

Figure S81. HSQC spectrum of γCyD2GluAc (D_2O, 500 MHz)

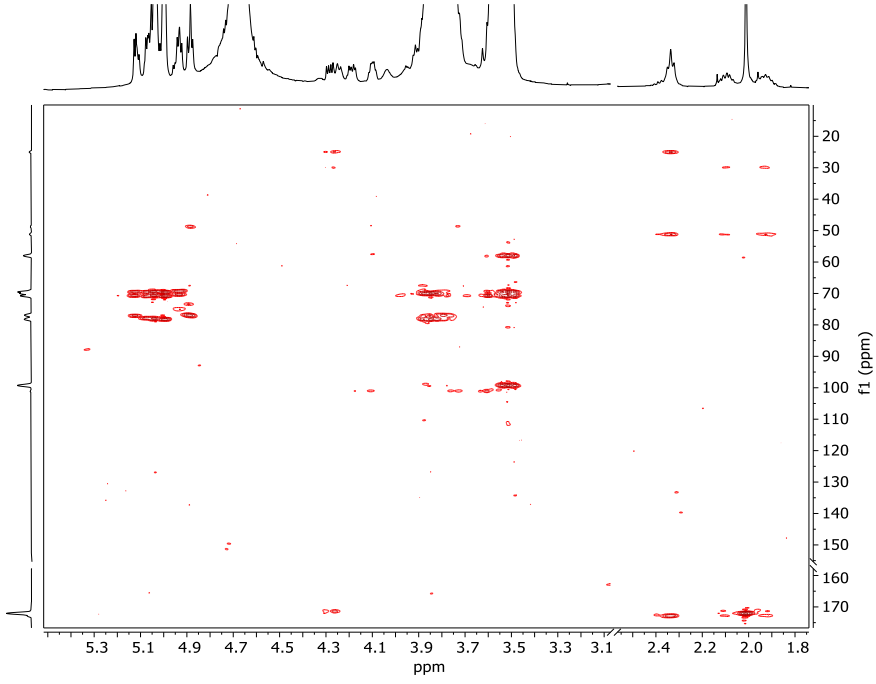

Figure S82. HMBC spectrum of γCyD2GluAc (D_2O, 500 MHz)

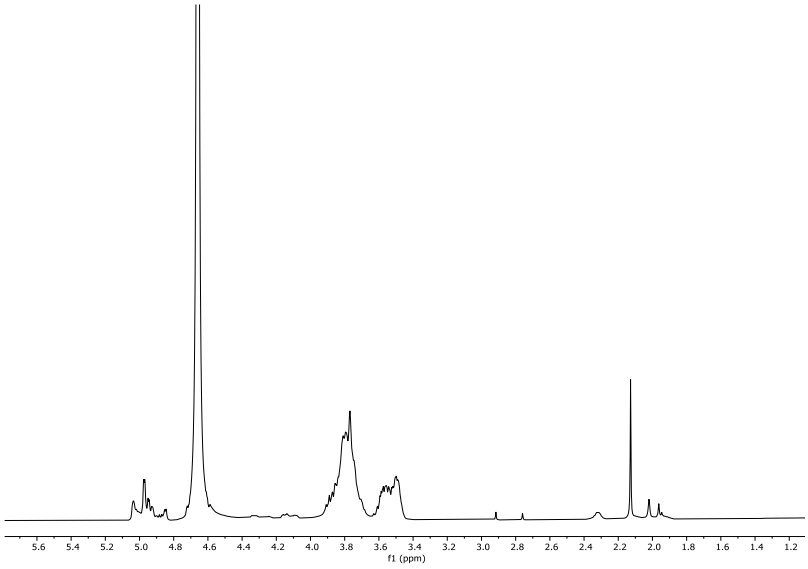

Figure S83. ^{1}H NMR spectrum of βCyD2GluAc (D2O, 500 MHz)

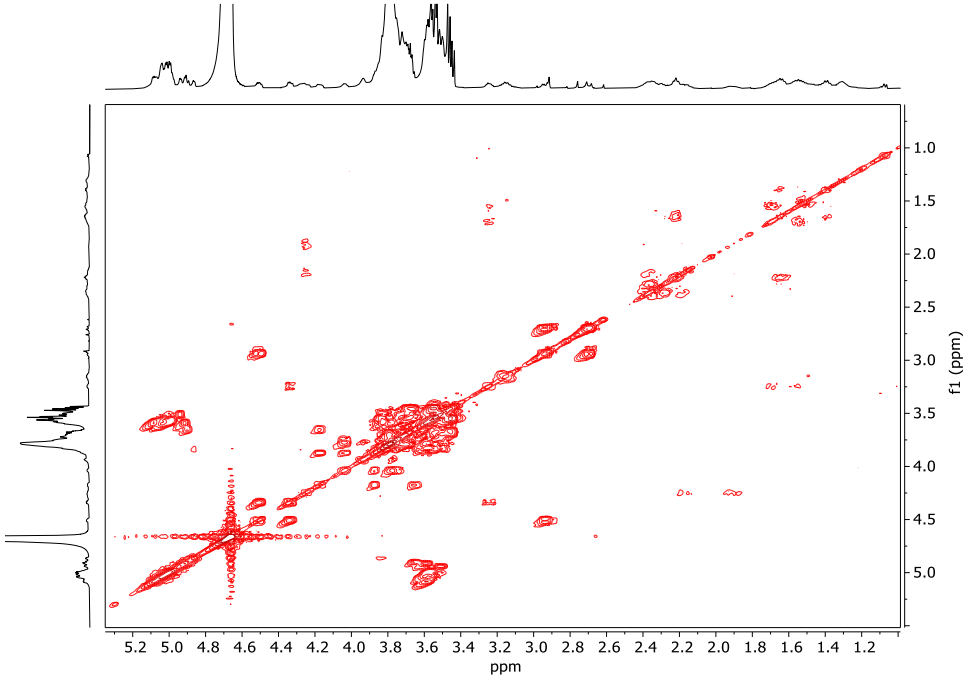

Figure S84. COSY spectrum of γCyD2GluBio (D_2O, 500 MHz)

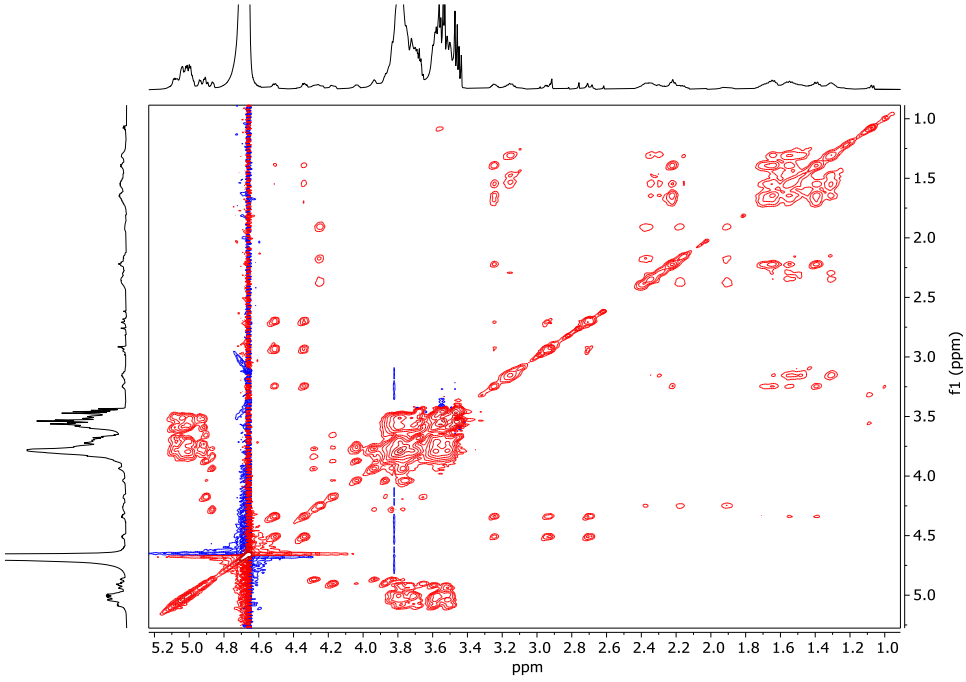

Figure S85. TOCSY spectrum of γCyD2GluBio (D_2O, 500 MHz)

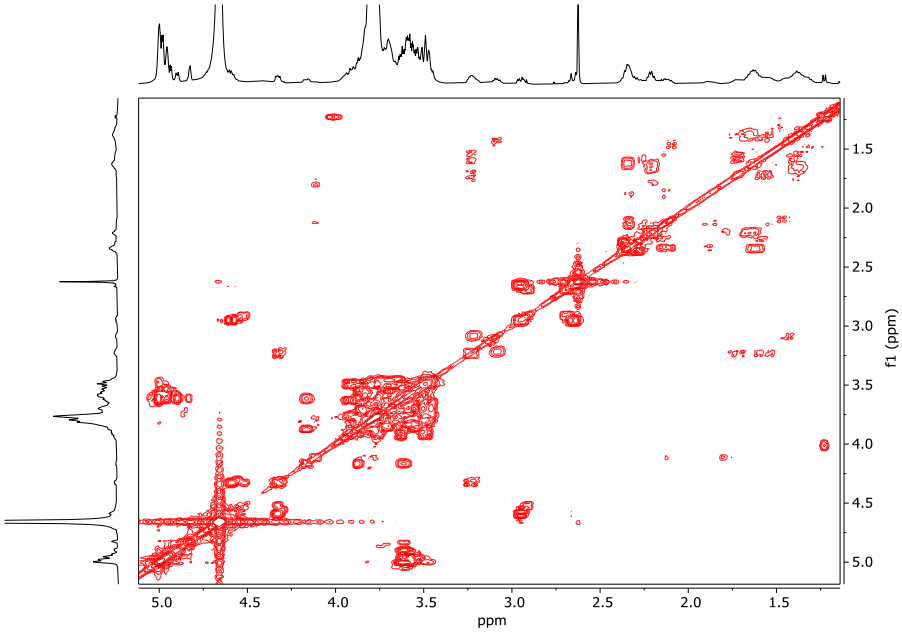

Figure S86. COSY spectrum of βCyD2GluBio (D_2O, 500 MHz)

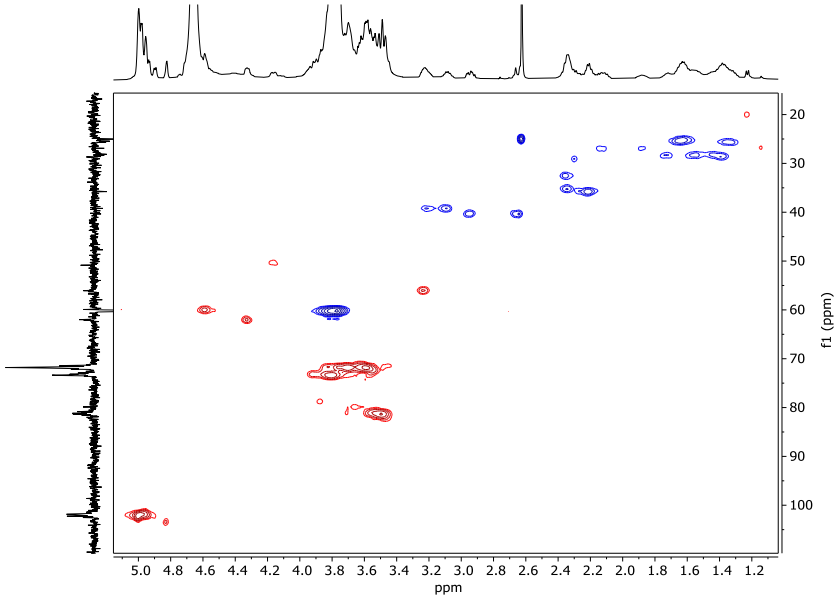

Figure S87. HSQC spectrum of γCyD2GluBio (D_2O, 500 MHz)

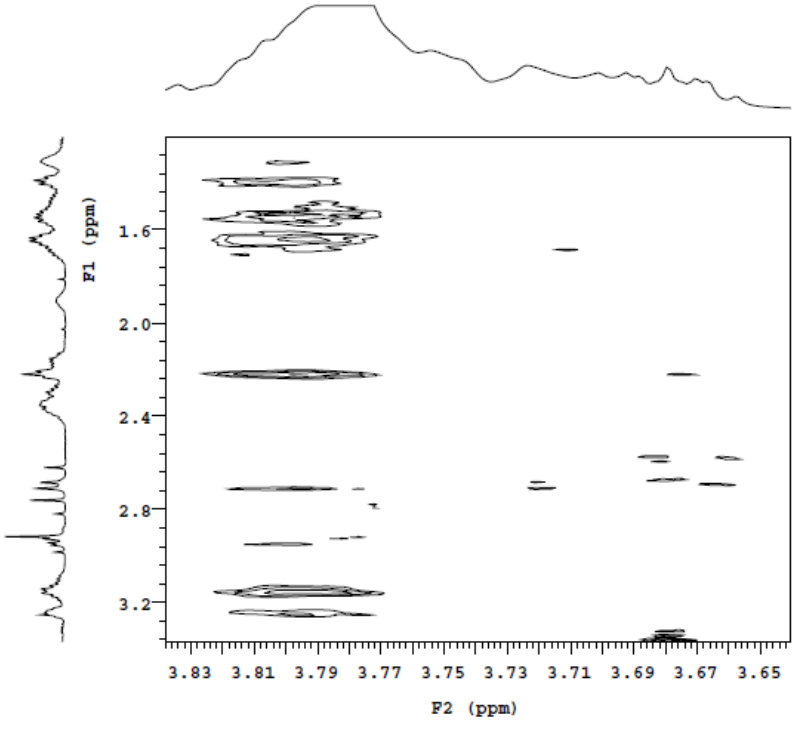

Figure S88. ROESY spectrum of γCyD2GluBio (D_2O, 500 MHz)

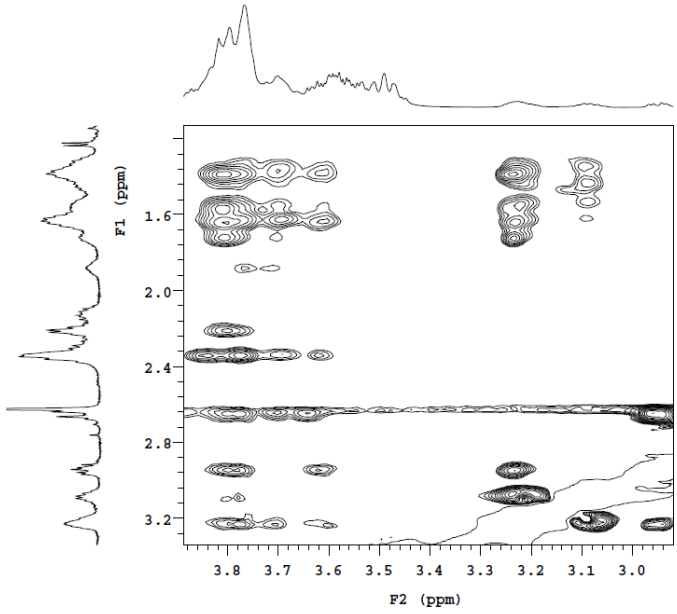

Figure S89. ROESY spectrum of βCyD2GluBio (D_2O, 500 MHz)

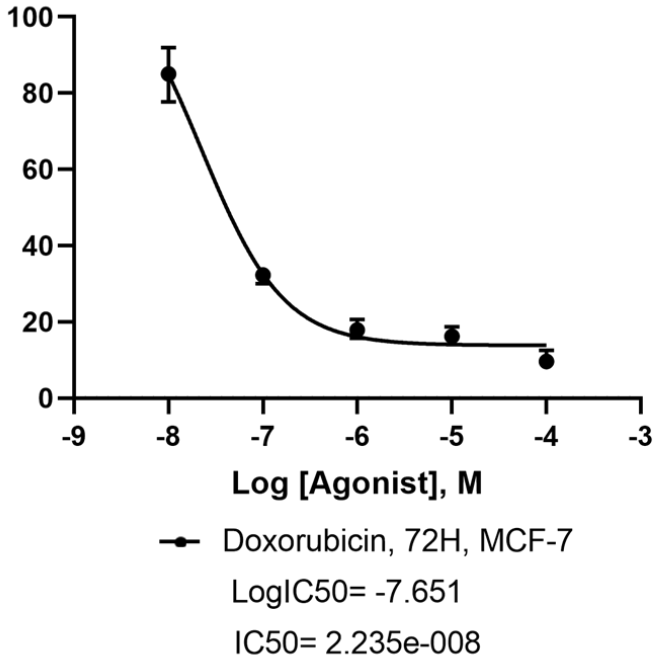

Figure S90. The dose-response curve was used to determine the half maximal inhibitory concentration (IC_{50}) of the drug (Dox) in MCF-7 cell line. The X values are the logarithms of molar concentration, the Y values show the responses.

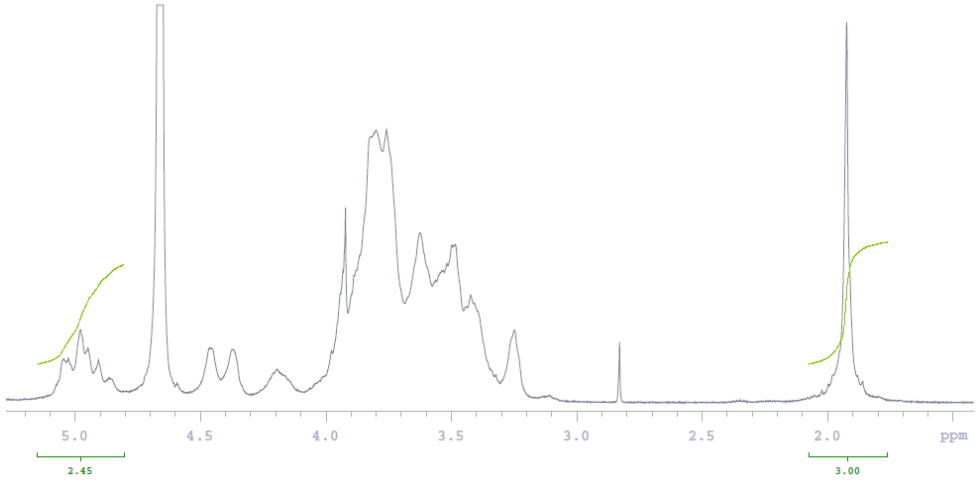

Figure S91. ^{1}H NMR spectrum of HALβCyD (D_2O, 500 MHz)

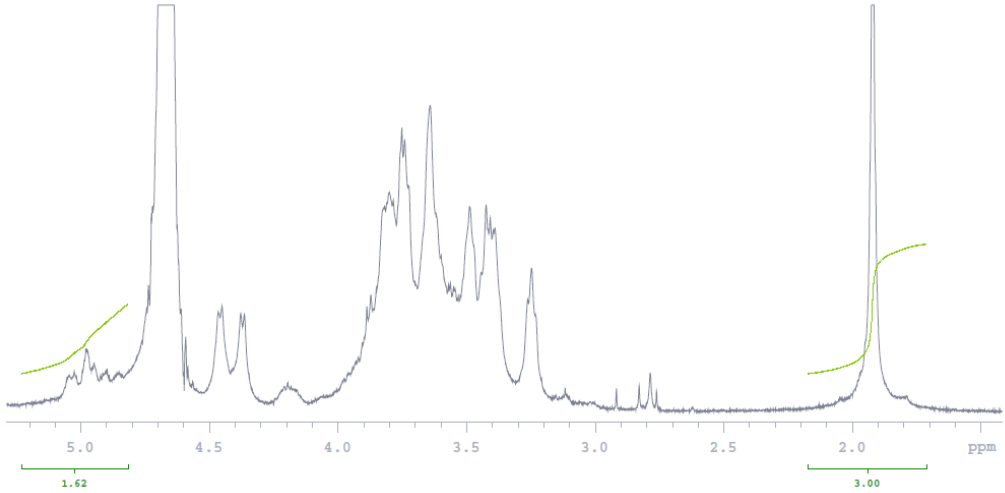

Figure S92. ^{1}H NMR spectrum of HAHβCyD (D_2O, 500 MHz)

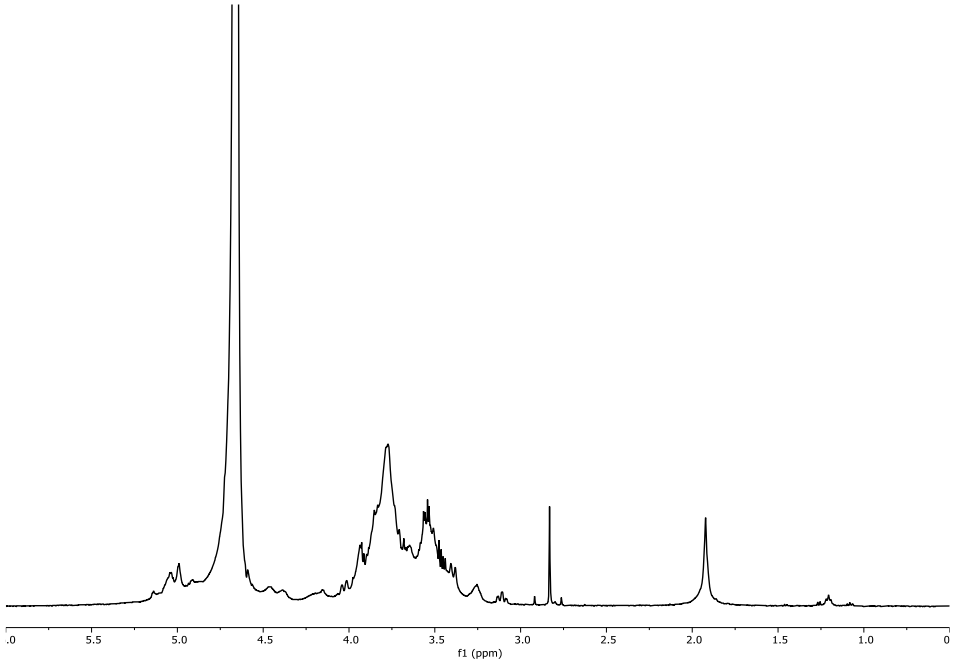

Figure S93. ^{1}H NMR spectrum of HAHγCyD (D_2O, 500 MHz)

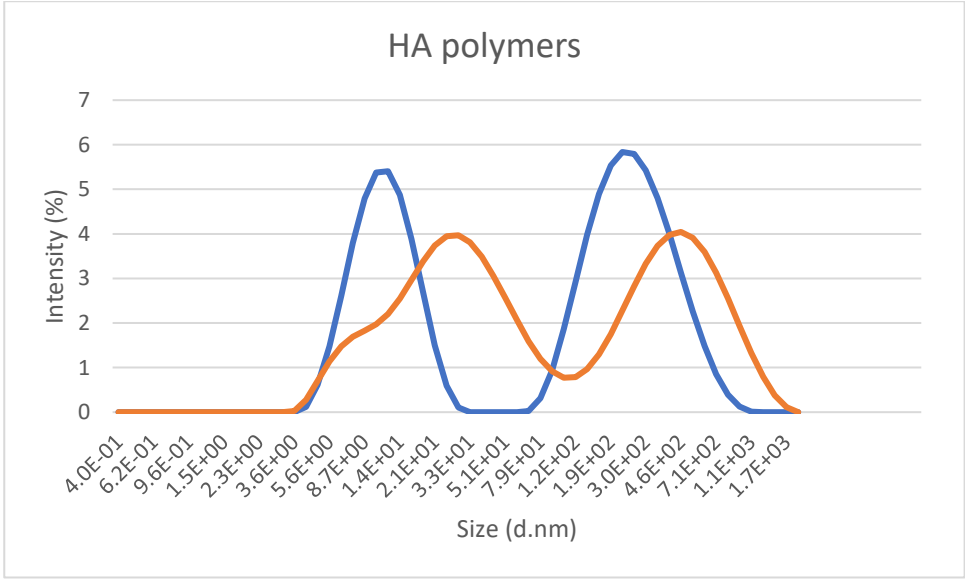

Figure S94. Size of HA polymers: HAH (orange), HAL (blue)

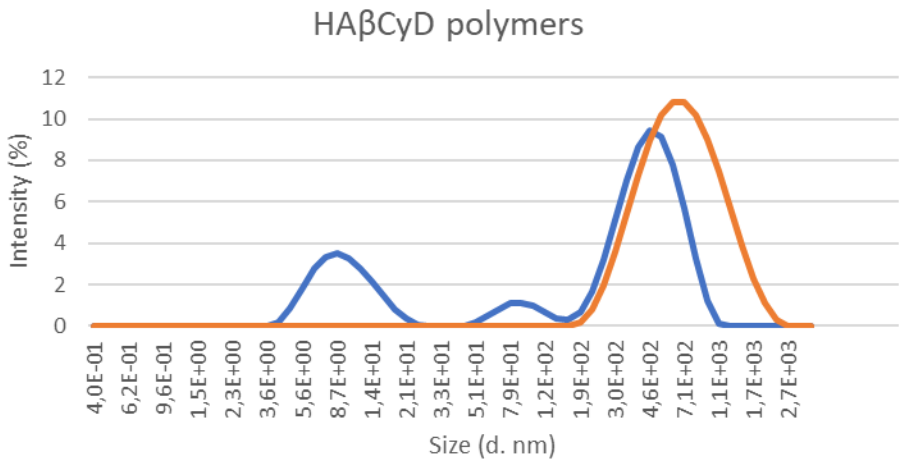

Figure S95. Size of HAHβCyD polymers: HAHβCyD (orange), HALβCyD (blue)

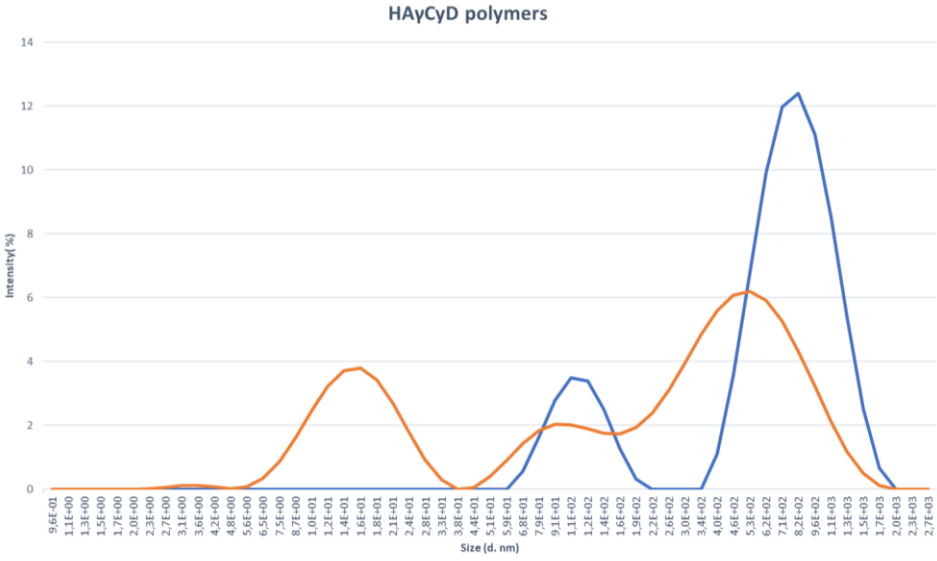

Figure S96. Size of HAHγCyD polymers: HALγCyD (orange), HAHγCyD (blue)

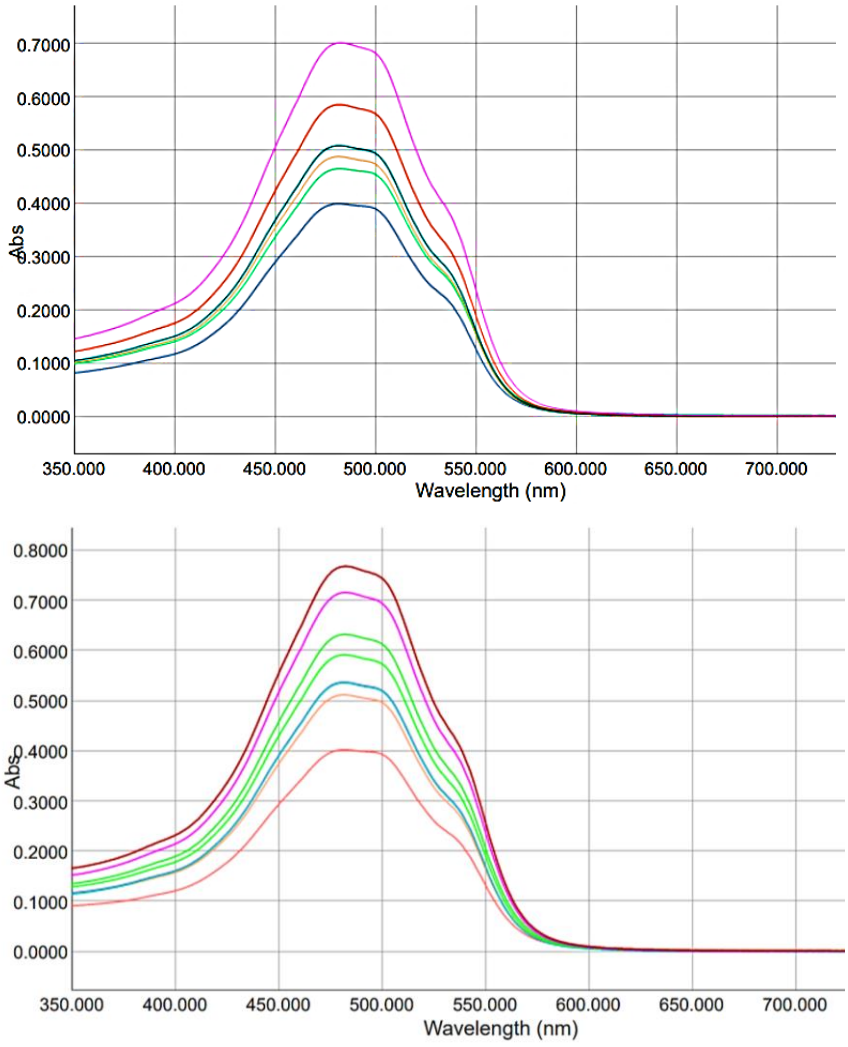

Figure S97. UV-vis spectra of saturated solution of Dox in the presence of an increasing concentration of the polymer: HALβCyD (Left) and HAHβCyD (right) at pH 7.4, phosphate buffer

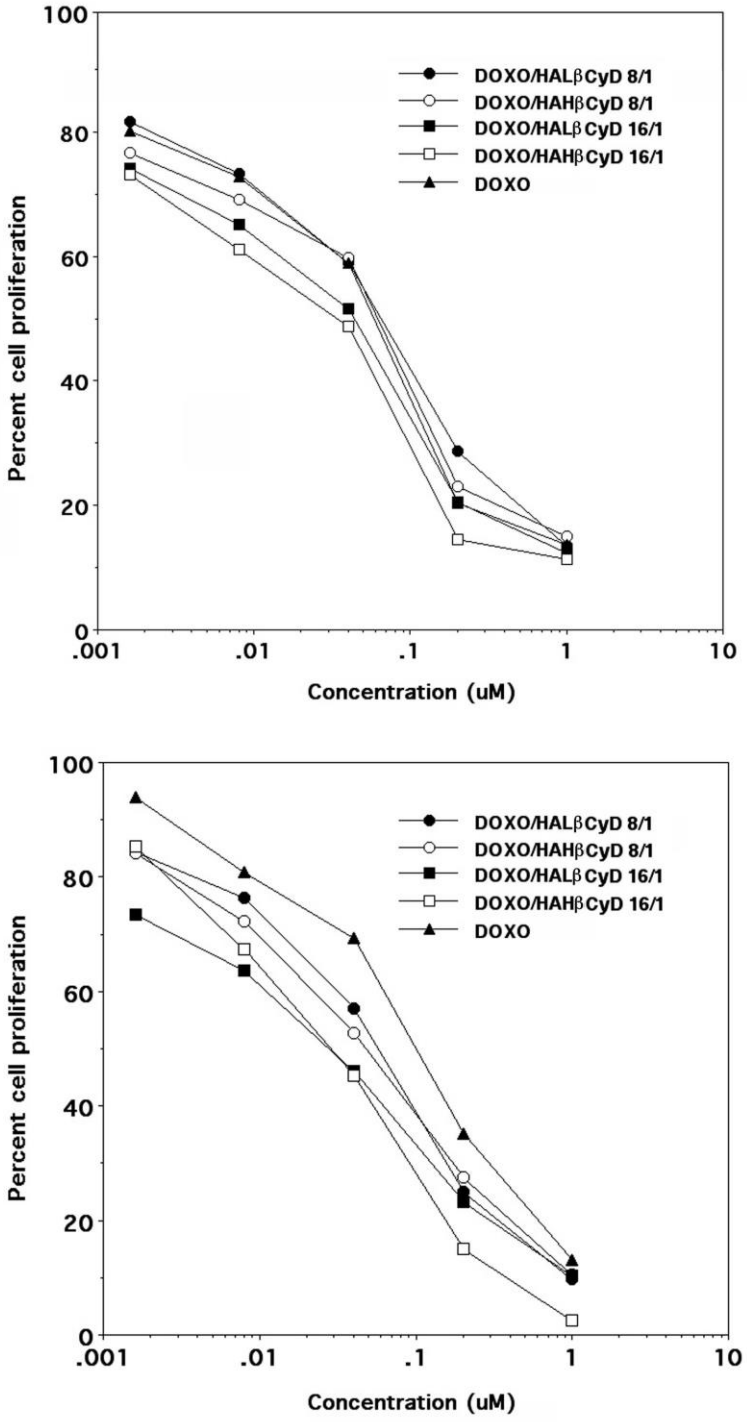

Figure S98. Graphs represent the mean dose-response curves of SK-N-SH (top) and SK-N-SH-PMA (bottom) cells treated with Dox or Dox/HALβCyD 8/1, Dox/HAHβCyD 8/1, Dox/HALβCyD 16/1, and Dox/HAHβCyD 16/1 complexes.

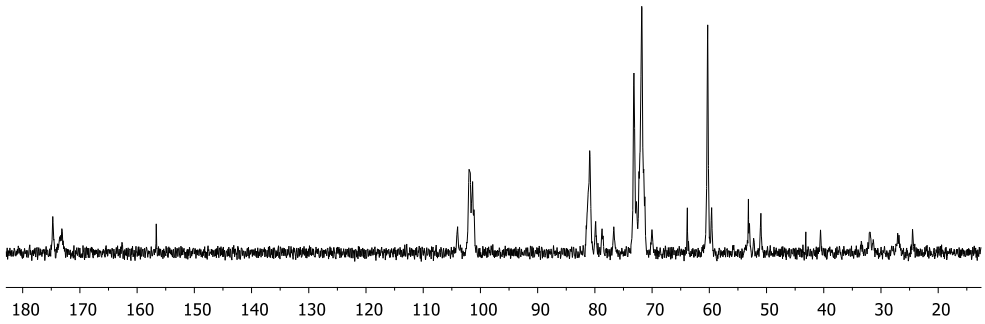

Figure S99. ^{13}C NMR spectrum of PGAβCyDArg1 (D_2O, 125 MHz)

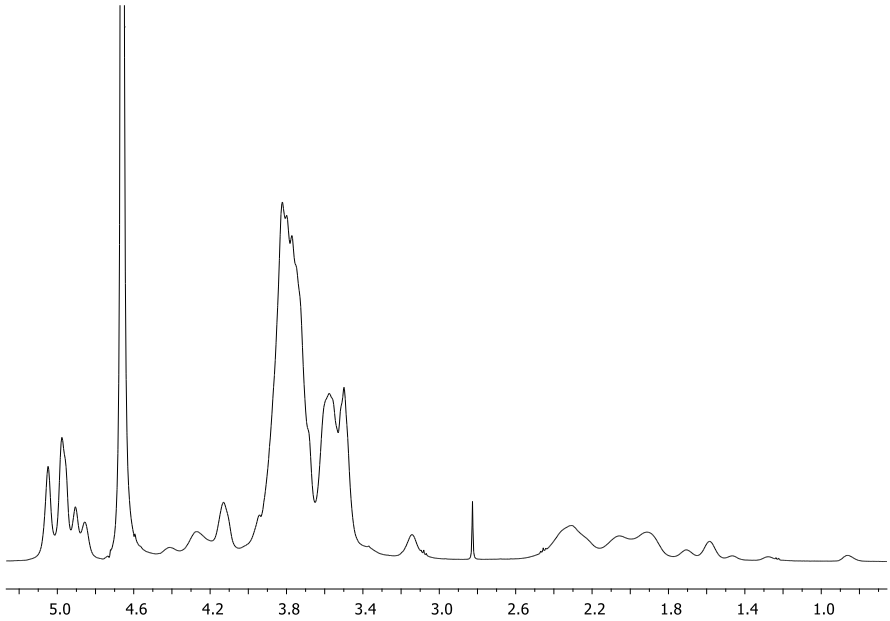

Figure S100. ^{1}H NMR spectrum of PGAβCyDArg2 (D_2O, 500 MHz)

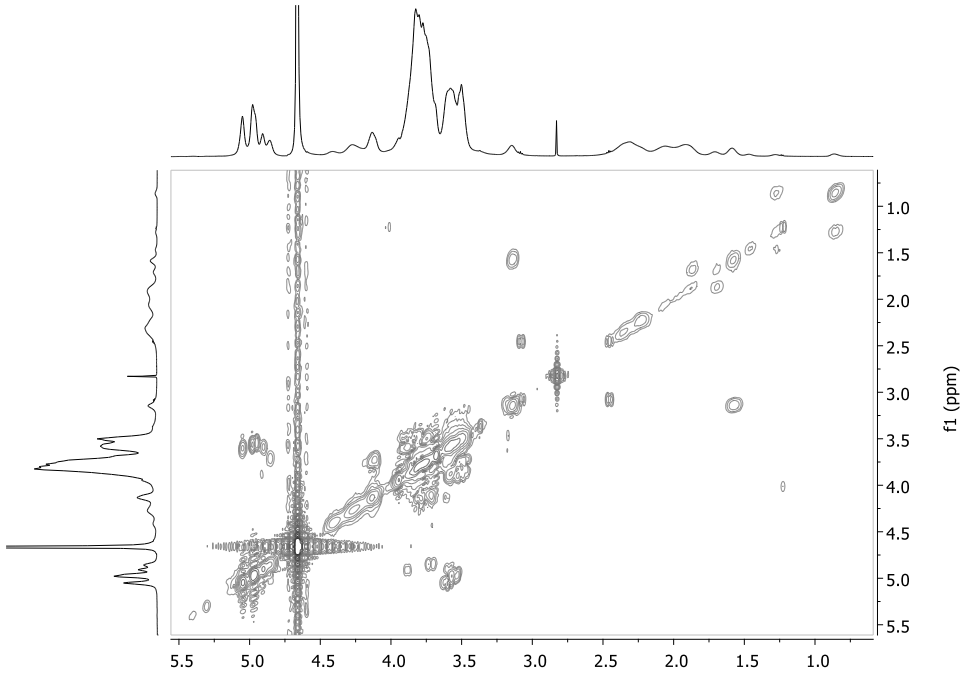

Figure S101. COSY spectrum of PGAβCyDArg2 (D_2O, 500 MHz)

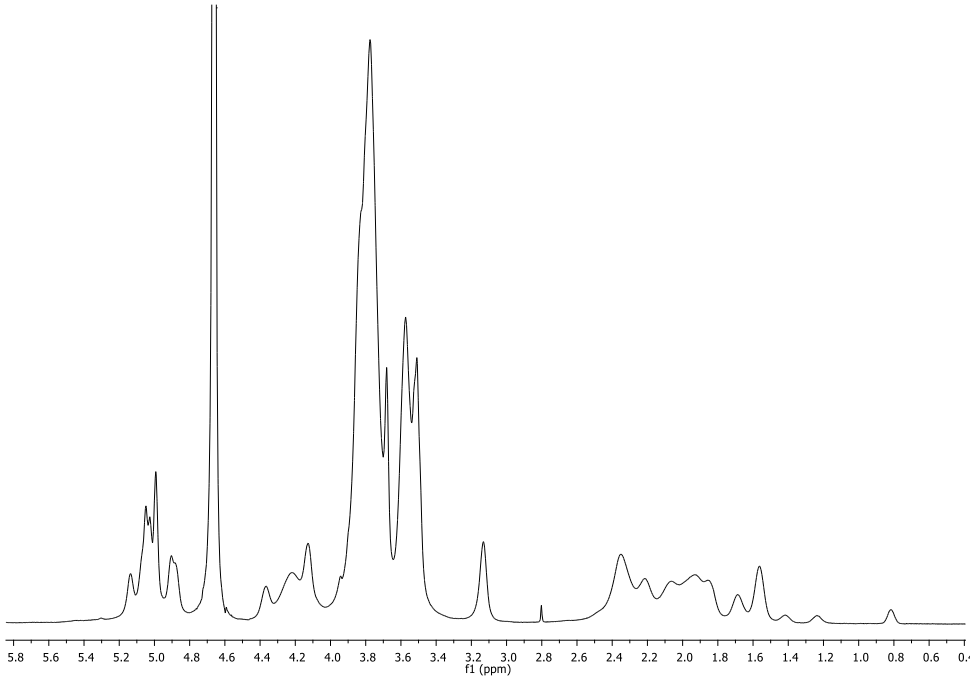

Figure S102. ^1H NMR spectrum of PGAγCyDArg3 (D_2O, 500 MHz)

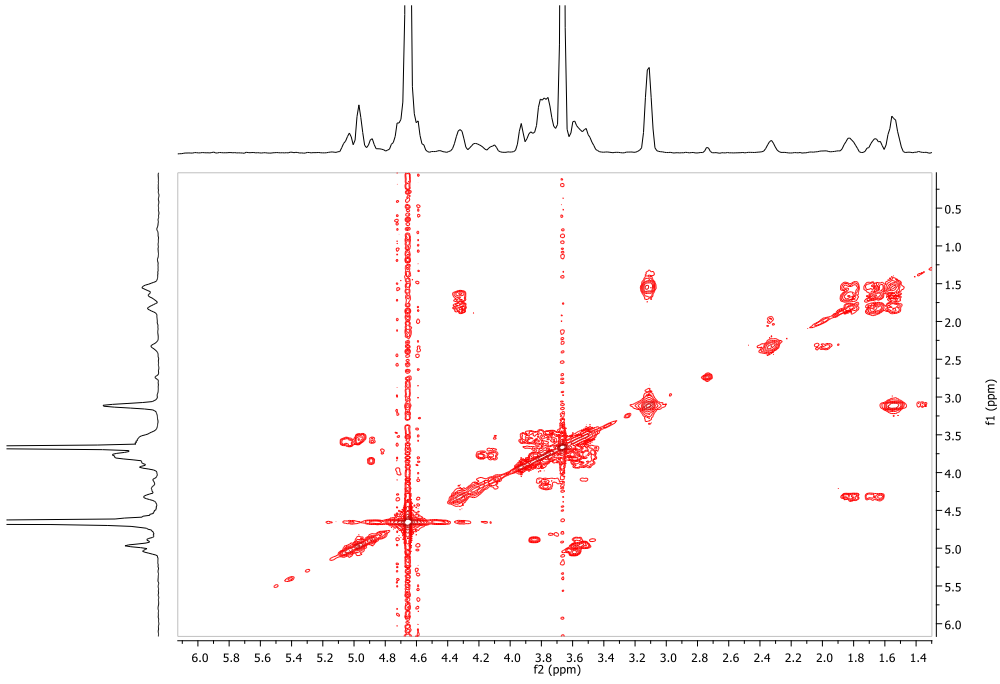

Figure S103. COSY spectrum of PGAβCyDArg4 (D_2O, 500 MHz)

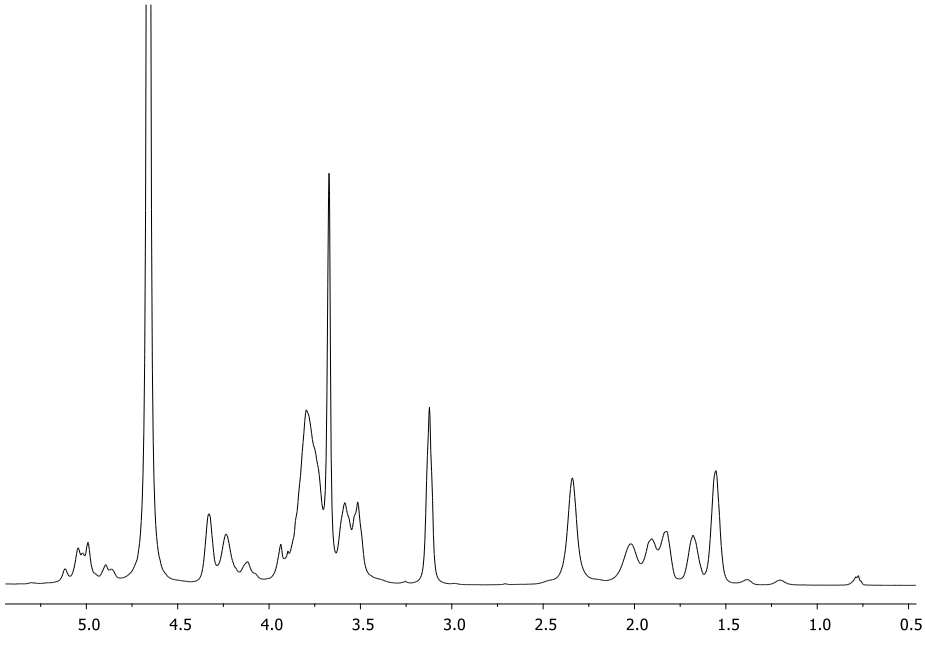

Figure S104. ^{1}H NMR spectrum of PGAγCyDArg5 (D_2O, 500 MHz)

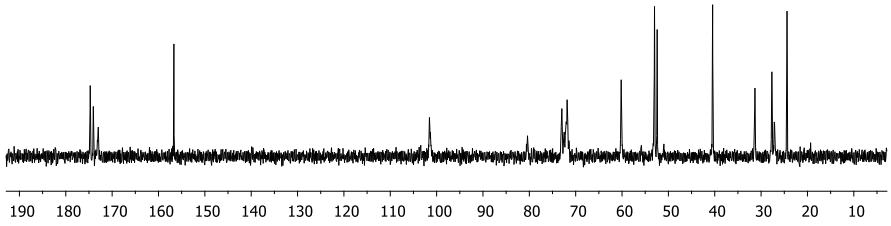

Figure S105. ^{13}C NMR spectrum of PGAγCyDArg5 (D_2O, 125 MHz)

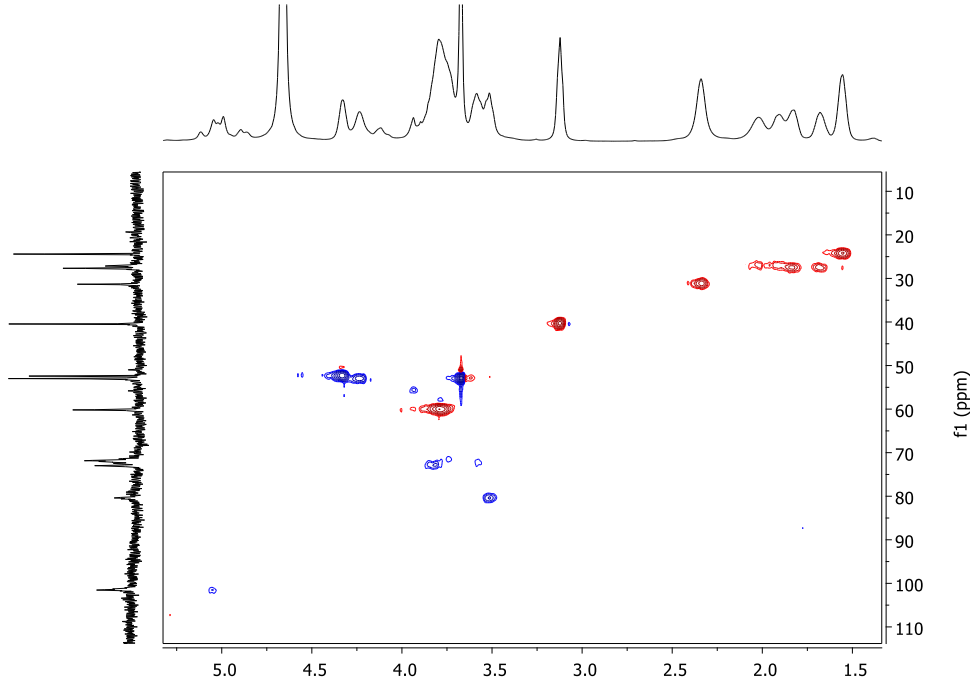

Figure S106. HSQC spectrum of PGAγCyDArg5 (D_2O, 500 MHz)

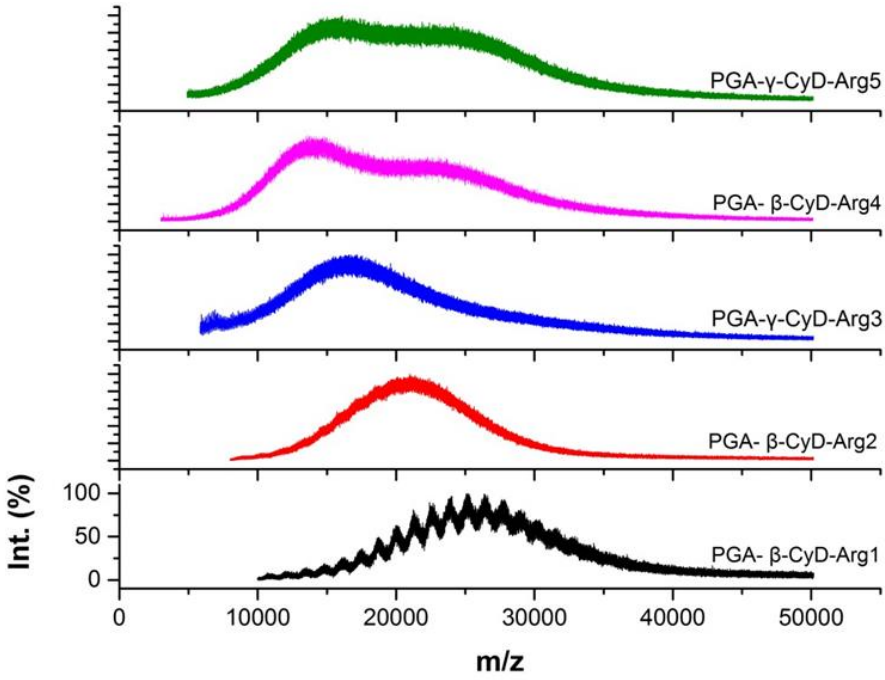

Figure S107. MALDI-TOF MS spectra of the PGAβCyDArg polymers

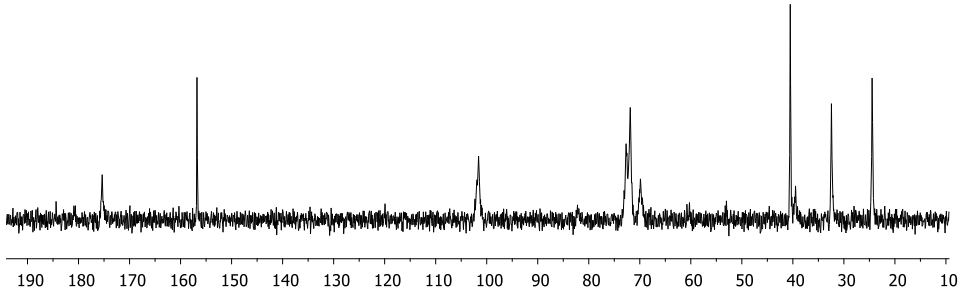

Figure S108. ^{13}C NMR spectrum of PGAβCyDGBA (D_2O, 125 MHz)

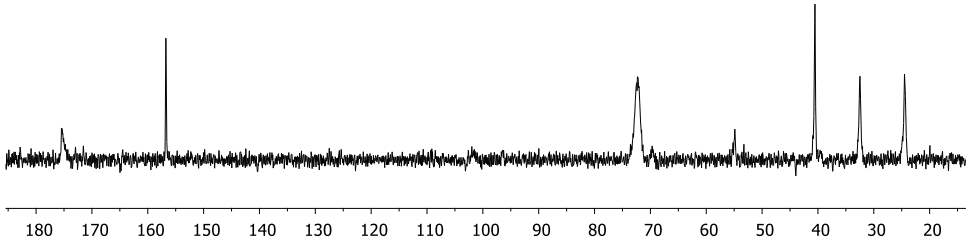

Figure S109. ^{13}C NMR spectrum of PGAγCyDGBA (D_2O, 125 MHz)

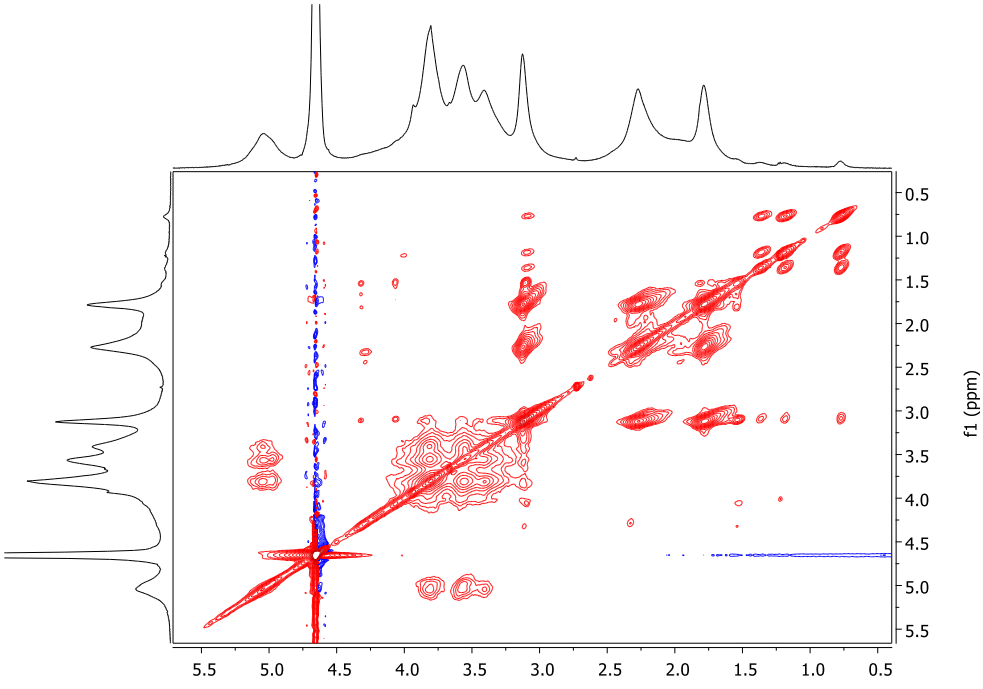

Figure S110. TOCSY NMR spectrum of PGAγCyDGBA (D_2O, 500 MHz)

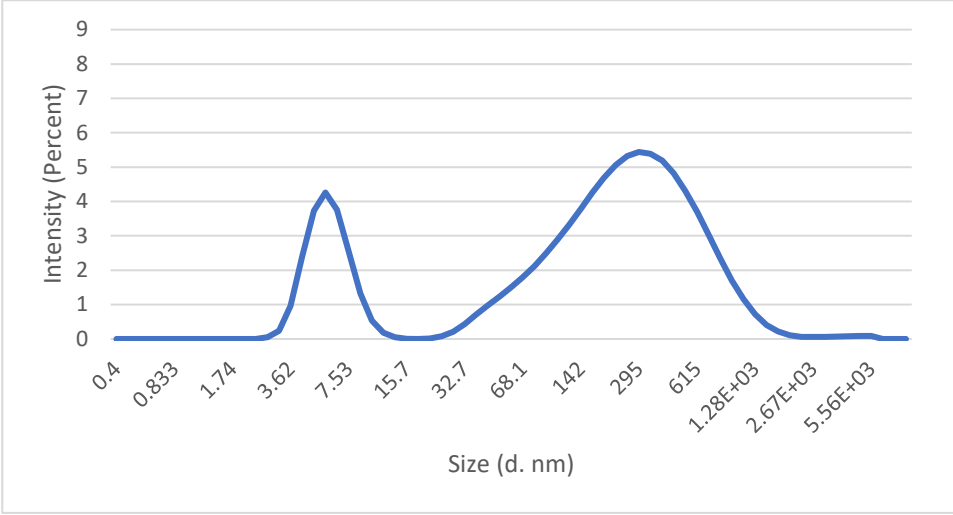

Figure S111. Intensity Size Distribution (DLS) of PGAβCyDArg1

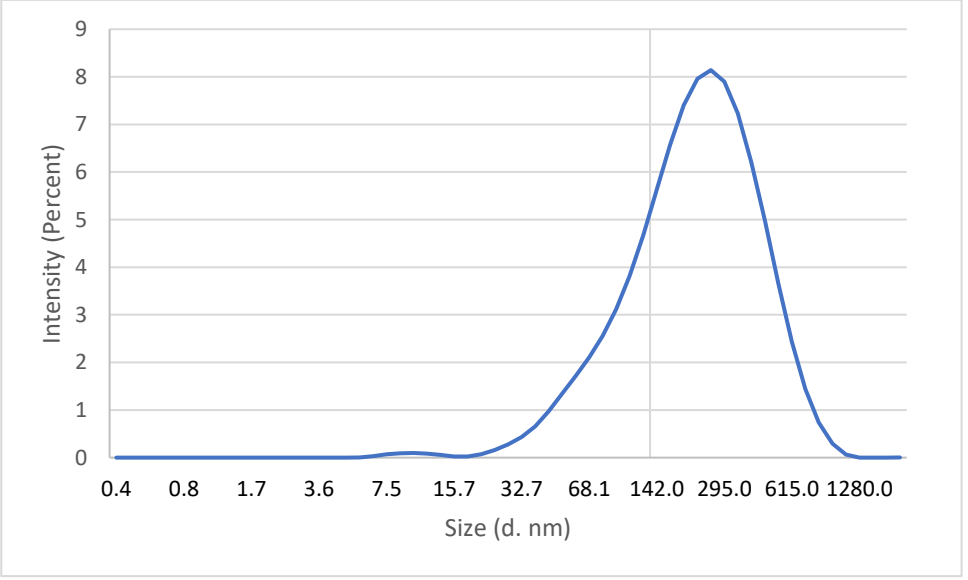

Figure S112. Intensity Size Distribution (DLS) of PGAβCyDGBA6

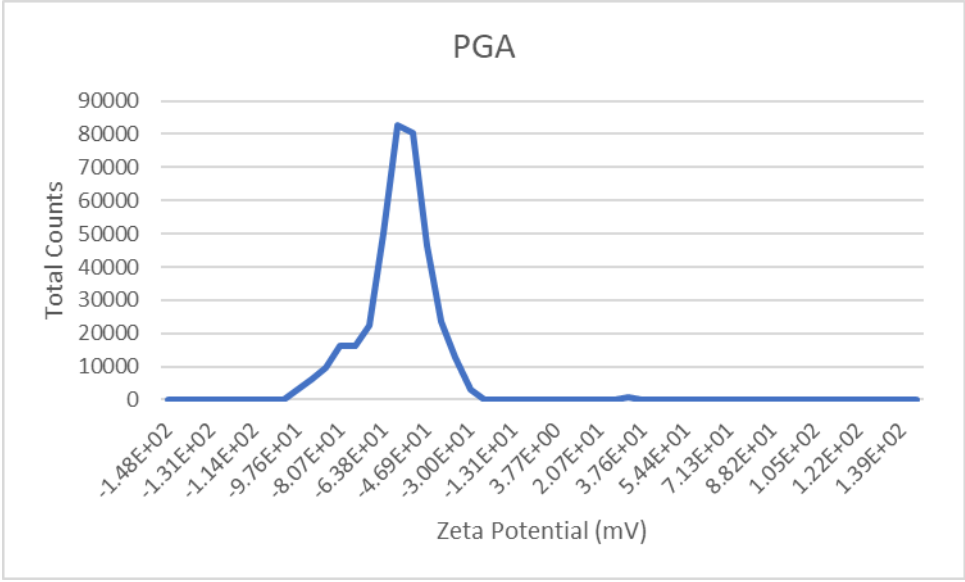

Figure S113. Zeta Potential (mV) of PGA

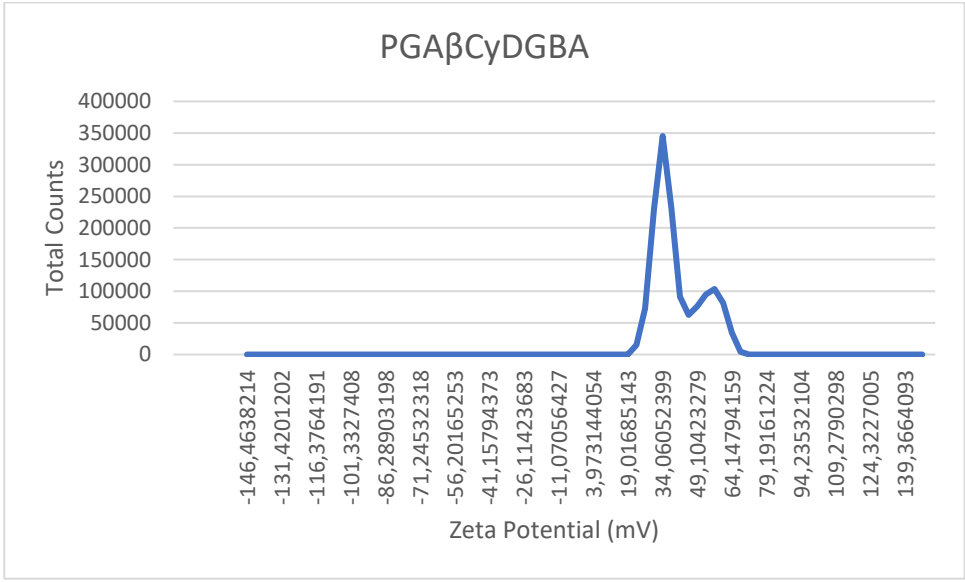

Figure S114. Zeta Potential (mV) of PGAβCyDGBA

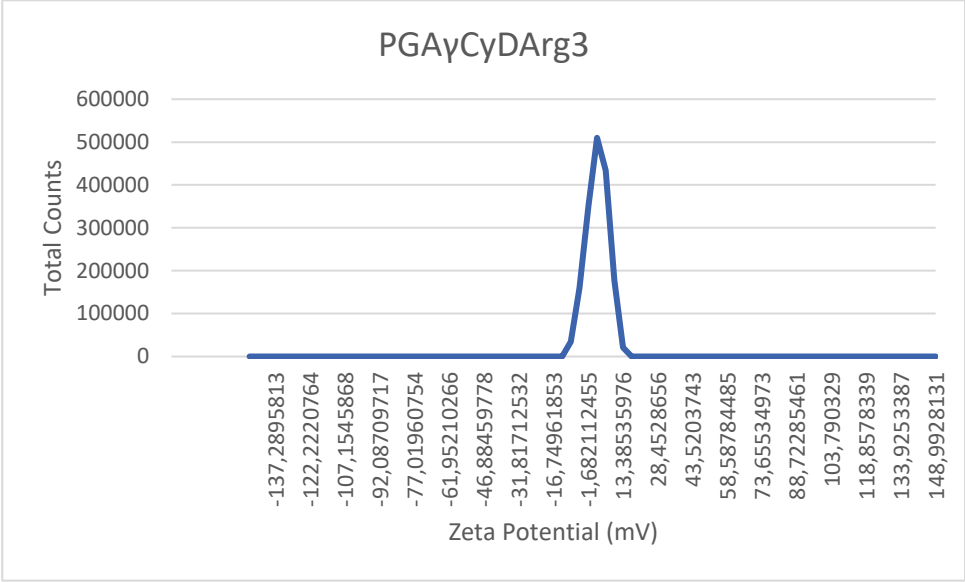

Figure S115. Zeta Potential (mV) of PGAγCyDArg3

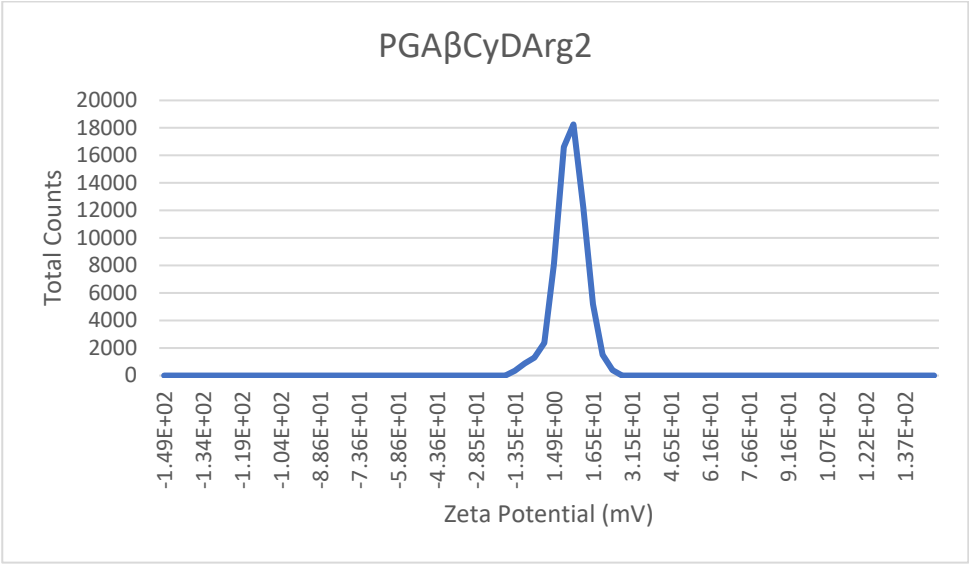

Figure S116. Zeta Potential (mV) of PGAβCyDArg2

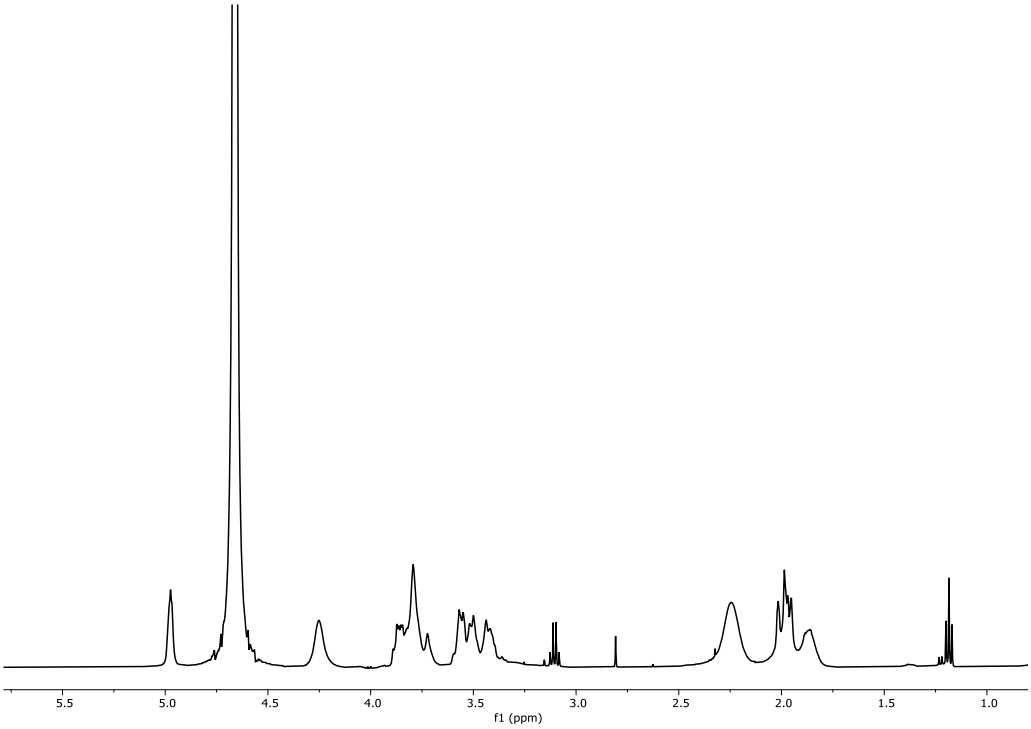

Figure S117. ^{1}H NMR spectrum of PGACyDPMOXA (D_2O, 500MHz)

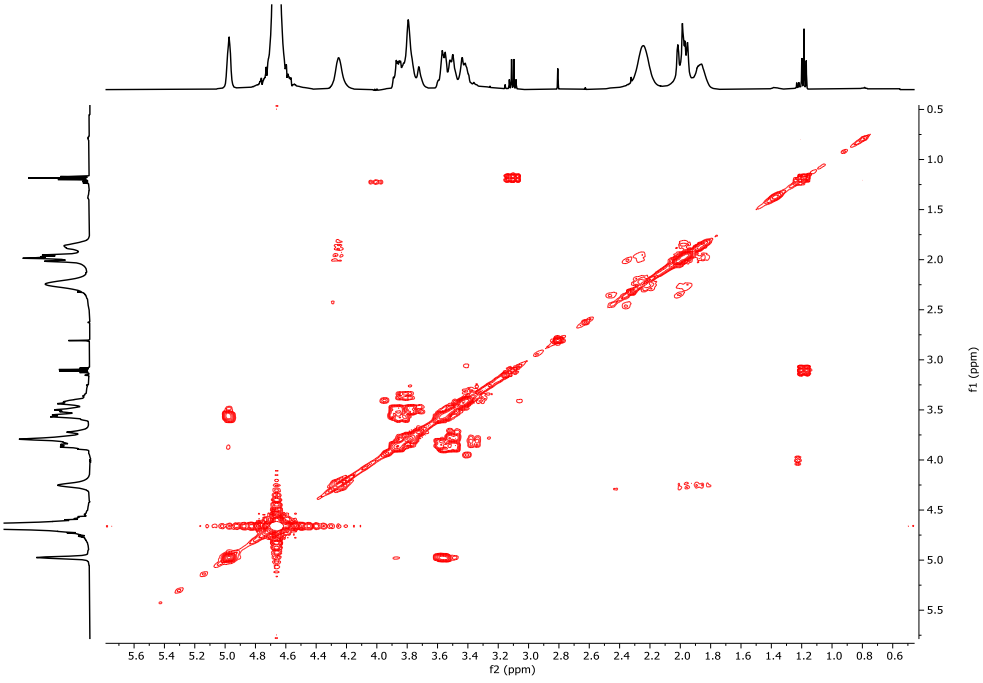

Figure S118. COSY spectrum PGACyDPMOXA (D_2O, 500 MHz)

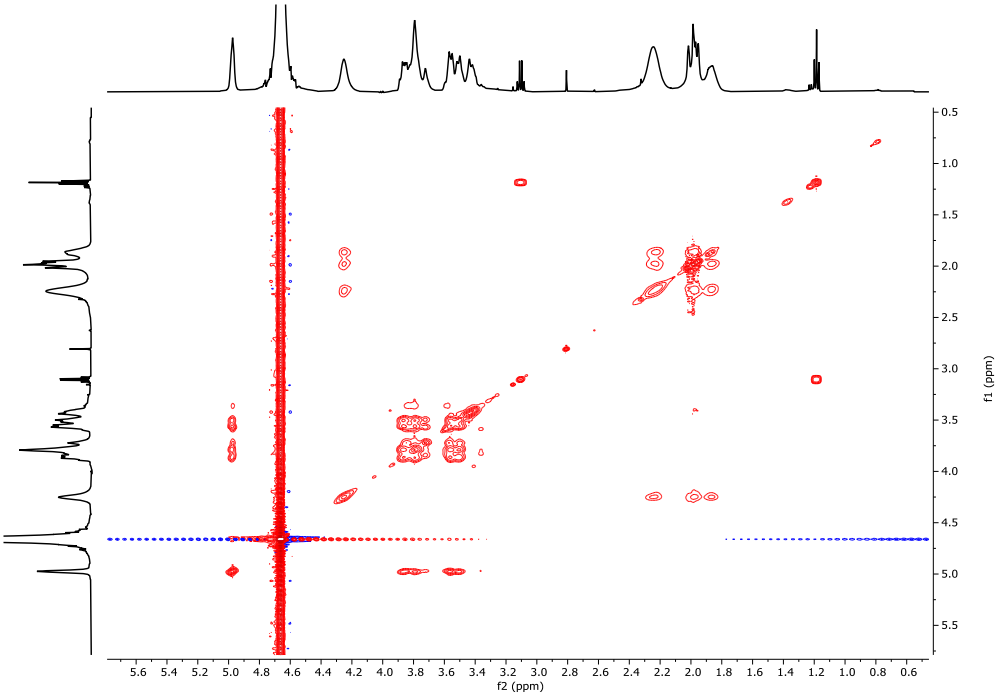

Figure S119. TOCSY spectrum PGACyDPMOXA (D_2O, 500 MHz)

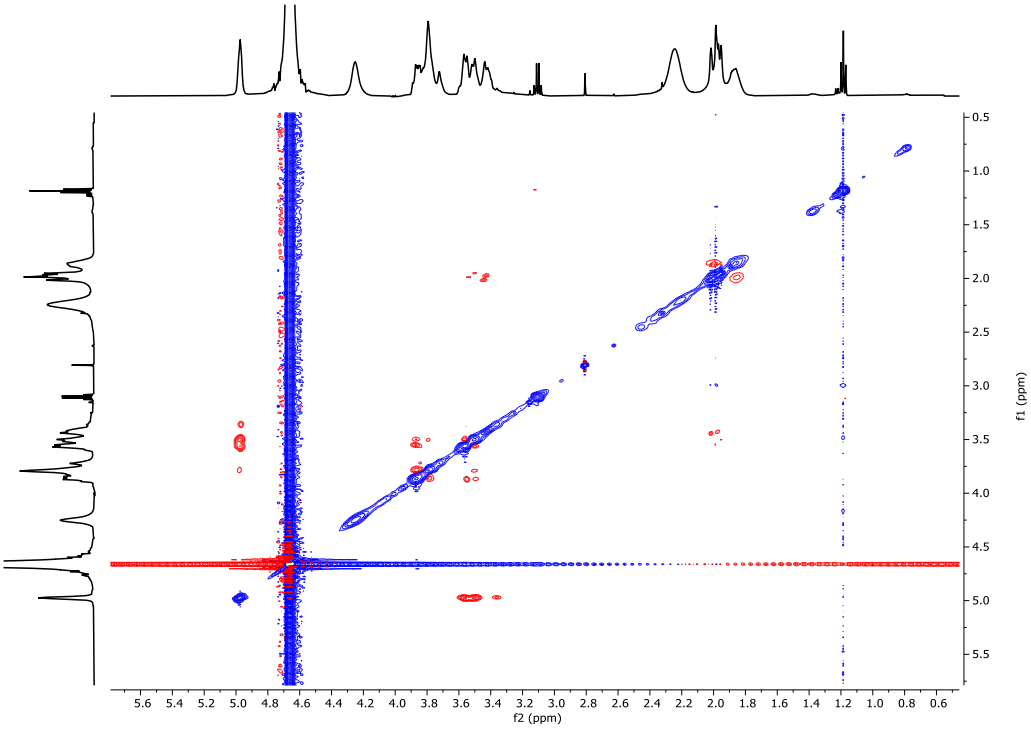

Figure S120. ROESY spectrum PGACyDPMOXA (D_2O, 500 MHz)

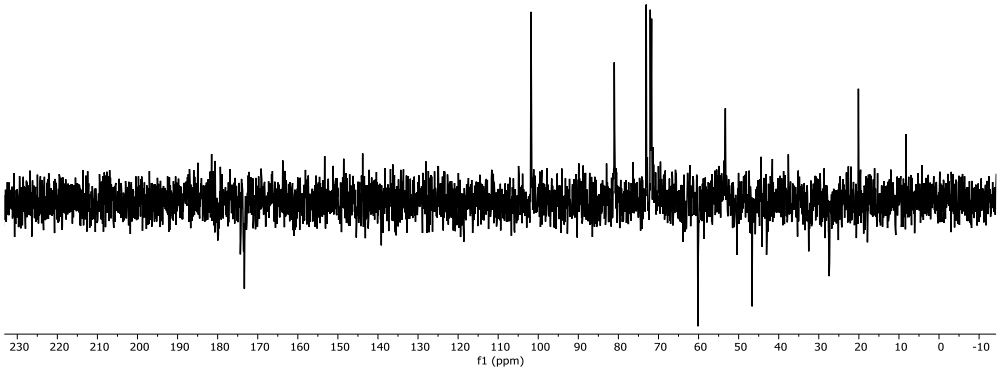

Figure S121. ^{13}C APT NMR spectrum of PGACyDPMOXA (D_2O, 125 MHz)

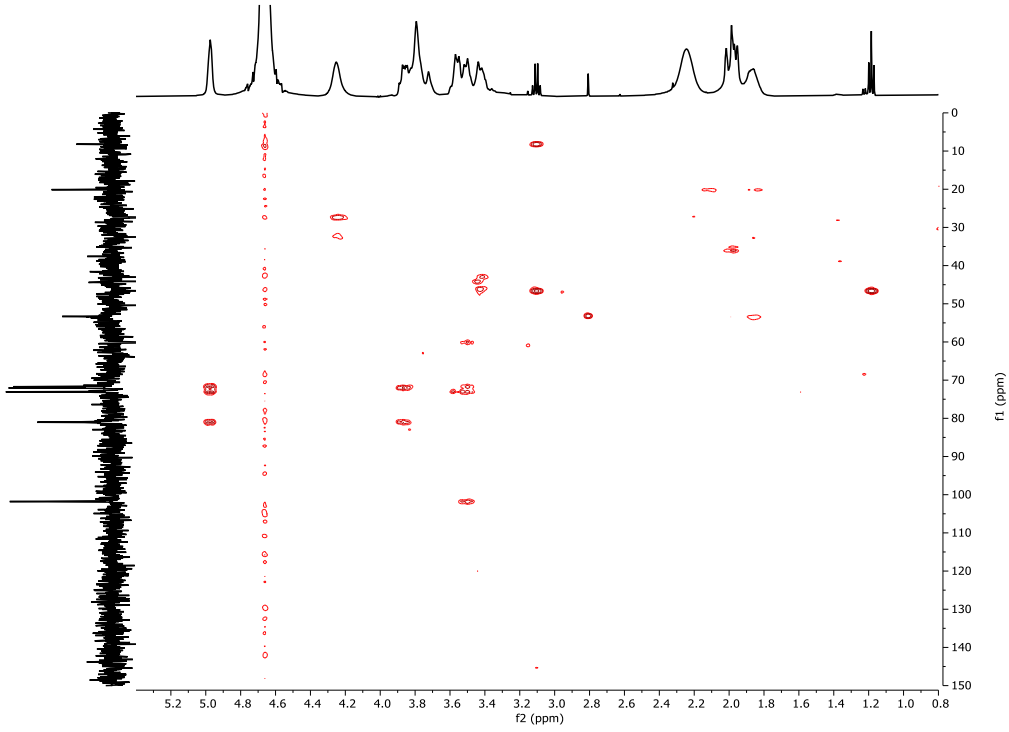

Figure S122. HMBC spectrum of PGACyDPMOXA (D_2O, 500 MHz)

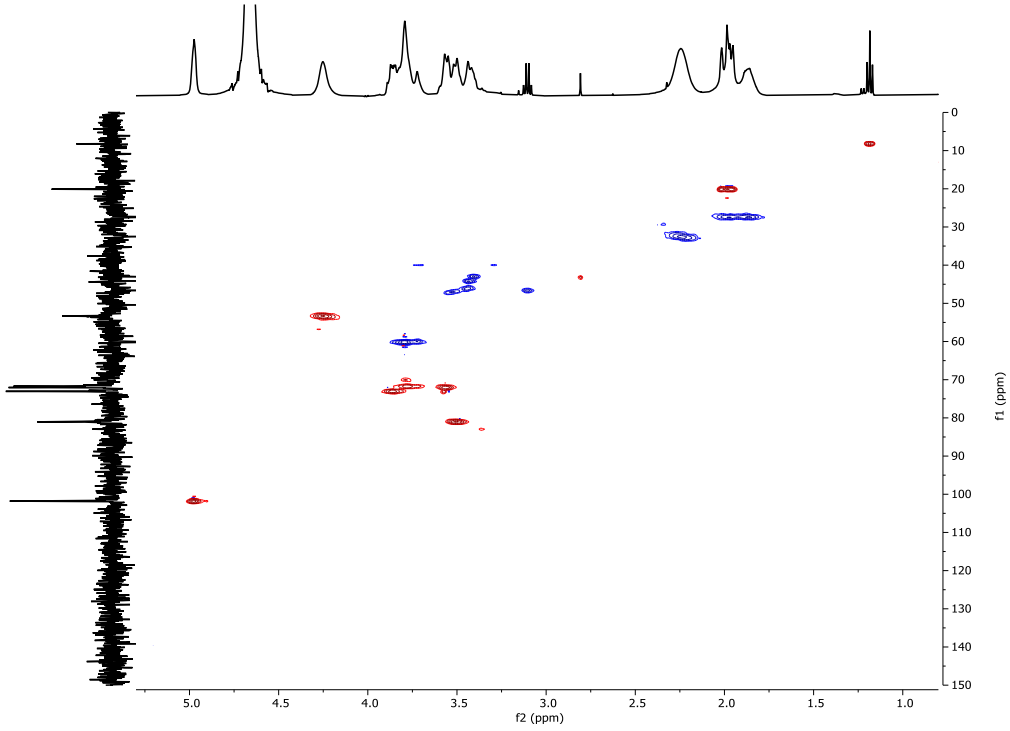

Figure S123. HSQC spectrum PGACyDPMOXA (D_2O, 500 MHz)

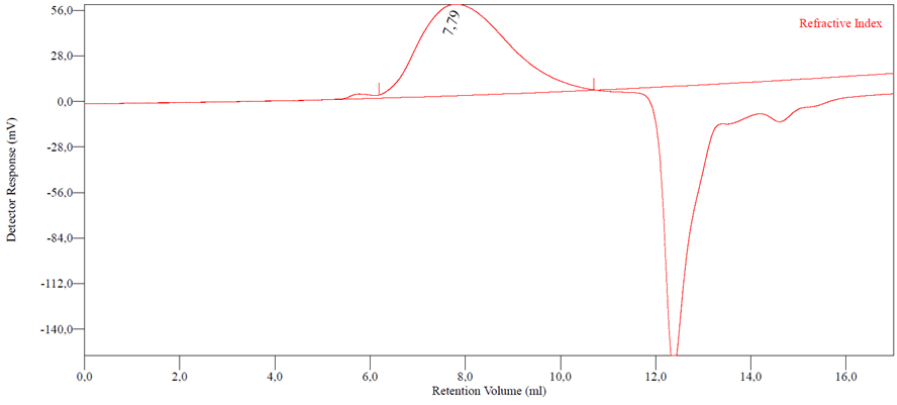

Figure S124. GPC of PMOXA

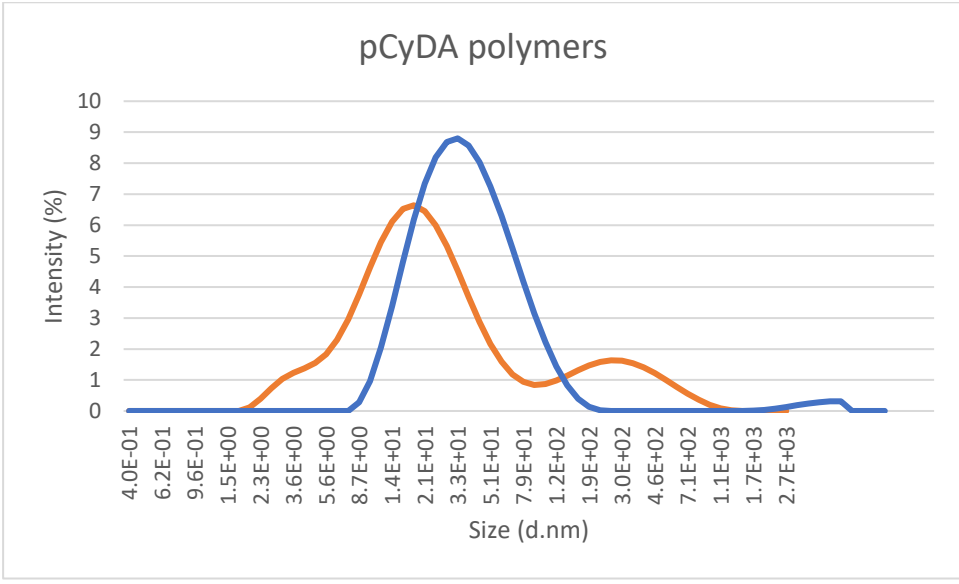

Figure S125. Intensity Size Distribution (DLS) of pCyDA polymers: pβCyD (blue), pγCyD (orange)

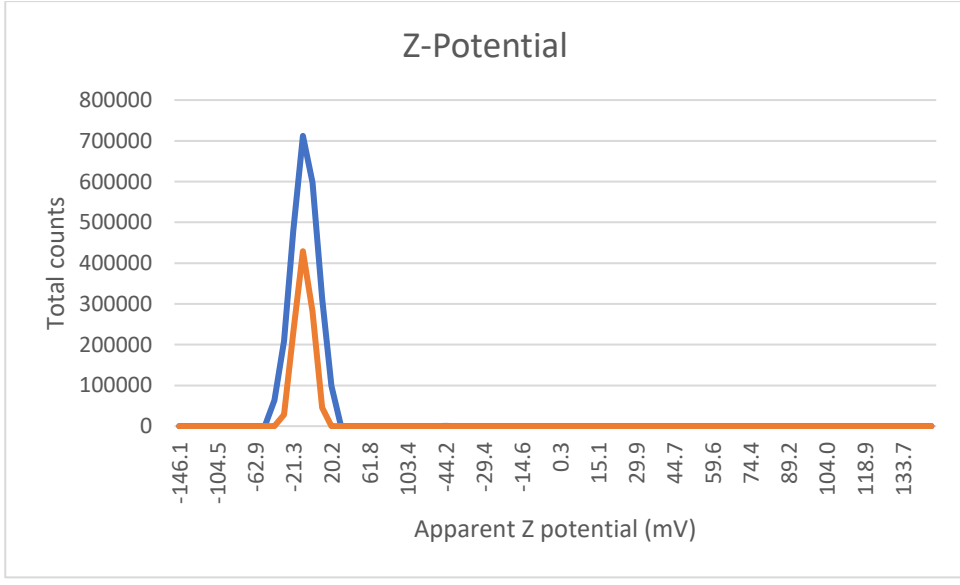

Figure S126. Z-potential (mV) of polymers: pβCyDA (blue), pγCyDA (orange)

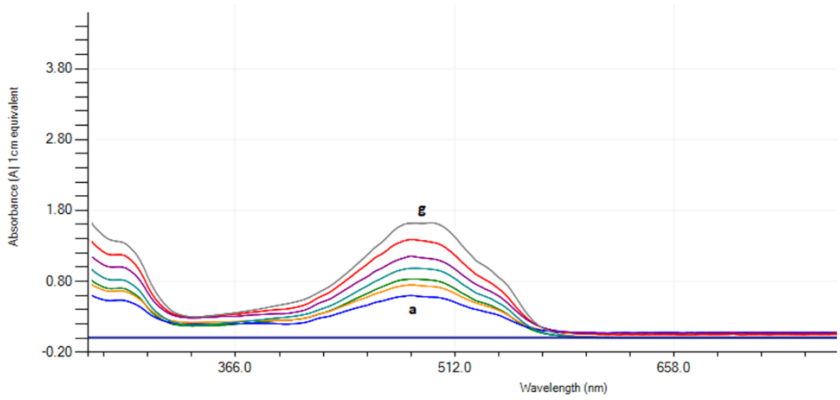

Figure S127. UV-vis spectra of Dox-pγCyDA (from a to g: free Dox to Dox with 8 mg/mL of pγCyDA)

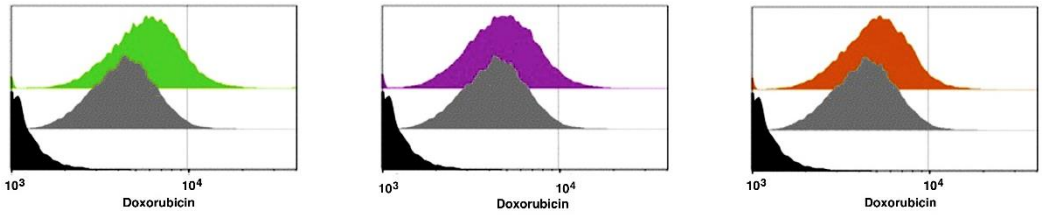

Figure S128. Representative experiment of Dox accumulation in HepG2 cells. Black histograms, control; dark gray histograms, Dox; colored histograms, as indicated below each box.

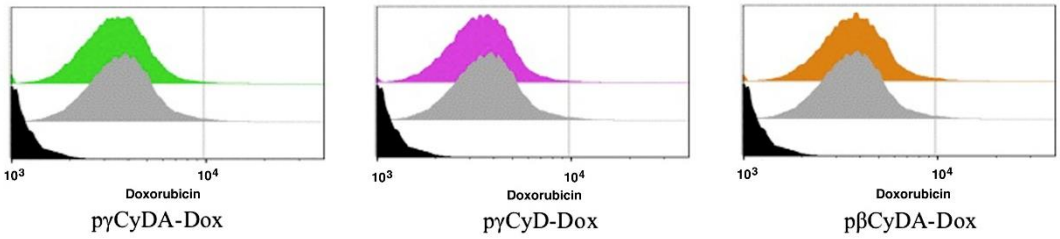

Figure S129. Representative experiment of Dox accumulation in A5492 cells. Black histograms, control; dark gray histograms, Dox; colored histograms, as indicated below each box.

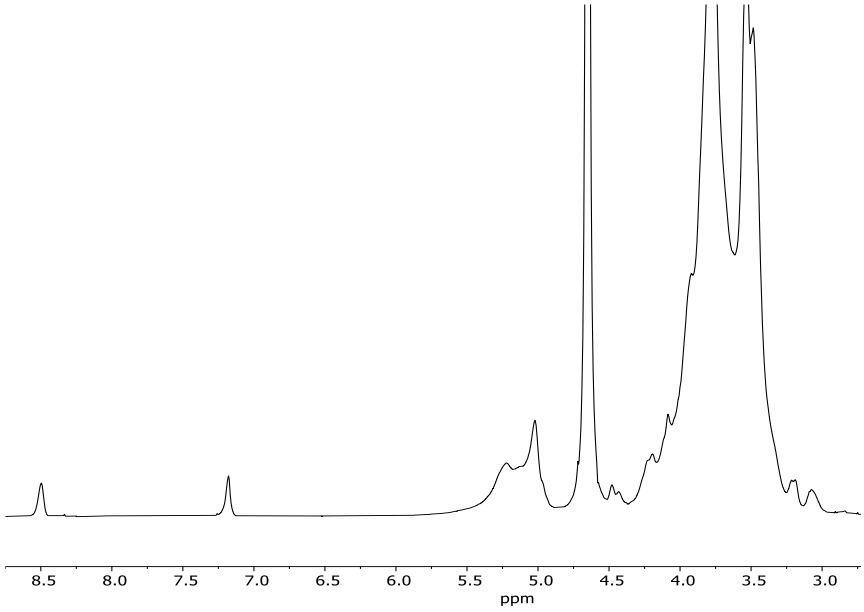

Figure S130. ^{1}H NMR spectrum of pγCyDHis (D_2O, 500MHz)

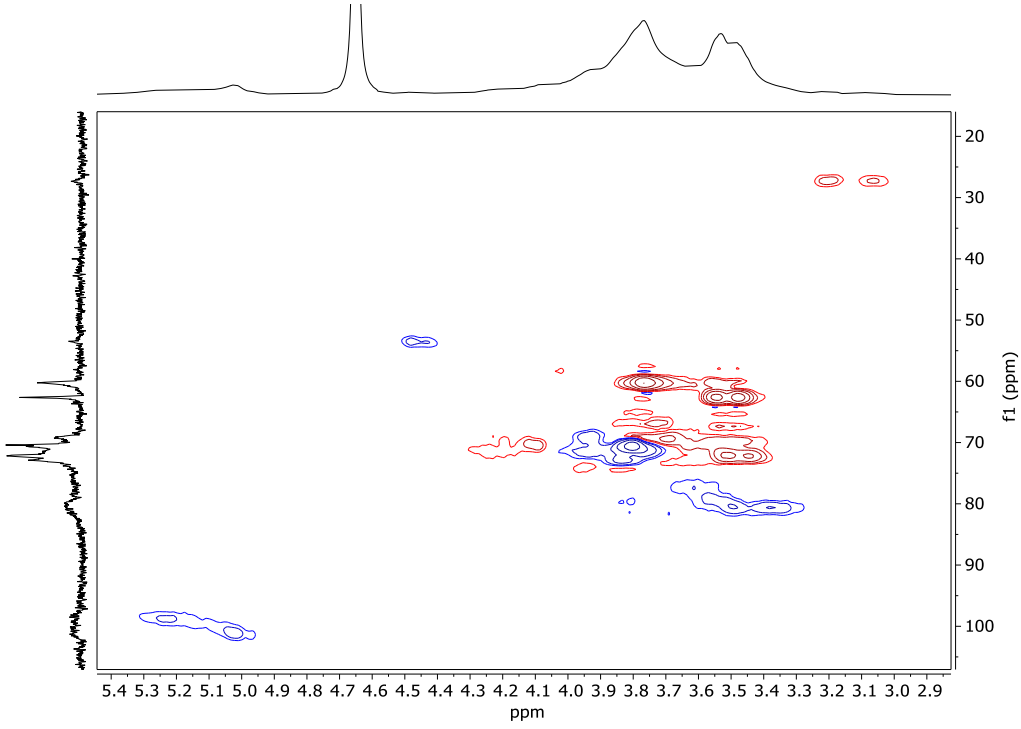

Figure S131. HSQC spectrum of pγCyDHis (D_2O, 500MHz)

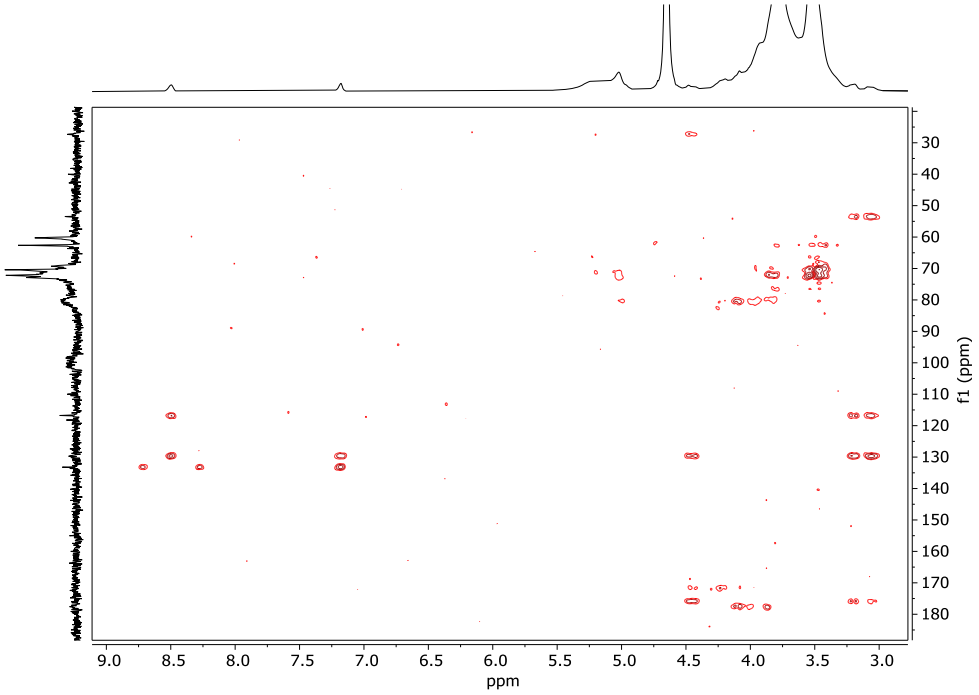

Figure S132. HMBC spectrum of pγCyDHis (D_2O, 500MHz)

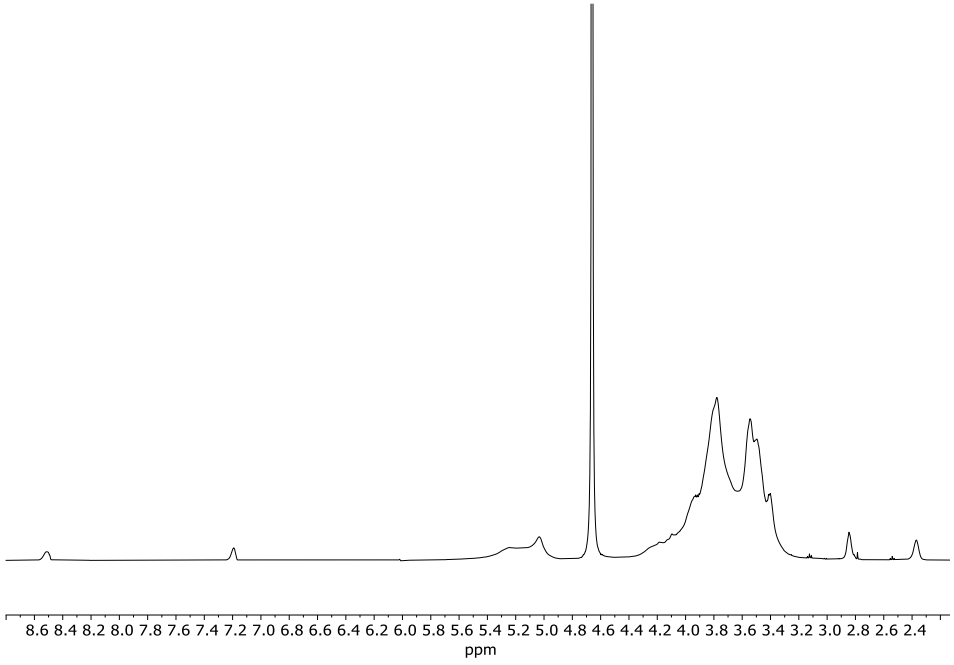

Figure S133. ^{1}H NMR spectrum of pγCyDCarc60 (D_2O, 500MHz)

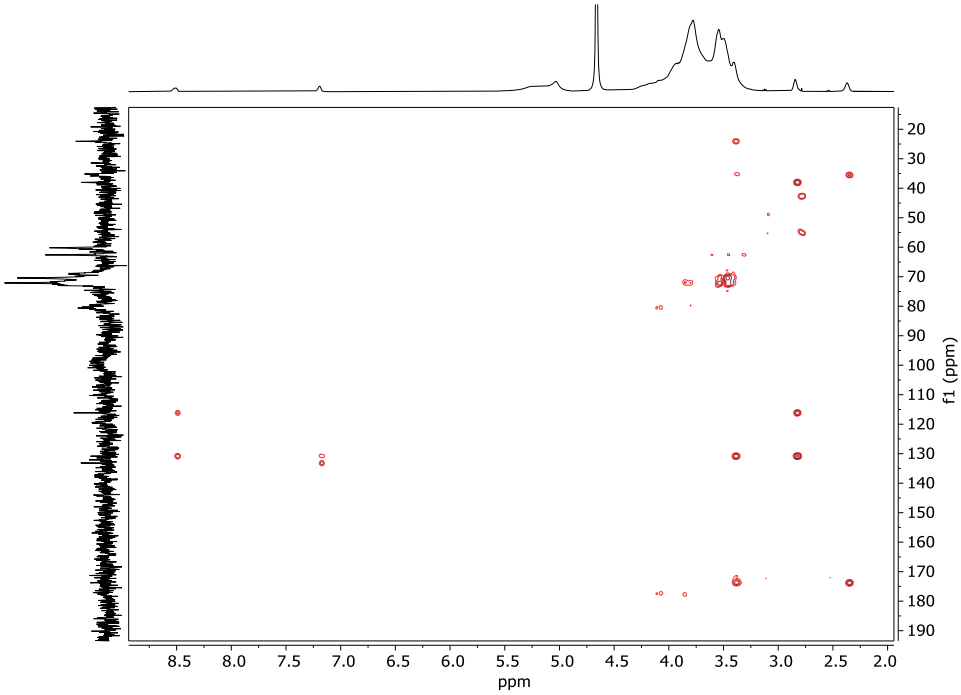

Figure S134. HMBC spectrum of pγCyDCar60 (D_2O, 500MHz)

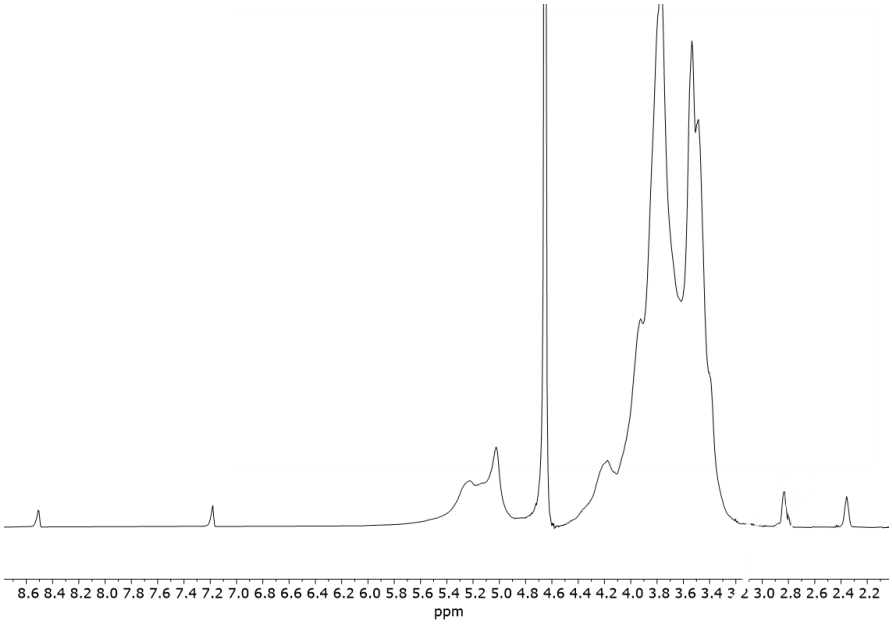

Figure S135. ^1H NMR spectrum of pγCyDCarc30 (D_2O, 500MHz)

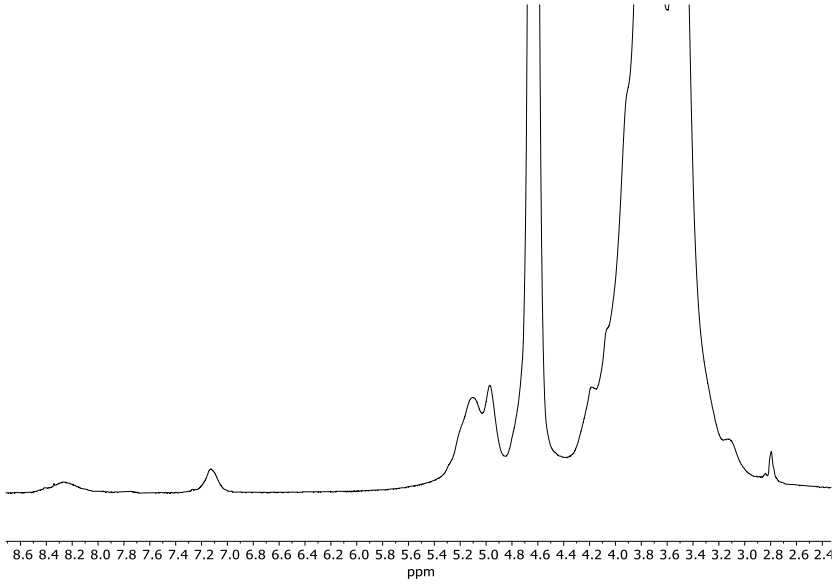

Figure S136. ^{1}H NMR spectrum of pβCyDHis (D_2O, 500MHz)

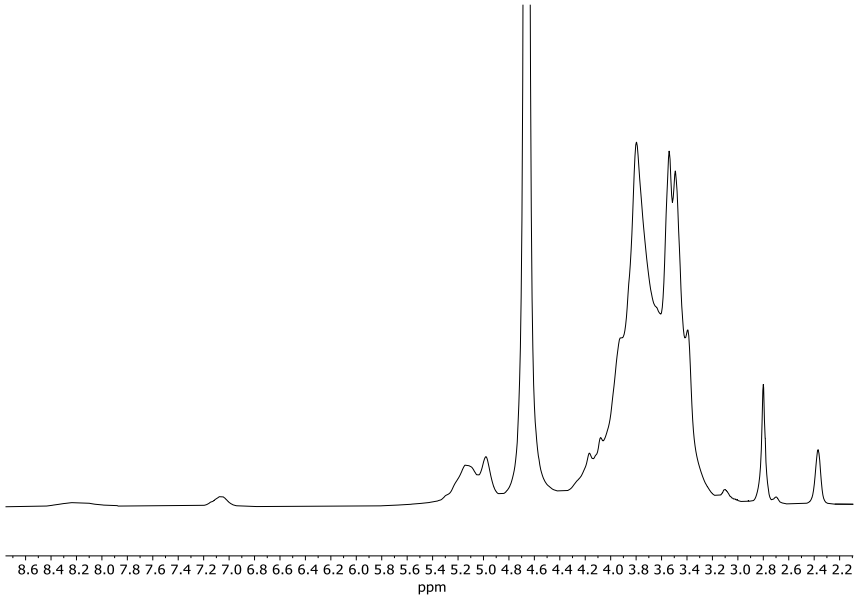

Figure S137. ^{1}H NMR spectrum of pβCyDCarc60 (D_2O, 500MHz)

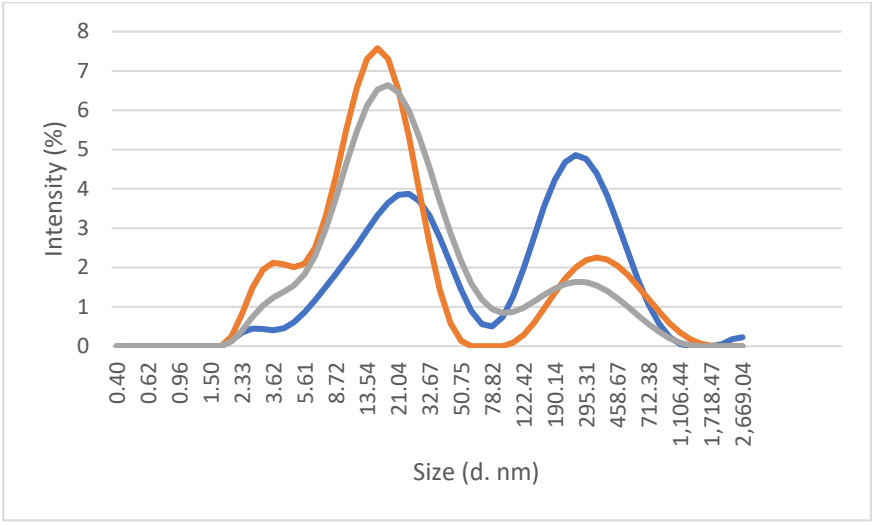

Figure S138. DLS spectra of pγCyD polymers: pγCyDCarc60 (blue), pγCyDHis (orange), pγCyDA (grey) (HEPES buffer, pH 7.4)

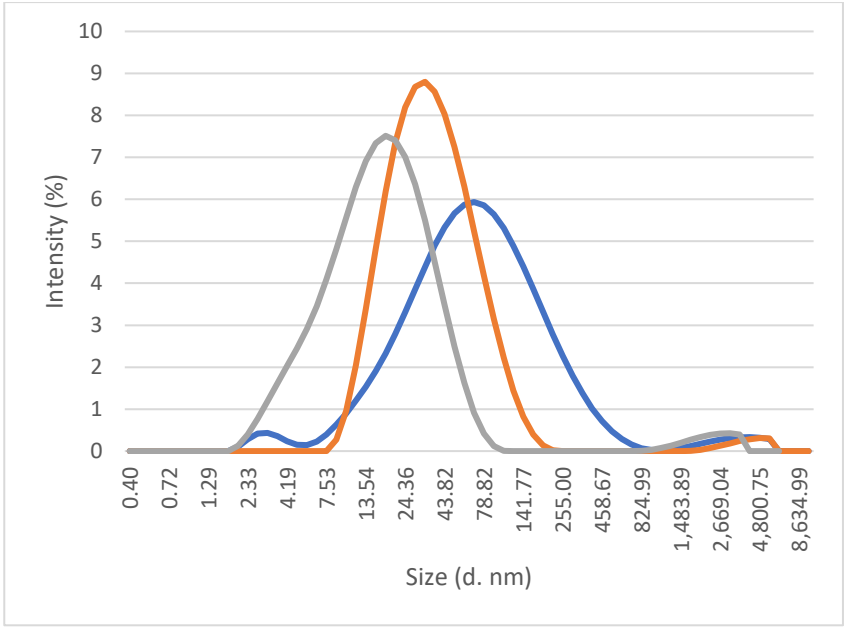

Figure S139. DLS spectra of pβCyD polymers: pβCyDCarc60 (blue), pβCyDA (orange), pβCyDHis (grey) (HEPES buffer, pH 7.4)

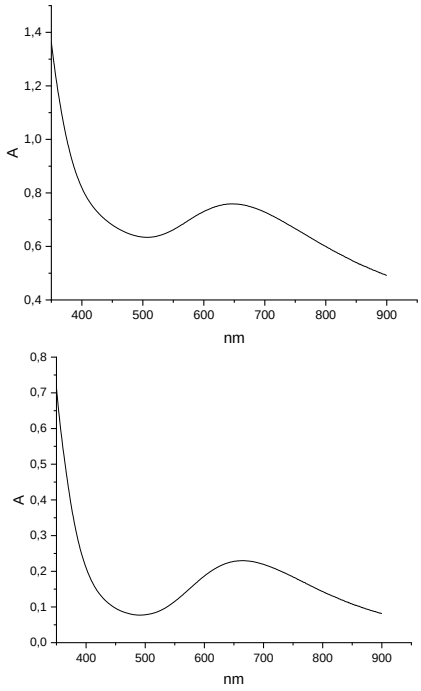

Figure S140. UV-vis spectrum of Cu^{2+}-pβCyDCar60 (left) and Cu^{2+}-pγCyDHis (right) (M/L 2:1, L is His or Carc moiety, M=5mM) at pH=7.4 HEPES

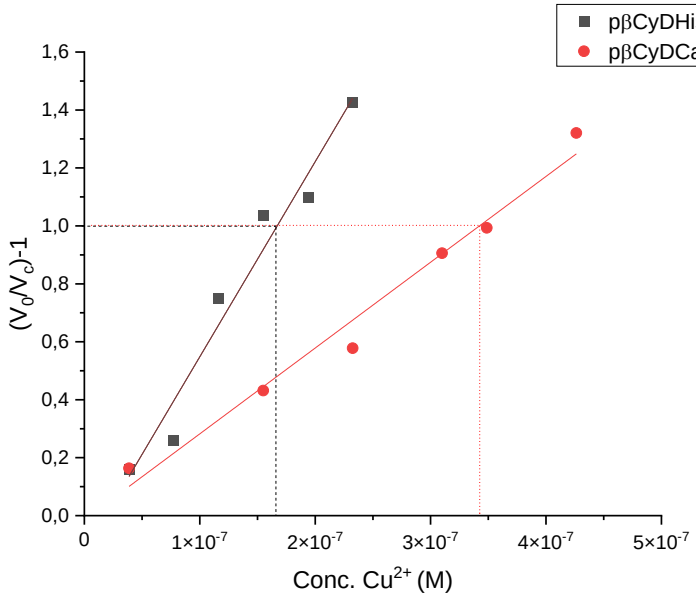

Figure S141. Superoxide dismutase activity assay: Vo is the NBT reduction rate and Vc is the NBT reduction rate in the presence of Cu^{2+}-pβCyDHis and pβCyDCarc60. The IC_{50} value is the complex concentration for which $(V_o/V_c) -1=1$

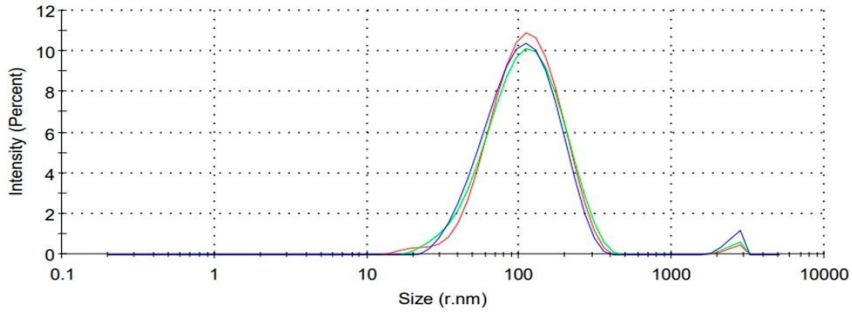

Figure S142. Size distribution by intensity for CySPION-FLUO Radius is 120 nm.

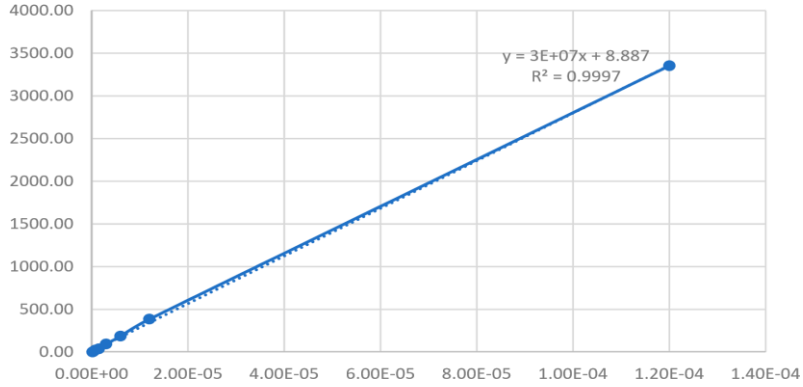

Figure S143. Calibration curve of LY

Table S14. Calibration curve of LY at 530nm

Concentration (M)	Fluorescence (530nm)
1.20E-04	3353.10
1.20E-05	385.40
6.00E-06	186.40
3.00E-06	93.00
1.50E-06	37.10
7.50E-07	22.20
3.75E-07	7.00
1.88E-07	0.00

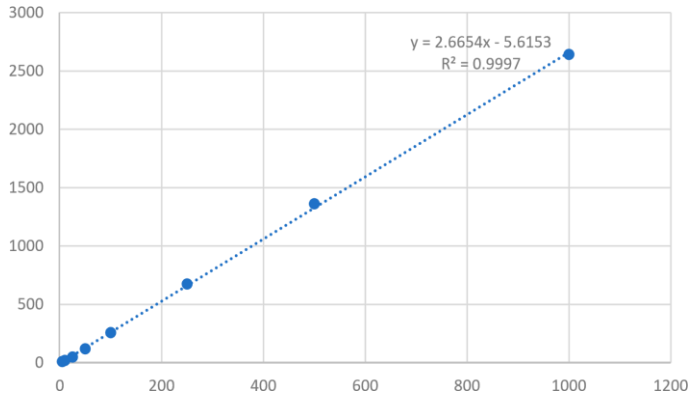

Figure S144. Calibration curve of PMOXA-FLUO

Table S15. Calibration curve of PMOXA-FLUO at 520nm

Concentration PMOXA-FLUO (µg/mL)	RFU (520 nm)
1000	2640.9
500	1361
250	673.6
100	256.4
50	118.3
25	48.3
10	18.4
5	9.1

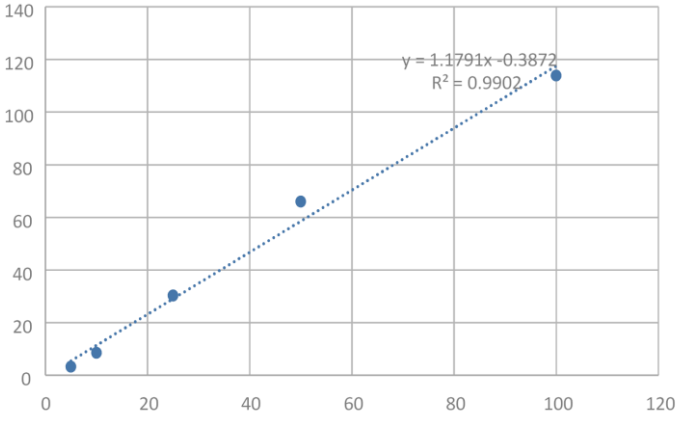

Figure S145. Calibration curve of CySPION-FLUO

Table S16. CySPION-FLUO at 520nm

Concentration CySPION-FLUO (µg/mL)	RFU (520 nm)
100	113.9
50	66
25	30.3
10	8.6
5	3.3

Table S17. Permeability values for LY, PMOXA-FLUO and CySPION-FLUO

Lucifer Yellow

Time (min)	Permeability (cm/s)
30	1.38536E-06
60	1.65806E-06
90	2.048E-06

PMOXA-FLUO

Time (min)	Permeability (cm/s)	Standard deviation
30	1.25396E-06	6.88833E-07
60	2.4988E-06	4.56429E-07
90	1.66836E-06	3.23723E-07

CySPION-FLUO

Time (min)	Permeability (cm/s)	Standard deviation
30	3.77893E-06	8.27035E-07
60	3.06986E-06	7.23057E-07
90	2.27464E-06	2.62875E-07

REFERENCES:

1. Selmani A, Kovačević D, Bohinc K (2022) Nanoparticles: From synthesis to applications and beyond. Adv Colloid Interface Sci 303:102640. https://doi.org/10.1016/j.cis.2022.102640

2. Khan I, Saeed K, Khan I (2019) Nanoparticles: Properties, applications and toxicities. Arab J Chem 12:908–931. https://doi.org/10.1016/j.arabjc.2017.05.011

3. Abid N, Khan AM, Shujait S, et al (2022) Synthesis of nanomaterials using various top-down and bottom-up approaches, influencing factors, advantages, and disadvantages: A review. Adv Colloid Interface Sci 300:102597. https://doi.org/10.1016/j.cis.2021.102597

4. Guido C, Maiorano G, Gutiérrez-Millán C, et al (2021) Erythrocytes and Nanoparticles: New Therapeutic Systems. Appl Sci 11:2173. https://doi.org/10.3390/app11052173

5. Ishtiaq M, al-Rashida M, Alharthy RD, Hameed A (2020) Chapter 15 - Ionic liquid–based colloidal nanoparticles: applications in organic synthesis. In: Shah MR, Imran M, Ullah S (eds) Metal Nanoparticles for Drug Delivery and Diagnostic Applications. Elsevier, pp 279–299

6. O P, R P (2001) Polymers in drug delivery. Curr Opin Chem Biol 5:447–451. https://doi.org/10.1016/S1367-5931(00)00227-1

7. Larson N, Ghandehari H (2012) Polymeric conjugates for drug delivery. Chem Mater Publ Am Chem Soc 24:840–853. https://doi.org/10.1021/cm2031569

8. Ringsdorf H (1975) Structure and properties of pharmacologically active polymers. J Polym Sci Polym Symp 51:135–153. https://doi.org/10.1002/POLC.5070510111

9. Mitchell MJ, Billingsley MM, Haley RM, et al (2021) Engineering precision nanoparticles for drug delivery. Nat Rev Drug Discov 20:101–124. https://doi.org/10.1038/s41573-020-0090-8

10. Raj S, Khurana S, Choudhari R, et al (2021) Specific targeting cancer cells with nanoparticles and drug delivery in cancer therapy. Semin Cancer Biol 69:166–177. https://doi.org/10.1016/J.SEMCANCER.2019.11.002

11. Carissimi G, Montalbán MG, Fuster MG, Víllora G (2021) Nanoparticles as Drug Delivery Systems. https://doi.org/10.5772/INTECHOPEN.100253

12. Jarai BM, Kolewe EL, Stillman ZS, et al (2020) Polymeric Nanoparticles. Nanoparticles Biomed Appl Fundam Concepts Biol Interact Clin Appl 303–324. https://doi.org/10.1016/B978-0-12-816662-8.00018-7

13. Fang J, Nakamura H, Maeda H (2011) The EPR effect: Unique features of tumor blood vessels for drug delivery, factors involved, and limitations and augmentation of the effect. Adv Drug Deliv Rev 63:136–151. https://doi.org/10.1016/J.ADDR.2010.04.009

14. Li H-J, Du J-Z, Du X-J, et al (2016) Stimuli-responsive clustered nanoparticles for improved tumor penetration and therapeutic efficacy. Proc Natl Acad Sci 113:4164–4169. https://doi.org/10.1073/PNAS.1522080113

15. Chiesa E, Greco A, Riva F, et al (2022) CD44-Targeted Carriers: The Role of Molecular Weight of Hyaluronic Acid in the Uptake of Hyaluronic Acid-Based Nanoparticles. Pharmaceuticals 15:103. https://doi.org/10.3390/ph15010103

16. Li C, Yu DF, Newman RA, et al (1998) Complete regression of well-established tumors using a novel water-soluble poly(L-glutamic acid)-paclitaxel conjugate. Cancer Res 58:2404–2409

17. Attia MF, Anton N, Wallyn J, et al (2019) An overview of active and passive targeting strategies to improve the nanocarriers efficiency to tumour sites. J Pharm Pharmacol 71:1185–1198. https://doi.org/10.1111/jphp.13098

18. You X, Wang L, Zhang J, et al (2023) Effects of polymer molecular weight on in vitro and in vivo performance of nanoparticle drug carriers for lymphoma therapy. Chin Chem Lett 34:107720. https://doi.org/10.1016/j.cclet.2022.07.063

19. Li G, He S, Schätzlein AG, et al (2021) Achieving highly efficient gene transfer to the bladder by increasing the molecular weight of polymer-based nanoparticles. J Controlled Release 332:210–224. https://doi.org/10.1016/j.jconrel.2021.02.007

20. Margaritis A, Manocha B (2010) Controlled release of doxorubicin from doxorubicin/γ-polyglutamic acid ionic complex. J Nanomater 2010:. https://doi.org/10.1155/2010/780171

21. Park S-B, Sung M-H, Uyama H, Han DK (2021) Poly(glutamic acid): Production, composites, and medical applications of the next-generation biopolymer. Prog Polym Sci 113:101341. https://doi.org/10.1016/j.progpolymsci.2020.101341

22. Nair LS, Laurencin CT (2007) Biodegradable polymers as biomaterials. Prog Polym Sci 32:762–798. https://doi.org/10.1016/J.PROGPOLYMSCI.2007.05.017

23. Kishida A, Murakami K, Goto H, et al (1998) Polymer Drugs and Polymeric Drugs X: Slow Release of 5-Fluorouracil from Biodegradable Poly(γ-Glutamic Acid) and its Benzyl Ester Matrices. J Bioact Compat Polym 13:270–278. https://doi.org/10.1177/088391159801300403

24. Manocha B, Margaritis A (2008) Production and Characterization of γ-Polyglutamic Acid Nanoparticles for Controlled Anticancer Drug Release. http://dx.doi.org/101080/07388550802107483 28:83–99. https://doi.org/10.1080/07388550802107483

25. Li C (2002) Poly(l-glutamic acid)–anticancer drug conjugates. Adv Drug Deliv Rev 54:695–713. https://doi.org/10.1016/S0169-409X(02)00045-5

26. JW S (2005) Paclitaxel poliglumex (XYOTAX, CT-2103): a macromolecular taxane. J Control Release Off J Control Release Soc 109:120–126. https://doi.org/10.1016/J.JCONREL.2005.09.033

27. Balogun-Agbaje OA, Odeniyi OA, Odeniyi MA (2021) Drug delivery applications of poly-γ-glutamic acid. Future J Pharm Sci 2021 71 7:1–10. https://doi.org/10.1186/S43094-021-00280-W

28. Pradeepkumar P, Sangeetha R, Gunaseelan S, et al (2019) Folic Acid Conjugated Polyglutamic Acid Drug Vehicle Synthesis through Deep Eutectic Solvent for Targeted Release of Paclitaxel. ChemistrySelect 4:10225–10235. https://doi.org/10.1002/slct.201902256

29. Maya S, Sarmento B, Lakshmanan V-K, et al (2014) Actively targeted cetuximab conjugated gamma-poly(glutamic acid)-docetaxel nanomedicines for epidermal growth factor receptor over expressing colon cancer cells. J Biomed Nanotechnol 10:1416–1428. https://doi.org/10.1166/jbn.2014.1841

30. Zhao Z, Ukidve A, Kim J, Mitragotri S (2020) Targeting Strategies for Tissue-Specific Drug Delivery. Cell 181:151–167. https://doi.org/10.1016/j.cell.2020.02.001

31. Kobatake E, Ikeda Y, Mie M (2022) Construction of protein nanoparticles for targeted delivery of drugs to cancer cells. Mater Adv 3:6262–6269. https://doi.org/10.1039/D2MA00419D

32. Kara G, Calin GA, Ozpolat B (2022) RNAi-based therapeutics and tumor targeted delivery in cancer. Adv Drug Deliv Rev 182:114113. https://doi.org/10.1016/j.addr.2022.114113

33. Salahpour Anarjan F (2019) Active targeting drug delivery nanocarriers: Ligands. Nano-Struct Nano-Objects 19:100370. https://doi.org/10.1016/J.NANOSO.2019.100370

34. Y Z, WM P (2001) Conjugation of brain-derived neurotrophic factor to a blood-brain barrier drug targeting system enables neuroprotection in regional brain ischemia following intravenous injection of the neurotrophin. Brain Res 889:49–56. https://doi.org/10.1016/S0006-8993(00)03108-5

35. U B, T Y, WM P (2001) Delivery of peptides and proteins through the blood-brain barrier. Adv Drug Deliv Rev 46:247–279. https://doi.org/10.1016/S0169-409X(00)00139-3

36. Meyer A, Auernheimer J, Modlinger A, Kessler H (2006) Targeting RGD Recognizing Integrins: Drug Development, Biomaterial Research, Tumor Imaging and Targeting. Curr Pharm Des 12:2723–2747. https://doi.org/10.2174/138161206777947740

37. Sun Y, Kang C, Liu F, et al (2017) RGD Peptide-Based Target Drug Delivery of Doxorubicin Nanomedicine. Drug Dev Res 78:283–291. https://doi.org/10.1002/DDR.21399

38. Yang W, Cheng Y, Xu T, et al (2009) Targeting cancer cells with biotin–dendrimer conjugates. Eur J Med Chem 44:862–868. https://doi.org/10.1016/J.EJMECH.2008.04.021

39. Balamurugan K, Ortiz A, Said HM (2003) Biotin uptake by human intestinal and liver epithelial cells: role of the SMVT system. Am J Physiol-Gastrointest Liver Physiol 285:G73–G77. https://doi.org/10.1152/ajpgi.00059.2003

40. Low PS, Kularatne SA (2009) Folate-targeted therapeutic and imaging agents for cancer. Curr Opin Chem Biol 13:256–262. https://doi.org/10.1016/J.CBPA.2009.03.022

41. Leamon CP, Low PS (1991) Delivery of macromolecules into living cells: a method that exploits folate receptor endocytosis. Proc Natl Acad Sci 88:5572–5576. https://doi.org/10.1073/PNAS.88.13.5572

42. H A, K M, T H (2017) Potential therapeutic application of dendrimer/cyclodextrin conjugates with targeting ligands as advanced carriers for gene and oligonucleotide drugs. Ther Deliv 8:215–232. https://doi.org/10.4155/TDE-2016-0064

43. O'Mahony AM, Ogier J, Desgranges S, et al (2012) A click chemistry route to 2-functionalised PEGylated and cationic β-cyclodextrins: co-formulation opportunities for siRNA delivery. Org Biomol Chem 10:4954–4960. https://doi.org/10.1039/C2OB25490E

44. Davis ME, Zuckerman JE, Choi CHJ, et al (2010) Evidence of RNAi in humans from systemically administered siRNA via targeted nanoparticles. Nat 2010 4647291 464:1067–1070. https://doi.org/10.1038/nature08956

45. Yasin A, Ren Y, Li J, et al (2022) Advances in Hyaluronic Acid for Biomedical Applications. Front Bioeng Biotechnol 10:910290. https://doi.org/10.3389/fbioe.2022.910290

46. Hou X, Zhong D, Chen H, et al (2022) Recent advances in hyaluronic acid-based nanomedicines: Preparation and application in cancer therapy. Carbohydr Polym 292:119662. https://doi.org/10.1016/j.carbpol.2022.119662

47. Amano Y, Sakura KL, Ohta S, Ito T (2022) Cisplatin–Chelated Iminodiacetic Acid–Conjugated Hyaluronic Acid Nanogels for the Treatment of Malignant Pleural Mesothelioma in Mice. Mol Pharm 19:853–861. https://doi.org/10.1021/acs.molpharmaceut.1c00797

48. Cowman MK, Lee H-G, Schwertfeger KL, et al (2015) The Content and Size of Hyaluronan in Biological Fluids and Tissues. Front Immunol 6:261. https://doi.org/10.3389/fimmu.2015.00261

49. Makkar S, Riehl TE, Chen B, et al (2019) Hyaluronic acid binding to TLR4 promotes proliferation and blocks apoptosis in colon cancer. Mol Cancer Ther 18:2446–2456. https://doi.org/10.1158/1535-7163.MCT-18-1225

50. Neumann A, Schinzel R, Palm D, et al (1999) High molecular weight hyaluronic acid inhibits advanced glycation endproduct-induced NF-κB activation and cytokine expression. FEBS Lett 453:283–287. https://doi.org/10.1016/S0014-5793(99)00731-0

51. Misra S, Hascall VC, Markwald RR, Ghatak S (2015) Interactions between Hyaluronan and Its Receptors (CD44, RHAMM) Regulate the Activities of Inflammation and Cancer. Front Immunol 6:

52. Fan X, Wang T, Han M, et al (2022) Dual CEA/CD44 targeting to colorectal cancer cells using nanobody-conjugated hyaluronic acid-modified mesoporous silica nanoparticles with pH- and redox-sensitivity. Mater Adv 3:4707–4717. https://doi.org/10.1039/D2MA00082B

53. Huang G, Huang H (2018) Application of hyaluronic acid as carriers in drug delivery. Drug Deliv 25:766–772. https://doi.org/10.1080/10717544.2018.1450910

54. Nagano O, Saya H (2004) Mechanism and biological significance of CD44 cleavage. Cancer Sci 95:930–935. https://doi.org/10.1111/j.1349-7006.2004.tb03179.x

55. Zhong L, Xu L, Liu Y, et al (2019) Transformative hyaluronic acid-based active targeting supramolecular nanoplatform improves long circulation and enhances cellular uptake in cancer therapy. Acta Pharm Sin B 9:397–409. https://doi.org/10.1016/j.apsb.2018.11.006

56. Kim K, Choi H, Choi ES, et al (2019) Hyaluronic Acid-Coated Nanomedicine for Targeted Cancer Therapy. Pharmaceutics 11:301. https://doi.org/10.3390/pharmaceutics11070301

57. Yu M, Jambhrunkar S, Thorn P, et al (2013) Hyaluronic acid modified mesoporous silica nanoparticles for targeted drug delivery to CD44-overexpressing cancer cells. Nanoscale 5:178–183. https://doi.org/10.1039/C2NR32145A

58. Peng H, Tang H, Jiang J (2016) Recent progress in gold nanoparticle-based biosensing and cellular imaging. Sci China Chem 59:783–793. https://doi.org/10.1007/s11426-016-5570-7

59. Cho HJ, Kim D, Li J, et al (2018) Zeolite-Encapsulated Pt Nanoparticles for Tandem Catalysis. J Am Chem Soc 140:13514–13520. https://doi.org/10.1021/jacs.8b09568

60. Stavropoulou AP, Theodosiou M, Sakellis E, et al (2022) Bimetallic gold-platinum nanoparticles as a drug delivery system coated with a new drug to target glioblastoma. Colloids Surf B Biointerfaces 214:. https://doi.org/10.1016/j.colsurfb.2022.112463

61. Mittal A, Roy I, Gandhi S (2022) Magnetic Nanoparticles: An Overview for Biomedical Applications. Magnetochemistry 8:107. https://doi.org/10.3390/magnetochemistry8090107

62. Canaparo R, Foglietta F, Limongi T, Serpe L (2020) Biomedical Applications of Reactive Oxygen Species Generation by Metal Nanoparticles. Materials 14:53. https://doi.org/10.3390/ma14010053

63. Chee CF, Leo BF, Lai CW (2018) 37 - Superparamagnetic iron oxide nanoparticles for drug delivery. In: Inamuddin, Asiri AM, Mohammad A (eds) Applications of Nanocomposite Materials in Drug Delivery. Woodhead Publishing, pp 861–903

64. Frantellizzi V, Conte M, Pontico M, et al (2020) New Frontiers in Molecular Imaging with Superparamagnetic Iron Oxide Nanoparticles (SPIONs): Efficacy, Toxicity, and Future Applications. Nucl Med Mol Imaging 54:65–80. https://doi.org/10.1007/s13139-020-00635-w

65. Veiseh O, Gunn JW, Zhang M (2010) Design and fabrication of magnetic nanoparticles for targeted drug delivery and imaging. Adv Drug Deliv Rev 62:284–304. https://doi.org/10.1016/j.addr.2009.11.002

66. Samrot AV, Sahithya CS, Selvarani A J, et al (2021) A review on synthesis, characterization and potential biological applications of superparamagnetic iron oxide nanoparticles. Curr Res Green Sustain Chem 4:100042. https://doi.org/10.1016/j.crgsc.2020.100042

67. Huang X, Li L, Liu T, et al (2011) The Shape Effect of Mesoporous Silica Nanoparticles on Biodistribution, Clearance, and Biocompatibility in Vivo. ACS Nano 5:5390–5399. https://doi.org/10.1021/nn200365a

68. Mahmoudi M, Simchi A, Milani AS, Stroeve P (2009) Cell toxicity of superparamagnetic iron oxide nanoparticles. J Colloid Interface Sci 336:510–518. https://doi.org/10.1016/j.jcis.2009.04.046

69. Wahajuddin null, Arora S (2012) Superparamagnetic iron oxide nanoparticles: magnetic nanoplatforms as drug carriers. Int J Nanomedicine 7:3445–3471. https://doi.org/10.2147/IJN.S30320

70. Balcells L, Fornaguera C, Brugada-Vilà P, et al (2019) SPIONs' Enhancer Effect on Cell Transfection: An Unexpected Advantage for an Improved Gene Delivery System. ACS Omega 4:2728–2740. https://doi.org/10.1021/acsomega.8b02905

71. Zhang T, Xu Q, Huang T, et al (2020) New Insights into Biocompatible Iron Oxide Nanoparticles: A Potential Booster of Gene Delivery to Stem Cells. Small 16:2001588. https://doi.org/10.1002/smll.202001588

72. Otieno E, Huang Y, Li N, et al (2023) Utilization of superparamagnetic iron oxide nanoparticles (SPIONs) as a vector for drug delivery. Appl Nanosci. https://doi.org/10.1007/s13204-023-02853-y

73. Reddy LH, Arias JL, Nicolas J, Couvreur P (2012) Magnetic Nanoparticles: Design and Characterization, Toxicity and Biocompatibility, Pharmaceutical and Biomedical Applications. Chem Rev 112:5818–5878. https://doi.org/10.1021/cr300068p

74. Dulińska-Litewka J, Łazarczyk A, Hałubiec P, et al (2019) Superparamagnetic Iron Oxide Nanoparticles—Current and Prospective Medical Applications. Materials 12:617. https://doi.org/10.3390/ma12040617

75. Patil RM, Thorat ND, Shete PB, et al (2018) Comprehensive cytotoxicity studies of superparamagnetic iron oxide nanoparticles. Biochem Biophys Rep 13:63–72. https://doi.org/10.1016/j.bbrep.2017.12.002

76. Vakili-Ghartavol R, Momtazi-Borojeni AA, Vakili-Ghartavol Z, et al (2020) Toxicity assessment of superparamagnetic iron oxide nanoparticles in different tissues. Artif Cells Nanomedicine Biotechnol 48:443–451. https://doi.org/10.1080/21691401.2019.1709855

77. Singh N, Jenkins GJS, Asadi R, Doak SH (2010) Potential toxicity of superparamagnetic iron oxide nanoparticles (SPION). Nano Rev 1:10.3402/nano.v1i0.5358. https://doi.org/10.3402/nano.v1i0.5358

78. Malhotra N, Lee J-S, Liman RAD, et al (2020) Potential Toxicity of Iron Oxide Magnetic Nanoparticles: A Review. Molecules 25:3159. https://doi.org/10.3390/molecules25143159

79. Wei H, Hu Y, Wang J, et al (2021) Superparamagnetic Iron Oxide Nanoparticles: Cytotoxicity, Metabolism, and Cellular Behavior in Biomedicine Applications . Int J Nanomedicine 16:6097–6113. https://doi.org/10.2147/IJN.S321984

80. Nelson NR, Port JD, Pandey MK (2020) Use of Superparamagnetic Iron Oxide Nanoparticles (SPIONs) via Multiple Imaging Modalities and Modifications to Reduce Cytotoxicity: An Educational Review. J Nanotheranostics 1:105–135. https://doi.org/10.3390/jnt1010008

81. Boutry S, Brunin S, Mahieu I, et al (2008) Magnetic labeling of non-phagocytic adherent cells with iron oxide nanoparticles: a comprehensive study. Contrast Media Mol Imaging 3:223–232. https://doi.org/10.1002/cmmi.256

82. Cengelli F, Maysinger D, Tschudi-Monnet F, et al (2006) Interaction of Functionalized Superparamagnetic Iron Oxide Nanoparticles with Brain Structures. J Pharmacol Exp Ther 318:108–116. https://doi.org/10.1124/jpet.106.101915

83. Bourrinet P, Bengele HH, Bonnemain B, et al (2006) Preclinical Safety and Pharmacokinetic Profile of Ferumoxtran-10, an Ultrasmall Superparamagnetic Iron Oxide Magnetic Resonance Contrast Agent. Invest Radiol 41:313. https://doi.org/10.1097/01.rli.0000197669.80475.dd

84. Hayashi K, Nakamura M, Sakamoto W, et al (2013) Superparamagnetic Nanoparticle Clusters for Cancer Theranostics Combining Magnetic Resonance Imaging and Hyperthermia Treatment. Theranostics 3:366–376. https://doi.org/10.7150/thno.5860

85. Vermeij EA, Koenders MI, Bennink MB, et al (2015) The In-Vivo Use of Superparamagnetic Iron Oxide Nanoparticles to Detect Inflammation Elicits a Cytokine Response but Does Not Aggravate Experimental Arthritis. PLoS ONE 10:e0126687. https://doi.org/10.1371/journal.pone.0126687

86. Yang R-M, Fu C, Fang J, et al (2016) Hyaluronan-modified superparamagnetic iron oxide nanoparticles for bimodal breast cancer imaging and photothermal therapy. Int J Nanomedicine Volume 12:197–206. https://doi.org/10.2147/IJN.S121249

87. Kumar M, Singh G, Arora V, et al (2012) Cellular interaction of folic acid conjugated superparamagnetic iron oxide nanoparticles and its use as contrast agent for targeted magnetic imaging of tumor cells. Int J Nanomedicine 7:3503–3516. https://doi.org/10.2147/IJN.S32694

88. Huang Y, Mao K, Zhang B, Zhao Y (2017) Superparamagnetic iron oxide nanoparticles conjugated with folic acid for dual target-specific drug delivery and MRI in cancer theranostics. Mater Sci Eng C 70:763–771. https://doi.org/10.1016/j.msec.2016.09.052

89. Mashhadi Malekzadeh A, Ramazani A, Tabatabaei Rezaei SJ, Niknejad H (2017) Design and construction of multifunctional hyperbranched polymers coated magnetite nanoparticles for both targeting magnetic resonance imaging and cancer therapy. J Colloid Interface Sci 490:64–73. https://doi.org/10.1016/j.jcis.2016.11.014

90. Suciu M, Ionescu CM, Ciorita A, et al (2020) Applications of superparamagnetic iron oxide nanoparticles in drug and therapeutic delivery, and biotechnological advancements. Beilstein J Nanotechnol 11:1092–1109. https://doi.org/10.3762/bjnano.11.94

91. Kobayashi S, Ohki A, Tanoue M, et al (2017) Comparative Study of Extracellular and Intracellular Magnetic Hyperthermia Treatments Using Magnetic Particle Imaging. Open J Appl Sci 07:647–660. https://doi.org/10.4236/ojapps.2017.712047

92. Hamoudeh M, Kamleh MA, Diab R, Fessi H (2008) Radionuclides delivery systems for nuclear imaging and radiotherapy of cancer. Adv Drug Deliv Rev 60:1329–1346. https://doi.org/10.1016/j.addr.2008.04.013

93. Tian X, Lara H, T. Wagner K, et al (2015) Improving DNA double-strand repair inhibitor KU55933 therapeutic index in cancer radiotherapy using nanoparticle drug delivery. Nanoscale 7:20211–20219. https://doi.org/10.1039/C5NR05869D

94. Gupta AK, Wells S (2004) Surface-modified superparamagnetic nanoparticles for drug delivery: preparation, characterization, and cytotoxicity studies. IEEE Trans NanoBioscience 3:66–73. https://doi.org/10.1109/TNB.2003.820277

95. D. Smolensky E, E. Park H-Y, Zhou Y, et al (2013) Scaling laws at the nanosize: the effect of particle size and shape on the magnetism and relaxivity of iron

oxide nanoparticle contrast agents. J Mater Chem B 1:2818–2828. https://doi.org/10.1039/C3TB00369H

96. Kanda T, Fukusato T, Matsuda M, et al (2015) Gadolinium-based Contrast Agent Accumulates in the Brain Even in Subjects without Severe Renal Dysfunction: Evaluation of Autopsy Brain Specimens with Inductively Coupled Plasma Mass Spectroscopy. Radiology 276:228–232. https://doi.org/10.1148/radiol.2015142690

97. Vangijzegem T, Lecomte V, Ternad I, et al (2023) Superparamagnetic Iron Oxide Nanoparticles (SPION): From Fundamentals to State-of-the-Art Innovative Applications for Cancer Therapy. Pharmaceutics 15:236. https://doi.org/10.3390/pharmaceutics15010236

98. Revia RA, Zhang M (2016) Magnetite nanoparticles for cancer diagnosis, treatment, and treatment monitoring: recent advances. Mater Today 19:157–168. https://doi.org/10.1016/j.mattod.2015.08.022

99. Liu JF, Jang B, Issadore D, Tsourkas A (2019) Use of Magnetic Fields and Nanoparticles to Trigger Drug Release and Improve Tumor Targeting. Wiley Interdiscip Rev Nanomed Nanobiotechnol 11:e1571. https://doi.org/10.1002/wnan.1571

100. Zhang Z, R. Wells CJ, M. King A, et al (2020) pH-Responsive nanocomposite fibres allowing MRI monitoring of drug release. J Mater Chem B 8:7264–7274. https://doi.org/10.1039/D0TB01033B

101. Zelepukin IV, Yaremenko AV, Yuryev MV, et al (2020) Fast processes of nanoparticle blood clearance: Comprehensive study. J Controlled Release 326:181–191. https://doi.org/10.1016/j.jconrel.2020.07.014

102. Pandey A (2021) Cyclodextrin-based nanoparticles for pharmaceutical applications: a review. Environ Chem Lett 19:4297–4310. https://doi.org/10.1007/s10311-021-01275-y

103. Braga SS (2022) Cyclodextrin superstructures for drug delivery. J Drug Deliv Sci Technol 75:103650. https://doi.org/10.1016/j.jddst.2022.103650

104. Mahjoubin-Tehran M, Kovanen PT, Xu S, et al (2020) Cyclodextrins: Potential therapeutics against atherosclerosis. Pharmacol Ther 214:107620. https://doi.org/10.1016/j.pharmthera.2020.107620

105. Bognanni N, Viale M, Distefano A, et al (2021) Cyclodextrin Polymers as Delivery Systems for Targeted Anti-Cancer Chemotherapy. Mol 2021 Vol 26 Page 6046 26:6046. https://doi.org/10.3390/MOLECULES26196046

106. Coisne C, Tilloy S, Monflier E, et al (2016) Cyclodextrins as Emerging Therapeutic Tools in the Treatment of Cholesterol-Associated Vascular and Neurodegenerative Diseases. Molecules 21:1748. https://doi.org/10.3390/molecules21121748

107. Dai L, Zou L, Meng L, et al (2021) Cholesterol Metabolism in Neurodegenerative Diseases: Molecular Mechanisms and Therapeutic Targets. Mol Neurobiol 58:2183–2201. https://doi.org/10.1007/s12035-020-02232-6

108. Coisne C, Hallier-Vanuxeem D, Boucau M-C, et al (2016) β-Cyclodextrins Decrease Cholesterol Release and ABC-Associated Transporter Expression in Smooth Muscle Cells and Aortic Endothelial Cells. Front Physiol 7:

109. Berry-Kravis E (2021) Niemann-Pick Disease, Type C: Diagnosis, Management and Disease-Targeted Therapies in Development. Semin Pediatr Neurol 37:100879. https://doi.org/10.1016/j.spen.2021.100879

110. Arora P, Dhingra N (2018) Cyclodextrin: A Versatile Ingredient. BoD – Books on Demand

111. Sitarska D, Tylki-Szymańska A, Ługowska A (2021) Treatment trials in Niemann-Pick type C disease. Metab Brain Dis 36:2215–2221. https://doi.org/10.1007/s11011-021-00842-0

112. Barnes PJ, Drazen JM, Rennard SI, Thomson NC (2008) Asthma and COPD: Basic Mechanisms and Clinical Management. Academic Press

113. Mora MMM, Sánchez KH, Santana RV, et al (2012) Partial purification and properties of cyclodextrin glycosiltransferase (CGTase) from alkalophilic Bacillus species. SpringerPlus 1:1–6. https://doi.org/10.1186/2193-1801-1-61

114. Grumezescu AM (2018) Organic materials as smart nanocarriers for drug delivery. Elsevier

115. Dodziuk H (2006) Molecules with Holes – Cyclodextrins. In: Cyclodextrins and Their Complexes. John Wiley & Sons, Ltd, pp 1–30

116. MacNicol DD, McKendrick JJ, Wilson DR (1978) Clathrates and molecular inclusion phenomena. Chem Soc Rev 7:65–87. https://doi.org/10.1039/CS9780700065

117. Bilensoy E (2011) Cyclodextrins in Pharmaceutics, Cosmetics, and Biomedicine: Current and Future Industrial Applications. Cyclodext Pharm Cosmet Biomed Curr Future Ind Appl. https://doi.org/10.1002/9780470926819

118. M M, SV K, P J, T L (2010) Self-assembled cyclodextrin aggregates and nanoparticles. Int J Pharm 387:199–208. https://doi.org/10.1016/J.IJPHARM.2009.11.035

119. Stappaerts J, Do Thi T, Dominguez-Vega E, et al (2017) The impact of guest compounds on cyclodextrin aggregation behavior: A series of structurally related parabens. Int J Pharm 529:442–450. https://doi.org/10.1016/j.ijpharm.2017.07.026

120. Poulson BG, Alsulami QA, Sharfalddin A, et al (2022) Cyclodextrins: Structural, Chemical, and Physical Properties, and Applications. Polysaccharides 3:1–31. https://doi.org/10.3390/polysaccharides3010001

121. Zhu X, Wu G, Chen D (2016) Molecular dynamics simulation of cyclodextrin aggregation and extraction of Anthracene from non-aqueous liquid phase. J Hazard Mater 320:169–175. https://doi.org/10.1016/j.jhazmat.2016.08.015

122. Cagno MP Di (2016) The Potential of Cyclodextrins as Novel Active Pharmaceutical Ingredients: A Short Overview. Mol 2017 Vol 22 Page 1 22:1. https://doi.org/10.3390/MOLECULES22010001

123. Schönbeck C, Holm R, Westh P (2012) Higher Order Inclusion Complexes and Secondary Interactions Studied by Global Analysis of Calorimetric Titrations. Anal Chem 84:2305–2312. https://doi.org/10.1021/AC202842S

124. Connors KA (1997) The Stability of Cyclodextrin Complexes in Solution. Chem Rev 97:1325–1358. https://doi.org/10.1021/cr960371r

125. Abdul Rauf Khan, Peter Forgo, Keith J. Stine and, Valerian T. D'Souza* † (1998) Methods for Selective Modifications of Cyclodextrins. Chem Rev 98:1977–1996. https://doi.org/10.1021/CR970012B

126. Liu R (2018) Water-Insoluble Drug Formulation. CRC Press

127. Walayat N, Xiong Z, Xiong H, et al (2020) The effectiveness of egg white protein and β-cyclodextrin during frozen storage: Functional, rheological and structural changes in the myofibrillar proteins of Culter alburnus. Food Hydrocoll 105:105842. https://doi.org/10.1016/j.foodhyd.2020.105842

128. Piñeiro Á, Pipkin J, Antle V, Garcia-Fandino R (2021) Aggregation versus inclusion complexes to solubilize drugs with cyclodextrins. A case study using sulphobutylether-β-cyclodextrins and remdesivir. J Mol Liq 343:117588. https://doi.org/10.1016/j.molliq.2021.117588

129. Piana LL, Basile L, Ragusa C, et al (2023) β and γ-Cyclodextrin dimers: design, characterization and in silico studies to explore the cooperative effect of the cavities. New J Chem 47:2520–2526. https://doi.org/10.1039/D2NJ04649K

130. Oliveri V, Bellia F, Vecchio G (2015) Cyclodextrin 3-Functionalized with 8-Hydroxyquinoline as an Antioxidant Inhibitor of Metal-Induced Amyloid Aggregation. ChemPlusChem 80:762–770. https://doi.org/10.1002/cplu.201402450

131. Wankar J, Kotla NG, Gera S, et al (2020) Recent Advances in Host–Guest Self-Assembled Cyclodextrin Carriers: Implications for Responsive Drug Delivery and Biomedical Engineering. Adv Funct Mater 30:1909049. https://doi.org/10.1002/ADFM.201909049

132. Bibby DC, Davies NM, Tucker IG (2000) Mechanisms by which cyclodextrins modify drug release from polymeric drug delivery systems. Int J Pharm 197:1–11. https://doi.org/10.1016/S0378-5173(00)00335-5

133. Evans CE, Stalcup AM (2003) Comprehensive strategy for chiral separations using sulfated cyclodextrins in capillary electrophoresis. Chirality 15:709–723. https://doi.org/10.1002/chir.10285

134. Kasal P, Jindřich J (2021) Mono-6-Substituted Cyclodextrins—Synthesis and Applications. Mol 2021 Vol 26 Page 5065 26:5065. https://doi.org/10.3390/MOLECULES26165065

135. Řezanka M (2016) Monosubstituted Cyclodextrins as Precursors for Further Use. Eur J Org Chem 2016:5322–5334. https://doi.org/10.1002/EJOC.201600693

136. Skiba M, Skiba-Lahiani M, Arnaud P (2002) Design of Nanocapsules Based on Novel Fluorophilic Cyclodextrin Derivatives and Their Potential Role in Oxygen Delivery. J Incl Phenom Macrocycl Chem 44:151–154. https://doi.org/10.1023/A:1023090528809

137. Subban Ganapathy H, Lee MY, Park C, Lim KT Sustained release applications of a fluoroalkyl ester-functionalized amphiphilic cyclodextrin by inclusion complex formation with water-soluble drugs in supercritical carbon dioxide. https://doi.org/10.1016/j.jfluchem.2008.09.005

138. Aykaç A, Martos-Maldonado MC, Casas-Solvas JM, et al (2012) Binding ability properties of β-cyclodextrin dimers linked through their secondary faces towards cancer chemotherapeutic agent methotrexate. J Drug Deliv Sci Technol 22:270–272. https://doi.org/10.1016/S1773-2247(12)50039-0

139. Liu Y, Li, Chen Y, et al (2005) Molecular Recognition Thermodynamics of Bile Salts by β-Cyclodextrin Dimers: Factors Governing the Cooperative Binding of Cyclodextrin Dimers. J Phys Chem B 109:4129–4134. https://doi.org/10.1021/jp045332v

140. Gascon JM, Oliveri V, McGown A, et al (2019) Synthesis and Study of Multifunctional Cyclodextrin–Deferasirox Hybrids. ChemMedChem 14:1484–1492. https://doi.org/10.1002/CMDC.201900334

141. Bognanni N, Bellia F, Vecchio G Cyclodextrin Polymers Functionalized with Histidine and Carcinine as Chelating Therapeutics for Copper Dyshomeostasis. ChemMedChem n/a:e202300035. https://doi.org/10.1002/cmdc.202300035

142. Dandawate P, Vemuri K, Khan EM, et al (2014) Synthesis, characterization and anti-tubercular activity of ferrocenyl hydrazones and their β-cyclodextrin conjugates. Carbohydr Polym 108:135–144. https://doi.org/10.1016/j.carbpol.2014.03.006

143. Sies H, Belousov VV, Chandel NS, et al (2022) Defining roles of specific reactive oxygen species (ROS) in cell biology and physiology. Nat Rev Mol Cell Biol 23:499–515. https://doi.org/10.1038/s41580-022-00456-z

144. Chen L, Chen Y, Zhang Y, Liu Y (2021) Photo-Controllable Catalysis and Chiral Monosaccharide Recognition Induced by Cyclodextrin Derivatives. Angew Chem 133:7732–7736. https://doi.org/10.1002/ange.202017001

145. Yaraki MT, Zahed Nasab S, Zare I, et al (2022) Biomimetic Metallic Nanostructures for Biomedical Applications, Catalysis, and Beyond. Ind Eng Chem Res 61:7547–7593. https://doi.org/10.1021/acs.iecr.2c00285

146. Yan F, Luo G (2012) Cyclodextrin-based Mimics of Selenoproteins. In: Liu J, Luo G, Mu Y (eds) Selenoproteins and Mimics. Springer, Berlin, Heidelberg, pp 223–247

147. Breslow R, Dong SD (1998) Biomimetic Reactions Catalyzed by Cyclodextrins and Their Derivatives. Chem Rev 98:1997–2012. https://doi.org/10.1021/cr970011j

148. Youngjun Lee, K. Devaraj N (2021) Lipase mimetic cyclodextrins. Chem Sci 12:1090–1094. https://doi.org/10.1039/D0SC05711H

149. Kitagishi H, Minegishi S (2017) Iron(II)porphyrin–Cyclodextrin Supramolecular Complex as a Carbon Monoxide-Depleting Agent in Living Organisms. Chem Pharm Bull (Tokyo) 65:336–340. https://doi.org/10.1248/CPB.C16-00767

150. Ueda T, Kitagishi H, Kano K (2012) PEGylation of an artificial O2 and CO receptor: synthesis, characterisation and pharmacokinetic study. Org Biomol Chem 10:4337–4347. https://doi.org/10.1039/C2OB07044H

151. Karasugi K, Kitagishi H, Kano K (2012) Modification of a dioxygen carrier, hemoCD, with PEGylated dendrons for extension of circulation time in the bloodstream. Bioconjug Chem 23:2365–2376. https://doi.org/10.1021/bc300303z

152. Fan MF, Wang HM, Nan LJ, et al (2020) The mimetic assembly of cobalt prot-porphyrin with cyclodextrin dimer and its application for H2O2 detection. Anal Chim Acta 1097:78–84. https://doi.org/10.1016/J.ACA.2019.11.002

153. Bellia F, Vecchio G, Rizzarelli E (2011) Carnosine derivatives: new multifunctional drug-like molecules. Amino Acids 2011 431 43:153–163. https://doi.org/10.1007/S00726-011-1178-6

154. Oliveri V, Giglio V, Vecchio G (2016) Cyclodextrins and Their Interaction With Metals. Ref Module Chem Mol Sci Chem Eng. https://doi.org/10.1016/B978-0-12-409547-2.12273-5

155. Oliveri V, Vecchio G (2018) Cyclodextrin-based nanoparticles. Org Mater Smart Nanocarriers Drug Deliv 619–658. https://doi.org/10.1016/B978-0-12-813663-8.00015-4

156. MARTÍN R, FRAGOSO A, CAO R (2003) Complexation of Bis(morpholyldithiocarbamato)copper(II), a Superoxide Scavenger, in β-Cyclodextrins. Supramol Chem 15:171–175. https://doi.org/10.1080/1061027031000078266

157. Oliveri V, Vecchio G (2018) Metallocyclodextrins in medicinal chemistry. Httpsdoiorg104155fmc-2017-0249 10:663–677. https://doi.org/10.4155/FMC-2017-0249

158. Lanza V, Vecchio G (2009) New conjugates of superoxide dismutase/catalase mimetics with cyclodestrins. J Inorg Biochem 103:381–388. https://doi.org/10.1016/j.jinorgbio.2008.11.017

159. Oliveri V, Zimbone S, Giuffrida ML, et al (2018) Porphyrin Cyclodextrin Conjugates Modulate Amyloid Beta Peptide Aggregation and Cytotoxicity. Chem – Eur J 24:6349–6353. https://doi.org/10.1002/chem.201800807

160. Oliveri V, Vecchio G (2016) Cyclodextrins as Protective Agents of Protein Aggregation: An Overview. Chem – Asian J 11:1648–1657. https://doi.org/10.1002/ASIA.201600259

161. Zhiqiang Wang †, Lei Chang ‡, William L. Klein ‡, et al (2004) Per-6-substituted-per-6-deoxy β-cyclodextrins Inhibit the Formation of β-Amyloid Peptide Derived Soluble Oligomers. J Med Chem 47:3329–3333. https://doi.org/10.1021/JM034224E

162. Camilleri P, Haskins NJ, Hewlett DR (1994) β-Cyclodextrin interacts with the Alzheimer amyloid β-A4 peptide. FEBS Lett 341:256–258. https://doi.org/10.1016/0014-5793(94)80467-2

163. Waite J, Cole GM, Frautschy SA, et al (1992) Solvent effects on beta protein toxicity in vivo. Neurobiol Aging 13:595–599. https://doi.org/10.1016/0197-4580(92)90062-3

164. P C, NJ H, DR H (1994) beta-Cyclodextrin interacts with the Alzheimer amyloid beta-A4 peptide. FEBS Lett 341:256–258. https://doi.org/10.1016/0014-5793(94)80467-2

165. Qin X rong, Abe H, Nakanishi H (2002) NMR and CD studies on the interaction of Alzheimer β-amyloid peptide (12–28) with β-cyclodextrin. Biochem Biophys Res Commun 297:1011–1015. https://doi.org/10.1016/S0006-291X(02)02337-9

166. Li G, Li Y-M (2022) Modulating the aggregation of amyloid proteins by macrocycles. Aggregate 3:e161. https://doi.org/10.1002/agt2.161

167. SJ W, R W, JD M, MR H (1995) Prolines and amyloidogenicity in fragments of the Alzheimer's peptide beta/A4. Biochemistry 34:724–730. https://doi.org/10.1021/BI00003A003

168. Wahlström A, Cukalevski R, Danielsson J, et al (2012) Specific Binding of a β-Cyclodextrin Dimer to the Amyloid β Peptide Modulates the Peptide Aggregation Process. Biochemistry 51:4280–4289. https://doi.org/10.1021/bi300341j

169. Gautam S, Karmakar S, Bose A, Chowdhury PK (2014) β-Cyclodextrin and Curcumin, a Potent Cocktail for Disaggregating and/or Inhibiting Amyloids: A Case Study with α-Synuclein. Biochemistry 53:4081–4083. https://doi.org/10.1021/BI500642F

170. Bognanni N, Bellia F, Viale M, et al (2021) Exploring Charged Polymeric Cyclodextrins for Biomedical Applications. Molecules 26:1724. https://doi.org/10.3390/molecules26061724

171. Giglio V, Bellia F, Oliveri V, Vecchio G (2016) Aminocyclodextrin Oligomers as Protective Agents of Protein Aggregation. ChemPlusChem 81:660–665. https://doi.org/10.1002/cplu.201600239

172. Ahmad AS, Ansari MA, Ahmad M, et al (2005) Neuroprotection by crocetin in a hemi-parkinsonian rat model. Pharmacol Biochem Behav 81:805–813. https://doi.org/10.1016/j.pbb.2005.06.007

173. Wong KH, Xie Y, Huang X, et al (2020) Delivering Crocetin across the Blood-Brain Barrier by Using γ-Cyclodextrin to Treat Alzheimer's Disease. Sci Rep 2020 101 10:1–12. https://doi.org/10.1038/s41598-020-60293-y

174. Liu Z, Ye L, Xi J, et al (2021) Cyclodextrin polymers: Structure, synthesis, and use as drug carriers. Prog Polym Sci 118:101408. https://doi.org/10.1016/j.progpolymsci.2021.101408

175. Xiao X, Teng F, Shi C, et al (2022) Polymeric nanoparticles—Promising carriers for cancer therapy. Front Bioeng Biotechnol 10:

176. Heidel JD, Schluep T (2012) Cyclodextrin-Containing Polymers: Versatile Platforms of Drug Delivery Materials. J Drug Deliv 2012:17. https://doi.org/10.1155/2012/262731

177. Thakor AS, Gambhir SS (2013) Nanooncology: The future of cancer diagnosis and therapy. CA Cancer J Clin 63:395–418. https://doi.org/10.3322/CAAC.21199

178. Young C, Schluep T, Hwang J, Eliasof S (2011) CRLX101 (formerly IT-101)–A Novel Nanopharmaceutical of Camptothecin in Clinical Development. Curr Bioact Compd 7:8–14. https://doi.org/10.2174/157340711795163866

179. Hesemans E, Buttiens K, Manshian BB, Soenen SJ (2022) The Role of Optical Imaging in Translational Nanomedicine. J Funct Biomater 13:137. https://doi.org/10.3390/jfb13030137

180. Mehta M, Polli JE, Seo P, et al (2023) Drug Permeability - Best Practices for Biopharmaceutics Classification System (BCS)-Based Biowaivers: A workshop Summary Report. J Pharm Sci 112:1749–1762. https://doi.org/10.1016/j.xphs.2023.04.016

181. Huang Q, Yan CH, Luo SX, et al (2022) Synthesis, Characteristics, and Pharmaceutical Properties of Ibuprofen-Cyclodextrin-PEG Conjugate. J Chem 2022:e3388712. https://doi.org/10.1155/2022/3388712

182. Liao R, Liu Y, Lv P, et al (2020) Cyclodextrin pendant polymer as an efficient drug carrier for scutellarin. Drug Deliv 27:1741–1749. https://doi.org/10.1080/10717544.2020.1856223

183. Alhakamy NA, Md S (2019) Repurposing Itraconazole Loaded PLGA Nanoparticles for Improved Antitumor Efficacy in Non-Small Cell Lung Cancers. Pharmaceutics 11:685. https://doi.org/10.3390/pharmaceutics11120685

184. and DWB, Davis* ME (2007) Physicochemical and Biological Characterization of Targeted, Nucleic Acid-Containing Nanoparticles. Bioconjug Chem 18:456–468. https://doi.org/10.1021/BC0603539

185. Zuckerman JE, Gritli I, Tolcher A, et al (2014) Correlating animal and human phase Ia/Ib clinical data with CALAA-01, a targeted, polymer-based nanoparticle containing siRNA. Proc Natl Acad Sci 111:11449–11454. https://doi.org/10.1073/pnas.1411393111

186. Bognanni N, Viale M, La Piana L, et al (2023) Hyaluronan-Cyclodextrin Conjugates as Doxorubicin Delivery Systems. Pharmaceutics 15:374. https://doi.org/10.3390/pharmaceutics15020374

187. Fiorica C, Palumbo FS, Pitarresi G, et al (2020) A hyaluronic acid/cyclodextrin based injectable hydrogel for local doxorubicin delivery to solid tumors. Int J Pharm 589:119879. https://doi.org/10.1016/j.ijpharm.2020.119879

188. Zawko SA, Truong Q, Schmidt CE (2008) Drug-binding hydrogels of hyaluronic acid functionalized with β-cyclodextrin. J Biomed Mater Res A 87A:1044–1052. https://doi.org/10.1002/jbm.a.31845

189. Renard E, Deratani A, Volet G, Sebille B (1997) Preparation and characterization of water soluble high molecular weight β-cyclodextrin-epichlorohydrin polymers. Eur Polym J 33:49–57. https://doi.org/10.1016/S0014-3057(96)00123-1

190. Agnes M, Pancani E, Malanga M, et al (2022) Implementation of Water-Soluble Cyclodextrin-Based Polymers in Biomedical Applications: How Far Are We? Macromol Biosci 22:2200090. https://doi.org/10.1002/mabi.202200090

191. Giglio V, Viale M, Bertone V, et al (2017) Cyclodextrin polymers as nanocarriers for sorafenib. Investig New Drugs 2017 363 36:370–379. https://doi.org/10.1007/S10637-017-0538-9

192. Skuredina AA, Tychinina AS, Le-Deygen IM, et al (2021) The formation of quasi-regular polymeric network of cross-linked sulfobutyl ether derivative of β-cyclodextrin synthesized with moxifloxacin as a template. React Funct Polym 159:104811. https://doi.org/10.1016/J.REACTFUNCTPOLYM.2021.104811

193. Anand R, Malanga M, Manet I, et al (2013) Citric acid–γ-cyclodextrin crosslinked oligomers as carriers for doxorubicin delivery. Photochem Photobiol Sci 12:1841–1854. https://doi.org/10.1039/C3PP50169H

194. Kozieł K, Łagiewka J, Girek B, et al (2021) Synthesis of New Amino—β-Cyclodextrin Polymer, Cross-Linked with Pyromellitic Dianhydride and Their Use for the Synthesis of Polymeric Cyclodextrin Based Nanoparticles. Polym 2021 Vol 13 Page 1332 13:1332. https://doi.org/10.3390/POLYM13081332

195. Girek T, Koziel K, Girek B, Ciesielski W (2020) CD Oxyanions as a Tool for Synthesis of Highly Anionic Cyclodextrin Polymers. Polym 2020 Vol 12 Page 2845 12:2845. https://doi.org/10.3390/POLYM12122845

196. Janko C, Ratschker T, Nguyen K, et al (2019) Functionalized Superparamagnetic Iron Oxide Nanoparticles (SPIONs) as Platform for the Targeted Multimodal Tumor Therapy. Front Oncol 9:

197. Puiu RA, Balaure PC, Constantinescu E, et al (2021) Anti-Cancer Nanopowders and MAPLE-Fabricated Thin Films Based on SPIONs Surface Modified with Paclitaxel Loaded β-Cyclodextrin. Pharmaceutics 13:1356. https://doi.org/10.3390/pharmaceutics13091356

198. Jeon H, Kim J, Lee YM, et al (2016) Poly-paclitaxel/cyclodextrin-SPION nano-assembly for magnetically guided drug delivery system. J Controlled Release 231:68–76. https://doi.org/10.1016/j.jconrel.2016.01.006

199. Li H, Peng E, Zhao F, et al (2021) Supramolecular Surface Functionalization of Iron Oxide Nanoparticles with α-Cyclodextrin-Based Cationic Star Polymer for Magnetically-Enhanced Gene Delivery. Pharmaceutics 13:1884. https://doi.org/10.3390/pharmaceutics13111884

200. S. Santos EC da, Watanabe A, D. Vargas M, et al (2018) AMF-responsive doxorubicin loaded β-cyclodextrin-decorated superparamagnetic nanoparticles. New J Chem 42:671–680. https://doi.org/10.1039/C7NJ02860A

201. Puglisi A, Bognanni N, Vecchio G, et al (2023) Grafting of Cyclodextrin to Theranostic Nanoparticles Improves Blood-Brain Barrier Model Crossing. Biomolecules 13:573. https://doi.org/10.3390/biom13030573

202. Estelrich J, Busquets MA (2021) Magnetic Nanoparticles as Delivery Systems to Penetrate the Blood-Brain Barrier. In: Morales JO, Gaillard PJ (eds) Nanomedicines for Brain Drug Delivery. Springer US, New York, NY, pp 173–208

203. Senturk F, Cakmak S, Kocum IC, et al (2022) Effects of radiofrequency exposure on in vitro blood-brain barrier permeability in the presence of magnetic nanoparticles. Biochem Biophys Res Commun 597:91–97. https://doi.org/10.1016/j.bbrc.2022.01.112

204. Puglisi A, Bassini S, Reimhult E (2021) Cyclodextrin-Appended Superparamagnetic Iron Oxide Nanoparticles as Cholesterol-Mopping Agents. Front Chem 9:795598. https://doi.org/10.3389/fchem.2021.795598

205. Vadlapudi AD, Vadlapatla RK, Pal D, Mitra AK (2013) Biotin uptake by T47D breast cancer cells: Functional and molecular evidence of sodium-dependent multivitamin transporter (SMVT). Int J Pharm 441:535–543. https://doi.org/10.1016/j.ijpharm.2012.10.047

206. Lei M, Chen G, Zhang M, et al (2021) A pH-sensitive drug delivery system based on hyaluronic acid co-deliver doxorubicin and aminoferrocene for the combined application of chemotherapy and chemodynamic therapy. Colloids Surf B Biointerfaces 203:111750. https://doi.org/10.1016/j.colsurfb.2021.111750

207. Ramesh K, Balavigneswaran CK, Siboro SAP, et al (2021) Synthesis of cyclodextrin-derived star poly(N-vinylpyrrolidone)/poly(lactic-co-glycolide) supramolecular micelles via host-guest interaction for delivery of doxorubicin. Polymer 214:123243. https://doi.org/10.1016/j.polymer.2020.123243

208. Saokham P, Muankaew C, Jansook P, Loftsson T (2018) Solubility of Cyclodextrins and Drug/Cyclodextrin Complexes. Mol J Synth Chem Nat Prod Chem 23:1161. https://doi.org/10.3390/molecules23051161

209. Anand R, Ottani S, Manoli F, et al (2012) A close-up on doxorubicin binding to γ -cyclodextrin: an elucidating spectroscopic, photophysical and conformational study. RSC Adv 2:2346–2357. https://doi.org/10.1039/C2RA01221A

210. London WB, Bagatell R, Weigel BJ, et al (2017) Historical time to disease progression and progression-free survival in patients with recurrent/refractory neuroblastoma treated in the modern era on Children's Oncology Group early-phase trials. Cancer 123:4914–4923. https://doi.org/10.1002/cncr.30934

211. Zustovich F, Lombardi G, Pastorelli D, et al (2011) Clinical experience and critical evaluation of the role of sorafenib in renal cell carcinoma. Open Access J Urol 3:69–82. https://doi.org/10.2147/OAJU.S7230

212. Pang Y, Eresen A, Zhang Z, et al (2022) Adverse events of sorafenib in hepatocellular carcinoma treatment. Am J Cancer Res 12:2770–2782

213. Phan C, Zheng Z, Wang J, et al (2019) Enhanced antitumour effect for hepatocellular carcinoma in the advanced stage using a cyclodextrin-sorafenib-chaperoned inclusion complex. Biomater Sci 7:4758–4768. https://doi.org/10.1039/C9BM01190K

214. Layre AM, Gosselet NM, Renard E, et al (2002) Comparison of the Complexation of Cosmetical and Pharmaceutical Compounds with γ-Cyclodextrin, 2-Hydroxypropyl-β-cyclodextrin and Water-Soluble β-Cyclodextrin-co-epichlorhydrin Polymers. J Incl Phenom Macrocycl Chem 43:311–317. https://doi.org/10.1023/A:1021287920274

215. Fülöp Z, Kurkov SV, Nielsen TT, et al (2012) Self-assembly of cyclodextrins: formation of cyclodextrin polymer based nanoparticles. J Drug Deliv Sci Technol 22:215–221. https://doi.org/10.1016/S1773-2247(12)50032-8

216. Fülöp Z, Nielsen TT, Larsen KL, Loftsson T (2013) Dextran-based cyclodextrin polymers: Their solubilizing effect and self-association. Carbohydr Polym 97:635–642. https://doi.org/10.1016/j.carbpol.2013.05.053

217. Giachino C, Viale M, Vecchio G (2019) Exploring the Functionalization of Polymeric Nanoparticles Based on Cyclodextrins for Tumor Cell Targeting. ChemistrySelect 4:13025–13028. https://doi.org/10.1002/slct.201903774

218. Guan H, McGuire MJ, Li S, Brown KC (2008) Peptide-Targeted Polyglutamic Acid Doxorubicin Conjugates for the Treatment of αvβ6-Positive Cancers. Bioconjug Chem 19:1813–1821. https://doi.org/10.1021/BC800154F

219. Oliveri V, Bellia F, Viale M, et al (2017) Linear polymers of β and γ cyclodextrins with a polyglutamic acid backbone as carriers for doxorubicin. Carbohydr Polym 177:355–360. https://doi.org/10.1016/J.CARBPOL.2017.08.103

220. Sedlák M (1996) The ionic strength dependence of the structure and dynamics of polyelectrolyte solutions as seen by light scattering: The slow mode dilemma. J Chem Phys 105:10123–10133. https://doi.org/10.1063/1.472841

221. Dobrynin A V. (2020) Polyelectrolytes: On the doorsteps of the second century. Polymer 202:122714. https://doi.org/10.1016/J.POLYMER.2020.122714

222. Giglio V, Viale M, Bertone V, et al (2018) Cyclodextrin polymers as nanocarriers for sorafenib. Invest New Drugs 36:370–379. https://doi.org/10.1007/s10637-017-0538-9

223. Chen Y, Pidhatika B, von Erlach T, et al (2014) Comparative assessment of the stability of nonfouling poly(2-methyl-2-oxazoline) and poly(ethylene glycol) surface films: An in vitro cell culture study. Biointerphases 9:031003. https://doi.org/10.1116/1.4878461

224. de la Rosa VR (2014) Poly(2-oxazoline)s as materials for biomedical applications. J Mater Sci Mater Med 25:1211–1225. https://doi.org/10.1007/s10856-013-5034-y

225. Napolitano A, d'Ischia M, Costantini C, Prota G (1992) A new oxidation pathway of the neurotoxin 6-aminodopamine. Isolation and characterisation of a dimer with a tetrahydro[3,4a]iminoethanophenoxazine ring system. Tetrahedron 48:8515–8522. https://doi.org/10.1016/S0040-4020(01)86599-6

226. Zirbs R, Lassenberger A, Vonderhaid I, et al (2015) Melt-grafting for the synthesis of core–shell nanoparticles with ultra-high dispersant density. Nanoscale 7:11216–11225. https://doi.org/10.1039/C5NR02313K

227. Amstad E, Gehring AU, Fischer H, et al (2011) Influence of Electronegative Substituents on the Binding Affinity of Catechol-Derived Anchors to Fe_3O_4 Nanoparticles. J Phys Chem C 115:683–691. https://doi.org/10.1021/jp1109306

228. Tagde P, Kulkarni GT, Mishra DK, Kesharwani P (2020) Recent advances in folic acid engineered nanocarriers for treatment of breast cancer. J Drug Deliv Sci Technol 56:101613. https://doi.org/10.1016/j.jddst.2020.101613

229. Giglio V, Oliveri V, Viale M, et al (2015) Folate–Cyclodextrin Conjugates as Carriers of the Platinum(IV) Complex LA-12. ChemPlusChem 80:536–543. https://doi.org/10.1002/cplu.201402342

230. Wang S, Lee RJ, Mathias CJ, et al (1996) Synthesis, Purification, and Tumor Cell Uptake of 67Ga-Deferoxamine−Folate, a Potential Radiopharmaceutical for Tumor Imaging. Bioconjug Chem 7:56–62. https://doi.org/10.1021/bc9500709

231. Juzeniene A, Thu Tam TT, Iani V, Moan J (2013) The action spectrum for folic acid photodegradation in aqueous solutions. J Photochem Photobiol B 126:11–16. https://doi.org/10.1016/j.jphotobiol.2013.05.011

232. Tyagi A, Penzkofer A (2010) Fluorescence spectroscopic behaviour of folic acid. Chem Phys 367:83–92. https://doi.org/10.1016/j.chemphys.2009.10.026

233. Shah S, Chandra A, Kaur A, et al (2017) Fluorescence properties of doxorubicin in PBS buffer and PVA films. J Photochem Photobiol B 170:65–69. https://doi.org/10.1016/j.jphotobiol.2017.03.024

234. Fijten MWM, Hoogenboom R, Schubert US (2008) Initiator effect on the cationic ring-opening copolymerization of 2-ethyl-2-oxazoline and 2-phenyl-2-oxazoline. J Polym Sci Part Polym Chem 46:4804–4816. https://doi.org/10.1002/pola.22814

235. Tian B, Hua S, Liu J (2020) Cyclodextrin-based delivery systems for chemotherapeutic anticancer drugs: A review. Carbohydr Polym 232:115805. https://doi.org/10.1016/J.CARBPOL.2019.115805

236. Zhang D, Zhang J, Jiang K, et al (2016) Preparation, characterisation and antitumour activity of β-, γ- and HP-β-cyclodextrin inclusion complexes of oxaliplatin. Spectrochim Acta A Mol Biomol Spectrosc 152:501–508. https://doi.org/10.1016/J.SAA.2015.07.088

237. Viale M, Monticone M, Maric I, et al (2018) Characterization of drug release from fibrin gels loaded with different pharmaceutical and experimental doxorubicin formulations. Pharmacol Rep 70:760–765. https://doi.org/10.1016/J.PHAREP.2018.02.014

238. Wiseman LR, Adkins JC, Plosker GL, Goa KL (1999) Oxaliplatin. Drugs Aging 14:459–475. https://doi.org/10.2165/00002512-199914060-00006

239. Branca JJV, Carrino D, Gulisano M, et al (2021) Oxaliplatin-Induced Neuropathy: Genetic and Epigenetic Profile to Better Understand How to Ameliorate This Side Effect. Front Mol Biosci 8:

240. Stankovic JSK, Selakovic D, Mihailovic V, Rosic G (2020) Antioxidant Supplementation in the Treatment of Neurotoxicity Induced by Platinum-Based Chemotherapeutics—A Review. Int J Mol Sci 21:7753. https://doi.org/10.3390/ijms21207753

241. Chen X, Wang H, Zhang Z, et al (2022) Case Report: Oxaliplatin-Induced Third-Degree Atrioventricular Block: First Discovery of an Important Side-Effect. Front Cardiovasc Med 9:

242. Jansook P, Ogawa N, Loftsson T (2018) Cyclodextrins: structure, physicochemical properties and pharmaceutical applications. Int J Pharm 535:272–284. https://doi.org/10.1016/J.IJPHARM.2017.11.018

243. Lamas GA, Navas -Acien Ana, Mark DB, Lee KL (2016) Heavy Metals, Cardiovascular Disease, and the Unexpected Benefits of Chelation Therapy. J Am Coll Cardiol 67:2411–2418. https://doi.org/10.1016/j.jacc.2016.02.066

244. Mohr I, Weiss KH (2019) Current anti-copper therapies in management of Wilson disease. Ann Transl Med 7:S69–S69. https://doi.org/10.21037/atm.2019.02.48

245. Aaseth J, Skaug MA, Cao Y, Andersen O (2015) Chelation in metal intoxication—Principles and paradigms. J Trace Elem Med Biol 31:260–266. https://doi.org/10.1016/j.jtemb.2014.10.001

246. Lumholdt LR, Holm R, Jørgensen EB, Larsen KL (2012) In vitro investigations of α-amylase mediated hydrolysis of cyclodextrins in the presence of ibuprofen, flurbiprofen, or benzo[a]pyrene. Carbohydr Res 362:56–61. https://doi.org/10.1016/j.carres.2012.09.018

247. Tang GP, Guo HY, Alexis F, et al (2006) Low molecular weight polyethylenimines linked by β-cyclodextrin for gene transfer into the nervous system. J Gene Med 8:736–744. https://doi.org/10.1002/jgm.874

248. Mashabela LT, Maboa MM, Miya NF, et al (2022) A Comprehensive Review of Cross-Linked Gels as Vehicles for Drug Delivery to Treat Central Nervous System Disorders. Gels 8:563. https://doi.org/10.3390/gels8090563

249. Deschamps P, Kulkarni PP, Gautam-Basak M, Sarkar B (2005) The saga of copper(II)–l-histidine. Coord Chem Rev 249:895–909. https://doi.org/10.1016/J.CCR.2004.09.013

250. Flancbaum L, N. Brotman D, Fitzpatrick JC, et al (1990) Existence of carcinine, a histamine-related compound, in mammalian tissues. Life Sci 47:1587–1593. https://doi.org/10.1016/0024-3205(90)90188-W

251. Babizhayev MA (2006) Biological activities of the natural imidazole-containing peptidomimetics n-acetylcarnosine, carcinine and l-carnosine in ophthalmic and skin care products. Life Sci 78:2343–2357. https://doi.org/10.1016/J.LFS.2005.09.054

252. Solana-Manrique C, Sanz FJ, Martínez-Carrión G, Paricio N (2022) Antioxidant and Neuroprotective Effects of Carnosine: Therapeutic Implications in Neurodegenerative Diseases. Antioxidants 11:848. https://doi.org/10.3390/antiox11050848

253. Árkosi Z, Paksi Z, Korecz L, et al (2004) Reinvestigation of the copper(II)–carcinine equilibrium system: “two-dimensional” EPR simulation and NMR relaxation studies for determining the formation constants and coordination modes. J Inorg Biochem 98:1995–2005. https://doi.org/10.1016/j.jinorgbio.2004.09.002

254. Babizhayev MA, Semiletov YA, Lul’kin YA, et al (2005) 3D molecular modeling, free radical modulating and immune cells signaling activities of the novel peptidomimetic l-glutamyl-histamine: possible immunostimulating role. Peptides 26:551–563. https://doi.org/10.1016/j.peptides.2004.11.012

255. Innovative Vision Products, Inc., 3511 Silverside Road, Suite 105, County of New Castle, Delaware USA., Ma B (2017) Treatment of Skin Aging and Photoaging with Innovative Oral Dosage Forms of Non-Hydrolized Carnosine and Carcinine. Int J Clin Dermatol Res 116–143. https://doi.org/10.19070/2332-2977-1700031

256. Wang M, Jin Z, Liu L, et al (2018) Inhibition of cyclodextrins on the activity of α-amylase. J Incl Phenom Macrocycl Chem 90:351–356. https://doi.org/10.1007/S10847-018-0789-X/FIGURES/7

257. Bonomo RP, D'Alessandro F, Grasso G, et al (2008) Carcinine-β-cyclodextrin derivatives as scavenger entities of {radical dot}OH radicals and SOD-like properties of their copper(II) complexes. Inorganica Chim Acta 361:1705–1714. https://doi.org/10.1016/j.ica.2007.01.021

258. Sarkar B, Wigfield Y (1967) The Structure of Copper(II)-Histidine Chelate. J Biol Chem 242:5572–5577. https://doi.org/10.1016/s0021-9258(18)99395-6

259. Mesu JG, Visser T, Soulimani F, et al (2006) New insights into the coordination chemistry and molecular structure of copper(II) histidine complexes in aqueous solutions. Inorg Chem 45:1960–1971. https://doi.org/10.1021/IC051305N/SUPPL_FILE/IC051305NSI20060111_110524.PDF

260. Picker SD, Fridovich I (1984) On the mechanism of production of superoxide radical by reaction mixtures containing NADH, phenazine methosulfate, and nitroblue tetrazolium. Arch Biochem Biophys 228:155–158. https://doi.org/10.1016/0003-9861(84)90056-0

261. Erxleben A (2018) Transition metal salen complexes in bioinorganic and medicinal chemistry. Inorganica Chim Acta 472:40–57. https://doi.org/10.1016/j.ica.2017.06.060

262. Zhang Y, Gong F, Wu Y, et al (2021) Poly-β-cyclodextrin Supramolecular Nanoassembly with a pH-Sensitive Switch Removing Lysosomal Cholesterol Crystals for Antiatherosclerosis. Nano Lett 21:9736–9745. https://doi.org/10.1021/acs.nanolett.1c03664

263. Shang L, Wang Q, Chen K, et al (2017) SPIONs/DOX loaded polymer nanoparticles for MRI detection and efficient cell targeting drug delivery. RSC Adv 7:47715–47725. https://doi.org/10.1039/C7RA08348C

264. Zhang J, Fu Y, Chowdhury MH, Lakowicz JR (2007) Enhanced Förster Resonance Energy Transfer on Single Metal Particle. 2. Dependence on Donor−Acceptor Separation Distance, Particle Size, and Distance from Metal Surface. J Phys Chem C 111:11784–11792. https://doi.org/10.1021/jp067887r

265. Carstea ED, Morris JA, Coleman KG, et al (1997) Niemann-Pick C1 Disease Gene: Homology to Mediators of Cholesterol Homeostasis. Science 277:228–231. https://doi.org/10.1126/science.277.5323.228

266. Dahl NK, Reed KL, Daunais MA, et al (1992) Isolation and characterization of Chinese hamster ovary cells defective in the intracellular metabolism of low density lipoprotein-derived cholesterol. J Biol Chem 267:4889–4896. https://doi.org/10.1016/S0021-9258(18)42914-6

267. dos Santos C, Buera MP, Mazzobre MF (2011) Phase solubility studies and stability of cholesterol/β-cyclodextrin inclusion complexes. J Sci Food Agric 91:2551–2557. https://doi.org/10.1002/jsfa.4425

268. Vruchte D te, Speak AO, Wallom KL, et al (2014) Relative acidic compartment volume as a lysosomal storage disorder–associated biomarker. J Clin Invest 124:1320–1328. https://doi.org/10.1172/JCI72835

269. Kou L, Sun J, Zhai Y, He Z (2013) The endocytosis and intracellular fate of nanomedicines: Implication for rational design. Asian J Pharm Sci 8:1–10. https://doi.org/10.1016/j.ajps.2013.07.001

270. Shi D, Mi G, Bhattacharya S, et al (2016) Optimizing superparamagnetic iron oxide nanoparticles as drug carriers using an in vitro blood–brain barrier model. Int J Nanomedicine 11:5371–5379. https://doi.org/10.2147/IJN.S108333

271. Pinheiro RGR, Coutinho AJ, Pinheiro M, Neves AR (2021) Nanoparticles for Targeted Brain Drug Delivery: What Do We Know? Int J Mol Sci 22:11654. https://doi.org/10.3390/ijms222111654

272. Li W, Zheng C, Pan Z, et al (2016) Smart hyaluronidase-actived theranostic micelles for dual-modal imaging guided photodynamic therapy. Biomaterials 101:10–19. https://doi.org/10.1016/j.biomaterials.2016.05.019

273. Glauert AM, Lewis PR (2014) Biological Specimen Preparation for Transmission Electron Microscopy. In: Biological Specimen Preparation for Transmission Electron Microscopy. Princeton University Press

274. Sherman H, Rossi AE (2019) A Novel Three-Dimensional Glioma Blood-Brain Barrier Model for High-Throughput Testing of Tumoricidal Capability. Front Oncol 9:

275. Cecchelli R, Aday S, Sevin E, et al (2014) A Stable and Reproducible Human Blood-Brain Barrier Model Derived from Hematopoietic Stem Cells. PLOS ONE 9:e99733. https://doi.org/10.1371/journal.pone.0099733

276. Miyamoto M, Naka K, Tokumizu M, Saegusa T (1989) End capping of growing species of poly(2-oxazoline) with carboxylic acid: a novel and convenient route to prepare vinyl- and carboxy-terminated macromonomers. Macromolecules 22:1604–1607. https://doi.org/10.1021/ma00194a016

277. Viale M, Cordazzo C, de Totero D, et al (2011) Inhibition of MDR1 activity and induction of apoptosis by analogues of nifedipine and diltiazem: an in vitro analysis. Invest New Drugs 29:98–109. https://doi.org/10.1007/s10637-009-9340-7

278. N G, K B, Cb B (1997) Absence of functional CD44 hyaluronan receptor on human NMYC-amplified neuroblastoma cells. Cancer Res 57:

279. Oliveri V, Puglisi A, Viale M, et al (2013) New Cyclodextrin-Bearing 8-Hydroxyquinoline Ligands as Multifunctional Molecules. Chem – Eur J 19:13946–13955. https://doi.org/10.1002/chem.201300237

280. Mosmann T (1983) Rapid colorimetric assay for cellular growth and survival: Application to proliferation and cytotoxicity assays. J Immunol Methods 65:55–63. https://doi.org/10.1016/0022-1759(83)90303-4

281. Cardullo N, Spatafora C, Musso N, et al (2015) Resveratrol-Related Polymethoxystilbene Glycosides: Synthesis, Antiproliferative Activity, and Glycosidase Inhibition. J Nat Prod 78:2675–2683. https://doi.org/10.1021/acs.jnatprod.5b00619

282. Cardullo N, Barresi V, Muccilli V, et al (2020) Synthesis of Bisphenol Neolignans Inspired by Honokiol as Antiproliferative Agents. Molecules 25:733. https://doi.org/10.3390/molecules25030733

283. Barresi V, Trovato-Salinaro A, Spampinato G, et al (2016) Transcriptome analysis of copper homeostasis genes reveals coordinated upregulation of SLC31A1,SCO1, and COX11 in colorectal cancer. FEBS Open Bio 6:794–806. https://doi.org/10.1002/2211-5463.12060

284. Viale M, Giglio V, Monticone M, et al (2017) New doxorubicin nanocarriers based on cyclodextrins. Invest New Drugs 35:539–544. https://doi.org/10.1007/s10637-017-0461-0